Medical University of South Carolina

MEDICA

2021

Uncovering the 'Hidden Fibrosis' of Pediatric Congenital Aortic Valve Stenosis via Targeted Mass Spectrometry Approaches

Cassandra Lucille Clift
Medical University of South Carolina

Follow this and additional works at: https://medica-musc.researchcommons.org/theses

"Uncovering the 'Hidden Fibrosis' of Pediatric Congenital Aortic Valve Stenosis via Targeted Mass Spectrometry Approaches"

by

Cassandra Lucille Clift

A dissertation submitted to the faculty of the Medical University of South Carolina in partial fulfillment of the requirements for the degree of Doctor of Philosophy in the College of Graduate Studies

Dept. of Cell and Molecular Pharmacology and Experimental Therapeutics

August 2021

Approved By:

Chairman, Advisory Committee _____

Peggi Angel

Co-Chairman _____

Richard Drake

_____

Lauren Ball

_____

Amy Bradshaw

_____

Don Menick

Acknowledgements

Table of Contents

Contents

LIST OF FIGURES

LIST OF TABLES

LIST OF ABBREVIATIONS

ECM: Extracellular Matrix

GAG: Glycosaminoglycan

CAVS: Congenital Aortic Valve Stenosis

PTM: Post-Translational Modification

HYP: Hydroxyproline

BAV: Bicuspid Aortic Valve

AV: Aortic Valve

PV: Pulmonary Valve

VEC: Valvular Endothelial Cell

VIC: Valvular Interstitial Cell

CNCCs: Neural Crest Cells

SHF: Second Heart Field

FACIT: Fibril Associated Collagens with Interrupted Triple Helices

Multiplexin: multiple triple helix domains and interruptions

EndMT: Endothelial to Mesenchymal Transition

MMPs: Matrix Metalloproteinases

TIMPs: Tissue Inhibitors of Metalloproteinases

ROS: Reactive Oxygen Species

MALDI: Matrix Assisted Laser Desorption Ionization

FT-ICR: Fourier Transform Ion Cyclotron Resonance

TOF: Time of Flight

TIMS: Trapped Ion Mobility Spectrometry

CHCA: α-Cyano-4-hydroxycinnamic acid

COLase3: Collagenase Type III

RIFD: Regions of Increased Collagen Fiber Density

ABSTRACT

CASSANDRA LUCILLE CLIFT. Uncovering the 'Hidden Fibrosis' of Pediatric Congenital Aortic Valve Stenosis via Targeted Mass Spectrometry Approaches (Under the direction of PEGGI ANGEL and RICHARD DRAKE).

Congenital aortic valve stenosis (CAVS) affects up to 10% of the world population without medical therapies to treat the disease. New molecular targets are continually being sought that can halt CAVS progression, particularly in pediatric patients where bioengineered solutions are not ideal. Collagen deregulation is a hallmark of pediatric CAVS yet remains mostly undefined. Here, histological studies were paired with high resolution accurate mass (HRAM) collagen-targeting proteomics and imaging mass spectrometry to investigate collagen fiber production with localized collagen regulation associated with human AV development and pediatric end-stage CAVS (pCAVS). Histological studies identified collagen fiber realignment and unique regions of high-density collagen in pCAVS. Proteomic analysis reported specific collagen peptides are modified with hydroxylated prolines (HYP), a post-translational modification critical to stabilizing the collagen triple helix. Quantitative data analysis reported significant regulation of collagen HYP sites across patient categories, providing insight to collagen-cell receptor binding.

In addition to chromatographic-based proteomic analysis, Matrix Assisted Laser Desorption Ionization imaging mass spectrometry (MALDI-IMS) methods were developed to further address the localized structure-function relationship of the extracellular matrisome in aortic valve tissue. Here, a novel serial enzyme strategy was developed to define the glycosaminoglycome, N-glycome, as well as the collagen and elastin proteome

from a single tissue section for MALDI-IMS applications. These multimodal MALDI-IMS techniques could define unique matrisome profiles based off tissue hemodynamics, as well as identify collagen localization unable to be detected by tradition histopathology. Finally, as a proof-of-concept study toward biomaterials applications, MALDI-IMS was used to localize human collagen-based hydrogels within an infarcted mouse heart, as well as analyze its impact on endogenous extracellular matrix (ECM) remodeling.

The studies presented in this dissertation are the first of their kind to detail the collagen types and HYP modifications associated with human AV development and pediatric CAVS. Additionally, our findings show evidence for the use of MALDI-IMS in assessing the therapeutic application of collagen-based biomaterials. We anticipate that this study will inform new therapeutic avenues that inhibit valvular degradation in pCAVS and bioengineered options for valve replacement.

Chapter 1: Literature Review

1.1 Valvular Anatomy & Fibrotic Diseases

1.1.1 Structural Extracellular Matrix in Aortic Valve Development

Just after the initial heart contractions occur (E16-22 days) in early embryonic valve development, the three endocardial aortic cushions form (E31-35 days) and begin to elongate as hydrophilic ECM proteins are deposited. At this time, the aortic valves (AVs) are primarily composed of the glycosaminoglycan (GAG) hyaluronan (HA), lined by endothelial cells [1-5]. Between E35-37, hyaluronan synthase-2 (Hyal2) activity (which catalyzes formation of the HA polymer) is elevated, forming a "jelly" in which cells of the developing AVs undergo endothelial to mesenchymal transition (EndMT)[1, 5-7]. During EndMT, cell populations concurrently proliferate and apoptose, additional ECM is deposited, and the endocardial cushion elongates (E37-42 days) [8]. This results in two unique populations of cells – valvular endothelial cells (VECs) and valvular interstitial cells (VICs). As healthy valves are avascular, VECs are responsible for regulating nutrients and biochemical signals from the blood to the VICs [9]. The VICs are responsible for organizing, maintaining, and remodeling ECM proteins [10-14]. Studies show proper VEC-VIC crosstalk is essential to valvular health [15-17]. Additionally, cardiac neural crest cells (CNCCs) and second heart field (SHF) precursors migrate to the newly formed endocardial cushions, promoting cell apoptosis and ECM regulation of the developing valve [13, 18-20]. Recent literature also shows a population of mesenchymal stem cells present within the aortic valve [21].

In late embryonic AV development (E20-39 weeks for humans) the valve leaflet stratifies into three distinctive layers – the collagen rich fibrosa, the GAG rich spongiosa, and the elastin rich ventricularis. Throughout development, the composition of GAGs changes. The once prominent HA is supplemented with chondroitin sulfate proteoglycans,

Figure 1. Flowchart displaying distribution of extracellular matrix proteins during the stages of valve development, from early embryonic through the mature aortic valve. GAG = glycosaminoglycan. SHF = second heart field; CNCC = cardiac neural crest cells; EndMT = Endothelial to mesenchymal transition. VIC = valvular interstitial cells. (Development information edited from Combs et al, 2009. ECM information edited from Peacock et al, 2008.)
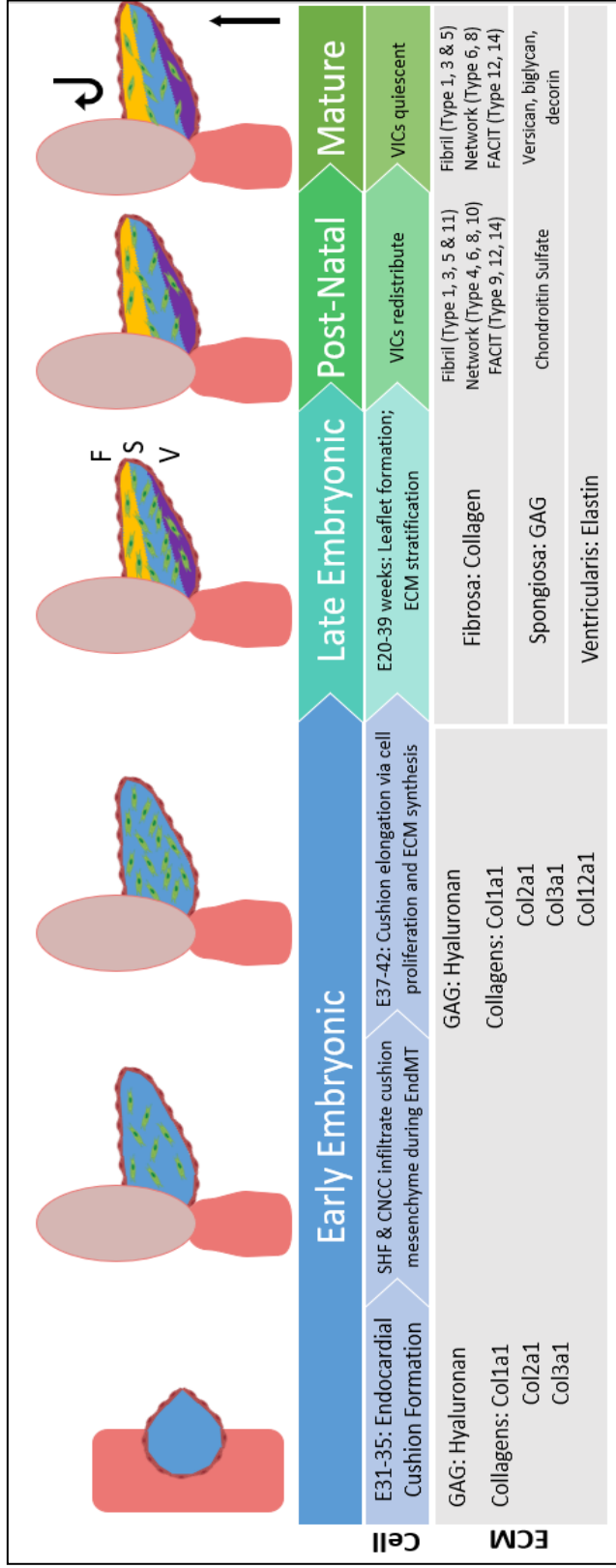
such as aggrecan and versican, as well as small leucine-rich proteoglycans such as biglycan and decorin, amongst others [22, 23]. Similarly, collagen type distributions change over the course of development. While fibril-type collagens I, II, and III are dominant in early development, later embryonic and post-natal development involves the deposition of network and FACIT type collagens as well (**Fig. 1; Section 1.2.1**). This data, however, is interpreted from mouse studies [22]. Similar studies have yet to be done extensively on post-natal human aortic valve tissues. In this review we focus on collagen-related changes in heart valve development and disease.

1.1.2 Congenital Aortic Valve Stenosis

Currently, congenital aortic valve stenosis (CAVS) accounts for 10% of all congenital heart defect cases, which affect 1 in 150 people [24]. CAVS progresses as an obstructive narrowing of the aortic opening due to enlargement of the AV leaflets through deregulated ECM production and results in heart failure. Approximately 90% of all CAVS cases are due to bicuspid aortic valve (BAV) [25]. Disease loci associated with BAV have been found on chromosomes 18q, 13q, and 5q and while the inheritability of BAV within certain families suggest a genetic component, only mutations in NOTCH1 signaling have been attributed directly to valvular stenosis [26, 27]. However, other genetic mutations have been associated with BAV-aortopathy [28]. Despite other genes being implicated in murine models of BAV (such as eNOS and GATA6 mutations), these have not been correlated to the valvular stenosis in humans [29, 30].

Most CAVS patients (90%) are stable until adulthood, where severe calcific lesions are the primary cause of valve replacement. In adult fibrocalcific AVS (FAVS), inflammation and adhesion are shown to increase along with mast cell infiltration [31, 32]. Adult cases also tend to have comorbidities, such as high blood pressure or coronary

artery disease, further confounding research [26]. The remaining 10% of all CAVS patients are pediatrics, where end-stage is defined by excessive ECM deposition, and no calcification (pCAVS) [31, 33]. A main feature of both pediatric and adult CAVS is bicuspid aortic valve. The dominant BAV morphology across all patients is the fusion of the right- and left-coronary leaflets (71%) [34]. The differences in dominant cusp fusion morphology (RL, RN, NL) has not been determined between pediatric and adult calcific CAVS. However, right and non-coronary fusion (R-N) are the most common predictor of pediatric valve dysfunction and intervention (35% of patients; >4-fold intervention increase) [35]. Literature acknowledges a distinct molecular profile between pediatric and adult calcific CAVS [31], but the molecular mechanisms behind the rapid progression of pCAVS remain to be elucidated.

1.1.3 CAVS Changes to Valvular ECM Architecture

A loss of ECM stratification is seen in both pediatric and adult cases of CAVS [31]. Hutson et al. set out to quantified changes in collagen architecture associated with adult calcific cases of CAVS [36]. Their group showed that collagen content in the GAG-dominant spongiosa layer doubled in the disease state. Collagen fiber width and density also significantly increased, with lysyl oxidase expression also increasing in the diseased fibrosa layer [36], however the corresponding post-translational modification (PTM) allysine has not yet been defined. Transcriptional studies in mice have shown that loss of crosslinking collagens 5a1 and 11a1 alters expression of fibrillar collagens 1 and 3, resulting in AV stenosis [26]. Similarly, CAVS studies of elastin, which crosslinks to collagen, has shown increased fragmentation correlated to increased calcification [37]. Fragmented elastin has also been seen in pediatric CAVS [31]. Di Vito et al recently published an extensive review of ECM alterations in adult calcific valve disease [38]. However, differential expression of collagen subtypes remains to be as extensively

explored in pediatric cases of CAVS. Our group recently reported that total collagen deposition increases in pediatric CAVS, along with collagen fiber misalignment relative to the endothelium, and regions of increased collagen fiber density (or "plaques"), as measured by histology [39]. ECM targeted proteomics in this study showed differential collagen subtype regulation (in α1(I), α2(I), α1(V), α2(V)) between pCAVS, normal, and tricuspid aortic valve insufficiency [39].

1.1.4 Hemodynamic Regulation in Aortic Valve Development & Disease

During late embryonic development and post-natal development, peak shear stresses range from 30-1500 dynes/cm^2 (with higher values occurring during stenosis), and these hemodynamics play a significant role in valve structure [10, 40]. During systole, shear stresses are unidirectional and pulsatile, stretching the leaflet, which primarily affects the elastin rich ventricularis. Contrarily, the aortic valve during diastole requires the stiffer collagen rich fibrosa to maintain structure and function, as oscillatory vortexes develop behind the leaflet. The GAG rich spongiosa act as shock absorbers during the entire cardiac cycle [41]. Hemodynamics play a role in collagen alignment in the healthy valve, which has been shown to align along the circumferential axis, parallel to the endothelium [39, 42]. In addition to hemodynamics, emerging subpopulations of VICs and differentially expressed genes can play a role in ECM stratification. In the ventricularis, Notch1 expression is dominant and may play a role in elastin deposition [1, 43]. In the spongiosa layer, BMP2 signaling promotes Sox9 expression and deposition of proteoglycans, such as aggrecan, versican, chondroitin sulfate, and decorin [1, 44]. In the fibrosa layer, Wnt signaling has been linked to promote the expression of fibroblast related ECM components such as fibrillar collagens Type I and III and fibronectin [1, 45].

CAVS-mediated alteration in hemodynamics influences all levels of molecular expression and feeds forward into deregulating the valvular structure [34]. Velocity field analysis has shown that the total kinetic energy, Reynolds shear stress, and viscous shear stress are all significantly higher in cases of BAV as compared to the normal tricuspid configuration, localized primarily to the fibrosa [41]. In adult calcific CAVS, the fused leaflets have a higher incidence of calcific nodule formation compared to the non-fused leaflet, correlating to an increase in shear stress [34]. Similarly, ex vivo analysis shows that abnormal hemodynamic shear stress may contribute to early adults CAVS pathogenesis [46]. During in vitro bioreactor conditioning studies, increased pressure has been directly attributed to increased leaflet strain [47]. Studies in VICs under variable strain (10, 14, and 20%) show significant increase in [^{3}H]-proline incorporation, indicating increased collagen synthesis [47]. These studies offer insight into how the increased shear stresses seen in BAV contribute to ECM deposition in CAVS.

Transcriptional regulation of critical genes differs during strain as well. For example, Ku et al showed Col3a1 is significantly upregulated as compared to a steady regulation of Col1a1 under strain [48]. Altered differentiation of VICs under strain shows an increase in expression of VCAM-1 (responsible for immune infiltration and cell migration) and a decrease in osteopontin (shown to be a calcification protectant) [47, 49]. During progression of CAVS, VIC undergo activation and become myofibroblast-like cells that express matrix metalloproteases (MMPs), cathepsins, and pro-inflammatory cytokines which can further stimulate osteogenic differentiation. While enzyme-induced turnover of ECM is essential in a healthy valve to maintain homeostasis under shear stresses, myofibroblast induced-remodeling is attributed excessive ECM deposition in CAVS [50]. To date, all hemodynamic studies have been completed on adult VICs or

VICs with osteogenic *in vitro* conditions, leaving pediatric hemodynamic regulation to be elucidated.

1.1.5 Myocardial Fibrosis and Bioengineered Solutions

As a proof-of-concept study, Chapter 6 of this dissertation outlines the use of targeted imaging mass spectrometry approaches to characterize collagen-subtypes in myocardial fibrosis treated with collagen-based hydrogels. While not specific to valvular disease, this proof-of-concept study aimed to use targeted imaging mass spectrometry approaches to distinguish between collagen subtypes originating from a human-collagen derived hydrogel as opposed to the native mouse myocardial fibrosis. To frame the context of that study, a brief outline of myocardial fibrosis follows.

Coronary artery disease is a common cardiovascular disease that leads to myocardial infarction. After an infarct, the myocardium undergoes active remodeling in three phases: 1) the inflammatory phase, when neutrophils infiltrate the damaged myocardium, secreting anti-inflammatory cytokines; 2) the reparative phase, when myofibroblasts replace lost ventricular tissue with ECM; and 3) maturation, when a stable, collagen-dense scar is formed [51]. This scar tissue formation is essential to prevent rupture of the myocardium, but an over-active fibrotic response leads to cardiac rhythmic dysfunction and heart failure [52]. With limited pharmacotherapeutic options, current research is aimed at restoring ECM within the infarct myocardium to prevent fibrosis and improve cardiac function [53, 54]. Injectable hydrogels are a promising therapeutic application to alleviate early stages of pathological myocardial remodeling [55]. Injectable biomaterials are composed of either synthetic or degradable matrix and can be seeded with therapeutic stem cells, growth factors, particles, and pharmacotherapeutics to encourage endogenous repair and provide structure support during healing [53, 55].

1.1.6 Current Treatment Options and Bioengineered Solutions

Despite the clinical significance of CAVS, surgical valve replacement and repair is still the only available treatment. Mechanical-based engineered valve replacement devices are not suitable for young children as they lack any growth potential as well as requiring lifelong anti-coagulation therapy[56]. However, in older pediatric cases, there has been success with a 55-90% freedom from reoperation at 15 years[57]. Tissue engineered valve replacements are currently unavailable in sizes smaller than 19mm, making them unsuitable for young pediatric cases. Like mechanical prosthesis, there is a lack of growth potential with tissue engineered replacements, but anti-coagulation therapy is not required[58]. Survival was reported to be 85% at 10 years, however the rate of reoperation is high – 65% at 10 years, with the median longevity being only 7.5 years[57]. Homografts are able to retain normal hemodynamic profiles over time, with small sizes available for small children. Homografts also do not require anti-coagulation therapy and have the added advantage of being more resilient to infection that tissue engineered prosthesis, however there is a limited donor pool [57, 59]. Despite these advantages, homografts show only a 60% survival at 10 years, and 30% at 20 years, and are not ideal for pediatric cases [60].

The limitations listed above are why the Ross procedure, which switches the native pulmonary valve into the aortic valve position, is currently the preferred treatment amongst young pediatric cases [61-63]. However, this procedure does not come without complications: children having undergone this procedure have a 14.3% mortality rate in the first year – after surviving the first year, the likelihood of the child needing an aortic or pulmonary reintervention later in life is 15.3% and 27.5%, respectively [57].

Mechanisms of failure of pulmonary valves in the aortic position during Ross procedures can be inferred from studies regarding proteomic differences between the two valves. Ikhumetse et al. found that when pulmonary derived VICs were exposed to cyclic aortic pressures, sulfated GAGs as well as collagen synthesis were significantly increased [64]. Angel et al aimed to characterize the difference between AV and PV via chromatographic proteomic approaches. The study found that only 50% of the proteome of the AV is shared with the PV. The PV proteome was abundant in hypoxia associated proteins such as H2AX but only sparingly expressed proteins that may be critical to healthy AV function, such as MFGe8 and Emilin-1 [65]. The role of PTMs in valvular failure has not been extensively explored.

1.2 Extracellular Matrix: Translational and Post-Translational Regulation in Fibrotic Disease

1.2.1 Collagen Sub-Types

The collagen superfamily consists of 28 sub-types, all sharing a common structural motif – the triple helical domain [66-69]. The triple helical domain of collagen sequences contains (Gly-X-Y)$_n$ repeats, where X and Y can be any amino acid. Most commonly, X corresponds to Proline (in 28% of cases) and Y corresponds to 4-hydroxyproline (in 38% of cases) with G-P-HYP being the most common repeating G-X-Y sequences (in 10.5% of cases)[69]. 3-hydroxyproline residues are less common that 4-hydroxyproline residues, but they have been identified in fibril types collagens, described below.

The collagen superfamily sub-types can be split into several subfamilies: fibril type, FACIT (fibril associated collagens with interrupted triple helices); membrane, multiplexin (multiple triple helix domains and interruptions), and other. Triple helical domains within these collagen regions are bracketed and intertwined with non-triple helical domains,

which include: laminin G-like domains, von Willebrand factor type A domains, fibronectin domains, nidogen binding domains, and endostatin domains, amongst others[70].

Collagen biosynthesis has been most extensively described in fibril type collagens [67]. Within the cell, pro-collagen molecules are translated, which consist of an N-terminal pro-peptide, and N-terminal telo-peptide, the central triple helical region, a C-terminal telopeptide and a C-terminal pro-peptide [66, 67]. Before secretion, these alpha chains are post-translationally modified, as described in Chapter 1.2.2. Still in the endoplasmic reticulum, once post-translationally modified, an essential protein HSP47 (heat shock protein 47) binds to procollagen and acts as a stabilizer and chaperon for extracellular secretion, along with other collagen chaperones, such as SPARC [67]. Before collagen fibril formation, propeptides of procollagens are cleaved by proteinases – the N-terminal propeptide by ADAMTS, and the C-terminal propeptide by BMP-1 (or furin, in the case of proα1(V)) [67].

Fibril type collagens are comprised two classes: major fibrils (type I, II, III) and minor fibrils (types V, XI, XXIV, and XXVII) [66, 67]. Fibril subtypes, or "classical collagens" form ordered fibrils from precursors or procollagens, comprising of major and minor fibrillar collagens. The minor fibrillar collagens serve to regulate fiber length and lateral molecular addition[71]. Once assembled, collagen fibrils can range from 15nm to 500nm, depending on the tissue of original, with a distinctive banding pattern occurring every 64 to 67nm [67, 72, 73]. As the name suggests, fibril type collagens associate with FACIT types – IX, XII, XVI, XIX, XX XXI, and XXII. These collagens are associated with general ECM stabilization and integrity. Membrane collagens are comprised of subtypes XIII, XVII, XXIII, and XVII. These are transmembrane proteins with functional interaction both with other cell-surface receptors and ECM proteins[74]. Finally, collagens XV and XVIII are

multiplexins. This collagen family consists of homotrimers that carry glycosaminoglycan chains, so are also proteoglycans[66, 68]. Other proteoglycan collagens are IX, XII, and XIV. Diseases of collagen subtypes are further reviewed in section 1.2.7.

1.2.2 Collagen Post-Translational Modifications

Extracellular matrix proteins make up the bulk of valvular tissues, and these proteins are abundantly post-translationally modified (**Fig. 2**). Essential post-translational modifications of collagen include hydroxylation of proline [75-77], N-glycosylation[77, 78], proteinase-initiated cleavage of the N- and C-terminal pro-peptides[77, 79], and oxidation of lysine[77, 80]. Hydroxylation is a major PTM of collagens that maintains structural integrity of the valve [81]. Hydroxylation of proline and hydroxylation of lysine are the two most abundant PTMs of collagen type proteins [69, 82]. These PTMs are necessary for the organization of collagen's triple helix structure as well as its thermal stability[83, 84]. In both collagen and elastin, hydroxyproline is a well-regulated modification, with between 20-24% of prolines being hydroxylated [69]. Prolyl hydroxylases are responsible for hydroxylation of proline in elastin as well as collagen, with an X-P-G amino acid sequence required substrate in most cases [85]. Elastin studies of the human aorta show that two specific prolines (P190, P615) have the highest degrees
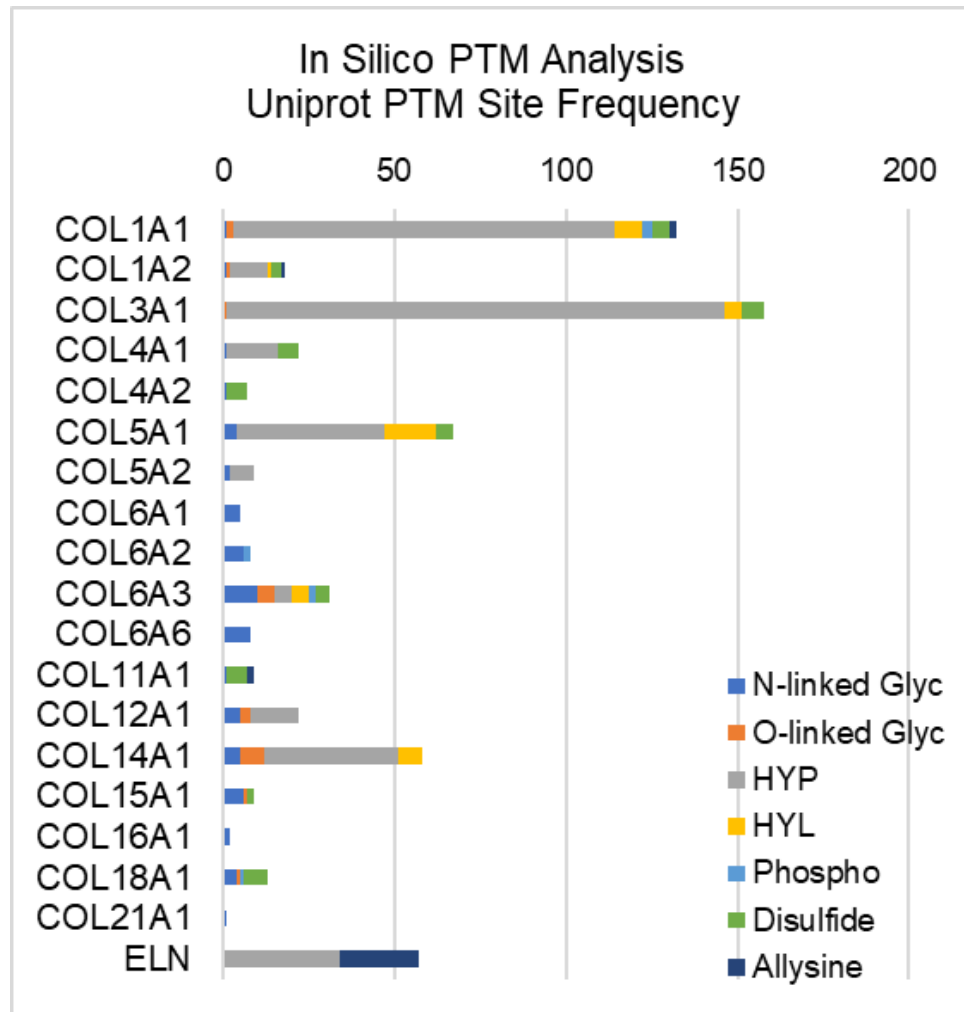
Figure 2: In silico post-translational modification site frequency analysis of valvular structural proteins (collagens and elastin) showing sites PTMs. Glyc: Glycosylation. HYP: Hydroxyproline. HYL: Hydroxylysine. Phospho: Phosphorylation.

of hydroxylation, suggesting site-specific regulation, however this has not been elucidated in the healthy or diseased AV [86]. Similarly, only a single study has attempted to perform site specific hydroxyproline mapping in health or diseased AV [39]. Other PTMs of structural ECM in the valve include O- and N-linked glycosylation, phosphorylation, allysine via Lysyl Oxidase, and collagen-lysyl intermolecular crosslinking (relative abundances via in silico analysis, **Fig. 2**).

1.2.3 Collagen Binding Partners

Collagens in the extracellular space are capability of interacting both to other ECM proteins and transmembrane proteins on the cell surface. In the ECM, collagens are capable of binding to elastin and glycosaminoglycans (as outlined above and in Chapter 1.2.4). Cell-Collagen interactions consistent of integrins, glycoprotein vi, dimeric discoidin receptors (DDR1 and DDR2), and LAIR-1/2, amongst others.

Integrins are a major family of cell-adhesion receptors that do not have kinase activities[87]. Collagens bind to integrins that contain a β1 subunit via their GFOGER sequences (where O is HYP) [67, 88, 89]. Interestingly, there are collagen fragments resulting from MMP degradation that are bioactive and capable of binding to several integrins (αvβ3, αvβ5 α3β1 α5β1)[67]. When bound to collagens, integrins have been shown to act as collagen organizers[72]. Fibril types collagens I-III bind DDR1 and DDR2 via the GVMGFO motif. Intracellularly, DDRs possess tyrosine kinase activities. Extracellularly, DDR1 and DDR2 inhibit collagen fibrillogenesis[90, 91]. Both LAIR-1/2 and glycoprotein VI bind to GPO motifs in collagens, with LAIRs having a higher affinity[92]. Glycoprotein VI is a platelet-unique membrane glycoprotein. Upon binding to collagen, a phosphorylation cascade is initiated by an immunoreceptor tyrosine-based activation motif (ITAM) downstream of GpVI, activating platelet binding within tissues[93]. LAIR-1, or

leukocyte-associated immunoglobulin-like receptor, possesses a single extracellular domain and binds to collagen as an immune receptor[90, 93]. Knowledge of cell-collagen binding domains elucidate further complexities of the extracellular matrix in pCAVS.

1.2.4 Non-Structural Extracellular Matrix

This review thus-far, and this dissertation, primarily focuses on the major structural ECM protein, collagen, and its role in valvular development ad disease. However, minor ECM proteins are critical to valvular development but are unexplored in this dissertation work. These proteins can be split into the follow categories: minor structural ECM proteins (such as vitronectin, fibronection, periostin, osteonectin, osteopontin, aggrecan); basement membrane proteins (laminin, perlecan, nidogen); and ECM remodeling proteins, such as matrix metalloproteinases (MMPs) and their inhibitors (TIMPs). For information regarding these extracellular matrix components in valvular tissues, we point the reader to the following reviews and original research papers [42, 94-102].

1.2.5 Role of PTMs in Cardiac Development and Disease

The role of PTMs in ECM proteins is largely unknown in pCAVS. While the PTM allysine has not been measured directly in CAVS, studies show an increase in the enzyme responsible for catalyzing the reactive aldehyde species, LOX [36]. Similarly, PLOD1, the enzyme responsible for catalyze hydroxylysine residues in collagen, was found to be unchanged in adult CAVS compared to controls [36], however, HYL was not measured directly. While hydroxyproline content has been measured in healthy aortic valves, this is used as a measurement of insoluble collagen content, not in a site-specific analysis [103, 104]. Our group recently reported the first study of collagen HYP quantification and site mapping with human pediatric CAVS tissue [39]. Overall, a reduction of collagen HYP content was seen, particularly in regions within collagen sequence required for integrin and glycoprotein vi binding [39].

Potential modifications of intracellular proteins regulated in the heart can include both enzymatic (such as acetylation, phosphorylation and ubiquitination) and non-enzymatic (such as nitrosylation) post-translational modifications. These PTMs have been mostly explored in age and aging-related myocardial diseases, but remain largely unexplored in pediatric valvular disease. Acetylation of histones 3 and 4 has been reported in CAVs and NCAVs from patients, although significantly higher in CAVs patients [105]. Similarly, acetylation plays a role in modulating the heart's response to I/R injury [106]. Glycogen Synthase Kinase 3β (GSK3β) – which has been found in cardiac fibroblast and implicated in ventricular remodeling – is both phosphorylated and s-nitrosylated in a site-specific manner relevant to its function in cardiac fibrosis [107, 108]. S-nitrosylation of USP9X has been shown to be enriched in NOTCH regulation of valvular calcification [109]. Additionally, studies have shown increases in ubiquitin-mediated proteolysis in heart failure [110]. While these studies are not specific to ECM proteins, data suggested that PTMs may be a potential therapeutic target in cardiac and valvular fibrosis.

1.2.6 Potential role of Oxidative Stress on ECM PTMs

Post-translational regulation via oxidation has been pinpointed as having a major role in other fibrotic diseases [111]. While inflammatory-derived Reactive Oxygen Species (ROS) has been implicated in adult CAVS, ROS is unexplored in pediatric valve disease [38]. Similarly, the role of ROS on PTMs in ECM in valvular development nor disease has been studied. ROS can alter the expression of ECM both by activating transcription factors involved in ECM protein expression (such as TGFB1) as well as modifying ECM proteins post-translationally [111] . Additionally, the hydroxylation of proline and lysine residues of collagen is highly redox dependent. Once lysine is hydroxylated, it serves as a synthesis starting point for proteins responsible for collagen and elastin crosslinking, such as desmosine [82, 111, 112] . Additionally, hydroxylated lysine 2 has been shown to have

glycosyl-transferase activity, serving as an anchor for O-glycosylation modification [69, 82]. In silico analysis of valvular collagen type proteins demonstrates a potential abundance of N- and O-glycosylation sites, amongst other PTMs (**Figure 2**). At high concentrations, ROS can initiate catabolization of these carbohydrate entities [111, 113]. Previously unexplored in pediatric CAVS, a recent publication by Angel et al. shows that N-glycosylation patterns are spatial regulated in aortic valve development and disease, with certain sialyted N-glycans being upregulated [114]. At low concentrations, ROS can induce GAG-degrading enzymes, such as Hyal2, indirectly effecting ECM turnover [23]. Recent studies have shown that GAGs can store growth factors and cytokines in the extracellular space; so, indirectly, depletion of GAGs via Hyal2 may modify receptor binding and activation [115]. ROS can also induced collagen degrading enzymes, such as matrix-metalloproteinase (MMPs), further suggesting a role of oxidative stress in ECM remodeling [116].

1.2.7 Role of ECM regulation and PTMs in Non-Valvular Disease

PTMs of ECM have been linked to various disease states, not limited to fibrotic diseases. While hydroxyproline and hydroxylysine modifications are essential to proper collagen fibril formation, over-hydroxylation of the protocollagen chains can delay collagen polymerization, resulting in altered additional PTMs, such as glycosylation [69, 82, 117]. This perturbs collagen's triple-helical structure further which in turn contributes to various disease states, such as Ehlers-Danlos syndrome and osteogenesis imperfecta [69, 118]. Similarly, under-hydroxylation can destabilize collagen's triple helix, also contributing to disease states, as seen in vitamin C deficiencies leading to scurvy [119]. Hydroxyproline modifications in collagen amongst other proteins has been implicated in oxygen-sensing pathways in cancer cells [120]. Hydroxylysine aldehyde–derived collagen cross-links have been found to be upregulated in lung tumor stroma [121]. Kamel et al shows that increased

hydroxylation of lysine in collagen increases the proliferation rate of uterine fibroids [122]. Additionally, increased tissue stiffness due to over hydroxylation of the ECM may not only contribute to progression of tumors and fibrotic diseases but may also influence diffusion of drug molecules within the disease microenvironment [123, 124]. For these reasons, characterization of not only the ECM, but also its PTMs, are critical for elucidating mechanisms of fibrotic diseases, such as pediatric end-stage CAVS.

1.2.8 Targeting ECM as a Therapeutic Strategy

Identified therapeutic strategies for adult CAVS, such as targeting of circulating lipid levels or osteogenic differentiation of VICs and mineral deposition directly, would not be appropriate for targeting the excessive fibrotic build-up of ECM seen pediatric end-stage [125]. The late diagnosis of fibrotic diseases limits therapeutic intervention before rapid ECM remodeling occurs. The future of fibrotic treatments may rely on proteomic strategies to identify new ECM biomarkers, resulting in earlier detection. Walraven and Hinz propose in their 2018 review that inhibiting fibrosis will depend on two main strategies: 1) targeting the myofibroblasts directly through stimulatory or suppressing cytokines and stimulating apoptosis; and/or 2) targeting the fibrotic ECM directly using targeted proteolytic enzymes [126]. Currently, the only FDA approved drugs on the market to treat any fibrotic disease (idiopathic pulmonary fibrosis) are Nintedanib and Pirfenidone. Previously thought to work through kinase-dependent fibrotic pathways [127], a recent study shows that these drugs inhibit collagen fibril assembly directly [128]. Another proposed anti-fibrotic therapeutic strategy is the targeting of hydroxyprolines via collagen prolyl-4-hydroxylase (CP4H). However, CP4H inhibitors lack selectivity – while promising results are seen *in vivo*, off target affects to redox homeostasis and iron metabolism are also seen [129]. Realistically, the goal of anti-fibrotic therapies in pediatric CAVS may not be to cure stenosis but instead

to delay the severity until patients reach an appropriate age and size for bioengineered options to be used without the need for repeated surgeries.

1.3 Characterization and Identification of the Extracellular Matrisome

While transcriptional regulation of the valvular ECM has been well characterized, low cell density and high ECM content warrant translational level studies. Translational and post-translational regulation of these proteins in pediatric CAVS remains to be fully elucidated, as the majority of literature focuses on adult calcific cases of CAVS. Acquiring information on spatial organization of molecular patterns of ECM proteins and their PTMs is essential to defining both disease and development.

1.3.1 Accessing the Extracellular Matrisome

The ECM proteome in pediatric valvular tissue has been difficult to characterize via conventional tryptic methods due to high levels of intra- and intermolecular crosslinking and PTMs. Brioschi et al published a comparative analysis of gel-based and gel-free proteomic methods to characterize the human mitral valve proteome, showing large variability between the four methods and only 12% of all proteins identified were associated with ECM pathways [130]. Schlotter et al used label-free tryptic proteomics techniques with isolated VICs and micro-dissected valvular tissues. Amongst other findings, they showed that collagen biosynthesis, collagen modification, GAG metabolism, and ECM degradation pathways were enriched in the adult CAVS isolates [131].

While these methods can implicate ECM pathways, ECM proteins specifically are not enriched. After years of advancement in valvular proteomic techniques [132, 133], the Barderas Lab enriched for ECM proteins in their 2D-LC MS/MS method on calcific AVS samples. The group found 13 differentially regulated ECM proteins in the adult calcific CAVS samples compared to controls. Of these, biglycan, periostin, prolargin, decorin, and

lumican (implicated in collagen fiber assembly) formed a protein-protein interaction network cluster. One collagen protein, Col6a1, was identified to be upregulated in adult CAVS [134]. Similarly, Bouchareb et al. used guanidine hydrochloride to extract the ECM for proteomic analysis, and identified two potential biomarkers of adult calcific CAVS – FNDC1 and MXRA5 [135]. While not on native valvular tissue, Syedain et al recently performed ECM enriched proteomic analysis on tri-tube valve conduits to analyze their regenerative capacity [136]. The Hansen Lab recently did a comparative study of a dozen ECM enrichment techniques for proteomics, comparing decellularization, extraction and single-shot analysis methods [137]. Outside of valvular biology, Naba et al have published several papers regarding proteomic ECM enrichment techniques in cancer tissues. Their methods to enrich for and increase identification of ECM peptides consist of: decellularizing fresh or frozen tissues; orthogonal fractionation techniques prior to LC-MS/MS; and including hydroxylation of prolines and lysines as dynamic modifications during searches. However, these enrichment methods are limited to fresh or frozen tissue, excluding formalin fixed paraffin embedded tissues[138-140].

Alternative enrichment approaches used by our group use ECM-targeting enzymes, such as collagenase type III and MMP12, to enzymatically enrich for the extracellular matrix [39, 141-145]. Bacterial collagenases target cleavage to the triple helical regions of proteins[146] – in this way, collagen subtypes as well as other extracellular matrix proteins with triple helical regions can be targeted without the need to decellularize samples. These studies were applied to valvular tissues for LC-MS/MS proteomics, with all proteins identified being of the extracellular matrix, and roughly half being collagen subtypes (Chapter 3) [39].

Serum proteomics is a potential source for biomarker discover in tissue diseases unable to be biopsied, such as valvular disease. To date, no proteomic analysis has been done on serum correlating to pediatric CAVS tissue. However, serum profiling has been done for cardiac failure [147, 148] and other fibrotic diseases such as idiopathic pulmonary fibrosis [149] and liver cirrhosis [150]. While there are many large-scale proteomic studies of serum profiles, ECM proteins are inherently difficult to enrich for [151]. Multimodal - omics approaches, such as epigenomics, transcriptomics, proteomics, and metabolomics, offer promising advantages to traditional characterization techniques, and together moves the field away from strictly characterization towards biomarker and pharmacotherapeutic target discovery, as well as to inform bioengineered solutions [152, 153].

1.3.2 Spatial Localization of the Matrisome using Imaging Mass Spectrometry

Despite advancements in multi-omics techniques listed above, bulk LC-MS/MS proteomics still exclude a key variable of disease pathology – spatial localization of dysregulated ECM within the tissue microarchitecture. Several mass spectrometry techniques exist that link the tissue proteome to its structure. One technique is Matrix-Assisted Laser Desorption/Ionization (MALDI) Imaging Mass Spectrometry (IMS). MALDI-IMS is a robust proteomic technique that spatially maps peptides from histological tissue sections. This is traditionally done by spraying the tissue with a thin, uniform layer of trypsin that, when analyzed in parallel to high resolution accurate mass proteomics, allows for the relative quantitation and localization of tryptic peptides to specific regions of the tissue. In addition to tryptic peptides, novel MALDI-IMS and LC-MS/MS techniques have been developed to specifically map ECM proteins, that until recently were unable to be accessed via conventional proteomic workflows [39, 142, 145, 154-157].

Proteomic imaging via MALDI-IMS may allow for greater protein identification and improved PTM evaluation compared to antibody-based histology strategies. Angel et al outlined the challenges of analyzing cardiac tissues with MALDI-IMS as well as the advancements that have been made in the field [158]. Mourino-Alvarez, et al took advantage of MALDI-IMS technology to characterize fresh frozen calcific AVS tissue. The group was able to visualize m/z peaks correlating to calcified, collagenous, and elastin rich tissue areas. Two peptides of interest were from collagen α3(VI) (responsible for calcium and collagen HYP accumulation deposited via human osteoblast-like cells) and NDRG2 (implicated in p53 mediated apoptosis and mineralization initiation) [159]. Recently, several studies have emerged using MALDI-IMS and other imaging mass spectrometry methods to characterize molecules associated with healthy and diseased aortic valve, such as N-linked glycans [114, 145], lipids [160-162], glycosaminoglycans [145], and peptides [145, 154, 158]. With normal and diseased valve tissue samples becoming less abundant on the bench due to increases in transcatheter aortic valve replacements [163], these multi-modal MALDI-IMS techniques are a promising tool that can be used to characterize ECM deposition and post-translational modifications during CAVS progression, in conjunction to histopathological evaluation [145, 155].

Chapter 2: Central Hypothesis

2.1 Significance

Congenital aortic valve stenosis (CAVS) accounts for 10% of all congenital heart defects, which effect 1 in every 150 people[24]. The dominant phenotype of CAVS is the fusion of two of the three leaflets, causing a narrowing of the aortic orifice, obstructing aortic outflow, leading to left ventricular hypertrophy and heart failure. Despite the clinical significance of this disease, no pharmacotherapeutics exist. The clinical paradigm for treatment is "watch and wait" until surgical valve replacement and repair is necessary to prevent heart failure. Most CAVS patients are stable until adulthood when they develop fibrocalcific AVS (FAVS), where the end-stage is valve calcification[164]. However, ~10% of all CAVS patients are pediatrics (pCAVS), where end-stage is defined as excessive ECM deposition. Bioengineered AV replacements are notably limited for pediatric patients due to their inability to grow with the patient, a lifelong requirement of anti-clotting agents, and repeated surgeries due to valve failure[57]. There remains a critical need to identify pharmacotherapeutic targets in pCAVS that may halt disease progression.

One knowledge gap is of collagen regulation in valvular disease. Collagens are the fundamental scaffolding of valvular structure that influences valvular, and thus cardiac function[8, 22]. Healthy AV development involves a stratification of ECM proteins into three distinct layers linked to a specific function: the elastin-rich ventricularis, glycosaminoglycan-rich spongiosa, and collagen-rich fibrosa (**Fig. 3**). During beginning of systole, pulsatile laminar shear stresses primarily affect the ventricularis – towards the end, vortices develop behind the leaflet, putting stress on the fibrosa. During diastole, the stiffer collagen-rich fibrosa maintains structure as oscillatory vortexes form behind the leaflet and compression occurs. The spongiosa acts as a shock absorber during the cardiac cycle[41]. Pediatric CAVS results in the destratification of collagens with other
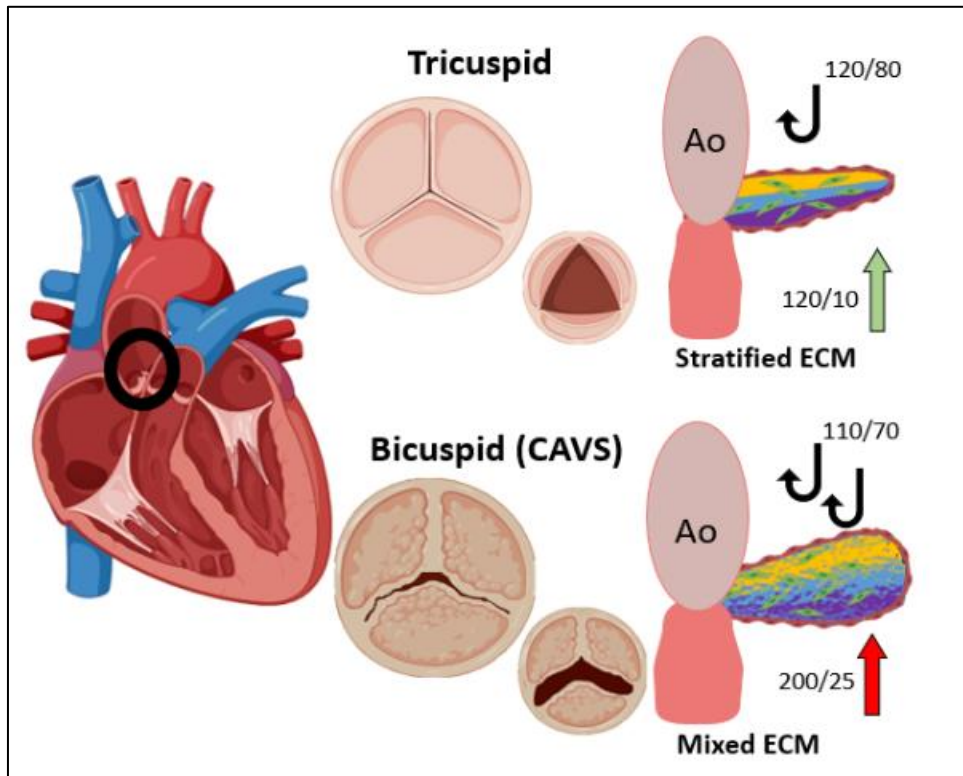
Figure 3: *pCAVS progresses as a destratification of the ventricularis (elastin; purple), spongiosa (GAGs, blue) and fibrosa (collagen, yellow) layers. Ao=aorta. Hemodynamic pressures shown (ex 120/80) are in mmHg.*

ECM proteins, making these layers indistinguishable[8] altering valvular function and leading to cardiac failure.

Multiple collagens are known for their cardiac remodeling potential and are involved in valvular development[2, 165, 166], yet translational and post-translational regulation of these critical proteins due to pCAVS remains unknown. A potential collagen PTM target is hydroxylation of proline (HYP) which is known to be critical to proper stabilization of collagen's triple helical structure, with literature evidence suggesting a role in cell migration and proliferation[167, 168]. Collagen HYP deregulation has been linked to several disease states associated with valvular disorders (i.e., Scurvy, Ehlers-Danlos syndrome, Osteogenesis Imperfecta) but has yet to be explored in pCAVS[117, 119, 169]. Poorly defined regulation of collagen subtypes' PTMs associated with pCAVS limits the use of targeted anti-fibrotics from being developed yet remain promising towards inhibiting the disease[128, 129]. ***The proposed research is significant because it will precisely define molecular mechanisms leading to the rapid dysregulation of collagen subtypes in pCAVS, with a focus on post-translational HYP regulation. In the long term, the proposed research may identify therapeutic targets to halt pCAVS progression, retaining function until bioengineered solutions can be used.***

The work outlined in this dissertation is significant at several levels:

A1) For the first time, we spatially define expression levels of collagen sub-types and HYP peptides in the context of a clinically well-defined cohort of human valve samples, with age matched tissues between 4 patient categories: normal, pCAVS, FAVS, and non-bicuspid pediatric AV insufficiency (AVI). Completion of the proposed work will therefore relate aortic valve pathological ECM structure to clinical function and patient hemodynamic profiles defined via echocardiogram.

A2) This dissertation outlines foundational work for studying collagen stabilizing PTMs in fibrotic cardiovascular disease. Novel information on collagen prolyl hydroxylation and network interactions will initiate studies on signaling factors driving collagen organization and deposition in CAVS.

A3) This work focuses on pediatric, as opposed to adult, end-stage CAVS, for which pharmacotherapeutic development has a significant clinical impact. We aim to change the paradigm of treatment from "watch-and-wait" surgical replacement to biomarker identification and early intervention with antifibrotics targeted to specific modifications of collagen subtypes, to halt progression until bioengineered solutions are feasible.

2.2 Specific Aims

In heart valve biology, organization of the extracellular matrix structure is directly correlated to valve function. This is especially true in cases of congenital aortic valve stenosis (CAVS), in which extracellular matrix (ECM) dysregulation is a hallmark of the disease, eventually leading to left ventricular hypertrophy and heart failure. Most CAVS patients are stable until adulthood when they develop fibrocalcific aortic valve stenosis (FAVS), where the end-stage requiring valve replacement is valve calcification[164]. However, around 10% of all CAVS patients are pediatrics, where end-stage is excessive ECM deposition at a young age, when bioengineered valve replacement options are not suitable. It is not currently known the underlying molecular mechanism that leads to the rapid ECM dysregulation seen in pediatric end-stage CAVS. ECM proteins have been shown to be upregulated in FAVS, but current literature acknowledges a distinct molecular profile between pediatric CAVS and adult FAVS[31]. There is a critical need to define molecular indicators of rapid ECM structural dysregulation in order to develop targeted

treatment which halts CAVS progression in pediatric cases, retaining function until bioengineered solutions can be used.

To address this problem, we will determine regulation of basic scaffold collagens and aortic valve (AV) structure by defining the ECM proteome. These data will be analyzed in a cohort of human AV tissues, with age-matched samples ranging between 2 weeks and 81 years represented, and AV function clinically defined via echocardiogram. We will use a recently developed parallel approach of high-resolution accurate mass chromatographic proteomics and imaging mass spectrometry methods that together report expression levels and spatial localization of collagens and other ECM proteins from thin tissue sections[39, 141-145]. Using these techniques, we will also define specific sites of post-translational modifications (PTMs) on ECM peptides and map the spatial distribution of these peptides across tissues. Our preliminary data suggests that the most abundant collagen subtypes are differentially expressed between normal and CAVS tissues, with collagens XVI, XVIII, and IV differentially abundant in normal tissues, and collagens I, III, and VI in CAVS tissues. Collagen fiber analysis shows that collagen fiber orientation is disorganized in CAVS, with a possible role of collagen stability identified, via hydroxylated proline (HYP) collagen site mapping. For example, site mapping of collagen α1(III) HYPs shows HYP sites are 29% more abundant and differentially localized in normal tissues compared to CAVS. Similarly, 60% of the top 10 differentially expressed peptides in normal tissues are hydroxylated compared to 30% in CAVS. Our approach is novel, as collagen HYP site maps have never been correlated to AV structure or function in normal or CAVS tissues.

Our central hypothesis is that there is a reduction in the extent of proline hydroxylation on primary fibril-type collagen sequences which can be localized to

valve structural abnormalities within pediatric end-stage congenital aortic valve stenosis. Specifically, we propose the following Aims:

Aim 1: Determine levels of collagen fiber and ECM dysregulation in CAVS tissues via conventional histopathological approaches. We hypothesize that increased collagen deposition that occurs in CAVS manifests in dysregulated collagen alignment, maturity, and density. Histopathological evaluation of collagen will be performed with traditional microscopy techniques, such as Picrosirius Red, Movat's Pentachrome, and Second Harmonic Generation Imaging. Results of collagen fiber distribution and density can then be correlated to clinical outcome and hemodynamic profile of pediatric CAVS patients in development and disease.

Aim 2: Determine association between differences in HYP sequences from main valvular scaffold collagens and pediatric end-stage CAVS. We hypothesize that reduction in the number of HYP modifications in primary fibril collagens α1(I), α2(I), and α1(III) correlates to the destabilized trilayer organization of the valvular collagen scaffold in pCAVS, independent of age at end-stage. High resolution, accurate mass (HRAM) tandem mass spectrometry will be used to sequence collagen subtype peptides and identify novel sites of hydroxyproline within the collagen sequence. Identified proteins will be used to predict regulators of CAVS collagen networks.

Aim 3: Define spatial localization of collagen HYP sequences relative to collagen structural signatures in AV development and pathologies. We hypothesize that pathological sites of collagen production within the pCAVS structure involve reduced HYP abundance in fibrillogenesis-associated collagen. State-of-the-art imaging mass spectrometry (IMS) methodologies, coupled with previously acquired peptides databases (Aim 2), will report expression levels and spatial localization of HYP modified collagen

peptides, across a clinically well-defined cohort of human AV tissues. These studies will define the molecular makeup of pCAVS' unique collagen signature, including regions of i) immature collagen production; ii) collagen fiber realignment; and iii) collagen plaques.

Goals and Impact: The overall goal of this project is to understand the molecular mechanisms involved in the rapid ECM dysregulation seen in pCAVS. A long-term goal is to shift the paradigm of pCAVS treatment from "watch-and-wait" until surgical repair is necessary, to pharmacotherapeutic intervention at an earlier diagnosis to attenuate disease progression. The proposed study will 1) Define histopathological variability in collagen deposition between pediatric and adult CAVS patients; 2) identify translational and post-translation regulation of collagen subtypes in pCAVS; 3) spatially define collagen regulators in pCAVS, 4) identify molecular imaging markers for pCAVS. These studies provide a foundation for collagen PTM studies in fibrotic cardiovascular disease.

2.3 Rationale & Approach
2.3.1 Specific Aim 1
Determine levels of collagen fiber and ECM structural dysregulation in CAVS tissues. Rationale: ECM proteins have been identified as dysregulated both in pediatric CAVS and adult FAVS via destratification of the ventricularis, spongiosa, and fibrosa layers[8, 31]. However, a study in human pediatric tissues with this sample size has not been performed in order to correlate ECM deregulation to changes in collagen fiber alignment, maturity, and density. Studies in breast tissue shows metastatic regions differ in collagen fiber maturity, thickness, and orientation[168]. We hypothesize thickened collagen fibers (i.e., "collagen plaques") that correspond to structural anomalies of pediatric CAVS are not detected in normal valves.

Experimental Design: Microscopy-based pathological evaluation will correlate ECM structure to clinical function. Serial tissue sections will be analyzed with three stains: (i)

Movat's Pentachrome, for collagen, elastin, and GAGs; (ii) Picrosirius Red (PSR), which, under polarized light, which elucidates collagen fiber orientation and thickness; and (iii) Herovici, for immature and mature collagen regions. PSR images will be taken with circularly polarized lenses to limit variability due to tissue orientation. Color Deconvolution will be done in ImageJ. CT-FIRE software will be used to quantify collagen fiber width, length, and angle and create a collagen "fiber score" that can be correlated to HYP expression.

Expected Outcomes: Movat's Pentachrome Color Deconvolution will quantify ratios of collagen, GAGs, and elastin over total stained area and identify the dominantly deregulated ECM type in CAVS. Color Deconvolution analysis of polarized PSR and Herovici stains will be able to determine statistical differences in collagen maturity and thickness between normal and CAVS samples. CT-FIRE collagen fiber analysis will be used to annotate vectors corresponding to individual collagen fibers, and create fiber angle distribution histograms, as well as quantify the area and distribution frequency of "collagen plaques" and determine correlation to disease state. This analysis can be done on varying regions of the valve (hinge, belly, and distal tip) in order to elucidate the role of hemodynamics on ECM stratification. The successful completion of this Aim will elucidate the relationship between ECM type dominance, collagen fiber orientation, collagen maturity, and collagen density to CAVS disease state.

Potential Pitfalls & Alternative Strategies: **1)** PSR is not sensitive enough to identify collagen plaques. This can be confirmed orthogonally via a) second harmonic generation imaging, b) IHC staining of main scaffold collagens I and III , and c) Herovici imaging. **2)** Statistical limitations may occur due to small sample sizes (5 normal; 12 CAVS, 5 AVI, 4 FAVS) and biological variability (see **Statistical Considerations**).

2.3.2 Specific Aim 2

Determine association between differences in HYP sequences from main valvular scaffold collagens and pediatric end-stage CAVS. Rationale: Translational and post-translational regulation of collagen subtypes remains mostly unknown in pediatric or adult CAVS. Hydroxylation of prolines (HYP) is a PTM that is critical in stabilizing the triple helix of collagen fibers through hydrogen bonding[21]. Collagen HYP levels are known to drive collagen organization in breast cancer, as well as result in changes to cell migration and proliferation[14,15]. Our preliminary data suggests that HYP levels may differ in pediatric CAVS as well**.** We hypothesize that the deregulation in 1) the number of HYP modifications in fibril type collagens α1(I), α2(I), and α1(III) correlates to the destabilized trilayer organization of the valvular collagen scaffold and is uniformly expressed in pediatric end-stage CAVS, regardless of age at end-stage.

Experimental Design: High resolution accurate mass (HRAM) proteomics will be performed on an expanding cohort of 26 FFPE tissues (**Table 1**). The cohort tissues are from age-matched patients across 4 categories: normal (n=5), pediatric end-stage CAVS (n=11), adult fibrocalcific AVS (FAVS) (n=5), and non-bicuspid aortic valve insufficiency (AVI) (n=5). We have previously shown that deglycosylating with PNGase F before ECM digestion results in greater peptide identification, with the additional benefit of retaining the N-glycan profile for further analysis[22]. Tissue is then digested with Collagenase Type III (COLase3) to detach ECM peptides. The use of COLase3 is a novel technique recently developed by our lab to improve upon the limitations of tryptic ECM digest in FFPE tissues.

Table 1: Current tissue cohort; continuously expanding via biorepository acquisition. normal (n=5), pediatric end-stage CAVS (n=11), adult fibrocalcific AVS (FAVS) (n=5), and non-bicuspid aortic valve insufficiency (AVI) (n=5). BSA: Body Surface Area

Patient Category	Age (years)	Gender	Race/ Ethnicity	BSA (m^2)	Leaflet Morphology	Valve Function
Normal	7.17 ± 7.5	75%M 25%F	75%C 25%L	1.03	Trileaflet	Normal
CAVS	6.90 ± 5.8	70%M 30%F	100%C	0.93	Bicuspid	Stenosis with AVI
AVI	7.35 ± 6.8	-	-	1.35	Trileaflet	AVI (no stenosis)
FAVS	55.75 ± 21.9	100%M	100%C	-	75% Trileaflet/ 25% Bicuspid	Myxomatous Degeneration with Calcification

Label free quantitation LC-MS/MS analysis will be done via data dependent acquisition on an Orbitrap Elite mass spectrometer equipped with a LC Packings U3000 nano-LC system (Thermo Scientific). CID Tandem mass spectra will be initially searched using MaxQuant version 1.6.3.3. MS/MS and then will be re-searched using a subset database of proteins identified at 0.05 FDR for Oxidation (Proline), and a peptide probability of 99%.

Expected Outcomes: The LC-MS/MS data acquired from this Aim will identify an expected 2500 peptides across 44 ECM proteins from our cohort of AV COLase3 digest samples. This peptide data will include corresponding m/z values that will allow us to identify peaks from our MALDI-IMS experiments in **Aim 3**. With the results of this Aim, we will sequence collagen type peptides and identify target novel sites of HYP in collagen that are differentially expressed in pediatric CAVS. With this same dataset, protein interaction networks will be created to determine regulators of CAVS collagen networks (proof of concept, **Fig. 4**[143]). To confirm our LC-MS/MS results, a minimum of one new regulator will be evaluated by IHC. Identified peptide targets (both hydroxyprolinated and unmodified) will be further evaluated via targeted proteomics for enhanced precision, validated quantitation, and sensitivity. Potential Pitfalls & Alternative Strategies. **1)** The use of nonspecific enzymes such as COLase3 may increase false discovery rate (FDR) of protein IDs. We will limit FDRs by using concatenated reverse databases in peptide searches, ensuring high peptide probabilities (>99%), and manually inspecting MS/MS data. **2)** Overall levels of HYP may not differ between disease states. HYP site maps along each ECM protein sequence will be performed to probe for specific domains that may differ in their HYP levels. **3)** PTMs other than HYP are invovled in collagen regulation.
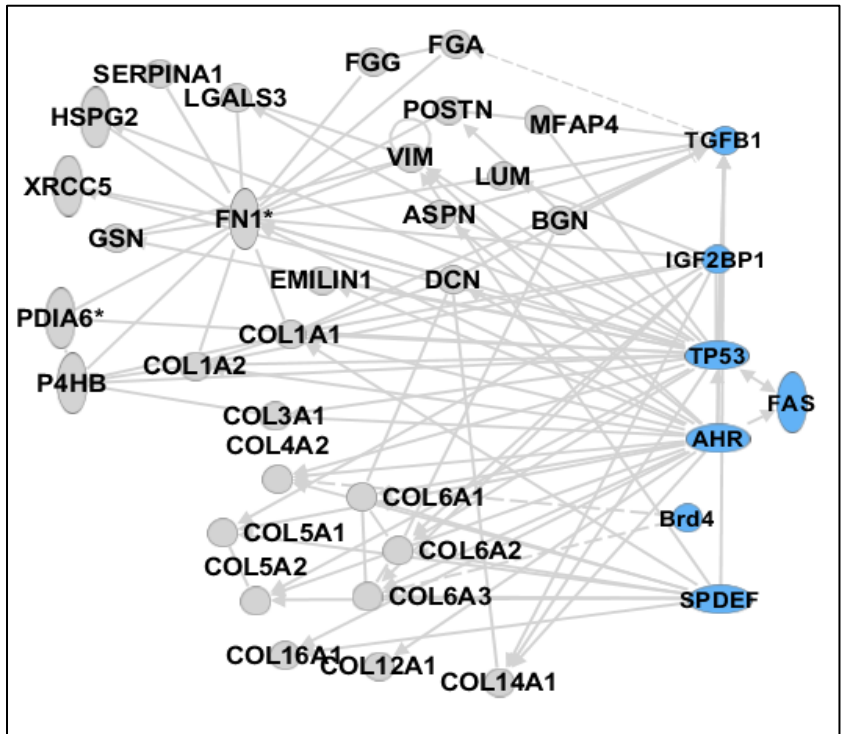
Figure 4: As a proof of concept, we show collagen interaction networks found by COLase3 proteomics on a tissue section of breast cancer, (blue: predicted signaling molecules). This same methodology will be applied to discover new signaling molecules driving CAVS collagen deposition. (*Angel et al, 2018*)

Secondary searches of the dataset can be performed to identify levels of other PTMs associated with crosslinking, such as hydroxylation of lysines. Our method also allows us to analyze changes in N-glycosylation. Collaborative labs have also developed an IMS method for observing O-glycosylation changes, a PTM directly linked to hydroxylation in lysine residues[23].

2.3.3 Specific Aim 3
Spatially localize HYP containing collagen peptides across healthy AV and CAVS tissues. Rationale: ECM stratification into the three layers fibrosa (collagen), spongiosa (GAG), and ventricularis (elastin) is part of healthy AV development, influenced in part by changing hemodynamics and oxidative stress[23, 41, 48-50, 170, 171]. During development, collagen distributions change: fibril-type collagens (COLI, II, and III) are present in early development, while network and FACIT type collagens (COLIV, VI, VIII, XIV) in late-embryonic/post-natal development. This data, however, is interpreted from mouse[22]. Similar studies have yet to be done on human AV. Collagen stability during this time, mediated by HYP, plays a critical role in collagen stratification *in vivo*, directly influencing AV function[41]. We hypothesize collagen sequences with HYP increase due to normal aging patterns and play a role in stratification; similarly, HYP levels change in the distal tip of CAVS valves where highest levels of hemodynamic stress and ECM destratification are observed at end-stage in pediatric CAVS.

Experimental Design: To spatially localize collagen HYP peptides across the valve, Matrix-Assisted Laser Desorption/Ionization (MALDI) coupled to Fourier Transform Ion Cyclotron Resonance (FT-ICR) Imaging Mass Spectrometry (IMS) will be used in parallel with HRAM proteomics (**Aim 2**). Tissues will be prepared in a similar manner as those used for HRAM proteomics, but instead will remain on the slide to be imaged via MALDI-IMS. MALDI-IMS analysis will be completed with a 7.0 Tesla solariX™ Legacy FT-ICR (Bruker Scientific,

LLC) operated in positive ion broadband mode spanning m/z range 500-4000. Images will then be visualized in FlexImaging v5.0 and analyzed using SCiLS (Bruker Daltonics). MALDI-IMS and HRAM LC-MS/MS data will be linked by accurate mass within ±5 ppm mass accuracy.

Expected Outcomes: It is our hypothesis that there is a unique regulation of collagen HYP in the CAVS tissue microenvironment contributing to progression. MALDI-IMS techniques used in this Aim will allow us to visualize and relatively quantify *in situ* peptides from collagens localized to AV structure or CAVS pathology. Heat maps of distinct peptides will be evaluated for correlation with ECM stains and markers of AV development (**Aim 1-2**). Spatial localization of collagen peptides throughout the AV may provide insight into the mechanical mechanism of valve degradation. For example, collagen peptides can be mapped to regions known to be particularly dysregulated in CAVS – such as the tip of the valve. Preliminary data analyzed via SCiLS segmentation analysis shows that the tip of the valve has a distinct molecular profile compared to the belly and the hinge region (**Fig. 5c**). This method is also capable of spatially localizing the distribution of collagen HYP peptides (**Fig. 5d, bottom**).
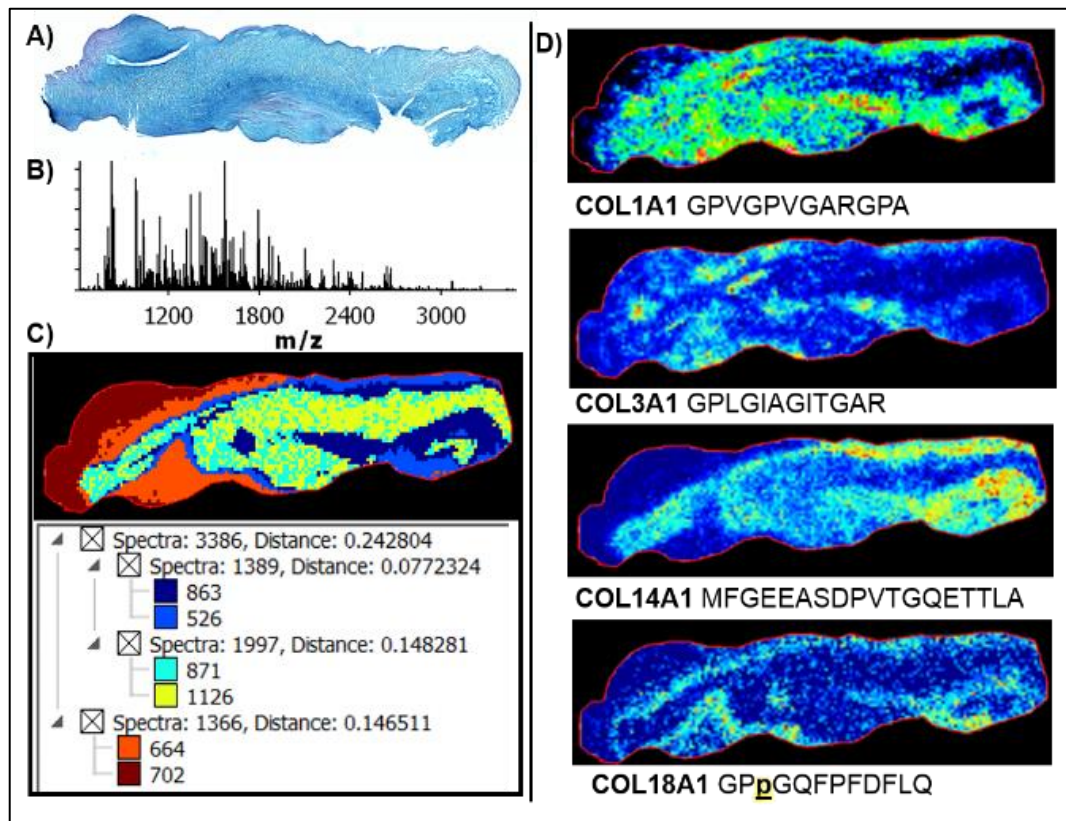
Figure 5: MALDI-IMS of collagens in CAVS. A) Hematoxylin, eosin & alcian blue stain shows structural features of the tissue. B) COLase3 total ion current by MALDI FT-ICR. C) Regionalization of spectral grouping across the valvular structure. Each color represents a distinct proteome. D) Examples of collagen image patterns found in the same experiment. The COL18A1 peptide represents a hydroxylated proline peptide.

Potential Pitfalls & Alternative Strategies: **1)** Collagen peptide signal is limited due to intra- and inter-molecular crosslinking. Sequential enzyme treatment with elastase and other MMPs may be used to increase access to collagen peptides[22]. **2)** Spatial mapping may indicate no correlation between hemodynamically stressed areas and collagen deregulation. An alternative approach is to perform *in vitro* analysis of cells undergoing shear stress via bioreactor conditioning to simulate hemodynamic conditions of CAVS[31]. We would perform MALDI-IMS on cultured cells to detect changes in HYP collagen peptides, and N-glycans.

Statistical Considerations:

Sample size and power analysis estimation using a two-group t-test indicates a minimal sample size of 8 per group will provide 98% power to detect a 2.56-fold change with a relative standard deviation of 0.65 due to biological variation. The Type I error probability of the null hypothesis is 0.001. The Collaborative Unit at MUSC is a biostatistics and bioinformatics resource available for statistical consultation.

Chapter 3: Collagen Fiber Regulation in Pediatric Congenital Aortic Valve Stenosis

The following chapter details the histopathological- and proteomics-based characterization of the ECM within our pediatric cohort of aortic valve tissues. Our goal was to ascertain the dominant ECM constituent being deposited within pediatric CAVS patients. Additionally, we aimed to characterize various parameters of the collagen that was being deposited – that is, its maturity, density, and orientation. Similarly, via, bulk chromatographic proteomic analysis, we aimed to determine collagen-sub type regulation within the different disease states. We also aimed to determine differential post-translational regulation via quantification of the hydroxyproline (HYP) content within the collagen peptides identified. The bulk of this chapter was included in a first-author manuscript published in Nature Scientific Reports in May 2021[39]. Experiments were performed by myself in addition to manuscript writing, data analysis, and final approval. Minor editorial and intellectual contributions were provided by co-authors [39].

4.1 Introduction

Congenital aortic valve stenosis (CAVS) accounts for 10% of all congenital heart defect cases, affecting up to 6 of every 1000 newborns[24]. There are two distinct subsets of this disease: 1) pediatric end-stage, characterized by a rapid engorgement of the structure with extracellular matrix (ECM); and 2) the more frequently studied adult end-stage, characterized by fibrocalcific lesions [172]. These defects result in a narrowing of the aortic opening, obstructing aortic outflow and leading to left ventricular hypertrophy and heart failure. Despite the clinical significance, there are no available therapeutics. The patient is managed by "watchful waiting" until deteriorating cardiac hemodynamics indicates a need for surgical intervention either through valve replacement or heart transplantation [173]. Bioengineered aortic valve replacements are especially limited for pediatric patients due to their inability to grow with the patient and lifelong requirements of anti-clotting agents, and serial surgeries to replace valves during somatic growth [57].

There is an ongoing need for identifying therapeutic targets, particularly for the pediatric population.

Collagens form the underlying scaffolding of valvular structure that influences valvular function and consequently cardiac function[8, 26, 166, 174-178]. Collagen is developmentally regulated and is required for appropriate heart function during somatic growth[178-180]. The normal human aortic valve has an ECM trilayer structure defined by a high density collagenous fibrosa facing blood outflow, an interior spongiosa composed of primarily glycosaminoglycans, and the elastin-rich ventricularis [178, 181]. In the mature human valve, a parallel alignment of collagen with valvular endothelium is critical for normal function [179, 181], highlighting the importance of collagen organization within the trilayer compartments as fundamental to valvular function. Pediatric CAVS produces excessive collagen deposition that mixes with other extracellular matrix proteins, creating a disorganized ECM structure, altering valvular function and leading to cardiac failure [8, 182, 183]. Although collagen deregulation is a hallmark of adult and pediatric valvular stenosis [184-186] and a potential prognostic and therapeutic target[187, 188], very little is known about the complexities of collagen fiber regulation in the human valve.

In the current study, we test the hypothesis that pCAVS disease mechanisms also include dysregulation of collagen fiber arrangements with an altered post-translational regulation. A total of 20 human AV tissue specimens with clinical data on AV function were evaluated. Histopathological stains paired with microscopy methods were used to define collagen fiber changes and collagen variation within the valvular structure. A collagen-targeting[141, 143, 144, 189] high-resolution accurate mass (HRAM) proteomics approach was used to measure collagen type composition and PTM regulation within the collagen structure. Protein-protein interaction analyses were done to determine possible

upstream regulators relevant to collagen deregulation observed in pCAVS. Upstream regulators were validated via immunohistochemistry. Results of this study indicate that pCAVS shows fundamental differences in collagen fiber organization, collagen type regulation, and regulation of proline hydroxylation of collagens. These studies are the first to report specific collagen regulation due to pCAVS, and establish a foundation for new translational and post-translational collagen studies in fibrotic cardiovascular disease.

4.2 Materials & Methods
4.2.1 Materials

Xylenes, 200 proof ethanol was from Fisher Scientific (Pittsburgh, PA, USA). Acetonitrile, Ammonium Bicarbonate, Calcium Chloride, Formic Acid, and Trizma Base were from Sigma-Aldrich (St. Louis, MO, USA). PNGase F Prime was purchased from N-Zyme Scientifics (Doylestown, PA). Collagenase type III (COLase3) (*C. histolyticum*) was purchased from Worthington Biochemical (Lakewood, NJ, USA).

4.2.2 Tissue Procurement

Aortic valve tissue samples were procured through the Vanderbilt Core Laboratory for Translational and Clinical Research and the National Disease Research Interchange. The aortic valve tissues were collected under the Vanderbilt Pediatric Congenital Heart Disease Biorepository, written informed consent was obtained, and the project was approved by the Vanderbilt Institutional Review Board (IRB) and the IRB at the Medical University of South Carolina. De-identified tissues were obtained during reparative or transplant surgeries and characterized by pre-operative function into three patient categories: normal tricuspid (normal), pediatric CAVS bicuspid (pCAVS), and aortic valve insufficiency tricuspid (AVI). Valvular function is from de-identified complete 2D, color and spectral Doppler, or M-mode echocardiogram reports acquired prior to valve resection,

54

replacement or heart transplant. The pCAVS patients were identified as being stenotic, predominantly bicuspid, and having mild aortic valve insufficiency. The AVI group only has aortic valve insufficiency, but are not stenotic and are all tricuspid. Adult CAVS samples (aCAVS) used in the qRT-PCR study showed no calcification by clinical annotation, with the except of SKU SB176. Pediatric ages used to stratify the population are based in National Institute of Child Health and Human Development (NICHD) pediatric terminology defining pediatric age groups in terms of clinical treatment, considering rapid somatic growth stages[190].

4.2.3 Histological Staining

The 5-µm thick formalin-fixed, paraffin-embedded tissue sections were stained with Picrosirius Red (PSR; Polysciences, Inc., Warrington, PA, USA), Movat's Pentachrome and Herovici (American Mastertech Scientific of StatLab, McKinney, TX, USA) following manufacturer's protocols. Optical light whole tissue scans were done using a high-resolution slide scanner (Nanozoomer, Hamamatsu, Japan). Polarized light images of PSR were taking with a Spinning Disk CARV II microscopy (BD Biosciences, San Jose, CA, USA), and manually stitched together using Photoshop (Adobe, San Jose, CA, USA). Movat's, PSR, and Herovici Color Deconvolution analysis was done using ImageJ[191] adjusting for RGB hue threshold color (Movat: Elastin 0-19, 170-255; GAG 80-169; Collagen 20-79) (PSR: Thin 46-190; Thick 0.45, 191-255) (Herovici: Immature 0-167; Mature 168-255). Percent of each color threshold is represented as a percent of total area stained (RGB 0-255). Collagen Plaque analysis was done using ImageJ[191]. Briefly, polarized light images were converted to 8-bit and thresholded to include all signal. Images were processed with a mean filter of 1 µm and a look-up table of Red/Green was applied. Regions of increased collagen fiber density (RIFD) were quantified by thresholding to

include the top 50% most dense signal (i.e., "green" component). Collagen fiber analysis (fiber length, width, angle) of PSR birefringent images were converted to 8-bit grayscale and analyzed using CT-FIRE[192].

Second Harmonic Generation (SHG) microscopy was performed on the same tissue section used for PSR studies. SHG images were collected with a *Spectra-Physics InSight X3 dual laser system and* excited at 860nm. SHG images and were collected at emission 432nm with a 45nm bandpass. SHG multichannel show overlay images collected at emission wavelengths: 432nm (±22.5 nm) (cyan; collagen SHG), 518nm (±22.5 nm) (green; collagen autofluorescence), 610nm (±35 nm) (red; PSR, elastin, and heme structures).

For immunohistochemistry, tissues were deparaffinized, antigen retrieved at pH 6 in sodium citate, then stained with HRP/DAB (ABC) Detection IHC Kit (Abcam, Cambridge, UK) according to manufacturer's instructions with the following modifications: all incubation times were increased to 15 minutes. Primary antibody BAMBI (polyclonal) was diluted 1:100 (Millipore Sigma, St. Louis, MO, USA). IHC stained tissues were counterstained with Mayer's hematoxylin (Electron Microscopy Sciences, Hatfield, PA, USA).

4.2.4 Proteomic Tissue Preparation

Proteomic studies used tissue sections adjacent to histological studies (~150 μm distance). Tissues were 5-μm thick and mounted on standard microscope slides (Tissue Tack, Polysciences, Inc., Warrington, PA, USA). For proteomic experiments, slides were heated at 60°C for 1 hour then dewaxed as follows: xylenes (3 min, two times), 200 proof ethanol (1 min, two times) 95% ethanol (1 min), 70% ethanol (1 min), HPLC water (3 min,

two times). Valve surface area was used to determine equivalent amount of tissue and valves were scraped with a razor off the slide into centrifuge tubes. 10 mM Tris pH 9 was added to each tube to cover the tissue. Tissues were ultrasonicated at 50% energy (Fisherbrand 120 sonic dismembrator;Fisher Scientific, Pittsburgh, PA, USA) for 2 minutes each and incubated at 60°C for two hours to antigen retrieve formalin-fixed crosslinks[193]. Samples were buffer exchanged into water and deglycosylated with 2 µg of PNGaseF PRIME (N-zyme Scientifics, Doylestown, PA) for two hours at 38°C at 450 rpm using a thermomixer (Eppendorf, Hamburg, Germany). Supernatant was removed, and samples were buffer exchanged into 10 mmol/L ammonium bicarbonate, 3 mmol/L CaCl2, pH 7.25 and treated with 4 µg of Collagenase Type III (COLase3) overnight, shaking at 38°C. An additional 4 µg of COLase3 was then added to each sample and incubated for 5 hrs at 38°C with mixing at 450 rpm. COLase3 activity of 3 Units/mL was confirmed prior to digestion by a colorimetric activity kit (ab196999, Abcam, Cambridge, MA). Samples were centrifuged at 16,000 g for 5 minutes at 4°C and supernatant collected for proteomic analysis. Samples were purified by C18 STAGE tip[194] (Pierce Biotechnology, Waltham, MA) followed by a C18 ZipTip (Millipore Scientific, Burlington, MA) according to manufacturer's protocol. Solutions were modified for STAGE tip using 90% acetonitrile, 5% formic acid (initialize and elute); 5% acetonitrile, 5% formic acid (equilibrate and wash). STAGE-tip eluate was dried down via speed vac and resuspended in 0.1% TFA in water. An additional C18 ZipTip according to manufacturer's protocol (Millipore Scientific) and sample resuspended in mobile phase A (2% acetonitrile, 0.2% formic acid).

4.2.5 Proteomics

Peptides were analyzed by data dependent acquisition on an Orbitrap Elite mass spectrometer equipped with a LC Packing U3000 nano-LC system (Thermo Scientific). Peptides were loaded onto a trap column and separated on a 75 μm x 30 cm classic pulled tip column (C18-Reprosil-AQ Pur RP 1.9 μm particles, Dr. Maisch, GmbH) at 60°C. The gradient was from 5% to 40% solvent B over 180 min, where solvent A was 0.2% v/v formic acid in water and solvent B was 98% acetonitrile with 0.2% v/v formic acid. An FTMS survey scan was acquired over a mass range of 400-1700 m/z at a resolution of 60,000 with an automatic gain control (AGC) target value of 10^6, followed by CID MS/MS of the top 10 most intense ions in the ion trap. Dynamic exclusion was enabled with a repeat count of 1, repeat duration of 30 s, and exclusion duration of 180 s. Data were searched using MaxQuant version 1.6.3.3 [195] against the human database (42,106 entries downloaded May 5, 2017) and a subset 1783 entries with keywords used (collagen, elastin, aggrecan, gelatin, osteonectin, perlecan, plasminogen, and fibronectin). Parameters included unspecified proteolytic enzyme, precursor mass tolerance of $\pm$ 20 ppm, and fragment mass tolerance $\pm$ 0.8 Da. Methionine oxidation, asparagine and glutamine deamidation were included as variable modifications. Proteins were identified with FDR≤0.05 and at least two peptides. Hydroxylated proline modification site localization probabilities were obtained by re-searching MS/MS using a restricted database of identified proteins and allowing for dynamic modification proline oxidation. Perseus[196] was used for protein and peptide level analyses.

4.2.6 Protein-Protein Interaction Network Analysis

Protein identifications were uploaded to Ingenuity Pathways Analysis (IPA; Qiagen Inc., https://www.qiagenbio informatics.com/products/ingenuity-pathway-analysis) to identify putative regulators of the protein dataset. Networks were calculated using

predicted relationships between regulators by p-value ≤ 0.01; a p-value < 1.0×10^{-12} was used for inclusion in the network. Upstream Regulator Networks were calculated using predicted relationships between regulators (CCR2, COLQ, IGF2BP1); a p-value <1.0 x 10-18 was used for inclusion of the upstream regulator network. Causal Network analysis was done to identify Master Regulators of the data (BAMBI) and a p-value < 1.0×10^{-12} was used for inclusion in the network.

4.2.7 Proteomic Data Analysis and Statistics

Perseus[196] was used for protein and peptide level analyses. Hierarchical clustering was performed in Perseus on ANOVA significant peptide intensities via a permutation-based FDR of 0.05 and 250 randomizations. Clustering parameters: Euclidean distance, average linkage, and k-means pre-processing. Peptide level quantification was determined using peak intensities from peptides scoring ≥ 75 after median normalization and considered as significant with a minimum two-fold change. Relative changes in protein abundance based on normalized protein intensities were evaluated by ANOVA and Mann Whitney U test, correcting for multiple comparisons (IBM SPSS Statistics, version 25). A Type I error probability of ≤0.1 was used to evaluate the significance of the result. MWU-test was used in histological studies to calculate raw p-values. For this small clinical cohort, p-values of ≤0.1 are reported as trending to significance and p-values of ≤0.05 were used determine significant results.

GO enrichment was performed through Geneontology.org[197, 198]. Genes were clustered to cellular component, biological process, or molecular function using Panther v14[199] filtered by Fisher's Exact (FE) p-values <0.001 and false discovery rates (FDR) of <0.005. Exported peak intensities are visualized as heatmaps after natural log transformation with MultiExperiment Viewer (http://www.tm4.org)[200].

4.2.8 Real Time Quantitative Reverse Transcription PCR

Aortic valve (AV) specimens were collected at the time of surgery or from an explanted heart. Samples were immediately flash-frozen and stored at -80°C till used for RNA extraction. Total RNA from AV tissues was isolated using RNeasy Kit (Qiagen, Germantown, MD), according to the manufacturer's instructions. The BAMBI gene expression level was validated by quantitative RT–PCR (qRT-PCR) using the Taqman method, as previously described[201]. Briefly, cDNA was generated using 100 ng of total RNA and High Capacity cDNA Synthesize Kit (Catalog # 4368814 Thermo Fisher Scientific). Predesigned BAMBI (catalog # Hs03044164) and GAPDH (catalog # Hs02758991) primers were obtained from Thermo Fisher Scientific and the qRT-PCR were run in triplicates according to the manufacturer's instructions. All Ct values were reported below 40, indicating acceptable PCR efficiency[202].

Table 2: Descriptive statistics of patient characteristics for all pediatric aortic valve (AV) tissue samples featured in the study. Normal AVs are from cardiac transplant patients where normal AV function is define by 2D echocardiogram. 2D Echocardiogram mean gradients define pre-operative AV function where a normal gradient is defined as <5 mmHg, mild stenosis as 5-25 mmHg, moderate stenosis as 25-50 mmHg, and severe stenosis as >50 mmHg. BSA: body surface area; C: Caucasian; L: Latino; AA: African American; MD: Myxomatous Degeneration. DB43 was included in pCAVS due to stenosis, but main diagnosis was Hypertrophic Cardiomyopathy. Pediatric Age Groups are defined by National Institute of Child and Human Development: Neonate (0-30d), Infant (1 mo – 2yrs), young Child (2-6 yrs), Child (6-12 yrs), Adolescent (12-18 yrs).

	SKU	Age (years)	Pediatric Age Group	Gender	Race/ Ethnicity	BSA (m²)	Leaflet Morphology	Aortic Valve Function
Normal	DB017	0.5	Infant	M	-	0.38	Trileaflet	Normal
	DB051	0.66	Infant	M	C	0.34	Trileaflet	Normal
	NDRI	2	Young Child	M	L	0.63	Trileaflet	Not recorded
	DB85	9	Child	F	C	0.95	Trileaflet	Normal
	DB27	17	Adolescent	M	C	2.2	Trileaflet	Normal
	Normal Averages	**7.17 ± 7.5**		**75%M 25%F**	**75%C 25%L**	**1.03**		
pCAVS	DB106	0.04	Neonate	M	C	0.21	Bicuspid	Severe Stenosis with AVI
	DB43	0.15	Infant	M	C	0.24	Trileaflet	Moderate stenosis with AVI*
	DB40	0.75	Infant	M	C	0.37	Bicuspid	Moderate Stenosis
	DB105	5	Young Child	M	C	0.72	Bicuspid	Moderate Stenosis with AVI
	DB119	5	Young Child	F	-	-	Bicuspid	Moderate Stenosis with AVI
	DB113	5	Young Child	-	-	-	-	Trivial Stenosis; Severe AVI
	DB18	6	Child	F	C	0.7	Bicuspid	Moderate Stenosis with AVI
	DB3	11	Child	F	C	1.5	Bicuspid	Moderate Stenosis with AVI
	DB117	12	Adolescent	M	-		Bicuspid	Moderate Stenosis with AVI
	DB41	14	Adolescent	M	C	1.6	Bicuspid	Moderate Stenosis with AVI
	DB16	17	Adolescent	M	C	2.1	Bicuspid	Moderate Stenosis with AVI
	CAVS Averages	**6.90 ± 5.8**		**70%M 30%F**	**100%C**	**0.93**		
AVI	DB114	0.17	Infant	F	-	-	Trileaflet	Trivial AVI
	DB007	0.58	Infant	-	-	-	Trileaflet	Mild nAVI
	DB108	10	Child	F	C	1.3	Trileaflet	Thickened with AVI
	DB83	10	Child	F	AA	1.4	Trileaflet	Trivial AVI
	DB032	16	Adolescent	-	-	-	Trileaflet	Mild nAVI
	AVI Averages	**7.35 ± 6.8**		**-**	**-**	**1.35**		

4.3 Results
4.3.1 Clinical and Morphological Characteristics of Study Cohort.

Collagen from human aortic valve samples was studied across four patient categories: normal, pediatric end-stage congenital aortic valve stenosis (pCAVS), and aortic valve insufficiency (AVI) (Table 2). Age-matched pediatric samples ranged from Neonates (2 weeks) to Adolescent (18 years), with an average patient age of 6.75 ± 6.06 years. Gender was predominantly male (15, 57.7%). The race was primarily Caucasian (16, 61.5%). For each patient, serial tissue sections were evaluated for histopathology of collagen by multiple staining methods and collagen fiber measurements. Translational and post-translational regulation of collagen was investigated by collagen targeted proteomics[203] using HRAM proteomics on regions approximately 100 μm in thickness adjacent to histological sections. In summary, this cohort represents a suitable pathological variation towards probing ECM distribution in human aortic valve development and pediatric end-stage disease.

4.3.2 Pediatric CAVS valves trend to be collagen dominant at a younger age of end-stage.

Color deconvolution of Movat's Pentachrome on the valve cohort was performed to determine the dominant ECM type in each patient category (**Fig 6A-B, Fig7**). Movat's Pentachrome stain showed an ECM trilayer in the normal valves with thickened, disorganized ECM due to pCAVS, consistent with previous literature reports on CAVS[8, 204]. We stratified the pediatric tissues by neonatal to early childhood (0-including 5 years of age; rapid growth and development) and middle childhood to early adolescence (age 6-18 years of age). While differences in elastin can be seen from patient to patient, elastin content was not statistically significantly different between patient
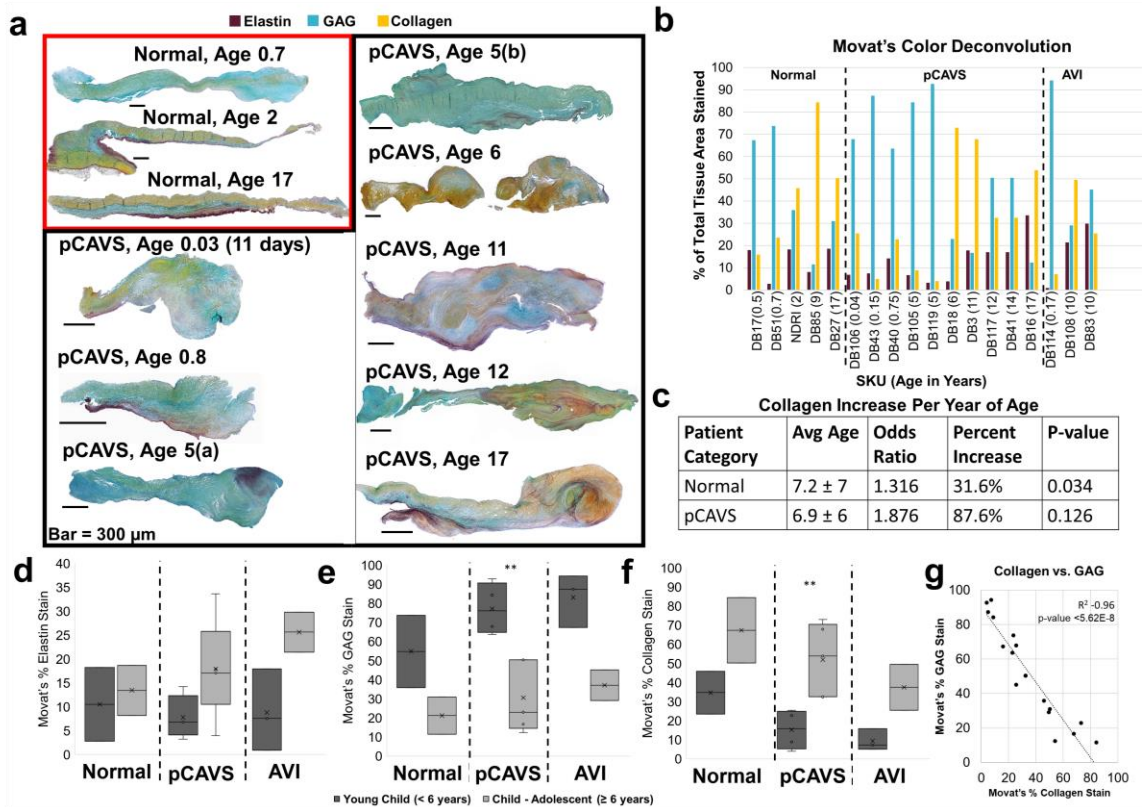
Figure 6: Histology analysis identifies ECM mixing and collagen dominance in pCAVS valves at a young end-stage. A. Examples Movat's Pentachrome staining between normal and age matched pCAVS samples. Blue stain corresponds to glycosaminoglycan (GAG) regions, dark purple to elastin, and yellow to collagen. Normal valves show traditional trilayer structure, while pCAVS valves show lack of trilayer and areas of ECM mixing **B.** Quantification of Movat's Staining via color deconvolution analysis. Blue = GAG, purple = Elastin, yellow = collagen. Shown as a percent of total Movat's stain area. **C.** Multinomial logistical regression analysis of Movat's Pentachrome Color Deconvolution data shows pCAVS valves are collagen dominant at a younger age than normal patients. Variables: ECM dominant category (GAG, elastin, or collagen); Patient Category (normal or pCAVS); Age (0-18 years). **D-F.** Quantification of Elastin, GAG, and Collagen (respectively) Movat's Pentachrome color deconvolution results (Fig. 1B) comparing two pediatric age groups: young child (Newborn to <6 years of age) and Child-Adolescent (6-18 years of age). **p-value 0.008, MWU test. pCAVS GAG decrease is concomitant with collagen increase across pediatric age categories **G.** Scatterplot of all data points across Normal, pCAVS, and AVI samples for collagen vs. GAG stain percent of total area of Movat's stain. Bar: 500µm. Spearman's correlation (R^2) -0.96 (p-value <5.62E-8). Normal n=5; pCAVS n=10; AVI n=3.
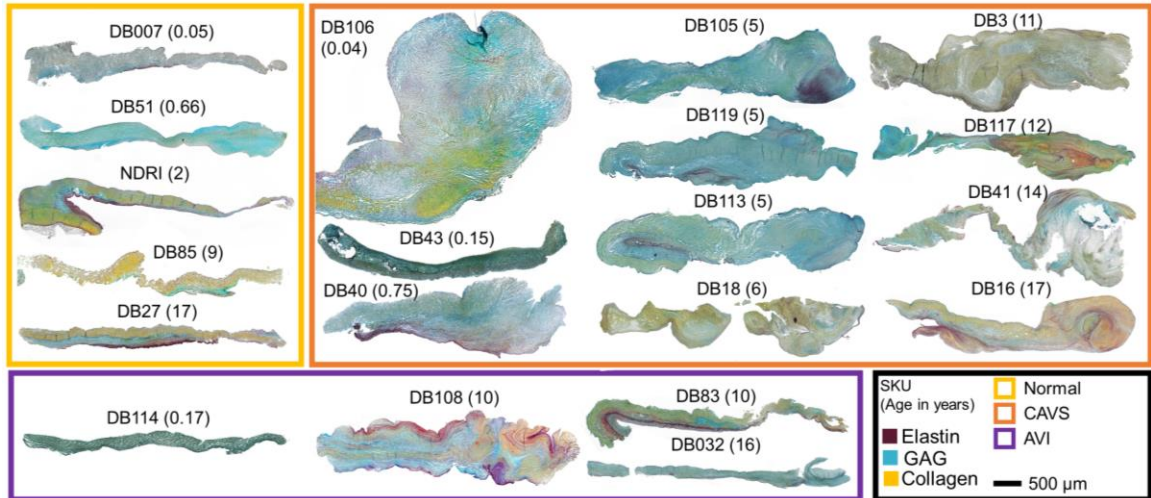
Figure 7: Movat's Pentachrome images of all valves studied in Figure 6. DB113 and DB32 are included as representative images only, due to delayed acquisition and manufacturer's difference in sample preparation.

categories (**Fig. 6B, D**). Pediatric patients in all categories showed decreased glycosaminoglycan (GAG) staining over time relative to patient age (**Fig. 6E**). GAG decrease was significant within the pCAVS category compared between two patient age groups: young children (77.2 ± 14%; pediatric age < 6 years, n=6) vs children to adolescents (30.6 ± 19%; pediatric age >6 years, n=5) (p-value 0.008) (**Fig. 6E-F**). Collagen content increased concomitant with decreasing GAG content over all patient groups (Spearman's correlation -0.96 (p-value <5.62E-8) (**Fig. 6G**). Interestingly, while collagen content progressively increased with age for each patient category, the likelihood of a pCAVS valve having a collagen dominant phenotype occurred at a younger age of end-stage. Histopathology evaluation revealed that the rate of collagen deposition increased by 56% in pCAVS compared to normal AV development. When accounting for age by multinomial logistical regression, analysis showed that the probability of a normal valve being in the collagen dominant ECM category increased by 32% (p-value 0.034, **Fig. 6C**) for every year of age. In contrast, pCAVS valves showed a trend to having a collagen dominant phenotype which increased by 88% (p-value 0.126, **Fig. 6C**) for every year of age. Collagen significantly increased in between pediatric patient age groups (34.7 ± 15.7% age<6 years; 67.4 ± 24.1% age ≥ 6 years, p-value 0.0079) (**Fig. 6F**). These results show that the ECM disorganization of pCAVS involves a progressive collagen dominant phenotype concomitant with GAG decreases.

4.3.3 Pediatric CAVS demonstrate high deposition of immature collagen compared to individual age-matched controls.

Herovici stain was used to assess valvular content of immature/smaller collagen fibers (blue) and mature/larger collagen fibers (purple) (**Fig. 8-9**) [205]. Immature collagen deposition varied by location on the valve structure and
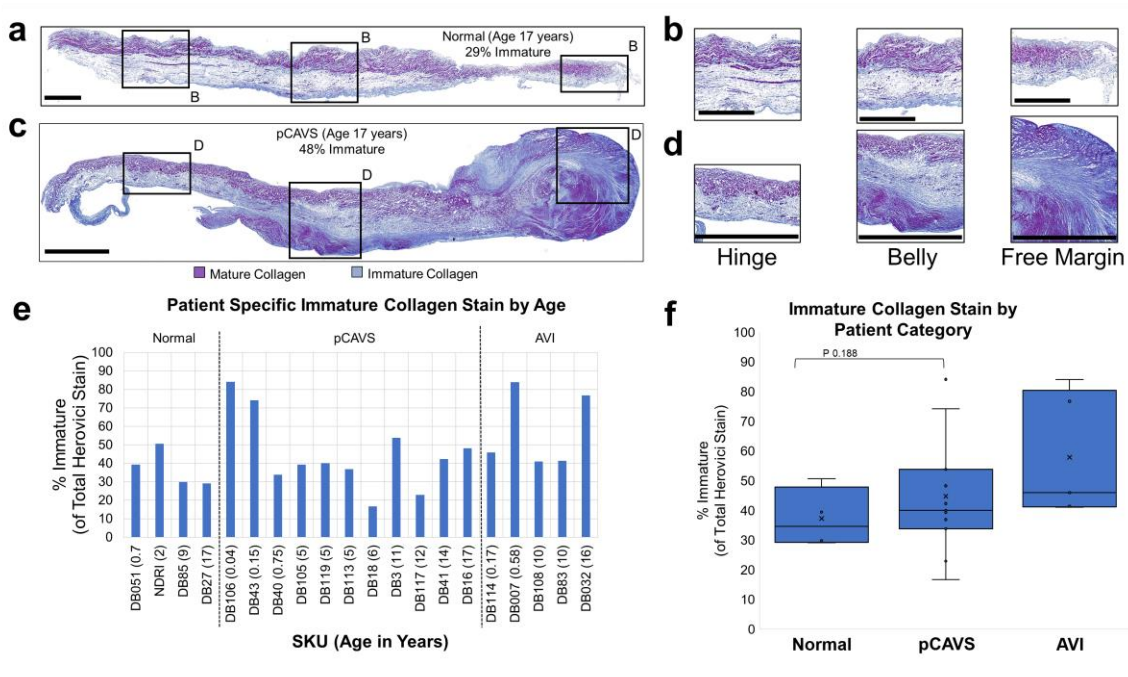
Figure 8: Pediatric CAVS demonstrate high deposition of immature collagen compared to age-matched controls. A-B. Herovici staining of SKU DB27, a 17-year-old normal sample with regions of Hinge, Belly, and Free Margin 10x zoom shown (**B**). Blue=immature. Purple-mature. Normal immature collagen production is localized to the ventricularis, while pCAVS immature production becomes increasing dysregulated towards the free margin. **C-D.** Herovici staining of SKU DB16, an age-matched CAVS sample with regions of Hinge, Belly, and Free Margin 10x zoom shown in **D**. **E.** Patient specific breakdown of Herovici color deconvolution analysis. pCAVS patients show increased immature collagen production compared to age matched controls. **F.** Boxplot showing quantification of Herovici color deconvolution, showing larger heterogeneity amongst pCAVS patients. Scale Bar: 300μm. Normal n=4; pCAVS n=11; AVI n=5.
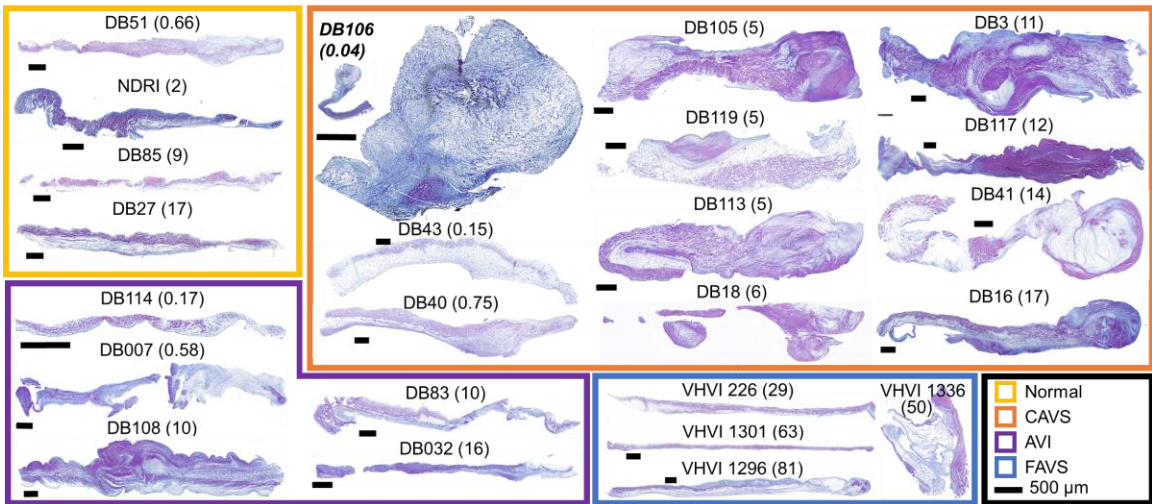
Figure 9: Herovici images for valves studied in Figure 8.

by pathology, suggestive of a link to mechanics of valve function. In trilayer regions close to the hinge region, normal valves and pCAVS showed immature collagen deposition in the spongiosa (**Fig. 8 A-D**). Within the belly of the leaflet, immature collagen deposition aligned with regions of ventricularis delamination. However, pCAVS showed sites of pathological mixtures of immature and mature collagen. For example, in SKU DB16, immature collagen appears mixed with mature collagen along the ventricularis closer to the hinge. The free edge of this valve contains significant mixtures of both immature and mature collagen, suggestive of a dynamic production of collagen in this region. By Herovici stain, all valves showed immature collagen deposition (**Fig. 8F**). Averaged across ages at end-stage, where there was no significant difference between normal and pCAVS levels of immature collagen. However, comparison of same age patients showed increases in immature collagen for age matched samples (ex. 19% increase in SKU DB16 vs DB27) (**Fig. 8E**). Overall, the data show that both normal and pCAVS continually produce immature collagen with pCAVS showing pathological mixes of both immature and mature collagen.

4.3.4 Pediatric end-stage CAVS valves have greater numbers of collagen fibers with localized regions of collagen density.

Collagen fiber measurements were done by Picrosirus Red (PSR) staining to characterize collagen fiber regulation (thickness, density, and alignment) (**Fig. 10-11**). Interestingly, all pCAVS valves showed localized areas of high-density collagen, confirmed by second harmonic generation microscopy (**Fig. 10A, 11**). Collagen fiber thickness was not significantly different between normal valves compared to pCAVS or AVI**.** However, larger interquartile ranges were observed in pCAVS (37-81% thick fibers) compared to normal valves (34-50% thick fibers), suggesting that pCAVS
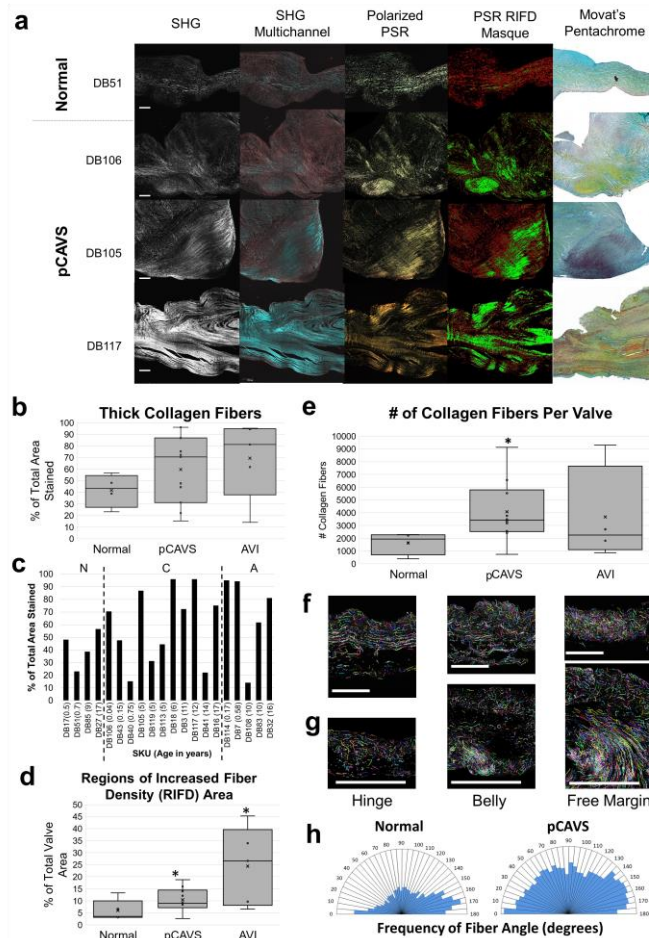
Figure 10: Pediatric end-stage CAVS valves have a greater number of collagen fibers with localized regions of collagen density. **A**. Collagen fiber visualization of select pCAVS and normal valves. From left to right: Second Harmonic Generation (SHG); SHG multichannel; Polarized picrosirius red (PSR); PSR Regions on Increased Fiber Density (RIFD) Masque; Movat's Pentachrome. Movat's Pentachrome: blue=GAGs, yellow=collagen, and purple=elastin. Scale Bar = 200µm. **B.** Boxplot showing quantification of PSR color deconvolution analysis. **C.** Patient-specific data of PSR color deconvolution analysis. pCAVS and AVI patients show larger heterogeneity across age groups compared to normal. **D.** Boxplot showing quantification of collagen RIFD areas normalized to total valve area. *p-value 0.024, MWU test. pCAVS and AVI patients have significantly more regions of high collagen fiber density compared to normal patients. **E.** Boxplot showing quantification of total number of collagen fibers as measured by CT-FIRE analysis. *p-value 0.014, MWU test. **F-G.** Hinge, Belly, and Free Margin (respectively) 10x zooms of PSR-polarized light signal overlayed with CT-FIRE mask of collagen fibers for normal (F; SKU DB27) and pCAVS (GI SKU DB16) (**Fig. 11**). **H.** Polar histogram showing frequency distribution of collagen fiber angles from 0-180°, across all normal valve samples (left) and pCAVS (right) relative to the endothelium. Normal n=4; pCAVS n=11; AVI n=5. CT-FIRE V2.0 Beta was used (https://eliceirilab.org/software/ctfire/).
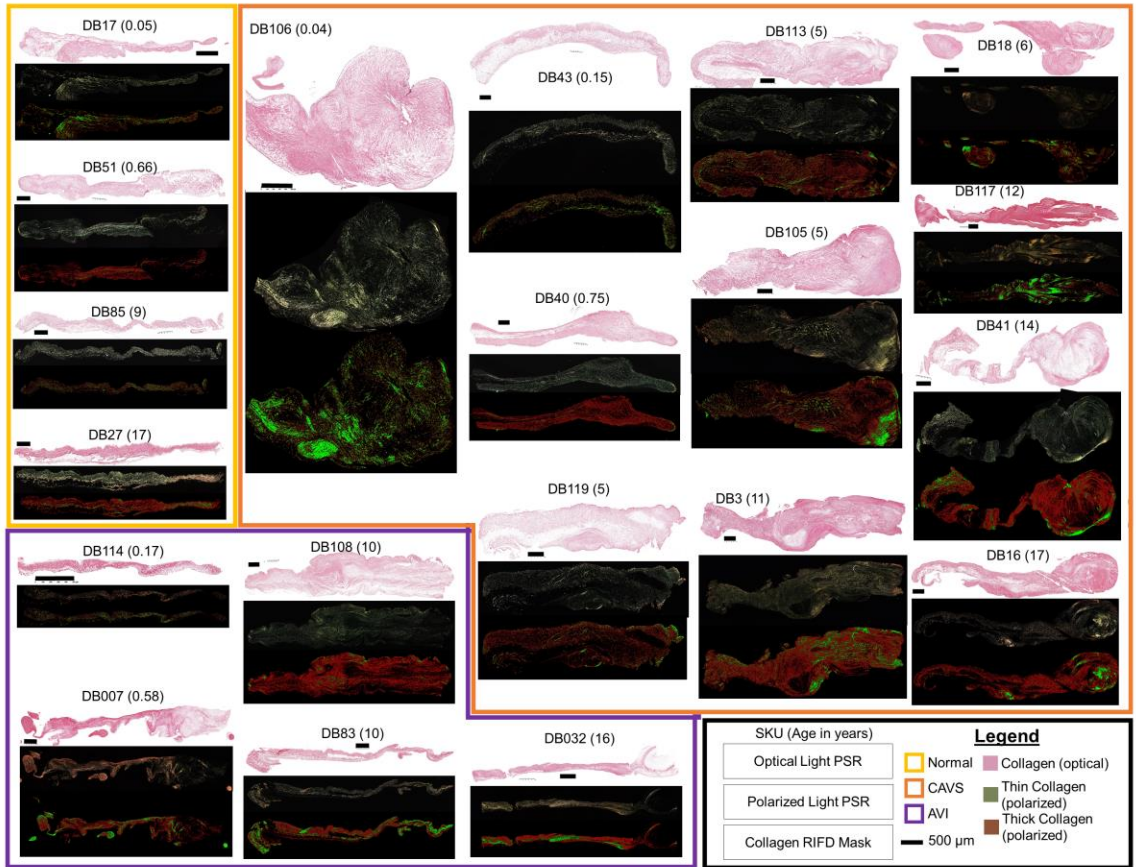
Figure 11: Optical and Polarized Picrosirius Red (PSR) images of valves studied in Figure 10. RIFD (Regions of Increased Fiber Density) masks are shown.

have increased heterogeneity of fiber thickness (**Fig. 10B-C**). Compared to normal valves, both pCAVS and AVI valves demonstrated a significant increase in regionalized collagen density normalized by area (p-value 0.024 and 0.019) (**Fig. 10A, D**). Localized areas of high-density collagen fibers did not appear to be specific to valvular anatomy and occurred at different locations within the leaflet. The amount of collagen fibers in pCAVS valves was significantly higher when compared to normal valves (2.5-fold more, p-value 0.014; normalized to cross-sectional area). **Fig. 10E**). Picrosirius Red staining, in combination with CT-FIRE software, was used to determine the collagen fiber angle alignment relative to endothelium. Collagen fiber angles in normal valve structures were primarily between 150-180° relative to endothelium (**SKU DB27, Figure 10F,H**), following previous observations in normal valve growth[175, 179, 185]. In comparison, the pCAVS valves showed a larger distribution of fiber angles (over 0-180° relative to the endothelium) along the length of the valve, suggestive of collagen fiber misalignment compared to normal controls (**Fig. 10G, H**). To summarize, the data shows that pCAVS valves are characterized by localization of high-density collagens and higher number of collagen fibers compared to normal valves.

4.3.5 Proteomic analysis indicates collagen structure is post-translationally regulated in pCAVS.

A collagen and ECM protein targeted proteomic analysis approach was next applied to the valve tissue cohort to understand how collagen fiber regulation corresponds with collagen protein structure regulation. The proteomics analysis workflow is summarized in **Figure 12** and described in Materials and Methods. A focus of the analysis was testing for hydroxylated proline (HYP) residues, a collagen post-translational modification essential to triple helical stability and collagen
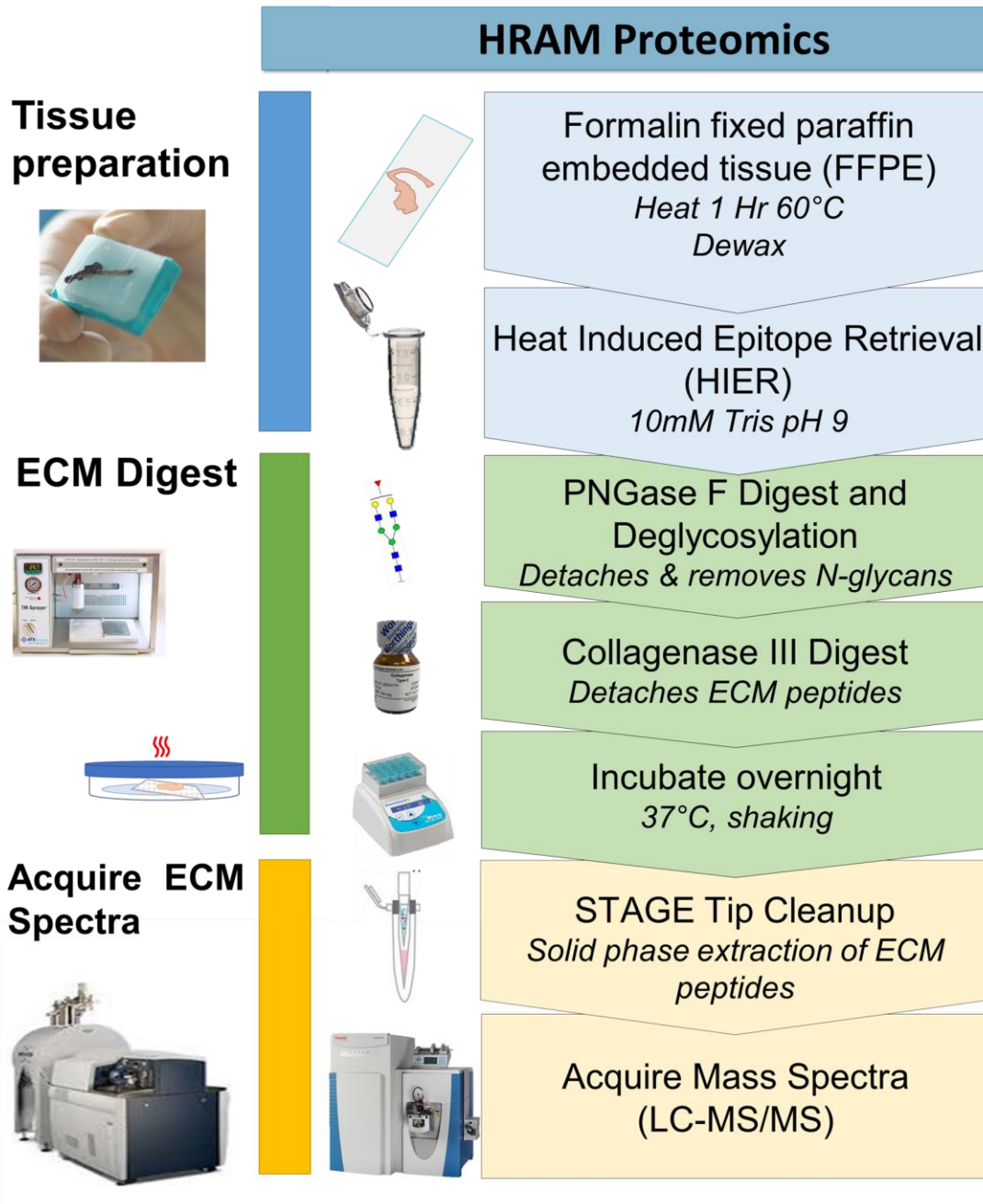
Figure 12: Collagenase Type III high resolution accurate mass (HRAM) Proteomics workflow on formalin-fixed paraffin embedded tissue sections.
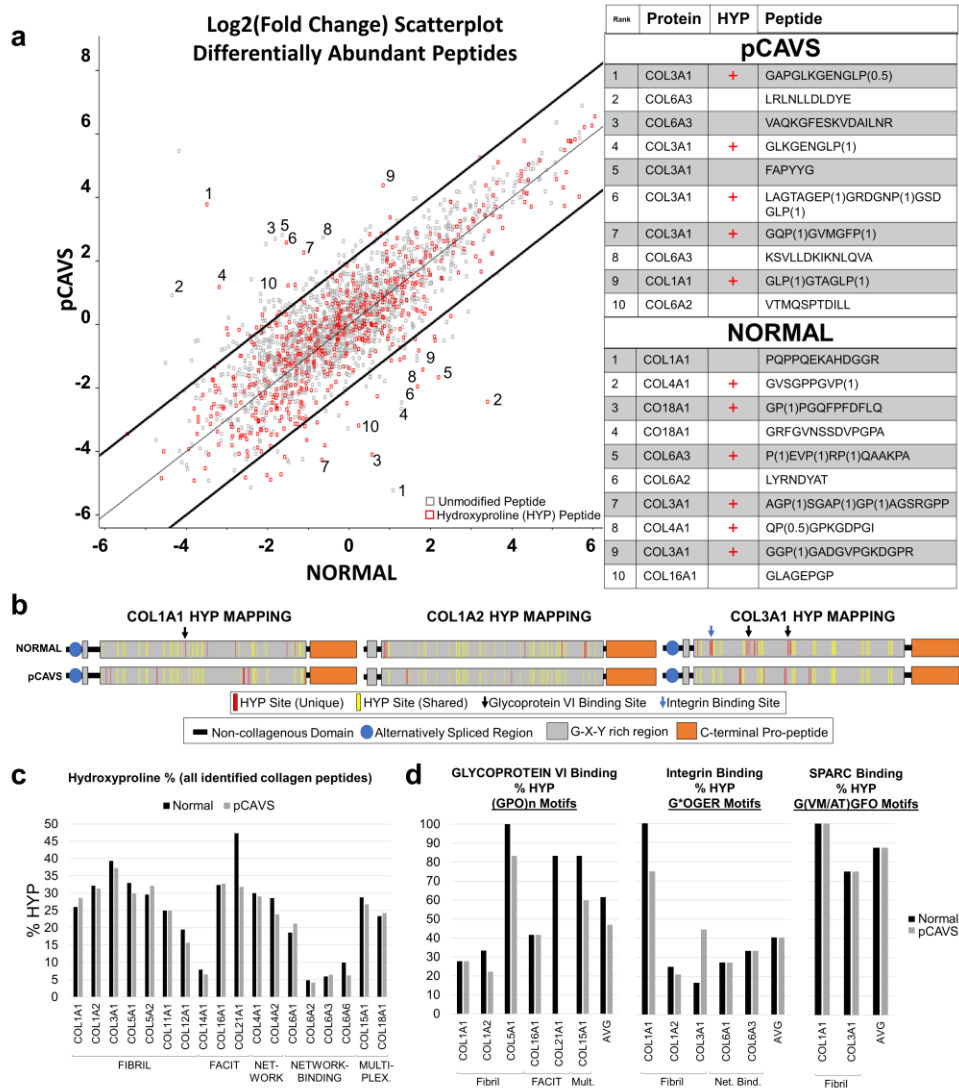
Figure 13: Pediatric CAVS valves have reduced HYP, including in collagen-ECM binding sites. A. log2(fold change) scatterplot of pCAVS vs. Normal peptides. Red squares are HYP containing peptides, grey squares are unmodified peptides. Bold lines indicate X+2 and X-2. Top 10 collagen peptides are annotated with corresponding sequence and protein shown (A, right). P(X) where X is between 0-1, indicated HYP probability at that site. Significantly regulated collagen subtypes differ between pCAVS and normal, with non-fibril types (multiplexin, FACIT) differentially regulated in normal. B. Representative HYP site mapping for COL1A1, COL1A2, and COL3A1, shown for Normal and pCAVS patients (DB27 and DB16, respectively). Normal sample contained more HYP sites than age matched controls. Unique HYP sites in Normal (top, red) are found in glycoprotein vi and integrin binding motifs. C. Quantification of HYP state of proteins in all peptides identified in normal (black) or pCAVS (grey). D. HYP percent in peptides containing glycoprotein vi, integrin, or SPARC binding motifs. Loss of HYP may indicate lack of collagen-ECM binding. Normal n=4, pCAVS n=11.

Table 3: Normal peptides identified with a LOG2(Fold Change) intensity value greater than 2 compared to pCAVS. PEP: Posterior error probability

Protein Name	Uniprot Accession Number	Uniprot Name	Gene Name	Sequence	Oxidation (P)	Oxidation (P) Probabilities	Charges	Mass	PEP	MQ Peptide Score	Intensity	MS/MS Count	Normal Log Transform Mean	pCAVS Log Transform Mean	AVI Log Transform Mean
Basement membrane-specific heparan sulfate proteo	P98160	PGBM_HUMAN	HSPG2	LVNTRSIEYSPQLEDAGSRE	0		3	2411.1605	0.000	122.8	2.E-07	4	2.325	-0.505	0.617
Basement membrane-specific heparan sulfate proteo	P98160	PGBM_HUMAN	HSPG2	NPSVQGGQCLPETNQAPL	1	NP(0.5)SVQGSQCQLP(0.014)ETNQAP(0.486)L	2	1885.8364	0.034	81.7	3.E-06	1	1.347	-1.029	NaN
Biglycan	P21810	PGS1_HUMAN	BGN	LHSNNITKVG	0		2	1082.5720	0.088	88.8	4.E-05	1	-1.762	-4.009	-2.481
Collagen alpha-1(I) chain	P02452	CO1A1_HUMAN	COL1A1	FLPQPPQEKAHDGGR	1	FLP(0.004)QP(0.195)P(0.801)QEKAHDGGR	2;3	1691.8380	0.025	87.7	2.E-07	1	1.623	-0.460	-0.201
Collagen alpha-1(I) chain	P02452	CO1A1_HUMAN	COL1A1	GIGGLNGLP	0		2	870.4447	0.027	108.5	4.E-06	5	1.671	-0.993	-2.153
Collagen alpha-1(I) chain	P02452	CO1A1_HUMAN	COL1A1	GSPGENGAPGQMGPR	1	GSP(0.5)GENGAP(0.5)GQMGPR	2	1444.5689	0.014	97.5	4.E-05	4	-1.081	-3.205	NaN
Collagen alpha-1(I) chain	P02452	CO1A1_HUMAN	COL1A1	IAGAPGFPGAR	1	IAGAP(0.5)GFP(0.5)GAR	2	1044.5352	0.007	111.8	6.E-06	10	1.257	-0.737	-1.330
Collagen alpha-1(I) chain	P02452	CO1A1_HUMAN	COL1A1	POPPQEKAHDGGR	0		3	1415.6906	0.162	83.1	8.E-05	1	1.076	-5.239	NaN
Collagen alpha-1(III) chain	P02461	CO3A1_HUMAN	COL3A1	ADGYPGKDGPR	0		2	1067.5360	0.078	85.3	1.E-05	1	-1.483	-4.338	NaN
Collagen alpha-1(III) chain	P02461	CO3A1_HUMAN	COL3A1	GEPGRDGNPGSDGLPGRDGSP	4	GEP(1)GRDGNP(1)GSDGLP(1)GRDGSP(1)	3	2056.8682	0.000	118.7	1.E-05	7	0.687	-2.264	-4.536
Collagen alpha-1(III) chain	P02461	CO3A1_HUMAN	COL3A1	GEPGRDGNPGSDGLPGRDGSP	1	GEP(0.25)GRDGNP(0.25)GSDGLP(0.25)GRDGSP(0.25)	3	2056.8682	0.000	133.9	1.E-06	3	1.250	-1.104	NaN
Collagen alpha-1(III) chain	P02461	CO3A1_HUMAN	COL3A1	GGPGADGVPGKDGPR	1	GGP(1)GADGVPGKDGPR	3	1351.6480	0.017	58.0	2.E-06	1	0.231	-3.189	-4.848
Collagen alpha-1(III) chain	P02461	CO3A1_HUMAN	COL3A1	GIKGENGPVGENGAPGPM	2	GIKGENG(0.5)P(0.5)GENGAP(0.25)GPM	3	1743.7621	0.000	234.8	6.E-06	18	2.095	-0.987	NaN
Collagen alpha-1(IV) chain	P02462	CO4A1_HUMAN	COL4A1	QPGPKGDPGI	1	QP(1)GP(0.999)KGDP(0.001)GI	1	996.4876	0.091	88.4	1.E-06	4	1.678	-1.958	-0.703
Collagen alpha-1(V) chain	P20908	CO5A1_HUMAN	COL5A1	GETGDVGQMGPP	1	GETGDVGQMGP(0.224)P(0.776)	1	1175.4755	0.048	91.3	2.E-05	2	-1.680	-4.722	NaN
Collagen alpha-1(V) chain	P20908	CO5A1_HUMAN	COL5A1	GLQGPVGLP	1	GLQGPVGLP(1)	1	1554.7903	0.122	100.2	4.E-06	3	0.523	-1.661	-1.499
Collagen alpha-1(VI) chain	P12109	CO6A1_HUMAN	COL6A1	FLTAGRTDPAHDVR	0		3	2265.9483	0.044	89.7	1.E-05	2	2.498	0.273	0.355
Collagen alpha-1(VI) chain	P12109	CO6A1_HUMAN	COL6A1	GEAGDEGNPGPDGAPGERGGPK	0	GEAGDEGNP(0.001)GP(0.005)DGAP(0.496)GERGGP(0.498)IG	3	1407.7219	0.033	100.4	6.E-06	6	-1.904	-4.896	NaN
Collagen alpha-1(VI) chain	P12109	CO6A1_HUMAN	COL6A1	VTAGRTDPAHDVR	0		2;3	1814.9483	0.023	80.9	6.E-07	7	0.524	-1.646	-0.103
Collagen alpha-1(VI) chain	P12109	CO6A1_HUMAN	COL6A1	VAVVGYSGTGQPPPERA	0		2	1466.6096	0.060	70.3	6.E-05	3	2.550	-0.394	1.959
Collagen alpha-1(XI) chain	P12107	CO1A1_HUMAN	COL11A1	MGPQGEPGPGPGQOGN	1	MGP(0.004)QGEP(0.831)GP(0.134)P(0.032)GQOGN	1	696.3443	0.143	77.7	1.E-06	1	1.044	-1.134	NaN
Collagen alpha-1(XVI) chain	Q07092	COGA1_HUMAN	COL16A1	GLAGEPGP	0		2	1364.6401	0.011	119.7	1.E-06	1	-0.018	-3.272	NaN
Collagen alpha-1(XVIII) chain	P39060	CO1A1_HUMAN	COL18A1	GPPGQPPFDLQ	1	GP(0.5)P(0.5)GQPPFDLQ	2	1359.6419	0.027	103.2	8.E-05	1	0.563	-4.107	-1.940
Collagen alpha-1(XVIII) chain	P39060	CO1A1_HUMAN	COL18A1	GRFGVNSDVPGPA	0		2	1057.5152	0.002	134.2	9.E-06	18	1.275	-2.657	NaN
Collagen alpha-2(I) chain	P08123	CO1A2_HUMAN	COL1A2	GARGSDGSVGPV	0		1;2	1271.5630	0.000	155.1	8.E-07	34	1.669	-1.130	-2.907
Collagen alpha-2(I) chain	P08123	CO1A2_HUMAN	COL1A2	GAVGSPVWGAPGEA	2	GAVGSP(1)VWGAP(1)VGEA	2	1843.8546	0.000	126.1	8.E-05	11	2.111	-0.500	-2.597
Collagen alpha-2(I) chain	P08123	CO1A2_HUMAN	COL1A2	GAVGSPVWGAPGEAGRDGNP	3	GAVGSP(1)VWGAP(1)VGEAGRDGNP(1)	2	2193.9159	0.000	113.3	1.E-05	2	-0.781	-3.500	-1.856
Collagen alpha-2(I) chain	P08123	CO1A2_HUMAN	COL1A2	GSPGVNGAPGEAGRDGNPGNDG	3	GSP(1)VWGAP(1)GEAGRDGNP(0.012)GNDGP(0.494)P(0.494)I	2	2209.9108	0.000	145.7	1.E-05	13	-2.024	-4.749	NaN
Collagen alpha-2(I) chain	P08123	CO1A2_HUMAN	COL1A2	GSPGVNGAPGEAGRDGNPGNDG	2	GSP(0.5)VWGAP(0.5)GEAGRDGNP(0.492)GNDGP(0.254)PI0.	2	754.3861	0.048	106.8	9.E-06	21	-1.047	-2.995	NaN
Collagen alpha-2(I) chain	P08123	CO1A2_HUMAN	COL1A2	LVGEPGPA	1	LVGEP(1)GPA	1	900.3825	0.036	99.1	9.E-06	1	1.705	-0.824	-0.352
Collagen alpha-2(I) chain	P08123	CO1A2_HUMAN	COL1A2	PGVWGAPGEA	2	GSP(0.5)VWGAP(0.5)GEAGRDGNP(0.492)GNDGP(0.254)PI0.	2	900.3825	0.036	99.1	5.E-05	1	-0.046	-2.481	NaN
Collagen alpha-2(I) chain	P08123	CO1A2_HUMAN	COL1A2	SPGVNGAPGEA	2	SR(1)GVWGAP(1)GEA	2	987.4145	0.095	82.7	1.E-05	1	-2.541	-4.824	NaN
Collagen alpha-2(VI) chain	P12110	CO6A2_HUMAN	COL6A2	LANIMFEQR	0		2	1075.5332	0.016	88.2	3.E-06	3	-0.565	-2.723	-1.652
Collagen alpha-2(VI) chain	P12110	CO6A2_HUMAN	COL6A2	LQGGRDLGEQN	0		2	1215.5684	0.021	99.8	6.E-06	2	-1.145	-4.243	-5.432
Collagen alpha-2(VI) chain	P12110	CO6A2_HUMAN	COL6A2	LYRNDYAT	0		2	1015.4611	0.134	79.7	2.E-06	1	1.298	-2.462	-3.148
Collagen alpha-3(VI) chain	P12111	CO6A3_HUMAN	COL6A3	FDFDEYQPEMLEKFR	0		2;3	2008.8877	0.052	112.4	4.E-05	29	3.658	1.615	1.560
Collagen alpha-3(VI) chain	P12111	CO6A3_HUMAN	COL6A3	HANTKVGELFLR	0		3	1373.7528	0.005	89.4	3.E-06	2	-2.426	-5.142	-5.191
Collagen alpha-3(VI) chain	P12111	CO6A3_HUMAN	COL6A3	PEVPRPQAAKPA	3	P(1)EVP(1)RP(1)QAAKPA	2	1307.6834	0.065	84.2	3.E-05	2	2.204	-1.657	NaN
Collagen alpha-3(VI) chain	P12111	CO6A3_HUMAN	COL6A3	PLR.NLLDLDYE	0		2	1472.7875	0.002	120.3	7.E-05	1	0.886	-1.794	-2.687
Dentin sialophosphoprotein	Q9NZW4	DSPP_HUMAN	DSPP	RSNTINQNTDKNTQNGDV	0		2	1838.7402	0.022	98.3	2.E-06	2	0.426	-1.985	NaN
Fibromodulin	Q06828	FMOD_HUMAN	FMOD	LBELHDHNQ	0		3	1258.6422	0.074	106.4	6.E-06	3	0.732	-1.649	-1.853
Fibromodulin	Q06828	FMOD_HUMAN	FMOD	LYLDHNNLTR	0		2;3	1273.6527	0.138	90.1	2.E-06	2	-0.259	-2.861	-4.221
Fibronectin	P02751	FINC_HUMAN	FN1	NLAPDSSSVVVSG	1	NLAP(1)DSSSVVVSG	1	1247.5881	0.062	81.3	1.E-07	6	2.403	0.070	-0.457
Tenascin-X	P22105	TENX_HUMAN	TENX	LLEETTVRTE	0		2	1189.6199	0.016	105.5	4.E-06	4	1.811	-1.432	-2.549
Vimentin	P08670	VIME_HUMAN	VIM	KNLQEEAEWYKSK	0		3	1651.8206	0.000	161.2	8.E-06	12	1.368	-0.746	-0.918

Table 4: pCAVS peptides identified with a LOG2(Fold Change) intensity value greater than 2 compared to Normal. PEP: Posterior error probability.

Protein Name	Uniprot Accession Number	Uniprot Name	Gene Name	Sequence	Oxidation (P)	Oxidation (P) Probabilities	Charges	Mass	PEP	MQ Peptide Score	Intensity	MS/MS Count	Normal Log Transform Mean	pCAVS Log Transform Mean	AVI Log Transform Mean
Asporin	Q9BXN1	ASPN_HUMAN	ASPN	SEIPNLPKS			1	1096.6128	0.007	120.3	4.E+05	7	-2.1048	0.1160	NaN
Basement membrane-specific heparan sulfate proteoglycan core protein				LAFTNEAFEKIPSETLNR											1.1328
Biglycan	P21810	BGH3_HUMAN	BGH3	IELLEDLLRYSKLYR	0		3	1800.9989	0.040	79.8	7.E+07	6	0.1578	2.4777	1.1328
Biglycan	P21810	PGS1_HUMAN	PGS1	LARVFSGLPDLK	0		3	1854.7803	0.003	73.8	1.E+07	2	-0.9563	1.4436	-0.9051
Biglycan	P21810	PGS1_HUMAN	PGS1	GLPDLRPPDAK	2	GLP(1)IGTAGLP(1)	2	871.4492	0.049	136.3	7.E+07	38	-0.5734	1.6439	1.6777
Collagen alpha-1(I) chain	P02452	C01A1_HUMAN	COL1A1	PPDEKAHDGGRYY	2		1	1516.7059	0.040	135.2	6.E+08	21	0.9425	4.6363	-0.0657
Collagen alpha-1(I) chain	P02452	C01A1_HUMAN	COL1A1	FAPYYG	1		1	716.3170	0.158	85.8	6.E+07	5	-0.2527	2.1925	1.0390
Collagen alpha-1(I) chain	P02461	C03A1_HUMAN	COL3A1	GAPGLKGENGLP	2	GAP(0.5)GLKGENGLP(0.5)	2	1125.5666	0.029	77.5	8.E+07	11	-1.6375	2.8232	1.1229
Collagen alpha-1(III) chain	P02461	C03A1_HUMAN	COL3A1	GLAGTAGEPGRDGNPGSGDGLP	3	GLAGTAGEP(1)GRDGNP(1)GSGDGLP(1)	2	1942.8504	0.000	95.1	1.E+07	1	-3.4981	3.7819	2.7079
Collagen alpha-1(III) chain	P02461	C03A1_HUMAN	COL3A1	GLKGENGLP	1	GLKGENGLP(1)	2	900.4553	0.029	123.1	2.E+06	1	-2.2755	-0.1069	NaN
Collagen alpha-1(III) chain	P02461	C03A1_HUMAN	COL3A1	GGPGVMGFP	1/2	GGPH(1)GWMGFP(1)	1/2	985.4011	0.017	107.3	1.E+07	9	-3.1905	1.1839	0.2164
Collagen alpha-1(III) chain	P02461	C03A1_HUMAN	COL3A1	GGPGVMGFP	0	GGPGVMGFP(1)	1/2	985.4011	0.020	118.0	8.E+07	19	1.0131	3.3746	-0.4589
Collagen alpha-1(III) chain	P02461	C03A1_HUMAN	COL3A1	GRPGRPGERGLPGPPGIKGPA	1	GRP(0.061)GPP(0.089)GERGLP(0.06)GP(0.001)PGIKGPA	1	2038.1194	0.056	113.1	1.E+07	10	-1.1158	2.2727	-0.0280
Collagen alpha-1(III) chain	P02461	C03A1_HUMAN	COL3A1	LAGTAGEPGSGRDGNPGSGDGLP	1	LAGTAGEP(0.5)GRDGNPGSGDGLP(0.5)	1	2591.2000	0.000	78.5	2.E+07	1	-1.7151	3.7576	0.0850
Collagen alpha-1(III) chain	P02461	C03A1_HUMAN	COL3A1	VAVGGLAGYPGP	0	VAVGGLAGYP(0.5)GP(0.5)	1	1088.5502	0.148	71.7	2.E+07	1	-2.1409	-0.0839	2.2532
Collagen alpha-1(IV) chain	P02462	C04A1_HUMAN	C04A1	DGLPGDMGPPG	0		1	1011.4331	0.168	73.7	2.E+07	1	-0.8143	1.6616	-1.7123
Collagen alpha-1(V) chain	P20908	CO5A1_HUMAN	CO5A1; COL1IA1	GAPGKPGPGGL	1	GAP(0.5)GKP(0.452)GP(0.048)GGL	1/2	980.4927	0.058	90.7	1.E+07	40	-1.5204	1.2157	0.0534
Collagen alpha-1(V) chain	P20908	CO5A1_HUMAN	CO5A1	GPPGTMLMLP	1	GP(0.5)P(0.5)GTMLMLP	1/2	1044.4984	0.000	138.4	9.E+06	6	-1.5024	1.2157	0.5555
Collagen alpha-1(V) chain	P20908; P12107	CO5A1_HUMAN; CO5A1_HUMAN	CO5A1	GSIGPGFP	2	GSIGP(1)GFP(1)	2	909.4292	0.030	108.8	6.E+06	7	0.5141	2.8417	-0.7466
Collagen alpha-1(VI) chain	P12109	CO6A1_HUMAN	CO6A1	IDTIVDMKNNEQV	0		3	1729.8920	0.000	178.7	1.E+08	6	-2.8423	2.9586	-2.4121
Collagen alpha-1(VI) chain	P12109	CO6A1_HUMAN	CO6A1	LVITDGRSDTGHDTTPLNV	0		2/3	2100.0811	0.037	59.2	4.E+07	8	-1.0554	-0.1752	1.4868
Collagen alpha-1(VI) chain	P12109	CO6A1_HUMAN	CO6A1	QYEHSGDMDEHS	0		2	1489.6160	0.048	52.7	5.E+06	2	-2.6176	-0.1115	-0.0316
Collagen alpha-1(XIV) chain	Q05707	COEA1_HUMAN	COEA1	VFTTEDVRAQQYLEDEVTTDSFR	0		2/3	2816.3392	0.000	166.7	1.E+08	11	-2.4074	-0.3436	-0.8350
Collagen alpha-2(VI) chain	P08123	CO1A2_HUMAN	CO1A2	GARGLPGERGRVGAPGP	1	GARGLP(1)GERGRVGAPGP	1	1618.8652	0.113	69.3	1.E+08	1	-0.7930	2.9586	0.4042
Collagen alpha-2(I) chain	P08123	CO1A2_HUMAN	CO1A2	GPSGPSGLP	1	GPSGPSGLP(1)GER	2	1125.5415	0.029	97.8	4.E+05	1	-2.7069	-0.1752	-4.5067
Collagen alpha-2(I) chain	P08123	CO1A2_HUMAN	CO1A2	GSPGNGPAGKEGPVGLPGIDGRP	3	GSP(1)GNGPAGKEGP(0.002)VGLP(0.998)GIDGRP(1)	2	2246.1291	0.064	86.0	5.E+06	1	-3.0070	-0.1115	NaN
Collagen alpha-2(I) chain	P08123	CO1A2_HUMAN	CO1A2	GVRGPNGDAGRPGEPGLM	2	GPAGVRGPNGDAGRP(1)GEP(1)GLM	2/3	1754.8113	0.019	91.1	5.E+06	3	-2.9732	-0.3157	-1.1215
Collagen alpha-2(I) chain	P08123	CO1A2_HUMAN	CO1A2	SGGGYDFGYDGDFYRA	0		2	1745.6968	0.000	145.2	1.E+07	14	-1.6850	0.7243	NaN
Collagen alpha-2(VI) chain	P08123	CO1A2_HUMAN	CO1A2	VGLGPGFMG	3		3	799.3898	0.152	77.9	2.E+06	1	-2.5026	-0.2940	NaN
Collagen alpha-2(VI) chain	P05997	CO5A2_HUMAN	CO5A2	GPVGSPGLP	1	GP(1)VGSP(1)GLP(1)	3	827.4025	0.091	89.7	6.E+07	6	3.2119	5.2425	NaN
Collagen alpha-2(VI) chain	P05997	CO5A2_HUMAN	CO5A2	FSYVDALG	0		2	573.3184	0.036	104.0	5.E+06	1	-3.8502	-1.1463	NaN
Collagen alpha-2(VI) chain	P12110	CO5A2_HUMAN	CO5A2	LGSGVDMDVLT	1/2		1/2	1280.5805	0.013	104.0	9.E+06	40	0.2975	2.6309	1.2559
Collagen alpha-2(VI) chain	A6NMZ7	CO6A6_HUMAN	CO6A6	LINANLLDS	0		1	971.5398	0.031	105.4	1.E+05	2	-3.1398	-3.8015	NaN
Collagen alpha-2(VI) chain	P12110	CO6A2_HUMAN	CO6A2	VTMQSPTDLL	1/2		1/2	1216.6373	0.013	104.0	3.E+07	10	-2.1749	0.9699	-0.0771
Collagen alpha-2(VI) chain	P12111	CO6A3_HUMAN	CO6A3	AAEGIPKLLVL	0		2	1122.7012	0.033	95.5	9.E+06	5	-2.0678	2.2197	0.8449
Collagen alpha-3(VI) chain	P12111	CO6A3_HUMAN	CO6A3	FMYDRFLRLNLDLDYE	1	FMYDRF(1)LRLNLDLDYE	3	2201.0827	0.023	87.5	1.E+06	1	-2.1313	0.3091	NaN
Collagen alpha-3(VI) chain	P12111	CO6A3_HUMAN	CO6A3	FRELPSLEQKL	0		2/3	1358.7558	0.000	147.7	4.E+08	61	1.1809	3.2767	4.2496
Collagen alpha-3(VI) chain	P12111	CO6A3_HUMAN	CO6A3	KEVLLDKKNLQVA	0		2/3	1567.9661	0.100	73.1	1.E+07	2	-0.6385	2.7878	1.6081
Collagen alpha-3(VI) chain	P12111	CO6A3_HUMAN	CO6A3	LGGPTPKTGAALEFVLRN	0		2/3	1835.9686	0.000	193.5	1.E+06	10	-1.6325	0.5093	0.4463
Collagen alpha-3(VI) chain	P12111	CO6A3_HUMAN	CO6A3	LQDKFLGPSPGVQGGRDWF	0		2/3	2094.0525	0.000	133.0	2.E+06	7	-3.3567	-0.0257	-3.1520
Collagen alpha-3(VI) chain	P12111	CO6A3_HUMAN	CO6A3	LRLNLDLDYE	0		2	1375.7187	0.000	102.5	2.E+07	3	-4.3541	0.0138	-3.1668
Collagen alpha-3(VI) chain	P12111	CO6A3_HUMAN	CO6A3	LTEDTLKVYLNK	0		2/3	1435.7922	0.025	102.5	2.E+07	3	-2.0618	0.1143	-3.3290
Collagen alpha-3(VI) chain	P12111	CO6A3_HUMAN	CO6A3	LTLLGGPTRNTGAALEFVLRN	0		3	2153.1845	0.000	191.6	4.E+06	7	-2.9610	-0.6900	-0.4187
Collagen alpha-3(VI) chain	P12111	CO6A3_HUMAN	CO6A3	PGEDGYGRYGDGEGPGER	1	GIPGEDGYGRYP(0.967)GDGEGGP(0.033)GER	2/3	1979.8046	0.001	122.3	2.E+07	30	-1.8448	0.5886	-1.6925
Collagen alpha-3(VI) chain	P12111	CO6A3_HUMAN	CO6A3	PGVGGKDKVVF	0		2	1770.9515	0.000	123.3	2.E+07	5	-1.7773	0.2732	NaN
Collagen alpha-3(VI) chain	P12111	CO6A3_HUMAN	CO6A3	VACKGFSKVDALNR	1		2/3	1129.6244	0.131	78.1	4.E+06	1	-3.7122	-0.5140	-1.4834
Collagen alpha-3(VI) chain	P12111	CO6A3_HUMAN	CO6A3	VLGPLPSRWGG	0		2/3	1773.9737	0.000	139.5	2.E+06	15	-1.8115	2.7017	3.0137
Collagen alpha-3(VI) chain	P12111	CO6A3_HUMAN	CO6A3	VRGFRELPNEERBMMS	0		2/3	2119.0888	0.000	157.3	4.E+07	32	-0.8885	1.4184	-0.2956
Collagen alpha-3(VI) chain	P12111	CO6A3_HUMAN	CO6A3	LHLDNNKLTRVPSG	0		2/3	2131.8544	0.000	113.1	1.E+08	10	1.5445	3.5750	2.2189
Decorin	P07585	PGS2_HUMAN	PGS2	LILWNNKGKVSPGA	0		3	1532.8423	0.007	125.5	2.E+07	5	-1.1238	1.3352	-0.3027
Decorin	P07585	PGS2_HUMAN	PGS2	LGIPPVLPVPRGFPP	0		2	1592.9330	0.002	90.9	2.E+07	17	-2.7646	1.1035	-1.0830
Fibromodulin	P35555	FBN1_HUMAN	FBN1	SPNISACIDNECEL	0		2	1620.7011	0.090	72.3	6.E+06	2	-2.0677	5.5099	NaN
Lumican	P51884	LUM_HUMAN	LUM	IARLPSGLP	0		2	922.5600	0.114	84.6	8.E+07	20	-1.9802	0.7323	0.3523
Lumican	P51884	LUM_HUMAN	LUM	IARLPSGLPVSL	0		2	1221.7445	0.012	119.5	3.E+07	5	-0.8069	1.2787	1.5403
Lumican	P51884	LUM_HUMAN	LUM	KNFPTVAENLENVY	0		2	1710.8101	0.022	110.1	2.E+06	5	-2.1286	2.7017	-1.0631
Lumican	P51884	LUM_HUMAN	LUM	LSFNQIARLPSGLPVSL	0		2/3	1811.0365	0.036	70.9	2.E+06	5	-4.5068	-1.2079	-3.8748
Microfibril-associated glycoprotein 4	P55083	MFAP4_HUMAN	MFAP4	LIVYSGPSVPVP	0		1/2	1234.6754	0.000	146.6	6.E+09	29	-2.4106	2.3157	2.3851
Serpin H1	P50454	SERPH_HUMAN	SERPHN	RSALGSNEWAV	0		3	1275.6295	0.030	96.0	4.E+05	4	-4.1809	5.4669	4.4257
Tenascin	P24821	TENA_HUMAN	TNC	IATVDSEYSIGYTGEKVPEITR	0		3	2340.2213	0.173	59.1	9.E+06	5	4.1459	1.4159	-0.9055
Tenascin	P24821	TENA_HUMAN	TNC	IKDVPSDRTTIDLTEDNQYS	0		2/3	2406.1343	0.000	90.9	2.E+07	5	-1.4715	0.6487	0.7481
Tenascin	P24821	TENA_HUMAN	TNC	NKKSPVSARVATY	0		2	1533.8515	0.121	71.0	9.E+07	5	-0.2405	1.9431	1.6421
Tenascin X	P22105	TENX_HUMAN	TNXB	IGPITTEGASPPFTARVPSS	0		3	2202.1321	0.000	163.9	3.E+06	11	-1.5615	0.6065	-0.7754
Tenascin X	P22105	TENX_HUMAN	TNXB	LLVGGDGKLISGLEPSTPYHF	0		3	2547.3585	0.002	101.6	1.E+06	4	-1.7289	0.7601	NaN
Tenascin X	P22105	TENX_HUMAN	TNXB	MRVPEGPGADHIERVLPGNRGA	0		1/2	2043.1117	0.004	108.1	8.E+07	43	-1.0627	0.7799	0.7046
Tenascin X	P22105	TENX_HUMAN	TNXB	WTVPEGGTGF	0		2/3	1752.8577	0.000	160.8	2.E+08	11	-0.4658	2.5801	2.2208
Vimentin	P08670	VIME_HUMAN	VIME	AKNLQEAEEWYKSK	0		3	2012.0480	0.003	104.9	5.E+07	4	-0.1309	2.1718	-0.5449
Vimentin	P08670	VIME_HUMAN	VIME	FANYIDKVRFLEDGQK	0		3	2238.2161	0.002	68.0	7.E+08	6	0.5245	3.0872	2.5203
Vimentin	P08670	VIME_HUMAN	VIME	FANYIDKVRFLEDGQNIL	0		2/3,4	2237.1119	0.000	114.2	1.E+08	13	-0.1345	2.6271	2.3966
Vimentin	P08670	VIME_HUMAN	VIME	LKGQGKSRLGDLYEEEMRE	0		2	1812.9622	0.024	83.6	1.E+05	3	-3.7943	-0.5447	NaN
Vimentin	P08670	VIME_HUMAN	VIME	LLEGEESRISLPLPNF	0		2	1968.0102	0.025	86.3	9.E+07	9	-2.0795	0.4440	1.1336
Vimentin	P08670	VIME_HUMAN	VIME	LPEKLQEEMLQREEAENT	0		2	2351.0958	0.021	89.5	3.E+08	6	1.5791	3.9456	4.2966
Vimentin	P08670	VIME_HUMAN	VIME	QEEAFL	0		1	948.4280	0.045	88.6	3.E+07	6	-2.0461	2.5316	0.9145

organization[69, 206]. From a total of 2985 peptides identified, with 126 peptides were differentially expressed between normal and pCAVS by a minimum of 2-fold change (**Fig. 13, Tables 3-4**). The majority of altered peptides were from collagen type proteins (87/126; 69%) and these included site-specific modifications of hydroxylated proline (**Figure 13A**). Hydroxyproline site mapping from age-matched normal and pCAVS valves suggested a strong potential for HYP site variation within the triple helical regions on fibril type collagens α1(I), α2(I), α1(III) (**Fig. 13B**). Site occupancy analytics showed 41 HYP sites in collage α1(I) were shared between normal and pCAVS valves; the normal valve showed 5 unique sites of HYP modification while the pCAVS valve showed 8 sites of HYP modification that were not detected in normal valves (**Fig. 13B**). Consistent with data across the abundantly changed peptides, normal valve collagen α2(I) and α1(IIII) contained more HYP sites than the age-matched pCAVS valve. In collagen α2(I), 41 sites were shared with 9 unique HYP sites in normal valve and only 3 unique HYP sites in the age matched CAVS sample However for collagen α1(III), the normal AV (SKU DB27) showed an additional 16 unique hydroxyproline sites, while 7 unique HYP sites identified in the pCAVS valve (SKU DB16; **Fig 13B**). Among patient groups, the overall percent change in HYP content showed more subtle variation (**Fig. 13C**), yet it is likely that regulation at key HYP sites has greater effects on collagen structure organization [69, 207].

Specific HYP binding site motifs were evaluated for pCAVS related changes. These included motifs for glycoprotein VI (collagen-induced platelet adhesion and activation), integrin (cell-surface receptor for collagen)[208] and SPARC (cell invasion) (**Fig. 13D**)[207]. Qualitatively, fibril type collagens α2(I) and α1(V) showed reduced HYP in glycoprotein VI binding sites. Similarly, collagen α1(I) demonstrated potential reduction

in HYP content for integrin binding sites. Collagen α1(XXI), which was recently found to be transcriptionally increased in cardiomyopathy remodeling[209], showed large decreases in pCAVS HYP content; in pCAVS, HYPs in known binding motifs of glycoprotein VI were undetected in collagen α1(XXI). The analysis of collagen structure variation by peptide analytics suggests that collagen HYP site regulation may contribute to human aortic valve status.

4.3.6 Valve status is characterized by a differential ECM proteome with primary activities of collagen interaction.

Protein level analysis was performed on the proteomic data (**Fig. 14, Table 5**) to further evaluate how non-collagen ECM proteins contribute to collagen regulation. Proteomic analysis identified a total of 44 ECM proteins, including 18 collagen type proteins, many of which have not been previously associated with the human aortic valve (**Fig. 14A**). When measuring total protein abundance, most collagens showed very little change between normal and pCAVS, suggesting that regulation at the level of post-translational modifications may play a larger role in AV collagen organization. However, there were multiple ECM proteins associated with collagen regulation detected as differentially regulated. The abundance of the proteins fibronectin (FN1) and Transforming Growth Factor Beta Induced protein (BGH3; cell-collagen adhesions[210]) were significantly increased in pCAVS compared to normal AV (2.5-fold, MWU p-value 0.04; 3.4-fold, MWU p-value 0.02, respectively). In AVI, collagen α1(I) and FN1 increased compared to normal AV tissue (1.6-fold, MWU p-value 0.02; 4.6-fold, MWU p-value 0.03). Additionally, the proteomics identified SPARC and VTN proteins only in the pCAVS proteomes, further validated as being upregulated via RNA-Seq (**Fig. 15**).
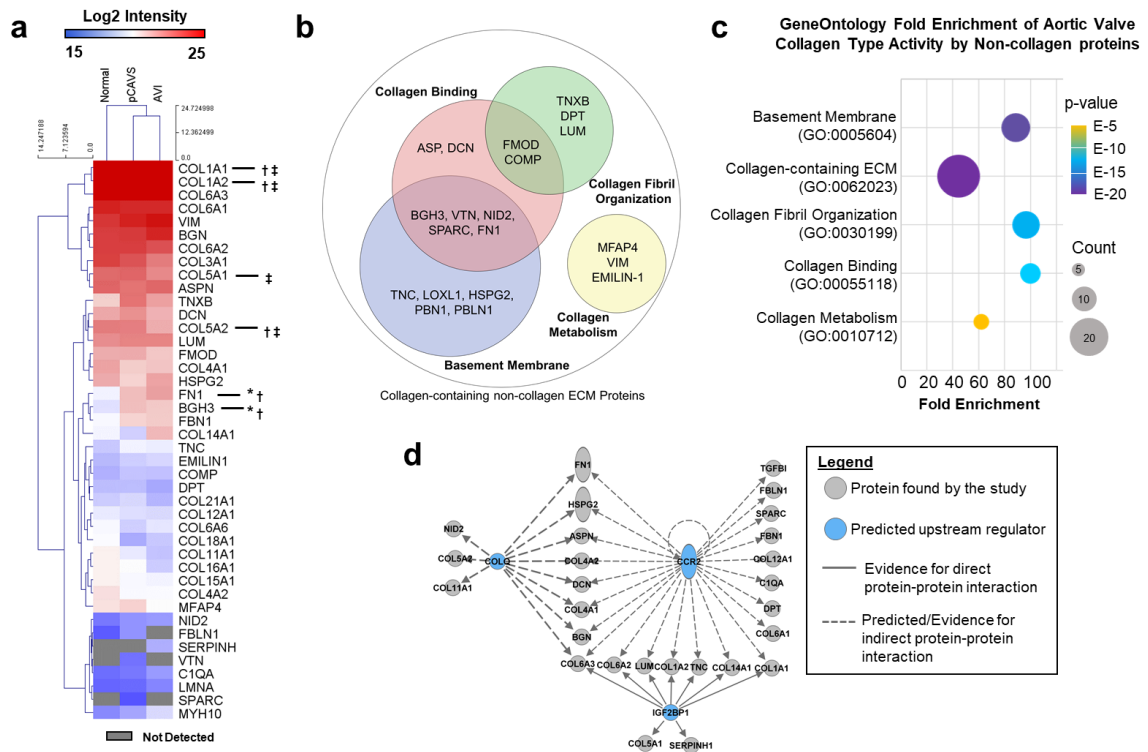
Figure 14: Extracellular matrix proteomics implicates collagen binding and collagen organization pathways. A. Aortic valve extracellular matrix proteins identified by the collagen-targeting proteomics. A total of 18 collagen proteins were identified with COL1A1, COL1A2 and COL6A3 being the most abundant collagens. Protein level quantification, which includes all peptides both unmodified and modified, revealed significant differences based on valve diagnoses in COL1A1, COL1A2, COL5A1, BGH3, FN1, and COL5A2. * Mann-Whitney U adj. p-value <0.05 normal AV compared to pCAVS, † Mann-Whitney U adj. p-value <0.05 normal AV compared to AVI, ‡ Mann-Whitney U adj. p-value <0.05 AVI compared to pCAVS. **B.** Gene Ontology Functional classification of non-collagen type proteins identified in the proteomics dataset. **C.** Gene Ontology Fold Enrichment analysis of collagen type function by non-collagenous proteins identified by proteomics, Fisher's exact p-value ≤ 1.84E-5, false discover rate ≤ 6.66E-3. Proteins associated with collagen binding had the highest degree of fold enrichment, followed by collagen fibril organization. **D.** Upstream analysis of the ECM proteome by Ingenuity Pathways Analysis to identify potential regulators that explain directional changes in aortic valve ECM proteins. Primary regulators affecting the proteome were C-C Motif Chemokine Receptor 2 (CCR2; Fisher's Exact p-value 1.13E-39), Collagen Like Tail Subunit Of Asymmetric Acetylcholinesterase (COLQ; Fisher's Exact p-value 9.67E-19), (Insulin Like Growth Factor 2 MRNA Binding Protein 1 (IGF2BP1, Fisher's Exact p-value 1.05E-18). Normal n=4, pCAVS n=11.
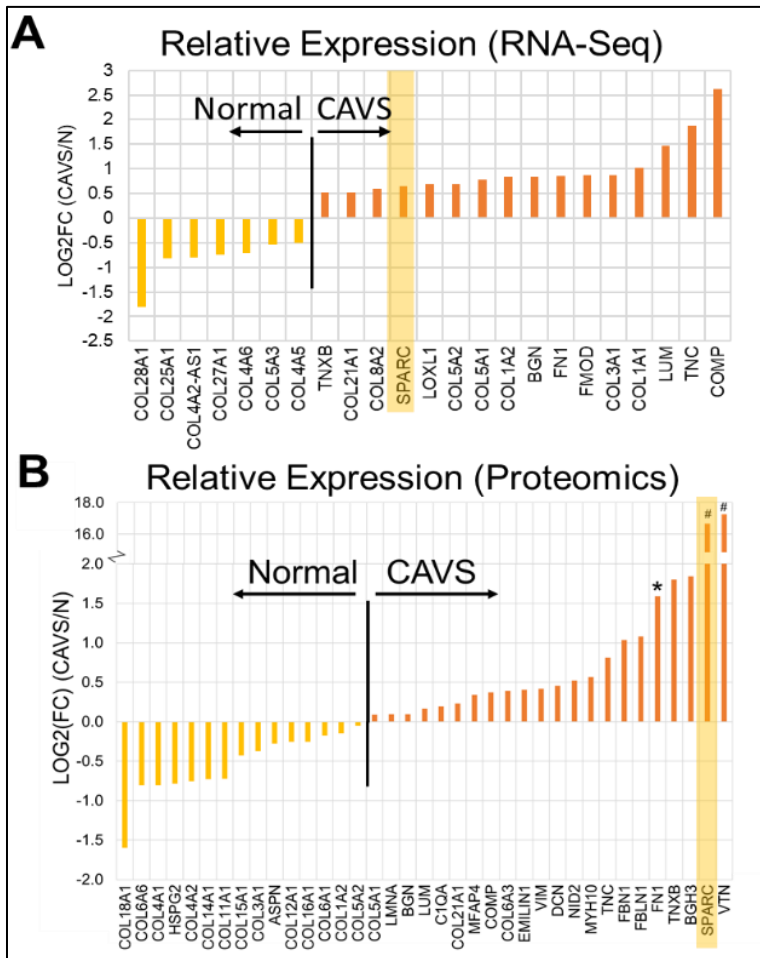
Figure 15: SPARC is enriched in pCAVS valves.
LOG2FC analysis of differentially abundant genes (**A**) and proteins (**B**, COLase3 proteomics) showing SPARC (highlighted), and fibrillogenesis associated collagens (COL5A1, COL3A1, COL1A1), are enriched in pCAVS.

Table 5: Proteins identified via Collagenase Type III LC-MSMS Proteomics. MWU: Mann Whitney U-Test

Protein Name	Protein Accession Numbers (Uniprot)	Gene Symbol	Normal Peptide counts (all)	pCAVS Peptide counts (all)	AVI Peptide counts (all)	Normal Peptide Counts (unique)	pCAVS Peptide Counts (unique)	AVI Peptide Counts (unique)	Normal Sequence Coverage [%]	pCAVS Sequence Coverage [%]	AVI Sequence Coverage [%]	Normal LOG2 Transform Intensity	pCAVS LOG2 Transform Intensity	AVI LOG2 Transform Intensity	Log2(FC) (pCAVS/SN)	Log2(FC) (AVI/N)	Log2(FC) (CAVS/AVI)	Norm-pCAVS MWU p value	Normal-AVI MWU p value	pCAVS-AVI MWU p value
Collagen alpha-6(VI) chain	sp|A6NMZ7|CO6A6	COL6A6	57	170	56	57	170	56	7.0	7.9	5.5	19.87	19.06	19.51	-0.81	-0.36	-0.45	0.226	0.730	0.510
Collagen alpha-1(I) chain	sp|P02452|CO1A1	COL1A1	307	1049	266	303	1035	264	23.0	29.6	19.4	26.36	26.34	25.11	-0.02	-1.25	1.23	0.949	0.016	0.001
Collagen alpha-1(III) chain	sp|P02461|CO3A1	COL3A1	196	687	167	130	437	99	21.5	26.8	18.3	23.74	23.37	22.58	-0.37	-1.16	0.79	0.661	0.063	0.180
Collagen alpha-1(IV) chain	sp|P02462|CO4A1	COL4A1	90	229	73	90	227	71	13.4	14.8	9.5	21.80	21.00	21.16	-0.80	-0.64	-0.16	0.343	0.413	1.000
Prelamin-A/C	sp|P02545|LMNA	LMNA	11	48	20	11	48	20	6.6	9.7	8.7	17.01	17.10	17.59	0.09	0.58	-0.49	1.000	1.000	0.165
Complement C1q subcomponent subunit A	sp|P02745|C1QA	C1QA	16	51	8	16	51	8	12.3	13.1	5.1	17.17	17.37	18.03	0.19	0.86	-0.66	0.851	1.000	0.513
Fibronectin	sp|P02751|FINC	FN1	50	334	95	50	334	96	6.4	14.5	9.7	19.77	21.35	21.92	1.59	2.15	-0.57	0.040	0.002	0.320
Vitronectin	sp|P04004|VTNC	VTN	9	45	5	2	17	1	4.4	8.3	1.9	0.00	17.25	0.00	17.25	0.00	17.25	UTC	UTC	UTC
Collagen alpha-2(V) chain	sp|P05997|CO5A2	COL5A2	81	323	61	81	322	61	11.9	15.9	7.7	22.56	22.51	21.59	-0.05	-0.97	0.92	0.949	0.949	0.005
Decorin	sp|P07585|PGS2	DCN	112	392	89	112	390	89	43.0	52.4	41.4	21.72	22.17	21.53	0.45	-0.19	0.64	0.226	0.413	0.180
Collagen alpha-2(I) chain	sp|P08123|CO1A2	COL1A2	487	1538	380	485	1533	379	33.9	37.7	28.2	26.23	26.09	25.28	-0.14	-0.95	0.81	1.000	0.016	0.001
Collagen alpha-2(IV) chain	sp|P08572|CO4A2	COL4A2	68	136	55	68	134	54	6.9	6.1	5.4	20.66	19.91	19.96	-0.75	-0.70	-0.05	0.489	0.556	0.827
Vimentin	sp|P08670|VIME	VIM	300	1224	456	294	1196	446	72.6	83.2	83.9	23.95	24.37	24.68	0.42	0.73	-0.31	0.489	0.190	0.827
SPARC	sp|P09486|SPRC	SPARC	4	18	2	4	18	2	5.8	9.2	1.7	0.00	16.67	0.00	16.67	0.00	16.67	UTC	UTC	UTC
Collagen alpha-1(XI) chain	sp|P12107|COBA1	COL11A1	57	202	45	18	85	19	6.7	9.2	5.2	20.31	19.58	18.84	-0.72	-1.47	0.74	0.190	0.667	0.333
Collagen alpha-1(VI) chain	sp|P12109|CO6A1	COL6A1	256	944	262	254	936	261	37.5	45.1	31.2	24.37	24.20	24.20	-0.18	-0.17	0.00	0.226	0.286	0.913
Collagen alpha-2(VI) chain	sp|P12110|CO6A2	COL6A2	243	848	238	241	840	235	30.9	34.6	27.1	23.79	23.78	23.43	-0.02	-0.36	0.35	0.949	0.190	0.221
Collagen alpha-3(VI) chain	sp|P12111|CO6A3	COL6A3	724	2839	724	724	2834	842	32.0	38.9	31.8	25.23	25.62	25.86	0.39	0.63	-0.24	0.138	0.063	0.441
Collagen alpha-1(V) chain	sp|P20908|CO5A1	COL5A1	147	503	118	108	385	91	12.1	14.7	9.5	22.94	23.03	22.35	0.09	-0.59	0.68	0.753	0.063	0.027
Biglycan	sp|P21810|PGS1	BGN	207	722	235	207	720	235	44.0	50.9	43.5	23.78	23.88	24.29	0.10	0.50	-0.41	1.000	0.413	0.583
Tenascin-X	sp|P22105|TENX	TNXB	115	660	134	115	660	134	12.1	20.9	11.0	20.95	22.75	21.87	1.80	0.93	0.87	0.056	0.730	0.320
Fibulin-1	sp|P23142|FBLN1	FBLN1	5	20	9	5	20	6	3.0	4.2	2.9	16.80	17.88	0.00	1.08	-16.80	17.88	0.056	UTC	UTC
Tenascin	sp|P24821|TENA	TNC	18	163	43	18	163	43	2.7	8.9	5.0	18.95	19.77	19.65	0.81	0.69	0.12	0.225	0.143	0.827
Fibrillin-1	sp|P35555|FBN1	FBN1	25	113	32	25	113	32	2.1	2.5	1.5	18.85	20.89	19.28	1.03	1.18	-0.14	0.280	0.190	0.827
Myosin-10	sp|P35580|MYH10	MYH10	46	73	41	15	73	26	2.1	2.6	3.0	17.70	18.27	19.79	0.57	1.57	-1.01	1.000	0.533	0.412
Collagen alpha-1(XV) chain	sp|P39059|CO5A1	COL15A1	35	139	15	35	139	41	8.0	8.4	5.1	20.28	19.85	18.96	-0.43	-0.49	0.06	0.753	0.413	0.827
Collagen alpha-1(VIII) chain	sp|P39060|CO8A1	COL8A1	16	69	15	15	39	15	6.9	2.9	2.4	19.97	18.37	18.82	-1.60	-0.59	0.03	0.374	1.000	0.545
Cartilage oligomeric matrix protein	sp|P49747|COMP	COMP	3	18	3	3	18	12	5.5	9.0	5.3	18.48	18.85	18.44	0.37	-1.01	0.34	0.769	1.000	0.949
Serpin H1	sp|P50454|SERPH	SERPINH	103	418	130	60	271	86	2.0	5.3	7.9	0.00	22.40	22.40	0.00	18.44	18.44	UTC	UTC	UTC
Lumican	sp|P51884|LUM	LUM	62	171	43	62	171	43	38.0	42.0	35.8	22.24	20.93	20.05	0.17	18.44	0.00	0.489	0.556	0.827
Microfibril-associated glycoprotein 4	sp|P55083|MFAP4	MFAP4	159	422	161	159	422	161	31.0	34.3	21.3	20.59	20.90	21.80	0.34	0.17	0.88	0.571	0.466	0.177
Basement membrane-specific heparan sulfate proteoglycan core protein	sp|P98160|PGBM	HSPG2	52	159	90	52	159	90	8.7	8.7	7.3	21.68	20.93	21.39	-0.78	-0.54	-0.90	0.280	0.905	0.377
Collagen alpha-1(XIV) chain	sp|Q05707|COEA1	COL14A1	121	443	104	117	430	103	8.7	9.1	11.2	19.82	20.90	21.11	-0.73	0.12	-2.30	0.280	0.286	0.090
Fibromodulin	sp|Q06828|FMOD	FMOD	30	123	32	28	111	29	44.3	50.7	34.3	21.64	21.65	21.11	0.00	1.57	0.54	1.000	0.190	0.267
Collagen alpha-1(XVI) chain	sp|Q07092|CO6A1	COL16A1	19	73	21	19	73	21	5.0	8.2	4.9	20.28	20.03	19.01	-0.25	-0.53	1.02	0.753	0.114	0.138
Dermatopontin	sp|Q07507|DERM	DPT	11	50	17	11	50	17	17.2	22.0	19.4	18.74	18.74	18.31	0.00	-1.27	0.42	0.641	0.133	0.280
Nidogen-2	sp|Q14112|NID2	NID2	47	277	70	47	277	70	2.1	3.5	2.4	17.35	17.87	18.03	0.52	0.42	-0.15	0.571	1.000	1.000
Transforming growth factor-beta-induced protein ig-h3	sp|Q15582|BGH3	BGH3	18	55	14	18	50	14	15.7	29.9	19.2	19.44	21.28	21.08	1.84	0.67	0.21	0.018	0.190	0.441
Collagen alpha-1(XXI) chain	sp|Q96P44|COLA1	COL21A1	56	197	64	56	197	64	6.3	7.5	4.3	19.00	19.24	18.58	0.23	1.64	0.65	0.489	0.057	0.126
Collagen alpha-1(XII) chain	sp|Q99715|CO2A1	COL12A1	42	115	38	42	115	38	5.8	7.0	5.4	19.61	19.35	19.29	-0.25	-0.42	0.06	0.753	0.005	1.000
Asporin	sp|Q9BXN1|ASPN	ASPN	2	11	0	2	11	0	18.7	22.9	17.3	23.02	22.74	23.00	-0.28	-0.32	-0.26	0.571	1.000	0.743
Dentin sialophosphoprotein	sp|Q9NZW4|DSPP	DSPP							0.7	1.3	0.0	0.00	0.00	0.00	-0.02	0.00	0.00	UTC	UTC	UTC
EMILIN-1	sp|Q9Y6C2|EMIL1	EMILIN1	24	109	32	24	109	32	7.5	10.9	7.2	18.64	19.04	19.21	0.40	0.57	-0.17	0.280	0.286	0.661

Table 6: Gene Ontology analysis results of non-collagen type proteins identified via Collagenase Type III LC-MSMS Proteomics. P-value is Fisher's exact p-value. FDR: false discovery rate

Fold Enrichment	Function	GO	Proteins	Protein Count	p-value	FDR	-LOG10(FDR)
88.65	Basement Membrane	GO:0005604	TNC, LOXL1, HSPG2, BGH3, VTN, NID2, SPARC, FN1, FBN1, FBLN1	10	1.66E-17	1.11E-14	13.95
44.61	Collagen-containing ECM	GO:0062023	TNC, LOXL1, C1QA, TNXB, ASPN, MFAP4, DPT, BGN, FMOD, HSPG2, DCN, LUM, EMILIN1, COMP, BGH3, VTN, NID2, SPARC, FN1, FBN1, FBLN1	21	4.58E-33	9.2E-30	29.04
96.53	Collagen fibril organization	GO:0030199	TNXB, DPT, FMOD, LUM, COMP	5	2.64E-09	5.26E-06	5.28
100	Collagen binding	GO:0005518	ASP, DCN, LUM, COMP, BGH3, VTN, NID2, SPARC, FN1	10	1.24E-16	1.96E-13	12.71
62.06	Collagen metabolism	GO:0010712	MFAP4, VIM, EMILIN-1	3	1.84E-05	0.00666	2.18

Gene ontology analyses identified that 26 of the 29 non-collagen proteins were associated with collagen-containing ECM (**Fig. 14B-C, Table 6).** Furthermore, very specific groups of proteins were involved in collagen binding, collagen fibril organization and collagen metabolism (**Fig 14B-C**).

To understand potential regulators of the dataset responsible for directional expression changes in pCAVS compared to normal, protein interaction networks were interrogated (**Fig. 14D**). While some regulators, such as TGFβ1, are known to be associated with ECM remodeling and deposition[211], three novel upstream regulators of the collagen proteome were identified that could account for change in expression patterns. This included C-C Motif Chemokine Receptor 2 (CCR2; Fisher's Exact p-value 1.13E-39), Collagen Like Tail Subunit Of Asymmetric Acetylcholinesterase (COLQ; Fisher's Exact p-value 9.67E-19), and (Insulin Like Growth Factor 2 MRNA Binding Protein 1 (IGF2BP1, Fisher's Exact p-value 1.05E-18). Both CCR2 and COLQ1 were implicated as inhibited in pCAVS based on directional changes[212, 213]. On the whole, proteomics identified new collagen types in the human valve and demonstrated that changes in pCAVS structure may identify target regulators of the collagen proteome.

4.3.7 BAMBI as a Potential Novel ECM Regulator of Pediatric Congenital Aortic Valve Stenosis

To identify master regulators that could be driving previously identified upstream regulators of the AV collagen proteome, causal network regulation analysis was performed. This analysis expands the scope of the upstream regulator analysis from **Figure 14** by integrating literature-observed cause-effect relationships (**Figure 16, 17A**). One such master regulator putatively identified was BMP and Activin Membrane-Bound Inhibitor homolog (BAMBI; p-value of overlap 1.16E-18) (**Fig. 17A**), previously identified
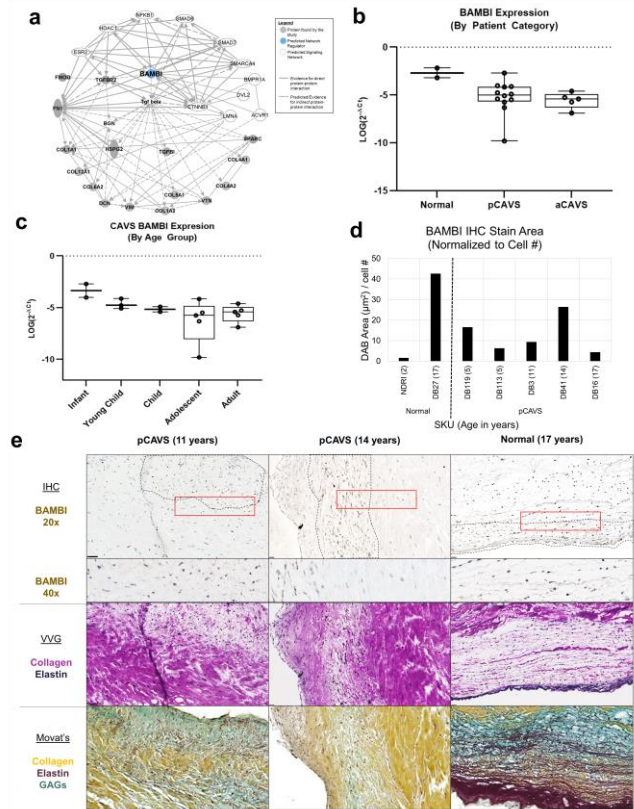
Figure 16: Proteomics based protein-protein interaction networks identify BAMBI as a potential master regulator of the collagen interactome in pCAVS. A. Protein-Protein Interaction network showing relationship BAMBI relative to the ECM proteome and key valvular development proteins. **B.** Quantification of qRT-PCR expression data on BAMBI (normalized to GAPDH), between patient categories. One-way ANOVA shows significant differential expression between patient categories (*p-value 0.013), with significant reduction in pCAVS (MWU *p-value 0.045) and trending reduction in aCAVS (MWU *p-value 0.053) compared to normal pediatric patients. (Normal n=2; pCAVS n=12; aCAVS n=5) **C.** Quantification of qRT-PCR expression data on BAMBI (normalized to GAPDH) of CAVS patients, compared between pediatric age categories (Infant n=2; Young Child n=3; Child n=2; Adolescent n=5; Adult n=6). A suggestive trending decrease of BAMBI expression as a function of pediatric age categories is seen (ANOVA p-value 0.096). **D.** DAB stain area quantification of BAMBI IHC of select valves in the cohort. **E.** Representative immunohistochemistry staining of BAMBI in a selection of pCAVS and normal valves 20x (top) and 40x zoom are shown. BAMBI positive cells appear highly localized, shown in dotted lines. Verhoeff van Geison (VVG) staining on the same valve section post-IHC study is shown (middle). Movat's Pentachrome staining of a serial valve section (bottom). Positive BAMBI staining in pCAVS corresponds heavily to areas low in collagen staining (VVG) and high in GAG staining (Movat's), while normal valve shows positive staining in collagen and elastin rich regions.
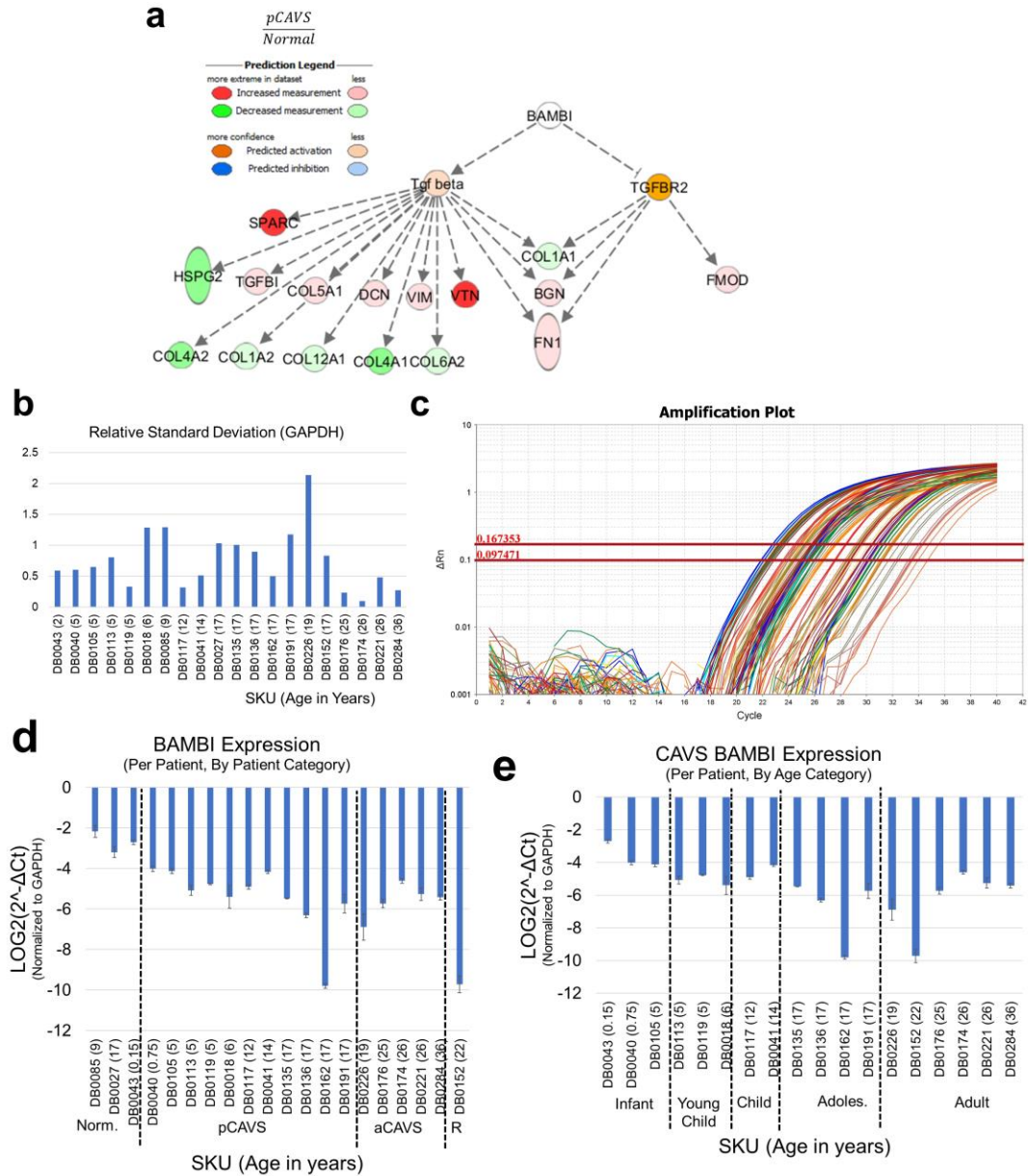
Figure 17: Causal network analysis implicating BAMBI and expression analysis. A)
Causal Network Analysis identifies a potential Master Regulator sorted by highest p-value
overall and of overlap: BAMBI (BMP and activin membrane-bound inhibitor homolog, p-
value 1.16E-18), based on trending expression patterns. **B**) Amplification plot of qRTPCR
experiments in **Figure 6b-d**. **C**) Relative standard deviation (RSD) of GAPDH across all
patient samples, sorted by age of patient. Average RSD is 0.75% ± 0.48%. **D**) Patient-by-
patient expression (shown via $LOG2(2^{-\Delta Ct})$, as normalized to GAPDH expression,
organized by patient disease category. **E**) Patient-by-patient expression (shown via
$LOG2(2^{-\Delta Ct})$, as normalized to GAPDH expression, organized by pediatric age
classification.

as both developmentally regulated[214] and a negative regulator of TGFβ1[215, 216]. Further studies have found that BAMBI may be biomechanically sensitive, and functions to protect murine heart from pressure overload through restraint of TGFβ signaling[217]. In this study, BAMBI was identified as having a high p-value of overlap, which unlike z-score-sorted regulators, is identified independently of the dataset's regulation weight or direction[218]. This preliminary identification of BAMBI was confirmed to have both direct and indirect interaction with proteins implicated in valve disease and development, such as ACVR1, DVL2, and SMARCA4 (**Fig. 16a**). Confirmational transcription-level analysis was performed on a cohort of fresh-frozen pediatric and adult aortic valve samples (Ta**ble 7**, **Fig. 16b&c, Figure 17**). Adult CAVS samples (aCAVS) used in this study showed no calcification by clinical annotation, with the except of SKU SB176. BAMBI expression was found to be significantly differentially regulated between patient categories of normal pediatric, pCAVS, and aCAVS (ANOVA p-value 0.013), with significant reduction in pCAVS (p-value 0.045) and trending reduction in aCAVS (p-value 0.053) compared to normal pediatric patients (**Fig. 16b**). Amongst CAVS patients, there is a suggestive trending decrease of BAMBI expression as a function of pediatric age categories (ANOVA p-value 0.096) (**Fig. 16c**).

IHC staining of BAMBI was performed to visualize translational expression relative to ECM staining in age-matched samples (young child age 2-5; adolescent age 12-18) (**Fig. 6d&e**). BAMBI was not abundantly detected in young normal valves (SKU NDRI, age 2) nor, in contrast, older adolescent pCAVS valves (SKU DB16, age 17) (**Fig. 16d&e**). In the normal valve sample, BAMBI was observed in ventricularis endothelium and in regions of elastin delamination, as visualized by Verhoeff van Gieson (VVG) staining of

Table 7: Descriptive statistics of patient characteristics for aortic valve samples used for rt-qPCR studies (**Fig. 15**). Normal aortic valves are from cardiac transplant patients where normal valve function is defined via 2D echocardiogram. 2D Echocardiogram mean gradients define pre-operative valve function where a normal gradient is defined as <5 mmHg, mild stenosisas 5-25 mmHg, moderate stenosis as 25-50 mmHg, and severe stenosis as >50 mmHg. BSA: body surface area; C: Caucasian. DB43 was included in pCAVS due to stenosis, but main diagnosis was Hypertrophic Cardiomyopathy

	SKU	Age (years)	Pediatric Age Group	Gender	Race/ Ethnicity	BSA (m²)	Leaflet Morphology	Aortic Valve Function
Normal	DB85	9	Child	F	C	0.95	Trileaflet	Normal
	DB27	17	Adolescent	M	C	2.2	Trileaflet	Normal
	Normal Averages	**7.17 ± 7.5**		**75%M 25%F**	**75%C 25%L**	**1.03**		
pCAVS	DB43	0.15	Infant	M	C	0.24	Trileaflet	Moderate stenosis with AVI*
	DB40	0.75	Infant	M	C	0.37	Bicuspid	Moderate Stenosis
	DB105	5	Young Child	M	C	0.72	Bicuspid	Moderate Stenosis with AVI
	DB119	5	Young Child	F	-	-	Bicuspid	Moderate Stenosis with AVI
	DB113	5	Young Child	-	-	-	-	Trivial Stenosis; Severe AVI
	DB18	6	Child	F	C	0.7	Bicuspid	Moderate Stenosis with AVI
	DB117	12	Adolescent	M	-		Bicuspid	Moderate Stenosis with AVI
	DB41	14	Adolescent	M	C	1.6	Bicuspid	Moderate Stenosis with AVI
	DB135	17	Adolescent	M	-	-	-	Moderate Stenosis with AVI
	DB136	17	Adolescent	M	-	-	Bicuspid	Moderate Stenosis with AVI
	DB162	17	Adolescent	F	-	-	Bicuspid	Moderate Stenosis with AVI
	DB191	17	Adolescent	M	-	-	Bicuspid	Moderate Stenosis with AVI
	pCAVS Averages	**6.90 ± 5.8**		**73%M 27%F**	**100%C**	**0.93**		
aCAVS	DB226	19	Adult	F	-	-	Trileaflet	Moderate Stenosis; no calcification
	DB176	25	Adult	F	-	-	Trileaflet	Moderate Stenosis with AVI; calcification
	DB174	26	Adult	M	-	-	Bicuspid	Moderate Stenosis; no calcification
	DB221	26	Adult	M	-	-	Bicuspid	Moderate Stenosis with AVI; no calcification
	DB284	36	Adult	F	-	-	Bicuspid	Severe Stenosis; no calcification
	aCAVS Averages	**26.4 ± 6.1**		**40%M 60%F**	**100%C**	**-**		
Ross	DB152	22	Adult	M	-	-		Pulmonary-AV Autograft with AVI

the same tissue section (**Fig. 16e, right**). BAMBI was also detected in spatially localized regions of mixed collagen-GAG, seen in Movat's Pentachrome staining (**Fig. 16e**). In pCAVS, only certain cells were BAMBI-positive and tended to be within the fibrosa-spongiosa mixed interstitium of GAG associated regions low in primary collagen (**Fig. 16e, left, center**). These data suggest that future studies on BAMBI may show its contribution to regional collagen deposition within the valve structure.

4.4 Discussion

Collagen forms the fundamental framework of the aortic valve starting from embryonic developmental stages onward; disease-driven changes deform the framework and ultimately lead to heart dysfunction[26, 180, 219-221]. In pCAVS, rapid and excessive production of ECM components increases leaflet thickness by up to 8-fold, leading to pediatric heart failure[183, 184, 222, 223]. Genomic studies, primarily characterized from adult end-stage phenotypes, show complex genetics with dissimilar patterns of inheritance, genetically heterogenous phenotypes, and multiple chromosomal regions that impact the ECM network directly or indirectly[222, 224-226]. Gender may also play a role – while bicuspid aortic valve is three times as likely to be found in males, females have more collagen deposition and less calcification[227, 228]. Surgical replacement of valves is an option in adults, but in children, valve replacements do not grow with the patient, leading to heart dysfunction and failure[229, 230]. Directly or indirectly targeting collagen production in pediatric end-stage CAVS may be a viable therapy inhibiting the disease, but very little is known about translational and post-translational regulation collagen and ECM components that form the working structure of the maturing aortic valve. The goal of this study was to identify the dynamic collagen regulation that occurs in pCAVS, including collagen sub-type regulation, collagen fiber alignment, and regulation of hydroxylated proline residues associated with triple helical stability.

The ECM trilayer structure was lost in pCAVS and the rate of collagen deposition trended to increasing by up to 56% per year compared to normal AV development (Figure 1). This coincides with previous reports that pCAVS involves overproduction of collagen to result in thickened valves [26, 183, 184]. Supporting this, immature collagen fibers were detected by staining in all ages of pCAVS localized to regions of mixed collagen and elastin, particularly valves that showed hypertrophic commissures. Significantly, the pCAVS valves showed that collagen fiber alignment with the endothelium is lost and resulted in a random fiber angle relative to endothelium that localized with stains for immature collagen fibers. An additional finding was that unique, pathologically confined regions of increased collagen density were observed in all pCAVS structures (Figure 3). This contrasted with measurements on normal valves in the study that showed where collagen fibers were parallel to the endothelium with the fibrosa staining for mature collagen fibers. Similar findings in normal human aortic growth have been reported, with emergence of collagen fiber alignment parallel to endothelium within maturing fibrosa[181]. Previous work in normal human aortic and pulmonary valve has shown that fibrosa collagen is circumferentially oriented and that uniformly distributed, densely packed collagen fibers emerge with age [179]. Age-related increases in collagen density in pCAVS were attributed to an imbalance of normal collagen synthesis and remodeling required to maintain appropriate collagen stretch dependent on local hemodynamics [179]. We also observed that for valves with aortic valve insufficiency, higher but more variable levels of thick collagen fiber production were observed compared to either normal or pCAVS valves, supporting that valvular function is a balance of collagen production and collagen degradation[26, 177, 178] with dependence on hemodynamics. Additional but unknown effects on collagen production and alignment may result from the cell type and density composition within the tissue microenvironment, in addition to the differential

88

effects of hemodynamics throughout the pCAVS structure. Alterations in collagen fiber alignment are an important component of the pCAVS end-stage and are a useful target in mechanistic studies on the disease.

Collagen PTMs are numerous and include non-enzymatic glycation, lysine and proline crosslinking, N- and O-linked glycosylation, and tyrosine sulfation[69, 231, 232]. Here, we focused on hydroxylation of proline (HYP) to understand collagen regulation in pCAVS. HYP is a primary collagen PTM that regulates triple helical stability and consequently has a large influence on collagen organization in tissue[69]. Regulation of HYP sites within the collagen structure alters fiber conformation and integrity and works to promote or protect the collagen structure from degradation[69, 232-234]. HYP is regulated by co-factors of iron, oxygen, and ascorbic acid, with dependency on nutritional status and oxidative stress [24, 69, 234-236]. Cell-specific and disease-specific regulation of prolyl hydroxylases P4HA1, P4HA2, P4HA3 drive HYP modification on collagen[236, 237]. Cell recognition of very specific sites of hydroxylated prolines along the collagen fiber results in signaling changes through integrins and the tyrosine kinase receptors discoidin domain receptors (DDRs)[238-241]. These cell-fiber interactions influence epithelial mesenchymal transition, cell proliferation survival and metastatic expansion[240, 242-245]. The current study identified up to 15% reduction of HYP content in pCAVS, dependent on collagen subtype. However, HYP changes appeared to be site specific. It is possible that changes in HYP sites may contribute to the rapid collagen degradation and remodeling of pCAVS[69]. Further, the sites of HYP loss in the pCAVS group aligned with regions of glycoprotein VI and integrin binding, which require the presence of HYP within the sequence. Integrins play a crucial role in cell-ECM interactions, with recent data suggesting a key role in dynamic connective tissue remodeling events during wound

healing [246]. Glycoprotein VI is a platelet specific glycoprotein that has been shown to have affinity for collagen in the dimeric form [247]. It has been reported that adult patients with AVS have decreased platelet function and aggregation, however the role of HYP content has not been explored as a potential mechanism[248]. This study identifies that HYP regulation on primary fibrillar collagens may contribute to intrinsic and extrinsic mechanisms of pCAVS and merits focused studies.

Histological studies identified localized regions of dense collagen formation in common with pCAVS. Protein level studies gave insight into the collagen composition of the pCAVS deregulated structures. Collagen α2(V) was found to have significant increases pCAVS compared to non-stenotic AVI valves. Importantly, collagen α2(V) has been reported within heterotypic collagen type I fibrils and plays an essential role in regulating fibrillogenesis and the size of collagen fibrils [249]. The histopathological finding of high-density collagen fiber regions in pCAVS may be reflective of the increased fibrillogenesis. However, to implicate collagen α2(V) directly spatially oriented proteomics would be required to understand localization and regulation of the highly density collagen sites compared to collagen type composition. With localized molecular biomarker identification, these regions of dense collagen fibers provide a potential mechanism of early-stage AV fibrosis molecular marker detection *in vivo* [250]. Amongst non-collagen type proteins, the enrichment of proteins associated with collagen binding, collagen fibril organization, and basement membrane was consistent with our histopathological findings of collagen fiber misalignment and HYP regulation in binding sites. Interestingly, collagen chaperone SPARC was found to be enriched in pCAVS compared to normal AV and AVI patients, independent of age (**Fig. 5a**). While never explored in healthy or disease AV, the overexpression of SPARC has been reported with under-expression of COL4A1 and other

network collagens in myocardium. Increases in SPARC has been linked to endothelial dysfunction, possibly via its binding to VCAM-1 and altered integrin interactions downstream[251]. Its abundance in pCAVS may suggest endothelial dysfunction. Research of healthy and diseased endothelial cell signaling in AV is ongoing, however direct correlation between VEC or VIC cell activation and corresponding collagen regulation remains to be explored [31, 252, 253].

The study identified BAMBI as a novel candidate that may be involved in valvular biology. BAMBI is a negative regulator of TGFβ1 signaling[215, 216] and positively modulates Wnt/β-Catenin pathways by increasing interactions with frizzled 5 and disheveled segment polarity protein 2 (DVL2)[214]. While never studied directly in AV disease or development, recent studies suggest that BAMBI is regulated in the myocardium to restrain hypertrophy and fibrosis[217]. In the current study, network analysis highlighted BAMBI as a predicted node amongst proteins known to be involved in valvular development and disease. Interestingly, the initial protein-level staining studies demonstrated that the human aortic valve has cell-specific and localized expression of BAMBI, particularly within the glycosaminoglycan-rich spongiosa. Furthermore, by transcriptional analysis of total valvular content, BAMBI expression appeared to decrease in both pediatric and adult calcific CAVS. It is conceivable that decreases in BAMBI may play a role in the excess ECM that is a hallmark of pCAVS. However, the role of BAMBI in regulating valvular biology remains undefined.

Chapter 4: Improving Enzymatic Access of Collagen
Proteome via MALDI-IMS

This chapter outlines a method developed to improve upon a targeted enzymatic method previously developed in the Angel Lab [141]. The Angel Lab developed enzymatic-based techniques to target the ECM with collagenase type III (COLase3) [203]. These methods were found to be appropriate for FFPE tissues and did not require decellularization. COLase3 methods have been used successfully in our lab in the past on breast, lung, and prostate[157, 189, 254]. However, COLase3 application alone had insufficient enzymatic access of valvular tissues to investigate the structure-function relationship of the extracellular matrisome in pCAVS sufficiently (Appendix A). To improve on MALDI-IMS data quality, a multi-modal MALDI-IMS method was used to remove extracellular matrix components potential bound to collagen subtypes (GAGs, elastin) and bulky post-translational modification (N-glycans), allow for better enzymatic access of COLase3. The bulk of this chapter was included as part of a publications in Analytical and Bioanalytical Chemistry (April 2021) and Multiplexed Imaging Mass Spectrometry (Springer, in press). Experiments were performed by myself in addition to manuscript writing, data analysis, and final approval. Minor editorial and intellectual contributions were provided by co-authors[145, 155].

4.1 Introduction

Fibrosis is a process characterized by excessive and disorganized extracellular matrix (ECM) involved in many organ diseases but especially heart, kidney, liver, and lung diseases. Fibrotic accumulation of ECM diminishes normal tissue function leading to obstruction of organ function[126, 255, 256]. This promotes disease progression and eventually leads to organ failure. A main challenge in fibrosis research is accessing the ECM to understand how ECM proteins yield feedback information promoting disease progression.

We describe a multiplexed imaging strategy exceptionally useful for fibrosis research that reports N-glycan and ECM information from tissue sections after histological staining. After histology staining, the tissue is analyzed sequentially for N-glycans and ECM peptides. N-glycans and ECM peptides are detected as 2D maps across the tissue using matrix-assisted laser desorption/ionization (MALDI) imaging mass spectrometry (IMS).

MALDI IMS is a robust technique that uses mass spectrometry to map molecules such as lipids, peptides, proteins and N-glycans from histological tissue samples[257-260]. MALDI IMS pinpoints molecular expression to groups of cells or regions of pathology in a tissue section. Thus, for fibrosis research comparisons may be made from differences in pathological regions, e.g., changes in stroma output and organization related to specific fibroblast populations compared to normal adjacent cells. MALDI-IMS has been used by our group and others to spatially probe thin formalin-fixed, paraffin-embedded (FFPE) samples for their N-glycan content by treating the tissue with the enzyme endopeptidase F (PNGase F)[161, 254, 260, 261]. Both the N-glycome and tryptic peptides can be accessed within the same tissue section[262]. Recently, we developed proteomic workflows using collagenase type III to specifically target and report on ECM proteins from FFPE tissues. ECM protein targeting by collagenase type III reproducibly reports on average 60-75 ECM proteins, including collagen types[141, 263]. Sequence analysis of identified ECM proteins revealed that each protein had on average 3.7 sites for N-glycosylation as depicted by the consensus sequence N-X-S/T≠P. A challenge with transferring a sequential approach to serial analysis of N-glycans and ECM from the same tissue section is that collagenase type III treatment can disrupt tissue histology. Here we describe a strategy that starts by capturing the tissue histology using a standard histology stain, hematoxylin and eosin (H&E). Hematoxylin dyes nuclear content dark purple; eosin

stains cytoplasm and stroma pink. After digital high-resolution capture of the stain, the same tissue section is processed for N-glycan and ECM peptide imaging mass spectrometry through sequential application of PNGase F and collagenase type III. Specific washing steps are required to remove matrix, enzymes, and the N-glycans between enzyme treatments. This multiplexed imaging approach is particularly useful for deep mining of ECM information from fibrotic tissue, as one 5 μm thick tissue section allows for pathological evaluation of ECM organization by staining as well as N-glycan signaling and ECM peptide data.

The extracellular matrix (ECM) consists of the non-cellular components of tissues and provides essential biochemical and biomechanical signaling[264]. The ECM is a complex environment of fibrous type proteins – such as collagen, elastin, and fibronectin – as well as proteoglycans, which consist of sulfated glycosaminoglycan (GAGs) chains covalently bound to a core protein. The GAGs present in the ECM can be sulfated (chondroitin sulfate, heparan sulfate, and keratan sulfate) or non-sulfated (hyaluronic acid) [265]. The most abundant fibrous proteins are collagen type proteins[264]. Collagens are both intra- and inter-molecularly crosslinked with elastin and other proteoglycans at mainly lysine residues. These proteins are also abundantly post-translationally modified, with hydroxyproline, hydroxylysine, and N- and O-linked glycans[68, 69]. PTMs at lysine residues as well as abundant intra- and intermolecular crosslinking of ECM components make this environment a unique analytical challenge for mass spectrometry-based approaches. To date, no single enzymatic targeting technique can elucidate all constituents of the extracellular matrix.

Enzymatically targeted techniques have been developed recently for multi-omics studies and can analyze tissue glycomics, glycoproteomics, and/or proteomics from a

single sample[266-268]. These techniques are largely serial LC-MS/MS strategies applied to fresh frozen tissue samples. While serial LC-MS/MS techniques allow for a large amount of identifications, the link between -omics data and tissue morphological structure is lost. Imaging Mass Spectrometry (IMS) methods, however, can be used to visualize the spatial distribution of analytes within tissue sections. One such IMS technique is Matrix-Assisted Laser Desorption/Ionization (MALDI) Imaging Mass Spectrometry (IMS). MALDI-IMS is a robust proteomic technique that can spatially map tryptic peptides from histological tissue sections[263]. This is done by spraying the tissue with a thin, uniform layer of trypsin that, when analyzed in parallel to high resolution accurate mass proteomics, allows for the relative quantitation and localization of tryptic peptide sequences to specific regions of the tissue. Although trypsin-based ECM-IMS techniques have been developed, these approaches decellularize fresh, unfixed tissue which is not an option for clinically archived formalin-fixed paraffin embedded (FFPE) tissue[269]. Novel MALDI-IMS techniques have been developed to enzymatically target ECM proteins via collagenase type III (COLase3) and elastase[141, 143], allowing peptide tissue mapping of ECM proteins that are largely trypsin-resistant.

In this study, we used MALDI-IMS techniques to visualize and relatively quantify *in situ* chondroitin sulfate (CS) GAGs, N-glycans and ECM peptides and proteoglycans from a single tissue section after serial treatment with enzymes. PNGaseF has been used to release N-glycans from thin FFPE tissue sections followed by MALDI-IMS[260]. Recently, PNGaseF and trypsin have been used in tandem, colocalizing the N-glycome to the tryptic proteome[262, 270]. Additionally, our lab has combined histological staining with MALDI-IMS to map complex ECM proteins in thin FFPE tissue sections[141, 143, 155]. While other studies have used IMS techniques to analyze GAG fragments[271], we

outline here the first enzymatically targeted study of chondroitin sulfate GAGs via MALDI-IMS techniques. By combining these enzymatic approaches, comprehensive mining of protein translational and post-translational information becomes possible. This is especially useful for understanding the complex ECM profile as GAG, N-glycan, collagen, and ECM peptide data can be analyzed from one FFPE tissue section.

4.2 Materials & Methods
4.2.1 Materials and Chemicals

All solutions were prepared using double distilled or HPLC grade water, following all necessary safety and waste disposal regulations. Xylenes, 200 proof ethanol was purchased from Fisher Scientific (Pittsburgh, PA, USA). Acetonitrile, Ammonium Bicarbonate, Calcium Chloride, Formic Acid, EDTA, Trizma Base, and Chondroitinase ABC were purchased from Sigma-Aldrich (St. Louis, MO, USA). PNGase F PRIME was purchased from N-Zyme scientific (Charleston, SC, USA). Collagenase type III (COLase3) (*C. histolyticum*) was purchased from Worthington Biochemical (Lakewood, NJ, USA). Porcine MMP12 (elastase) was purchased from Alfa Aesar (Fisher Scientific, Pittsburgh, PA).

4.2.2 Specimens

Aortic valve tissue biopsy was procured through the Vanderbilt Core Laboratory for Cardiovascular Translational and Clinical Research and the National Disease Research Interchange. Tissue procurement for banking was approved by the Vanderbilt Institutional Review Board (IRB) and for project use by the Medical University of South Carolina IRB. Tissues were fixed overnight in 10% neutral buffered formalin (American Mastertech), cut through the central portion of the cusp, and embedded in paraffin blocks.

4.2.3 Tissue Preparation & Histology

Formalin-fixed, paraffin-embedded tissue was cut to 5 µm thick sections via microtome and mounted onto microscope slides (Tissue Tack, Polysciences, Inc., Warrington, PA, USA) then dehydrated overnight at 37°C prior to storage at room temperature. Tissues were stained with Verhoeff Van Gieson (Verhoeff solution for elastin; Van Gieson counterstain for collagen), Movat's Pentachrome (Alcian Blue for GAG, Saffron for collagen, Resorcin-Fuchsin for elastin, and Woodstain Scarlet-Acid Fuchsin for muscle), or Alcian Blue alone (Polysciences, Inc.), following manufacturer's protocols. All staining protocols included a hematoxylin counterstain.

For N-glycan and ECM peptide MALDI-IMS studies, FFPE tissues were prepared as previously described[141, 260]. Chondroitinase imaging preparation is novel to this study. Briefly, a 1 mg/mL Chondroitinase ABC (Sigma Aldrich, St. Louis, MO, USA) solution was prepared in 60mM Ammonium Acetate (pH 8 with sodium hydroxide). Solution was sprayed with a TM Sprayer M3 (HTX Imaging, Chapel Hill, NC, USA) under the following parameters: 15 passes, crisscross pattern, 3.0 mm track spacing, velocity of 1200 mm/min, and a dry time of zero. Before enzymatic digest, four antigen retrieval conditions (20 minutes, 95°C) were studied: 1) EDTA pH 8; 2) Citraconic Buffer pH 3; 3) Tris pH 9; and 4) Double antigen retrieval of Citraconic, wash and desiccate, then Tris.

FFPE aortic valve tissue sections were digested with COLase3 after serial treatment with chondroitinase, PNGaseF (N-Zyme Scientifics), elastase, and for MALDI-IMS experiments. Trypsin (Porcine Pancrease, Sigma Aldrich, St. Louis, MO, USA) was applied during preliminary studies to determine the effects of a single enzyme before COLase3. Spray conditions for all enzymes were as previously published [141, 260]. Samples were digested in high humidity at 37.5°C for either 2 hours (chondroitinase,

PNGaseF) or 5 hours (elastase, COLase3). A 7 mg/mL solution of alpha-cyano-4-hydroxycinnamic acid (CHCA) matrix solution was prepared in 50% acetonitrile and 0.1% trifluoroacetic acid (TFA; for chondroitinase, PNGaseF imaging) or 1.0% TFA (for elastase, COLase3 imaging). CHCA matrix solution prepared for peptide imaging was spiked with a standard of 200 femtomole/L [Glu1]-fibrinopeptide B human (GluFib) (Sigma-Aldrich, St Louis, MO, USA). CHCA automatic spray conditions included: 79°C, 10 psi, 70 µl/min, 1300 velocity, and 14 passes with a 2.5 mm offset. Slides for peptide imaging were rapidly dipped (<1 second) in cold 5mM ammonium phosphate and immediately dried in a desiccator.

4.2.4 Chondroitin Sulfate Standard Preparation

A dilution series of digested CS standards were spotted onto a MALDI plate for CS peak validation. Standard used was chondroitin sulfate sodium salt from shark cartilage (Sigma Aldrich, St. Louis, MO, USA). Dilution shown was 5 µM of CS. Samples were brought up in 60 mM ammonium Acetate pH 8 and digested with 4 µg of Chondroitinase ABC. Samples were incubated overnight, shaking at 38°C. Samples were spotted with 0.5 µl of digest solution onto a MALDI plate and sprayed with CHCA as previously described.

4.2.5 Imaging Mass Spectrometry

Tissues were analyzed by MALDI-FT-ICR (7.0 Tesla solariX™ Legacy FT-ICR (Bruker Scientific, LLC, Bremen, Germany) operated in positive ion broadband mode over m/z range 500-4000. Laser settings used were 300 shots/pixel with a 45 µm stepsize. The average laser shot was measured to be approximately 25 µm x 30 µm. A lock mass of 1570.6768 (GluFib peptide) was used for peptide IMS studies. Images were visualized in

FlexImaging v5.0 and analyzed using SCiLS 2017a version 5.00.9510 (Bruker Scientific, LLC, Bremen, Germany). All images shown are normalized to total ion current.

Chondroitin Sulfate fragmentation and ion mobility data was acquired using a Trapped Ion-Mobility Time-of-Flight Mass Spectrometer (timsTOF fleX) (Bruker Scientific, LLC, Bremen, Germany) equipped with a dual ESI/MALDI source. The samples were analyzed in positive ion Q-TOF mode and scanned at a mass range from 500 – 4000 m/z. The SmartBeam 3D 10 kHz laser was set to 33% power, scan range of 20 µm for X and Y and resulting field size of 24 µm for X and Y. The measured average spot size was 18.66 µm for X and 19.94 µm for Y. Additional instrument parameters for CS studies include: an ion transfer time of 125 μs, pre pulse storage time of 25 μs, a collision RF of 4000 Vpp, a collision energy of 15 eV, an ion energy in the quadrupole of 5 eV, a TIMS funnel 1 RF of 500 Vpp, a TIMS funnel 2 RF of 500 Vpp and a multipole RF of 500 Vpp. After MS acquisition, the data was imported into SCiLS Lab 2020a (Bruker Scientific, LLC, Bremen, Germany) and normalized to total ion current. CS peaks were identified by accurate mass using a database created in GlycoWorkBench [272].

Spectra shown were analyzed using mMass version 5.5.0. Putative peptide identifications are based on our previously acquired databases from many tissue samples on human aortic and same valvular tissues [10-11]. This analysis does not include peaks with biologically relevant spatial distribution that have not yet been sequenced. Percent fold change was calculated as: $\frac{\ln(serial\ enzyme\ peak\ intensity)}{\ln(single\ enzyme\ peak\ intensity)} * 100$. Here, serial enzyme peak intensity is the intensity measured from tissue samples that had undergone serial-enzyme digest, as opposed to a single enzyme digest.

4.3 Results
4.1 The Aortic Valve as a Prototype Model Tissue for ECM Analysis

Human stenotic bicuspid aortic valves were used to develop this method since the hallmark of aortic valve stenosis is overproduction of ECM. Histopathological evaluation was done as an initial assessment of the tissue. Movat's Pentachrome (MP) (**Fig. 18a, 1a'**), Verhoeff van Geison (VVG) (**Fig. 18b, 18b'**) and Alcian Blue stain (**Fig 18c**) show elastin, collagen, and GAGs are present throughout the length of the valve leaflet. A dense band of collagen can be seen clearly in the medial of the leaflet via the MP stain (**Fig. 18a, outlined**). In the same region, reduced GAG deposition can be seen via Alcian Blue staining (**Fig. 18c, outlined**). Elastin fibers can be seen at higher magnification to be present throughout the leaflet, both via MP and VVG staining (**Fig. 18a-b**). These morphological features were used to show GAGs, collagen, and elastin are abundant throughout the length of the leaflet and to further validate localization of MALDI-IMS data in later figures.

Potential regulation of collagen PTMs was quantified via in silico analysis (**Fig. 18 d-e**). Uniprot Amino Acid Modification database analysis of confirmed sites, similar sites, and consensus sequences shows that all collagen-type proteins identified via our COLase3 MALDI-IMS and LC-MS/MS method contain at least one N-linked glycosylation site (N-X-S/T site, where X is any amino acid besides proline), with as many as 15 sites per collagen-type protein. Previous analysis of acquired COLase3 using LC-MS/MS methods indicated that 4.8% of all ECM peptides identified in our database are potential glycopeptides (146 out of 3024 peptides have an N-X-S/T site) [141, 143]. Additionally, PTMs, such as hydroxyproline and hydroxylysine are abundant in collagen type proteins, with as many as 150 hydroxyproline sites present in COL3a1. These modifications on
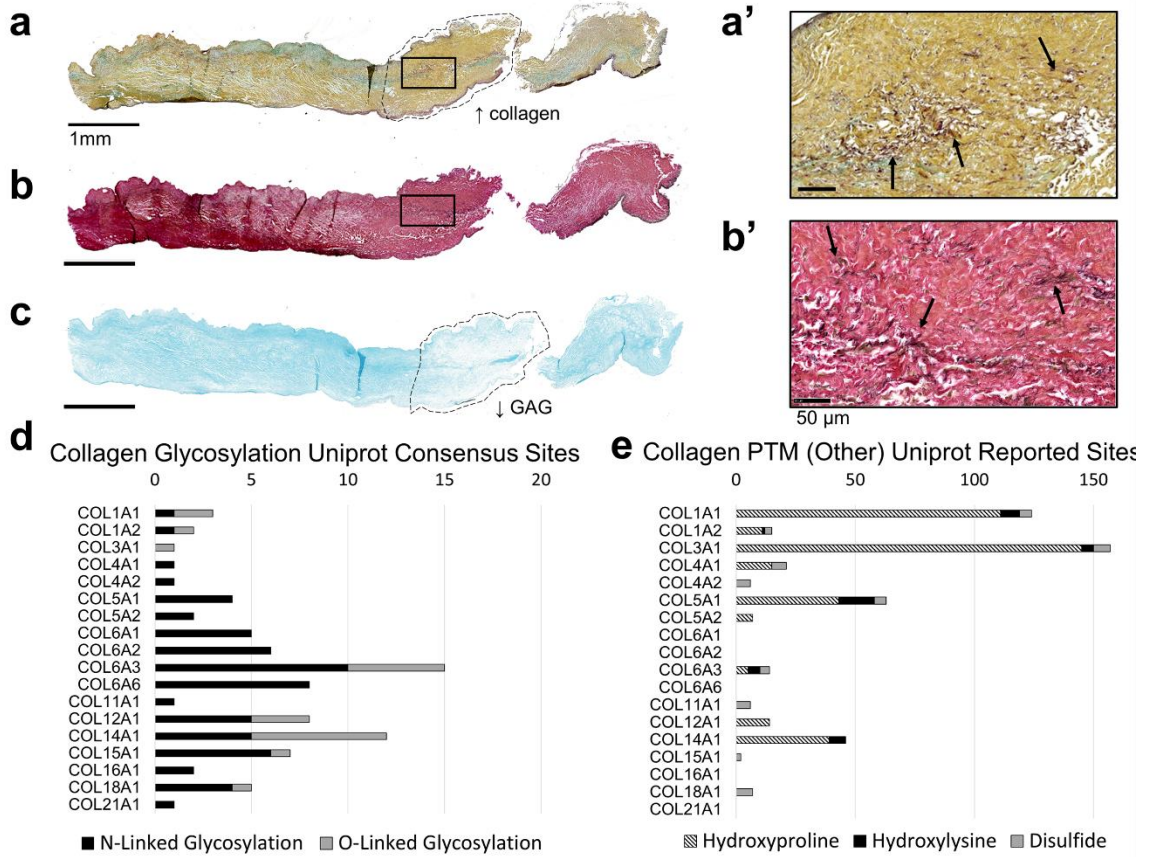
Figure 18: **Method development tissue (pediatric bicuspid aortic valve) displays aberrant ECM production and post-translational modifications ideal for ECM studies**. **a**. Movat's Pentachrome staining with GAGs in blue, elastin in purple, and collagen in yellow. 20x magnification of the square in **a** is seen in **a'**. **b**. Verhoeff van Gieson staining with collagen in red/pink and elastin in purple/black. 20x magnification of the square in **b** is seen in **b'**. **c**. Alcian blue staining shown GAGs present throughout the valve. **d**. In silico PTM site count analysis of N- and O-linked glycans (**d**) and hydroxyproline, hydroxylysine, and disulfide modifications (**e**). Uniprot reported sites for each protein were obtained from the Uniprot compiled Amino Acid Modification database. Both published confirmed sites and sites identified by similarity and consensus sequences were included in **d-e**.
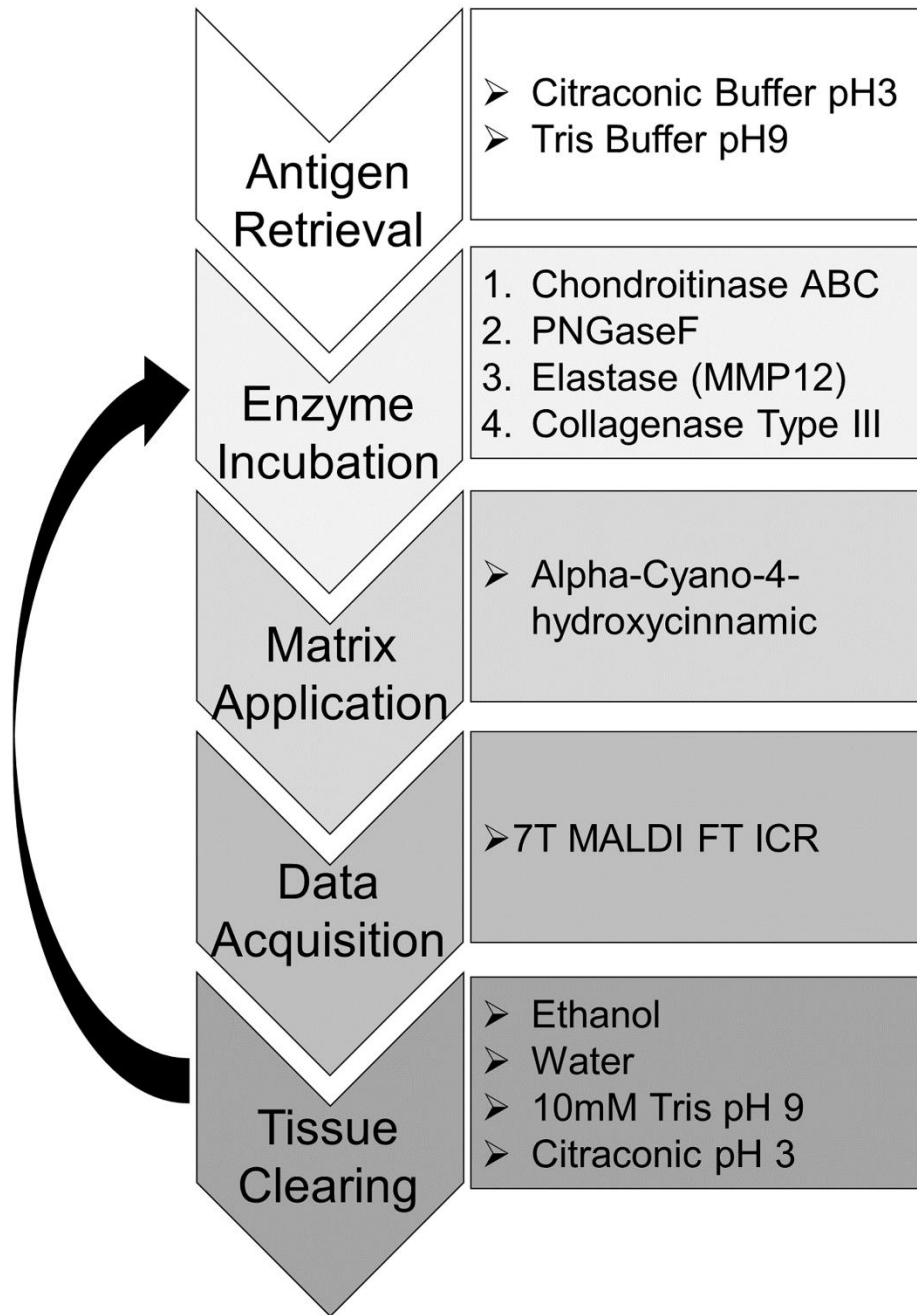
Figure 19: MALDI-IMS multi-enzyme workflow. A single FFPE tissue section is taken through four serial enzyme treatments to target CS GAGs, N-glycans, elastin, and collagen and other ECM peptides. Images are acquired via a MALDI-FT-ICR instrument between each enzyme treatment.

lysine residues prevent conventional tryptic digests from accessing ECM proteins [82, 273], indicating a targeted enzymatic strategy would be adventageous, including enzymes targeting N-glycosylation and proteomics databases searched for hydroxylysine and hydroxyproline.

Aortic valve tissues are comprised of both activated and inactivated valvular interstitial fibroblasts – the average size being approximately 5x30μm and 7x10μm, respectively. Additionally, these aortic valve tissues studied are relatively low cell density. A serial section of the valve sample shown in **Figure 18** was measured to have an average cell density of 370 cells/mm^2 (Appendix F-G). These data suggest that imaging mass spectrometry-based methodologies are conducted at an appropriate resolution for ECM-based studies in these tissues.

4.2 Imaging Mass Spectrometry Workflow

An overview of the optimized MALDI-IMS workflow can be seen in **Figure 19**. Optimization of PNGaseF, elastase, and COLase3 have been completed in previous studies[141, 155, 260]. Optimization of Chondroitinase ABC for MALDI-IMS included investigating antigen retrieval conditions, concentrations, incubation times, and optimal matrix application. Antigen retrieval steps (Citraconic Buffer pH3 and Tris pH9) were completed serially before the serial enzyme treatment. Specific washing steps to remove analytes were completed to prevent cross-contamination between imaging acquisitions [262]. Within this study, no significant reduction in spatial resolution was seen, as compared to the first image of the series.

4.3 Method Optimization for Chondroitin Sulfate Imaging MS

This method targets chondroitin sulfates (CS) via application of chondroitinase ABC. CS is an abundant glycosaminoglycan (GAG) of repeating glucuronic acid (GlcUA) and N-acetylgalactosamine (GalNAc) di-saccharides in the extracellular space, and are known to be upregulated in cardiac, pulmonary, and liver fibrosis [274-276]. Previous work has shown via LC-MS/MS analysis that tissue treated with chondroitinase ABC can be used to detect CS chains of 1-3 repeats in multiple sulfation states [268, 277, 278]. Similar results were seen in our studies. A single sulfated CS chain as well as two examples of multiply-sulfated dimers can be seen in **Figure 20a-b**. Previous LC-MS/MS-based studies have shown that other enzymes targeted to GAGs, such as hyaluronidase and heparan lysase, can be used in tandem to chondroitinase ABC to serially access the proteoglycome [266]. Ongoing studies aim to incorporate these enzymes into MALDI-IMS multi-enzyme workflows.

An antigen retrieval study was done to optimize the chrondroitinase IMS method (**Fig. 20a**). Antigen retrieval of FFPE tissues reverses protein chemical modification induced via formalin [279]. It is known that the pH of the antigen retrieval solution alters enzymatic access for purposes of MALDI IMS studies, with incubation time and temperature also
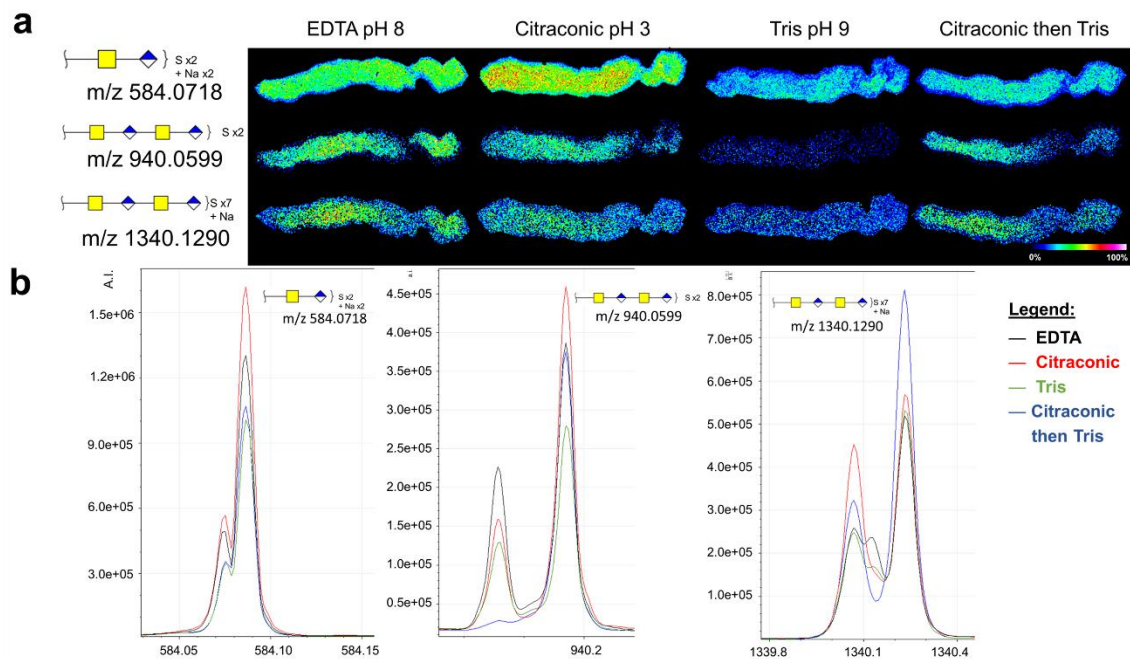
Figure 20: Chondroitinase ABC MALDI-IMS method is capable of imaging several chain lengths and sulfation states of CSs. a. Antigen retrieval study on serial aortic valve tissue sections to determine optimal conditions for MALDI-IMS acquisition. Three representative CSs are shown. **b.** Corresponding peaks to images shown in **a**, with all four antigen retrieval conditions overlayed: EDTA (black); Citraconic (red); Tris (green); Citraconic then Tris (blue).

playing role [280]. The pH category shown represents pH of different antigen retrieval conditions, suggesting differential specificity to CS under different antigen retrieval conditions (**Fig 20a**). Chondroitinase ABC preferentially cleaves CSs, however other GAG structural classes are cleaved when the digestion buffer is prepared at different pHs [281]. The final antigen retrieval method for the multi-enzyme study was condition #4 (Methods 2.3, Citraconic then Tris). While other conditions were more optimal for CS imaging, antigen retrieval for N-glycan and COLase3 imaging have been already optimized with Citraconic, pH 3 and Tris pH 9 buffers, respectively [141, 260].

The theoretical mass values for some chondroitinase products had a similar mass defect and m/z value as matrix peaks. For example, a single GalNAc-GlcUA chain has a theoretical m/z of 379.0794, while CHCA [2M+H]+ has a theoretical m/z of 379.0925 [282]. To confirm the peaks chosen did in fact correspond to CSs and not matrix, on-tissue fragmentation was performed using MALDI and trapped ion mobility combinations on a timsTOF fleX mass spectrometer. Peak m/z 1340.129 was fragmented via CID to obtain the MS/MS spectra seen in **Figure 21**. Serially increasing collision voltages shows a loss of sulfate state, chain length, and chain formation with fragmented ions corresponding to GalNAc and GlcUA also seen. To further validate this, ion mobility analysis was also performed on- and off-tissue. **Figure 22** shows that the on-tissue ion mobility data displays two unique populations – one corresponding to matrix-only signal taken off tissue, and one corresponding to tissue treated with chondroitinase ABC. These experiments were also done on spotted CS standards for further validation (**Fig. 22**). Trapped ion mobility analysis can be used in further studies to not only to distinguish between isobaric matrix and GAG peaks, but also between isobaric GAG species of differential sulfation states and acid species[283, 284].
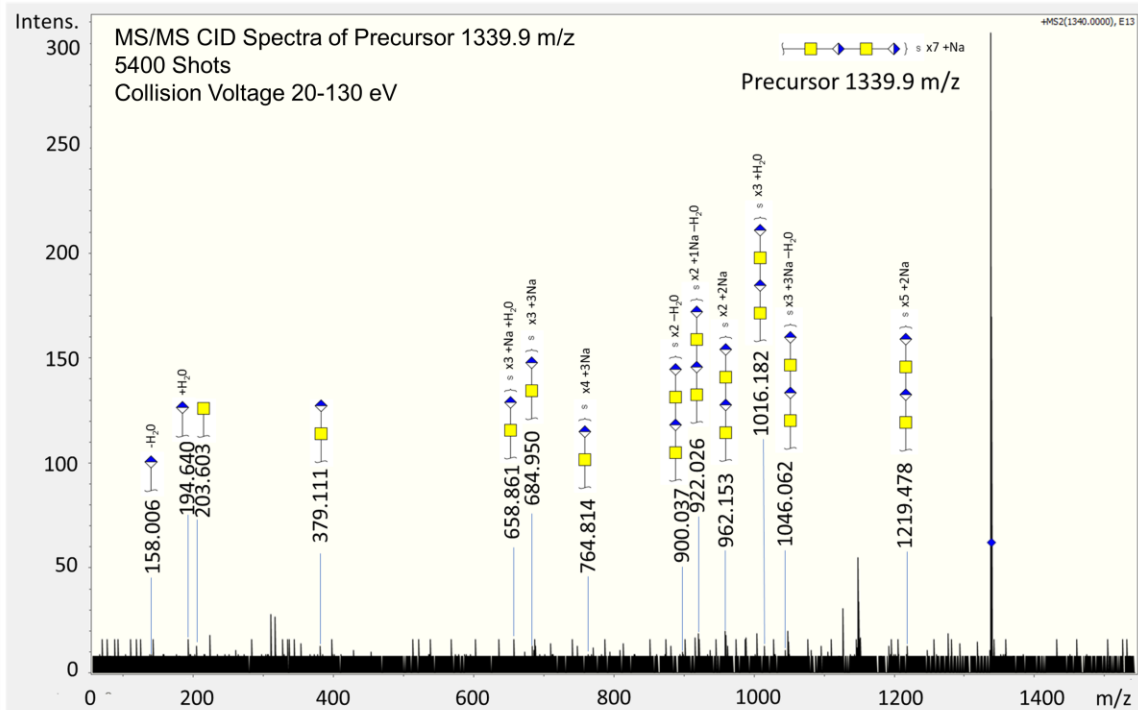
Figure 21: Fragmentation of precursor m/z 1339.9 shows evidence of isobaric CS peak with matrix. Summed spectra of CID fragmentation across 5400 shots and increasing collision voltages between 20-130eV. Summed spectra shows loss of sulfation state, chain length, and chain formation with fragmented ions corresponding to GalNAc and GlcUA seen.
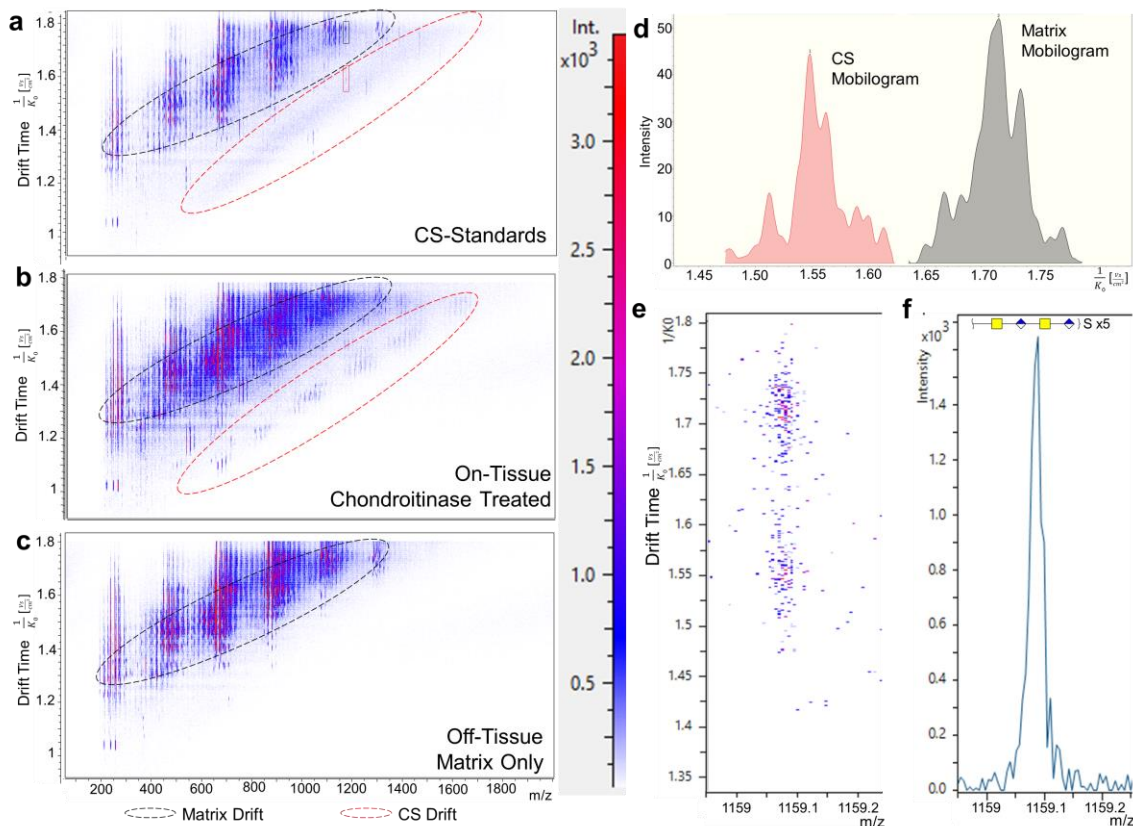
Figure 22: Ion mobility analysis of CS standards and tissue shows unique drift populations of matrix and CS species at isobaric peaks. a. Heat map of spotted CS standards. **b.** Heat map of shots taken on-tissue treated with chondroitinase ABC. **c.** Heat map of shots of matrix only, taken on the same chondroitinase ABC treated slide but off-tissue. **d.** Mobilograms for the CS and Matrix drifts shown in **(e)** for the isobaric peak shown in **(f)**. 10280 shots were summed for all TIMS experiments.
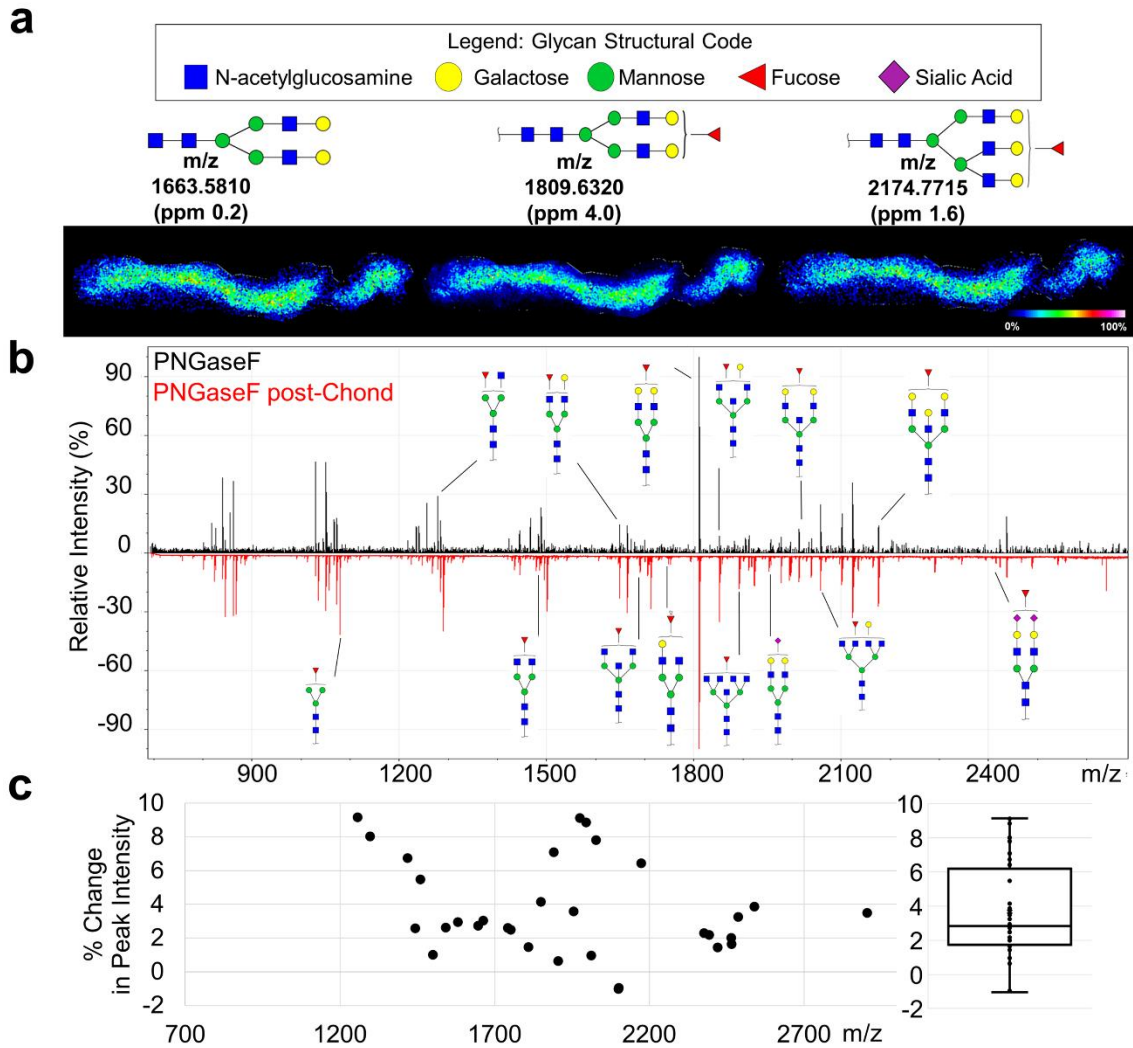
Figure 23: N-glycan signal by PNGaseF was improved by removal of CS GAGs via Chondroitinase ABC. a. Three representative N-glycan images with corresponding structures. **b.** Annotated spectra with PNGaseF treated tissue alone (top, black) and PNGaseF treated post-CS GAG removal (bottom, red). **c.** Quantification of the percent change in peak signal intensity for all glycans identified. Each point represents an N-glycan peak with a boxplot of the data shown to the right.

4.4 N-glycosylation imaging may be improved by chondroitin sulfate removal

N-glycosylation patterns were then obtained from the same tissue section, with N-glycan signal improved by removal of GAGs (**Fig. 23a-b**). A total of 25 N-glycans were identified by MALDI-IMS after CS-removal, while only 10 N-glycans were identified using PNGase F alone. Quantification of N-glycan peak intensity shows that N-glycan signal was improved by removal of CSs, with a maximum of 9.2% and a mean of 3.7 ± 2.8% increase in peak intensity after CS removal, averaged across 32 identified N-glycan peaks (**Fig. 23c**). While many classes of N-glycans were identified (high-mannose, fucosylated, sialylated, bisecting), no single class was uniquely affected by removal of CSs. Removal of CSs may impact enzyme access of PNGaseF to N-glycosylation sites of small-leucine rich proteoglycans (SLRPs). Many SLRPs are found in healthy and stenotic heart valves, such as biglycan, decorin, and versican [285]. Studies with decorin show that both CS-linker and N-glycan sites are present within the primary sequence [281], which could potentially affect enzymatic access for analytical purposes.

4.8 PNGaseF imaging is compatible with Hematoxylin & Eosin pre-treatment

Another goal of this study was to combine histopathological evaluation with the enzymatic methods used to access to the extracellular matrix via MALDI-IMS. A challenge with these studies is that tissue histology can be disrupted with enzymes targeting the extracellular matrix, such as the elastin and collagenase used in future studies below. Our goal was to stain the tissue section with Hematoxylin and Eosin (H&E), take a high-resolution digital capture, and then use the same tissue section in MALDI-IMS studies (**Figure 24**). Initial studies performed determined the effect of H&E staining on PNGaseF treatment. Based on the relative intensity of glycans identified via MALDI-IMS, there was no significant reduction in signal intensity with H&E treatment before PNGaseF as
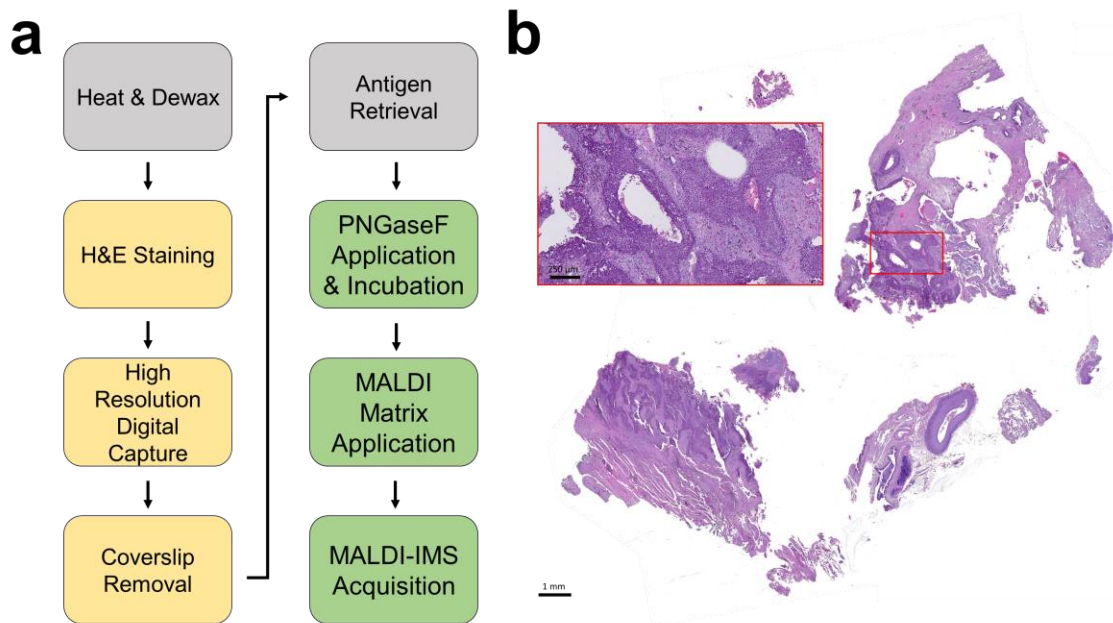
Figure 24 Workflow of histology compatible MALDI-IMS method. **a.** A single FFPE tissue section is taken through hematoxylin & eosin staining and then PNGaseF treatment to target N-glycans. Images are acquired via a MALDI-FT-ICR instrument after PNGaseF enzyme treatment. **b**. High resolution digital capture of Hematoxylin and Eosin stain of the tissue before proceeding with N-glycan and collagen peptide imaging (**Figure 23,25**). Nuclei is stained in dark blue/purple, while cytoplasm is pink.
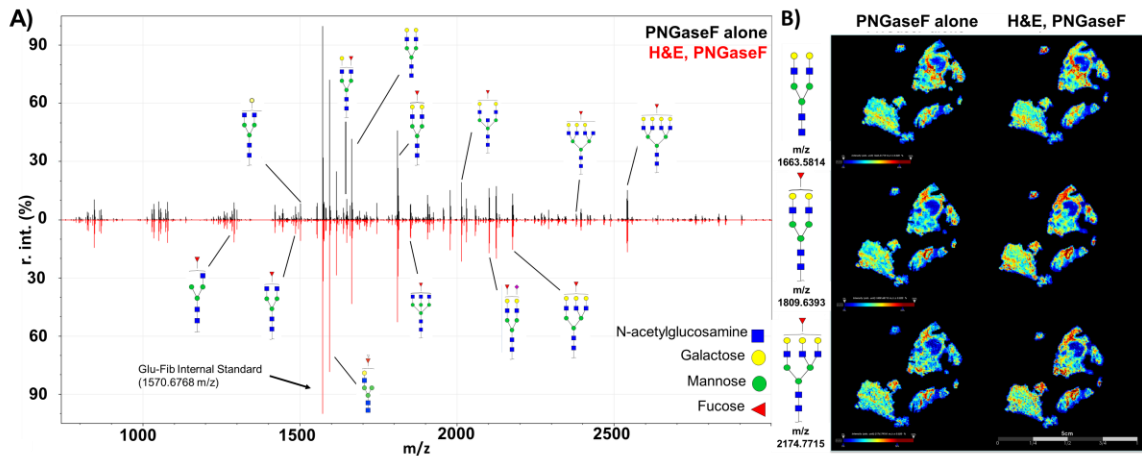
Figure 25: Comparison of N-glycan imaging data due to PNGase F application either alone or applied after H&E staining. (a) Overall average mass spectrum of PNGase F treated tissue (top, black) and PNGase F treated tissue after undergoing H&E staining (bottom, red). N-glycan structures corresponding to m/z are shown. (b) Examples of N-glycan images created as heat maps of the corresponding m/z peak intensity. N-glycan structure and m/z are shown left of each image, created using GlycoWorkbench 2.0 [272]. Peak 1570.6768 m/z corresponds to the Glu1-Fibrinopeptide B (Glu-Fib) internal standard spikes in at 200 femtomole/microliter.
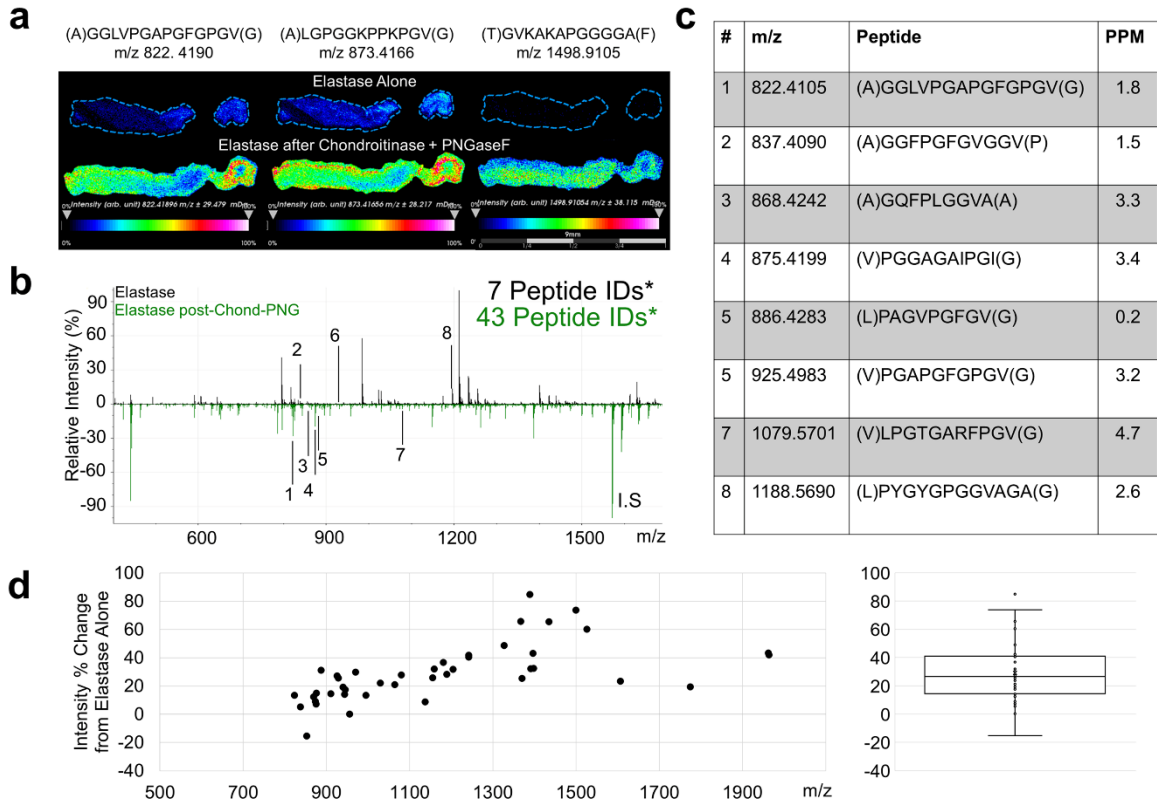
Figure 26: Detection of elastin peptides by Elastase is improved by PNGaseF and Chondroitinase ABC pretreatment. a. Representative images and corresponding m/z values of three elastin peptides. b Annotated spectra with elastase alone (top, black) and elastase post-CS and N-glycan removal (bottom, green), with corresponding annotations in c. Identified peptide counts are out of 48 peptides IDs via acquired LC-MS/MS databases. d. Quantification of the percent change in peak signal intensity for all elastin peptides identified. Each point represents an elastin peptide peak with a boxplot of the data shown to the right. *Putative peptide IDs from databases acquired from a different tissue cohort.

compared to PNGaseF alone (**Figure 25a**). Similarly, representative images show comparable spatial distribution of glycans, independent of H&E treatment (**Figure 25b**).

4.5 Elastin imaging by elastase is improved after N-glycan and CS removal

After removal of sugar moieties, we evaluated whether the deglycosylation steps improved detection of ECM peptides following elastase or COLase3 digestions (**Figure 26**). Preliminary studies determined that the order with which the peptide-cleaving enzymes (elastase, COLase3) was applied has little effect on overall peptide signal intensity. Elastase was applied to the tissue previously treated with Chondroitinase ABC and PNGaseF, with a control tissue treated in parallel with only elastase under the same antigen retrieval conditions. The elastase signal was greatly improved by deglycosylation and removal of CS. This increase in signal intensity is shown clearly via three representative images (**Fig. 26a**). Without CS and N-glycan removal, 7 putative elastin peptides were observed (**Fig. 26b-c**). With CS and N-glycan removal 42 putative peptides were detected, with a 29% increase in average peak intensity (**Fig. 26d; Table 8**).

Consistent with histopathological evaluation, elastin peptides were seen throughout the length of the leaflet. Interestingly, the area of the leaflet that stained heavily for collagen was lower in signal intensity. This could be due to the intermolecular crosslinking of collagen and elastin, limiting enzymatic access. Here, initial treatment with COLase3 may improve localized elastase signal in these areas. While elastin does not contain any consensus sites for N-glycosylation, tropoelastin aggregates can crosslink with certain proteoglycans and glycoproteins in the extracellular space [286, 287]. Matrix glycoproteins have been thought to play a role in elastin fiber orientation, while

Table 8: Putative Peptide IDs of elastin peptides derived from Elastase (MMP12) imaging mass spectrometry. Intensity values are normalized by TIC (Total Ion Current). Chond: Chondrotinase ABC treated. NG: PNGaseF treated.

Centroid [m/z]	± [Da]	Putative Peptide Identification	Modification	Max Intensity Elastase Alone	Max Intensity Elastase post-Chond-NG
822.4190	0.0295	(A)GGLVPGAPGFGPGV(G)	None	2.6E+05	1.4E+06
837.4090	0.0291	(A)GGFPGFGVGVGGV(P)	None	9.8E+04	1.8E+05
852.4045	0.0265	(V)FYPGAGLGA(L)	None	4.2E+05	5.7E+04
868.4242	0.0295	(A)GQFPLGGVA(A)	1Deamidated	5.1E+04	1.9E+05
873.4166	0.0282	(A)LGPGGKPPKPGV(G)	None	7.1E+05	2.4E+06
874.4179	0.0337	(V)FYPGAGLGA(L)	None	4.0E+05	1.0E+06
875.4199	0.0329	(V)PGGAGAIPGI(G)	None	6.1E+04	3.2E+05
886.4386	0.0307	(L)PAGVPGFGV(G)	None	2.2E+04	5.0E+05
910.4536	0.0354	(A)QFGLGPGIGV(A)	1Deamidated	3.0E+04	1.4E+05
925.4983	0.0164	(V)PGAPGFGPGV(G)	None	6.1E+03	6.6E+04
928.4002	0.0152	(V)GAGGFPGFGV(G)	None	1.0E+04	1.1E+05
939.4689	0.0160	(A)GQFPLGGVAA(R)	1Deamidated	1.4E+04	9.1E+04
943.4293	0.0169	(V)GVGGVGVPGGA(G)	None	1.5E+04	5.9E+04
944.4568	0.0101	(A)AKAQFQAA(A)	2Deamidated	1.1E+04	5.5E+04
955.4231	0.0321	(A)KFGAGAAGV(L)	None	8.5E+04	8.7E+04
969.4907	0.0206	(A)PKLPGGYGL(P)	None	7.5E+03	1.1E+05
994.4364	0.0392	(A)QFGLVPGVGV(A)	None	4.4E+04	1.9E+05
1029.5049	0.0412	(A)GKAGYPTGT(G)	1Xlink:DSS1	1.3E+04	1.1E+05
1063.5128	0.0495	(I)IHPSQPGGVPGA(V)	None	4.9E+04	4.8E+05
1079.5696	0.0299	(V)LPGTGARFPGV(G)	None	1.9E+04	2.9E+05
1136.5752	0.0438	(L)PGGYGLPYST(G)	None	5.5E+04	1.5E+05
1154.5792	0.0254	(L)PGVYPGGVLPGA(R)	None	1.0E+04	1.1E+05
1158.5788	0.0330	(A)GVPGFGAGADEGV(R)	None	8.9E+03	1.7E+05
1180.5562	0.0247	(V)PGVGVPGVGV(P)	None	1.2E+04	3.7E+05
1188.5690	0.0216	(L)PYGYGPGGVAGAA(G)	None	6.7E+03	8.2E+04
1203.5700	0.0268	(V)PGAPGFGPGVGV(P)	None	6.9E+03	1.2E+05
1241.6165	0.0081	(L)GKSCGRKRK(-)	None	3.6E+03	1.1E+05
1241.6308	0.0062	(T)YGVGAGGFPGFGV(G)	None	3.6E+03	1.0E+05
1326.6959	0.0196	(I)KAPKLPGGYGL(P)	None	2.3E+03	1.0E+05
1366.8156	0.0361	(I)PGGVPGGVFYPGAGL(G)	None	2.6E+03	4.7E+05
1369.6442	0.0350	(L)PYGFGPGGVAGAA(G)	None	1.2E+04	1.3E+05
1388.7253	0.0299	(A)LGALGYQGGA(C)	None	1.2E+03	5.3E+05
1390.6470	0.0227	(S)IIHPSQPGGV(P)	None	9.9E+03	1.9E+05
1395.6660	0.0639	(A)GGFPGFGVGVGGIPGV(A)	None	3.1E+03	1.0E+05
1397.6684	0.0247	(A)FPAGAFPGA(L)	None	4.0E+03	6.1E+04
1434.6566	0.0258	(V)PGFGVGAGVPGFGA(G)	None	1.4E+03	1.6E+05
1498.9105	0.0381	(T)GVKAKAPGGGGA(F)	None	3.3E+03	1.3E+06
1525.8351	0.0340	(V)PGFGVGAGVPGFGV(G)	None	2.6E+03	2.9E+05
1605.7924	0.0752	(A)KYGAAGLGGV(L)	None	5.4E+03	4.1E+04
1773.8071	0.0834	(V)GPFGGPQPGVPLGYPIKA(P	None	7.2E+03	4.1E+04
1962.0014	0.1164	(I)PGVGPFGGQQPGVPL(G)	1Deamidated	2.6E+03	7.9E+04
1962.9823	0.0047	(I)PGVGPFGGQQPGVPL(G)	2Deamidated	2.6E+03	7.1E+04
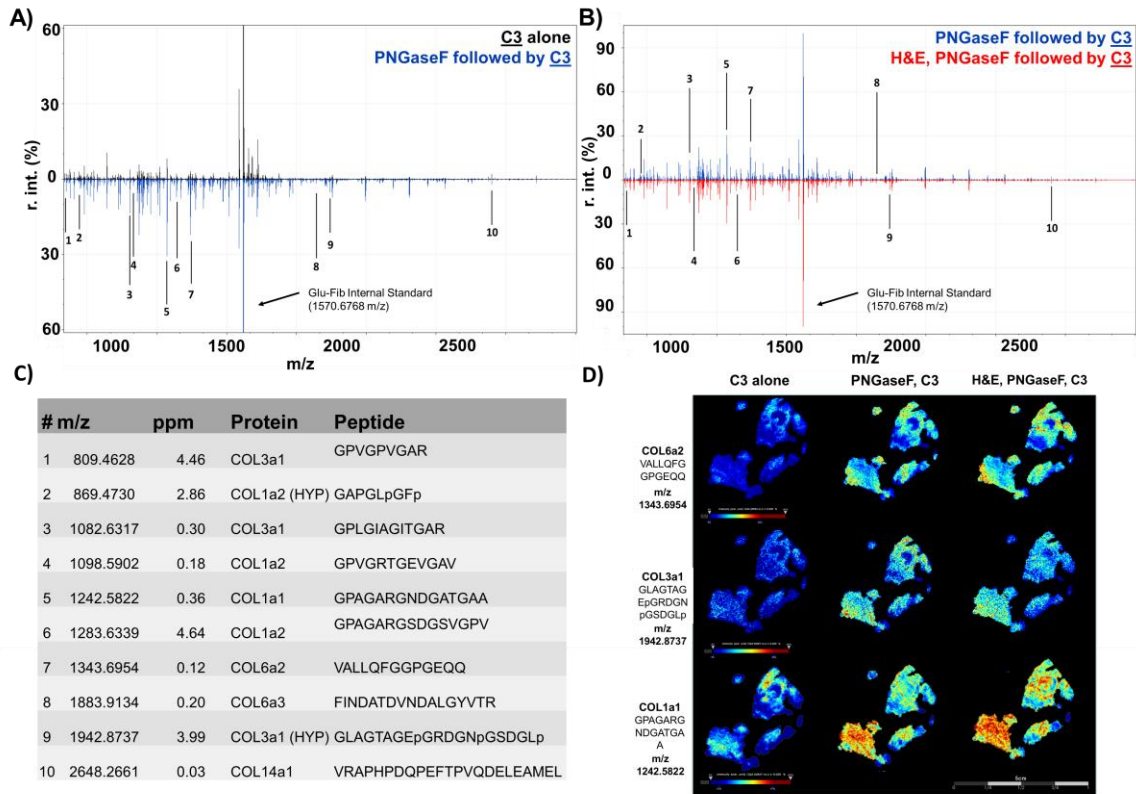
Figure 27: Comparison of ECM peptides detected with collagenase type III (C3) application after different sequential treatments. C3 was applied alone, after deglycosylation of the tissue with PNGase F or after both H&E staining and deglycosylation. (a) Overall average mass spectrum of Collagenase Type III treated tissue (top, black) and Collagenase Type III treated tissue after undergoing PNGase F digest and deglycosylation (bottom, blue). Annotated collagenase peptides and corresponding proteins are shown to the right. (b) Overall average mass spectrum of Collagenase Type III treated tissue after PNGase F and deglycosylation (top, blue) and Collagenase Type III treated tissue after undergoing H&E staining, PNGase F digest and deglycosylation (bottom, red). Annotated collagenase peptides and corresponding proteins are shown in (c). (d) Examples of collagen peptide images created as heat maps of the corresponding m/z peak intensity. Collagen peptide sequence and m/z are shown left of each image. Peak 1570.6768 m/z corresponds to the Glu1-Fibrinopeptide B (Glu-Fib) internal standard. Peptide m/z have been annotated via previously generated databases.

proteoglycans have been implicated in elastin fibrogenesis [287, 288]. These interactions may be responsible for decreased enzymatic access of elastase to the fibrotic aortic valve tissue without deglycosylation and CS removal.

4.6 Collagenase peptide imaging is compatible with pre-treatment of other ECM-targeting enzymes

Preliminary studies were performed with deglycosylation alone as a proof-of-concept multi-enzyme strategy with collagen and ECM peptides as the final analyte. Here we have shown that deglycosylating tissues with PNGaseF before COLase3 treatment allows for capture of both the N-glycome and collagen proteome while improving collagen peptide signal versus COLase3-treatment alone (**Figure 27a**). Similar to previous studies with PNGaseF and histopathological evaluations (**Figure 25**), multi-enzyme studies on H&E-stained tissue show that H&E has no detrimental effect on the collagen signal (**Figure 27b-d**). In addition to comparing relative intensities between tissue treatment groups, hierarchical clustering analysis was performed to unbiasedly determine if the PNGaseF MALDI-IMS signal had a unique spatial distribution and spectral profile as compared to the collagenase (**Figure 28**).

To expand upon these studies as part of a multi-enzyme strategy including chondroitinase ABC and elastase, additional COLase3 experiments were done to evaluate the quality of the signal after single enzyme treatments. While removal of certain analytes, such as N-glycans improved the COLase3 signal more than others, no single enzyme treatment detrimentally effected the COLase3 signal (**Fig. 29a-d; 30**). Consistent with previous studies by our lab, deglycosylation with PNGaseF had the greatest effect on improved COLase3 signal (**Fig. 29a,c**).

N-glycan Image Data **Collagen Peptide Image Data**

A)

B)

Spectra: 9330, Distance: 0
Spectra: 4730, Distance: 0.175793
1 (0-0) (Spectra: 2005) ——— Matrix
Spectra: 2725, Distance: 0.0813094
2 (0-1-0) (Spectra: 1126)
3 (0-1-1) (Spectra: 1599)

N-glycan Image Data

Spectra: 4600, Distance: 0.144223
4 (1-0) (Spectra: 2418) ——— Matrix
Spectra: 2182, Distance: 0.412098
Spectra: 2161, Distance: 0.0816199
5 (1-1-0-0) (Spectra: 1400)
6 (1-1-0-1) (Spectra: 761)
7 (1-1-1) (Spectra: 21)

Collagen Peptide Image Data

Figure 28: Example of image segmentation analysis used to identify shared tissue regions between N-glycan and collagen peptides detected by MALDI-IMS on the same tissue section. (a) Output of image segmentation analysis performed with a combined list of identified N-glycan and collagen peptide peaks from the same tissue section. The blue region from N-glycan imaging and orange region from collagen peptide imaging display similar regions of interest. (b) Segmentation analysis showing hierarchal clustering. N-glycan or image data type are annotated by color. Image segmentation was done with SCiLS (Bruker Scientific, LLC).
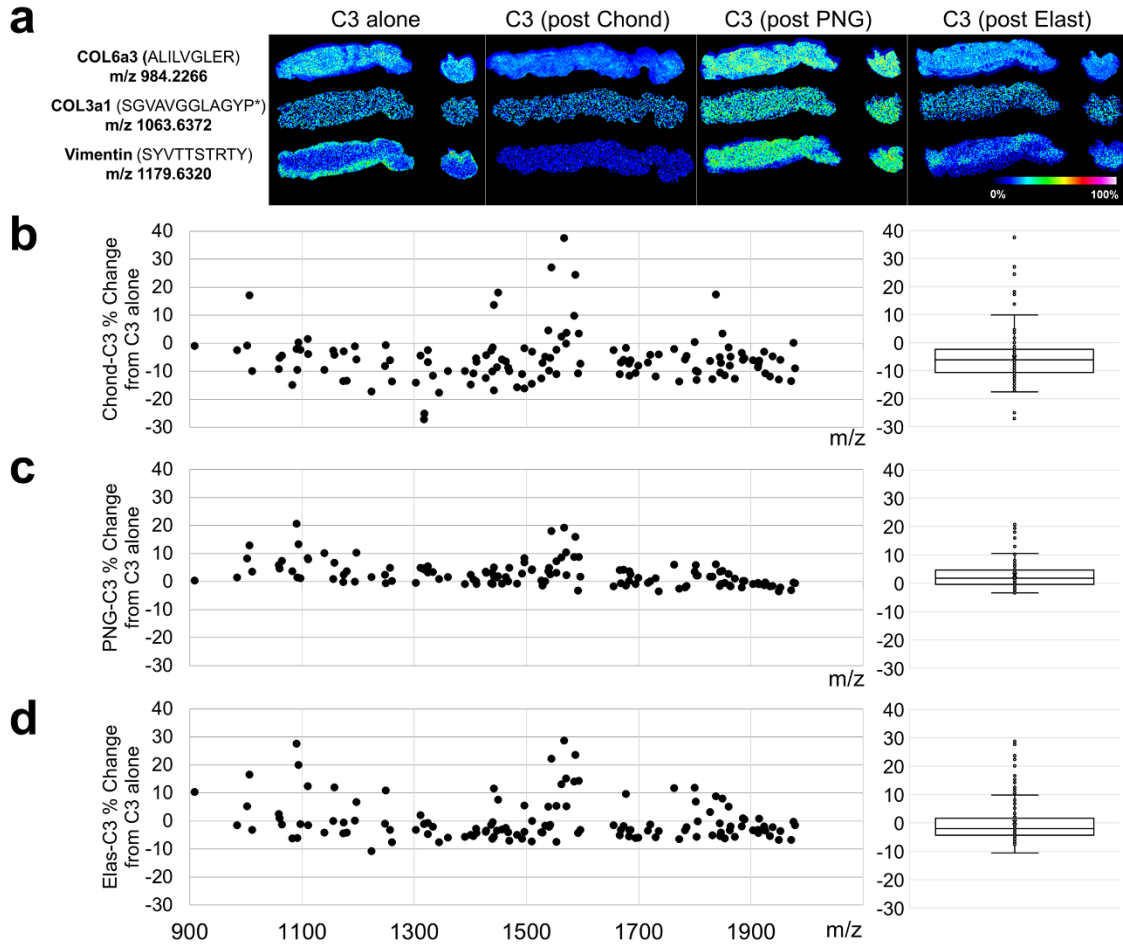
Figure 29: Single enzyme treatment does not detrimentally alter Collagenase Type III collagen peptide signal. a. Representative images of COLase3 digests either after antigen retrieval only (C3 alone) or after digestion with a single ECM-targeting enzyme and analyte removal. From left to right: COLase3 control, post-chondroitinase, post-PNGaseF, and post-elastase. Three ECM peaks are shown: collagen 6a3 peptide (top), collagen 3a1 peptide (middle), and vimentin peptide (bottom**). b-d.** Quantification of the percent change in peak signal intensity for all COLase3 peptides identified after chondroitinase ABC (**b**), PNGaseF (**c**), and elastase (**d**) incubation and analyte removal as compared to control. Each point represents a COLase3 peptide peak with a boxplot of the data shown to the right. No single enzyme treatment had a significant effect on COLase3 signal intensity. P* indicates hydroxyproline.
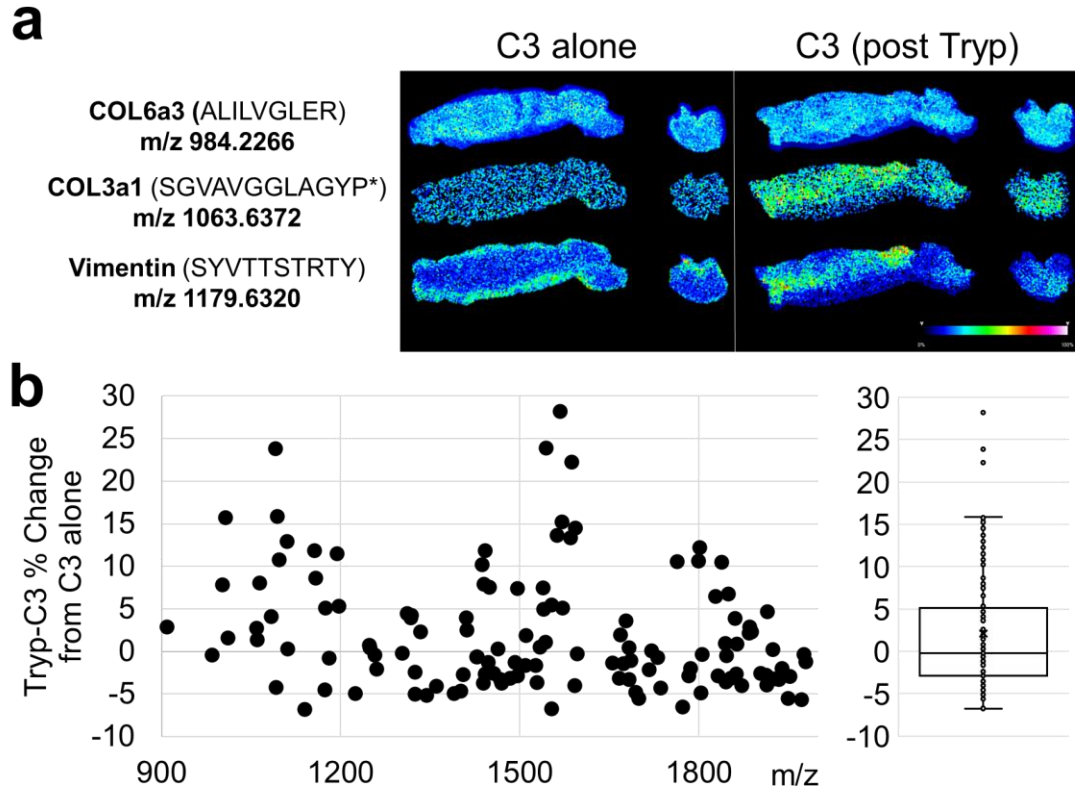
Figure 30: Collagenase peptide imaging is compatible with pre-treatment of trypsin.
A. Representative images of COLase3 digests either after antigen retrieval only (C3 alone) or after digestion with a trypsin. Three ECM peaks are shown: collagen 6a3 peptide (top), collagen 3a1 peptide (middle), and vimentin peptide (bottom**). B.** Quantification of the percent change in peak signal intensity for all COLase3 peptides identified trypsin incubation and analyte removal as compared to control. Each point represents a COLase3 peptide peak with a boxplot of the data shown to the right. P* represents hydroxyproline.

4.7 Multi-enzyme treatment reproducibly increases enzymatic access to ECM peptides

The same tissue section treated with chondroitinase, PNGaseF and elastase was finally treated with COLase3 to image collagen and other ECM peptides (**Fig. 31a-d**). Quantification of signal intensities between the two methods shows an average of 3.1% increase in peak intensity (mean across all samples and peptides) (**Fig. 31f**) and an 82 ± 15% increase in total number of peptides identified (mean across all samples) (**Fig. 31g**). Peptides containing the PTM hydroxyproline (HYP) were also able to be identified (**Fig. 31a, c**). HYP peptides were not uniquely enriched in this method compared to non-modified peptides. In addition to collagen-type proteins, other ECM peptides were also identified, such as the proteoglycans decorin, perlecan, and fibrinogen (**Fig. 31b**). COLase3 has low secondary proteolytic activity, with a primary cleavage site at the Y-G bonds of G-X-Y sequence in triple helical protein structures. Because of this, the specificity of this enzyme is not limited to collagen-type proteins but many ECM proteins with triple helical regions [146]. This study was tested for reproducibility across three different human aortic valve samples (**Fig. 31a-c, g; Fig. 32)**

a
COL1a2 (GP*P*GMTGFP*)
m/z 908.5208 (7.7 ppm)

Perlecan (LAGIDTLLIRA)
m/z 1155.7124 (3.2 ppm)

COL1a1 (GPPGPP*SAGFDFS)
m/z 1248.6223

b
Decorin (LTELHLDGNKISR)
m/z 1495.8037 (12.8 ppm)

COL18a1 (LKDELLFPSWEA)
m/z 1447.8591

COL6a2 (MLPDSTEIDQDTINR)
m/z 1747.8170

c
COL3a1 (GPAGIP*GFP*)
m/z 944.4202

Fibrinogen (LTTNIMEILR)
m/z 1203.6767 (2.3 ppm)

COL6a2 (MLPDSTEIDQDTINR)
m/z 1747.8170 (8.8 ppm)

d

e

#	m/z	Protein	Peptide	PPM
1	891.4129	COL1A1	GSP*GFQGLP*	8.9
2	1173.5977	COL6A2	LLQFGGPGEQQ	6.4
3	1203.6795	FIBA	LTTNIMEILR	2.3
4	1405.7415	POSTN	LASALRPDEYTL	6.5
5	1426.8243	PRELP	IPPGVFSKLENLL	4.4
6	1437.7904	FIBA	LRPAPPPISGGGYR	4.1
7	1447.7484	COL18A1	LKDELLFPSWEA	1.0
8	1462.7215	COL6A3	NIDSEEVGKIASNS	13.4
9	1495.8014	DCN	LTELHLDGNKISR	14.4
10	1747.8323	COL6A2	MLPDSTEIDQDTINR	8.8

f

g

Figure 31: Collagenase Type III collagen peptide signal and reproducibility study after removing the Chondroitin Sulfates, N-Glycans, and Elastin peptides. a-c. Representative images of COLase3 peptides in three separate aortic valve samples that have been digested with the serial enzyme methodology. **d**. Annotated spectra with of COLase3 alone (top, black) and COLase3 signal post-CS-N-glycan-elastin removal, with corresponding peptide sequences shown in **e**. **f.** Quantification of the percent change in peak signal intensity for all COLase3 peptides identified. Each point represents an COLase3 peptide peak with a boxplot of the data shown to the right. **g.** Quantification of total number of peptides identified between C3 alone (black) and C3 post-CS-N-glycan-elastin removal (grey). Data shown for the three tissues in **a-c**. P* indicates hydroxyproline.

123
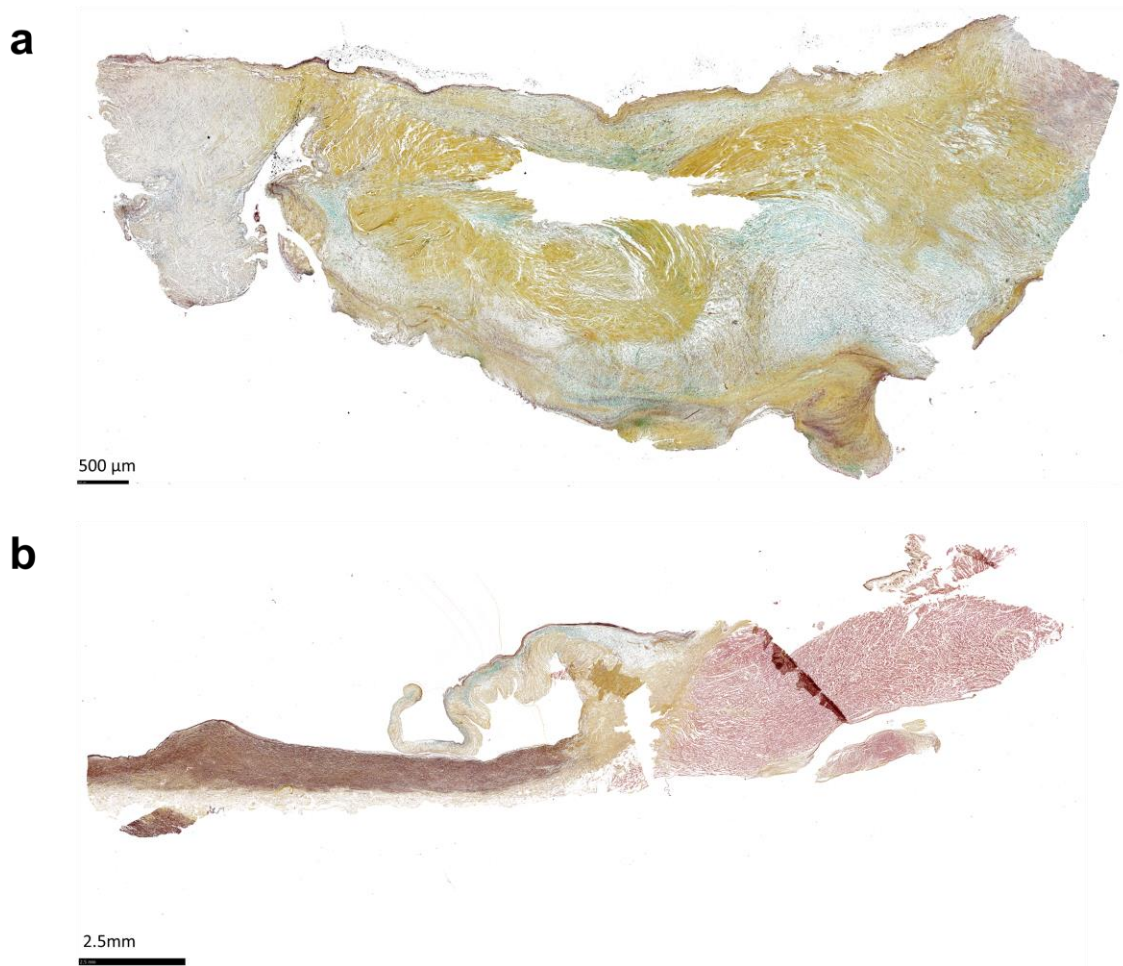
Figure 32: Aortic Valve tissue sections used for reproducibility studies. a-b. Movat's Pentachrome staining of tissue sections with GAGs in blue, elastin in purple, and collagen in yellow. Tissue shown in **b** has portions of the outflow tract (OT) and aortic wall still attached. OT has minimal collagen staining. Aortic valve in **b** is highlighted by dotted line.

4.4 Discussion

The serial application of Chondroitinase ABC, PNGaseF, Elastase, and Collagenase Type III, along with specific washing steps, allows for the mapping of the complex ECM from the same 5 μm tissue section. This multimodal approach may be useful for deep mining of extracellular matrix information from difficult to obtain tissues, as one tissue section can be evaluated for 1) pathology via histology 2) CS GAGs, 3) N-glycans, 4) elastin, and 5) collagens and other ECM peptides. Ongoing studies aim to incorporate i) hyaluronidase treatment to visualize hyaluronic acid; ii) endoglycosidase F3, to identify core-fucosylated N-glycan structures; and iii) trypsin, to further probe the ECM and non-ECM proteome. This multi-enzyme strategy is beneficial in clinical and biomedical research studies of the extracellular matrix, where patient samples may be limited.

Chapter 5: Structure-Function Relationship of Extracellular Matrix in Pediatric Congenital Aortic Valve Stenosis

5.1 Introduction

This chapter outlines the localized targeting of collagen type peptides within the valve structure. Collagens are the fundamental scaffolding of valvular structure that influences valvular function and thus cardiac function. It has been well documented that the stratification into the three valve layers (fibrosa, collagen; spongiosa, GAGs; and ventricularis, elastin) that is seen in healthy AVs becomes disorganized in CAVS [8, 36, 204]. Healthy AV function is heavily dependent on this trilayer ECM structure, regulated by developmental cell signaling, hemodynamics, and biomechanical forces [289]. However, the translational and post-translational regulation of these critical proteins remodeling in pediatric disease remains poorly understood.

We have previously identified that collagens are the major ECM constituents being deposited in pCAVS, concomitantly with GAG loss. However, collagen sub-type regulation remains to be explored in a spatially relevant manner, translatable to structure-function relationships. There are 28 collagen subtypes, all with unique roles in biomechanical structure of tissues, immune infiltration, signaling molecule storage, ECM-targeted protease activation, and cell signaling [66, 67]. In human mitral valves, relative abundances of collagen subtypes are as follows: Type I, 74%; Type III, 24%; and Type V, 2% [289]. Similar ratiometric studies have yet to be done in healthy AVs. Similarly, these studies may be limited by techniques that inefficiently access non-fibril subtypes. In the AV, these fibril-type collagens are primarily distributed in the fibrosa layer to provide support against cyclic hemodynamic forces during systole. While it is known that the fibrosa layer is lost in pCAVS (Chapter 3), what is unknown is if this destratification is correlated to a localized deposition of different collagen subtypes that may contribute to

biomechanical instability and further matrix remodeling. This is the topic of the current study.

Spatially defining the collagen proteome in a high-throughput manner remains an analytical challenge. Matrix-assisted laser desorption/ionization imaging mass spectrometry (MALDI-IMS) is an imaging technique that reports spatial localization and relative quantitation of collagen protein sequences, including PTMs, in thin tissue sections. Previously, untargeted MALDI-IMS studies have been performed on calcific aortic valve samples [159]. While some ECM peptides were identified, the un-targeted nature of this study showed more of a proof of concept than a quantitative analysis of the ECM as related to valve structure. Our technique, optimized in Chapter 4, allowed for approximately 150 ECM peptides, primarily from collagen sub-types, to be identified from each valve sample (Fig. 31).

In this study, we are delineating collagen regulation in a cohort of pediatric and adult CAVS samples through interdisciplinary approaches. Microscopic histopathological evaluation via picrosirius red staining is used to visualize collagen fiber thickening and orientation due to CAVS (Chapter 3). These regions of localized collagen dysregulation are being probed for their unique collagen proteome. Peptide sequences and post-translational modifications (PTMs) are being detailed by parallel MALDI-IMS studies. This chapter outlines the first report of collage peptide localization within a pediatric cohort of human CAVS samples. Here we have identified specific collagen peptides that colocalize with histopathologically identified regions of collagen dysregulation. This study also identifies a unique matrisome profile that may be developmentally regulated within the aortic valve, independent if disease status. Overall, this chapter outlines a novel application of MALDI-IMS in valvular research.

5.2 Materials & Methods
4.2.1 Materials

Xylenes, 200 proof ethanol was from Fisher Scientific (Pittsburgh, PA, USA). Acetonitrile, Ammonium Bicarbonate, Calcium Chloride, Formic Acid, and Trizma Base were from Sigma-Aldrich (St. Louis, MO, USA). PNGase F Prime was purchased from N-Zyme Scientifics (Doylestown, PA). Collagenase type III (COLase3) (*C. histolyticum*) was purchased from Worthington Biochemical (Lakewood, NJ, USA).

4.2.2 Tissue Procurement

Aortic valve tissue samples were procured through the Vanderbilt Core Laboratory for Translational and Clinical Research and the National Disease Research Interchange. The aortic valve tissues were collected under the Vanderbilt Pediatric Congenital Heart Disease Biorepository, written informed consent was obtained, and the project was approved by the Vanderbilt Institutional Review Board (IRB) and the IRB at the Medical University of South Carolina. De-identified tissues were obtained during reparative or transplant surgeries and characterized by pre-operative function into three patient categories: normal tricuspid (normal), pediatric CAVS bicuspid (pCAVS), and aortic valve insufficiency tricuspid (AVI). Valvular function is from de-identified complete 2D, color and spectral Doppler, or M-mode echocardiogram reports acquired prior to valve resection, replacement or heart transplant.

3.2.3 Tissue Preparation & Histology

Formalin-fixed, paraffin-embedded tissue was cut to 5 µm thick sections via microtome and mounted onto microscope slides (Tissue Tack, Polysciences, Inc.,

Warrington, PA, USA) then dehydrated overnight at 37°C prior to storage at room temperature. Tissues were stained with Verhoeff Van Gieson (Verhoeff solution for elastin; Van Gieson counterstain for collagen), Movat's Pentachrome (Alcian Blue for GAG, Saffron for collagen, Resorcin-Fuchsin for elastin, and Woodstain Scarlet-Acid Fuchsin for muscle), or Alcian Blue alone (Polysciences, Inc.), following manufacturer's protocols. All staining protocols included a hematoxylin counterstain.

FFPE aortic valve tissue sections were digested with COLase3 after serial treatment with PNGaseF (N-Zyme Scientifics) for MALDI-IMS experiments. Spray conditions for all enzymes were as previously published [11, 12]. Samples were digested in high humidity at 37.5°C for 5 hours. A 7 mg/mL solution of alpha-cyano-4-hydroxycinnamic acid (CHCA) matrix solution was prepared in 50% acetonitrile and 1.0% TFA. CHCA matrix solution prepared for peptide imaging was spiked with a standard of 200 femtomole/L [Glu1]-fibrinopeptide B human (GluFib) (Sigma-Aldrich, St Louis, MO, USA). CHCA automatic spray conditions included: 79°C, 10 psi, 70 µl/min, 1300 velocity, and 14 passes with a 2.5 mm offset. Slides for peptide imaging were rapidly dipped (<1 second) in cold 5mM ammonium phosphate and immediately dried in a desiccator.

6.2.5 MALDI-Imaging Mass Spectrometry

Images were acquired using a Trapped Ion-Mobility Time-of-Flight Mass Spectrometer (timsTOF fleX) (Bruker Daltonik, Bremen, Germany) equipped with a dual ESI/MALDI source. The samples were analyzed in positive ion Q-TOF mode and scanned at a mass range from 600 – 2500 m/z. The SmartBeam 3D 10 kHz laser was set to 8% power, scan range of 10 µm for X and Y and resulting field size of 14 µm for X and Y. The images were collected with 300 shots per pixel and a 20 µm step size in between pixels. Additional instrument parameters include: an ion transfer time of 125 µs, pre pulse storage

time of 25 µs, a collision RF of 4000 Vpp, a collision energy of 15 eV, an ion energy in the quadrupole of 5 eV, a TIMS funnel 1 RF of 500 Vpp, a TIMS funnel 2 RF of 500 Vpp and a multipole RF of 500 Vpp. After MS acquisition, the data was imported into SCiLS Lab 2020a (Bruker Daltonik) and normalized to total ion current.

Putative peptide identifications are based on our previously acquired databases from many tissue samples on the identical human aortic valvular tissues [10-11]. This analysis does not include peaks with biologically relevant spatial distribution that have not yet been sequenced with targeted proteomic analysis.

5.3 Results & Discussion
5.3.1 Overview

A total of 19 human aortic valve tissues were used in this study. Patients were categorized as follows: pediatric normal (n=4), pediatric bicuspid AVS (n=10), and adult fibrocalcific AVS (n=5). Clinical characteristics can be found in Table 9. Data in this chapter includes both histopathological evaluation of the ECM as well as two-dimensional mapping of collagen and other ECM peptides via MALDI-Imaging Mass Spectrometry techniques. A total of 152 putative peptides were identified in this dataset, with an additional 110 peaks that showed biologically relevant spatial distribution that were not identified in our database. These peaks may be potential candidates for future experiments in targeted proteomics (**Fig. 1**). The majority of putative peptide identifications were from collagen sub-type proteins (55%), with the remaining peptides putatively identified from ECM and collagen associated proteins, such as proteoglycans (DCN), ECM glycoproteins (Tenascins, Emilin-1, COMP, MFAP4), and proteins associated with cell-ECM binding (BGH3, FBN1, ASPN).

5.3.2 Extracellular Matrix Patterns within Normal Trilayer Aortic Valve Structure

Our MALDI-IMS methods outlined in this chapter use collagenase type III (COLase3) to enzymatically target proteins with triple helical regions (primarily collagen sub-types) from FFPE aortic valve (AV) tissue sections. These studies were performed on tissues that had been previously evaluated for ECM distribution and collagen spatial regulation (Chapter 3). An example of MALDI-ECM-IMS evaluation of a tricuspid, normal pediatric valve can be seen in Figure 33, relative to a serial section stained via Movat's Pentachrome. Three examples of putatively identified collagen subtype peptides can be seen, with dominate distribution shown within the fibrosa layer, as expected based on

Table 9: Descriptive statistics of patient characteristics for all pediatric and adult aortic valve tissue samples featured in the study. 2D Echocardiogram mean gradients define pre-operative valve function where a normal gradient is defined as <5 mmHg, mild stenosis as 5-25 mmHg, moderate stenosis as 25-50 mmHg, and severe stenosis as >50 mmHg. BSA: body surface area; C: Caucasian; L: Latino; AA: African American; MD: Myxomatous Degeneration

	SKU	Age (years)	Pediatric Age Group	Gender	Race/ Ethnicity	BSA (m^2)	Leaflet Morphology	Valve Function
Normal	DB051	0.66	Infant	M	C	0.34	Trileaflet	Normal
	NDRI	2	Young Child	M	L	0.63	Trileaflet	N/A
	DB85	9	Child	F	C	0.95	Trileaflet	Normal
	DB27	17	Adolescent	M	C	2.2	Trileaflet	Normal
	Normal Averages	**7.17 ± 7.5**		**75%M 25%F**	**75%C 25%L**	**1.03**		
CAVS	DB106	0.04	Neonate	M	C	0.21	Bicuspid	Severe Stenosis with AVI
	DB43	0.15	Infant	M	C	0.24	Trileaflet	Moderate stenosis with AVI
	DB40	0.75	Infant	M	C	0.37	Bicuspid	Moderate Stenosis
	DB119	5	Young Child	F	-	-	Bicuspid	Moderate Stenosis with AVI
	DB113	5	Young Child	-	-	-	-	Trivial Stenosis; Severe AVI
	DB18	6	Child	F	C	0.7	Bicuspid	Moderate Stenosis with AVI
	DB3	11	Child	F	C	1.5	Bicuspid	Moderate Stenosis with AVI
	DB117	12	Adolescent	M	-		Bicuspid	Moderate Stenosis with AVI
	DB41	14	Adolescent	M	C	1.6	Bicuspid	Moderate Stenosis with AVI
	DB16	17	Adolescent	M	C	2.1	Bicuspid	Moderate Stenosis with AVI
	CAVS Averages	**6.90 ± 5.8**		**70%M 30%F**	**100%C**	**0.93**		
FAVS	VHVI1296	81	Adult	M	C	-	Trileaflet	MD and Calcification
	VHVI1301	63	Adult	M	C	-	Bicuspid	MD and Calcification
	VHVI1336	50	Adult	M	C	-	Trileaflet	Extensive Calcification
	VHVI226	29	Adult	-	-	-	Trileaflet	N/A
	FAVS Averages	**55.75 ± 21.9**		**100%M**	**100%C**	**-**		
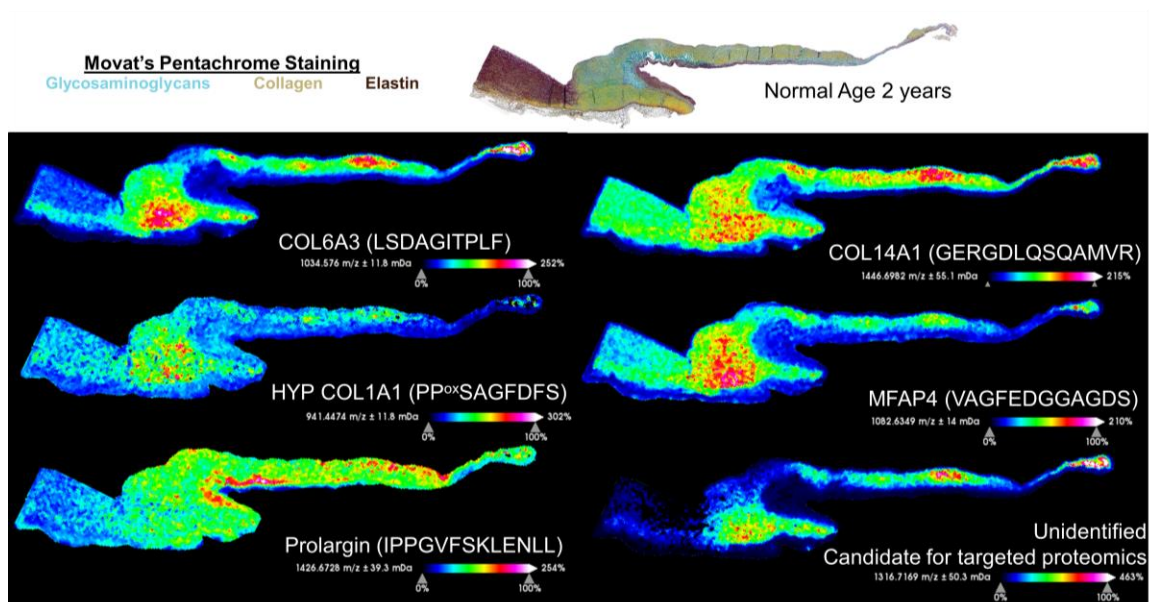
Figure 33: Representative extracellular matrix peptides within normal trilayer valvular structure. Top: extracellular matrix profiling via Movat's Pentachrome staining (Blue: GAGs; Yellow: Collagen; Purple: Elastin). Below: Representative MALDI-IMS heatmaps of putatively identified ECM peptides within the valve structure. Peptides from several collagen subtypes are identified along with other ECM peptides. Bottom right shows a potential candidate for targeted proteomics based upon biologically relevant spatial distribution patterns.

histopathological evaluation. As can be seen, this method can identify peptides from multiple collagen subtypes, with putatively peptides from collagens α3(VI), α1(XIV), and α1(I) shown. Similarly, this method was able to putatively map post-translationally modified peptides, with an example of a hydroxyproline containing collagen α1(I) peptide shown. Since COLase3 can target non-collagen type proteins with triple helical regions, we were also able to putatively identify peptides from MFAP4 and Prolargin. Interestingly, MFAP4, or Microfibril-associated glycoprotein 4, is strongly associated with elastin-fiber formation [290] and has been found to be increased in aortic aneurysm patients of bicuspid aortic valve [291]. A prolargin peptide (1426.6728 m/z, IPPGVFSKLENLL) was found to be abundant within the elastin-rich ventricularis of the normal pediatric AV (Fig. 33). In previous studies, small leucine-rich repeat proteoglycans, such as prolargin, were found to be associated with elastin fibers and serve in galectin binding [292].

5.3.3 Uncovering 'Hidden Fibrosis' via MALDI-ECM-IMS

Conventional histopathological analysis of collagen is done with various stain techniques, such as Movat's Pentachrome, Picrosirius Red, Herovici, and Masson's Trichrome – some examples of which are shown in Figure 34 (left). It has been well noted in literature that the mechanism of these stains targets fibril type collagens, and while basement membrane collagens may be highlighted with silver-nitrate based stains [293], FACIT and other collagen subtypes may be left unstained without targeted affinity-based methods. Uncovering fibrosis-associated peptides that may be unstained by conventional histology is one application of MALDI-ECM-IMS. Examples of this can be seen in Figure 34B. In this pCAVS valve, there is a band of tissue that is unstained for collagens but is positive for GAGs, suggesting this is not tissue loss during preparation. A serial section of tissue was then used for MALDI-ECM-IMS. As can be seen via segmentation
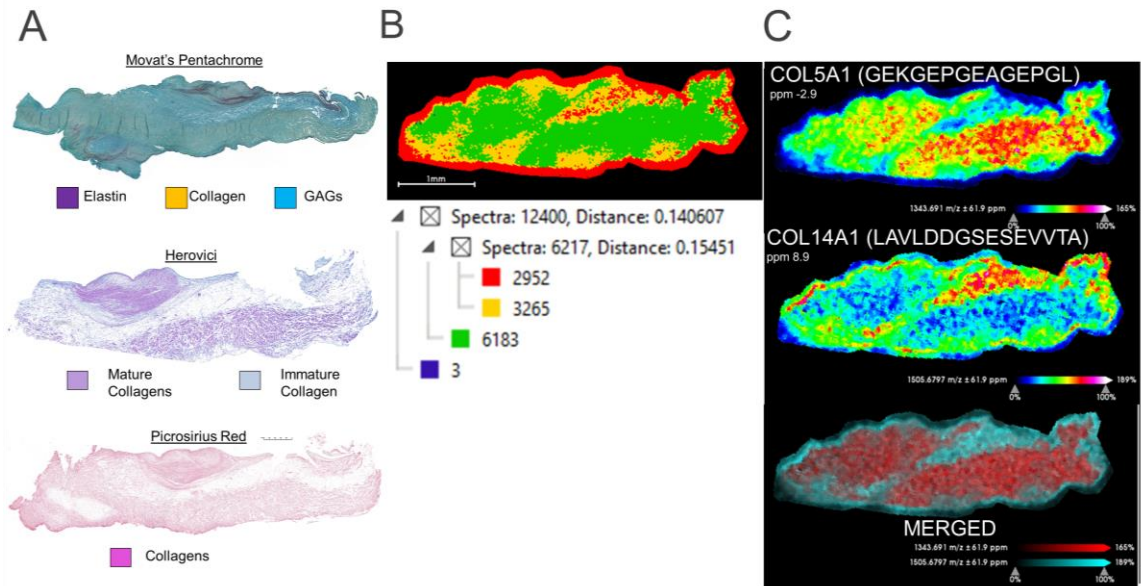
Figure 34: MALDI-ECM-IMS identifies putative collagen peptides unstained via conventional histology. A) ECM targeted histology stains on serial sections of valve tissue studied. SKU DB119 (age 5). Top: Movat's Pentachrome (Blue: GAGs; Yellow: Collagen; Purple: Elastin); Middle: Herovici (Blue: immature collagen; purple: mature collagen); Bottom: Picrosirius Red, optical light (Red: Collagen). A band of tissue can be seen in PSR and Herovici stains that stains positively for GAGs in MP. B) Segmentation analysis of the MALDI-ECM-IMS identified peaks, showing unique proteomes between sections positively and negatively stained for collagen in A. C) Representative images of peptides that colocalize with regions identified in B. Top: a peptide from fibril-type COL5A1. Middle: a peptide from FACIT-type COL14A1. Bottom: Merged image.

analysis, there are unique proteomes associated with regions unstained for collagen (Fig 34B, yellow) and those than positively stain for collagen (Fig. 34B, green). Two representative peaks aligning with those segmentation clusters are shown. The fibril type collagen peptide (m/z 1343.6910; COL1α1(V), GEKGEPGEAGEPGL) correlates to the collagen stain while the FACIT type collagen (m/z 1505.6797; COLα1(XIV), LAVLDDGSESEVVTA) correlates to the region unstained by collagen histology techniques. This, in combination with Figure 33, shows the application of MALDI-ECM-IMS to uncover the translational and post-translational regulation of tissues in a spatially defined manner, previously inaccessible by conventional histology.

5.3.4 MALDI-ECM-IMS Putatively Identifies Collagen-Subtype Composition of Collagen "Plaques" within pCAVS

Previous studies used microscopy-based techniques to identify collagen signatures uniquely associated with pCAVS – primarily: increased collagen deposition, loss of trilayer structure, misaligned collagen fibers relative to the endothelium, and, most significantly, increased regions of increased collagen fiber density, or RIFDs. MALDI-IMS was used to in this study to determine the collagen-subtype regulation occurring within these localized collagen RIFDs. A total of 10 ECM peptides were found to colocalize with previously identified RIFDs within a representative pCAVS patient (Table 10). Figure 35A-B shows the histology-defined RIFD in a pCAVS sample (B), along with the lack of RIFD shown in the age matched control (A). Figure 35C shows two representative images of MALDI-IMS mapped peptides that colocalize with these regions. Not all peptides that correlated to RIFDs were statistically differentially expressed between normal and pCAVS when taking into account expression across the entire tissue. However, it is clear via
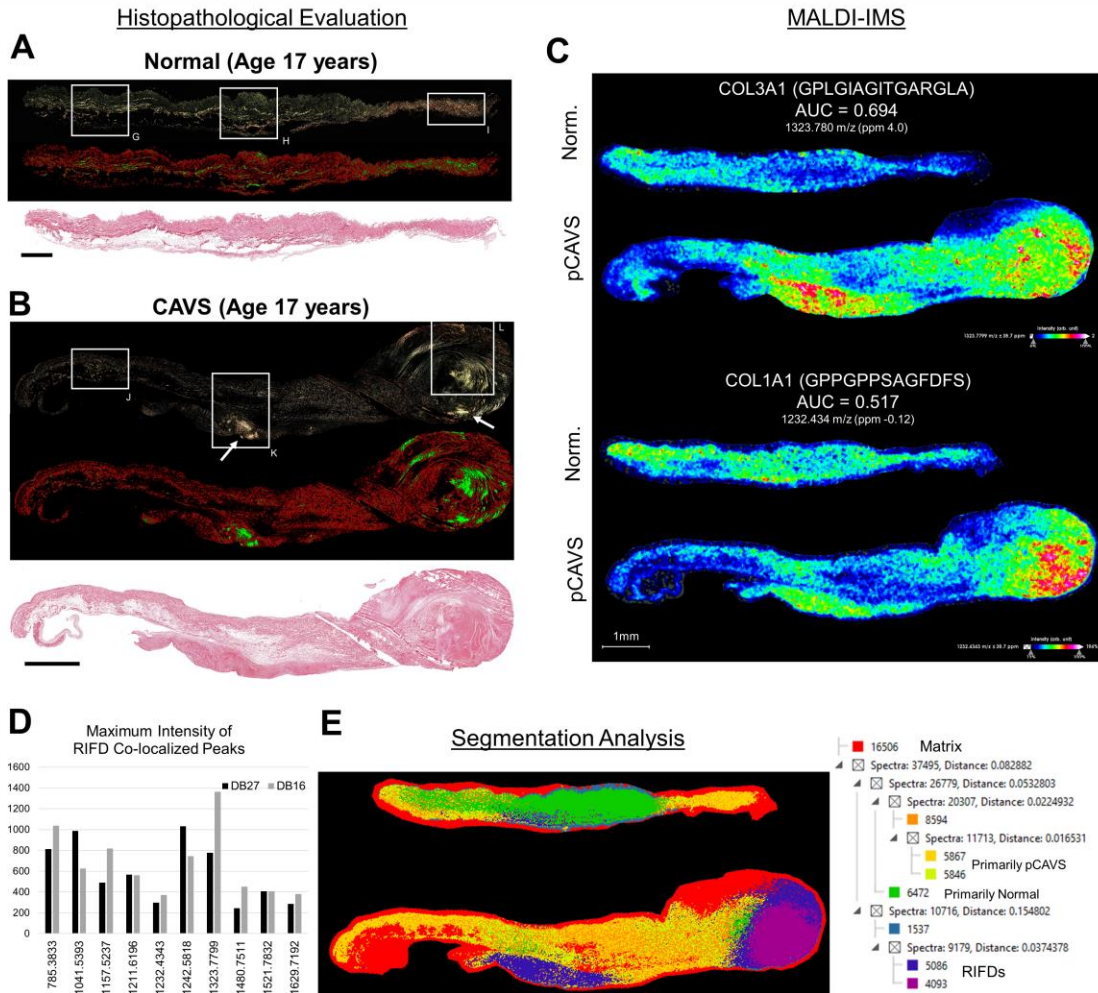
Figure 35: MALDI-ECM-IMS identifies putative peptides colocalized with RIFDs. A) Picrosirius Red stain of a normal pediatric valve (SKU DB27, age 17). Top: Polarized light image; Middle: RIFD mask (see Chapter 3); Bottom: Optical light image. B) PSR stain on age-matched pCAVS valve (SKU DB16, age 17). Top: Polarized light image; Middle: RIFD mask (see Chapter 3); Bottom: Optical light image. White arrows show RIFDs. C) Representative MALDI-IMS data of two putatively identified peptides that colocalize with RIFDs in DB16 (B). D) Maximum intensity values for all RIFD colocalized peaks identified, DB27 and DB16 shown. E) Segmentation analysis on all peaks identified within these two valves. Unique proteome distribution is seen in purple colocalizing to RIFDs (purple).

Table 10: Putatively identified peptides colocalizing with RIFDs. Colocalization threshold was 0.065.

m/z	Colocalization Score with Collagen RIFDs	Peptide	HYP Probability Sequence (if modified)	Protein	(+1H) Theorhetical	ppm
785.383	0.66	GLPGTGGPP	GLP(0.5)GTGGP(0.002)P(0.498)	Collagen alpha-1(III) chain OS=Homo sapiens GN=COL3A1 PE=1 SV=4	785.384	-0.3
1041.539	0.65	NTEFKNTRTNEKVELQE		Vimentin OS=Homo sapiens GN=VIM PE=1 SV=4	1041.519	19.6
1157.524	0.77	VNENLENYY		Lumican OS=Homo sapiens GN=LUM PE=1 SV=2	1157.511	11.1
1211.620	0.72	GGAVPIGIGIGNAD		Collagen alpha-3(VI) chain OS=Homo sapiens GN=COL6A3 PE=1 SV=5	1211.643	-19.0
1242.582	0.66	GLKGNEGPPGPPG	GLKGNEGP(0.5)P(0.5)GP(0.5)P(0.5)G	Collagen alpha-1(V) chain OS=Homo sapiens GN=COL5A1 PE=1 SV=3	1242.564	14.0
1480.751	0.66	GKEGPVGLpGIDGRp		Collagen alpha-2(I) chain OS=Homo sapiens GN=COL1A2 PE=1 SV=7	1480.776	-16.7
1521.783	0.68	LTDLEPATEYTLR		Isoform 4 of Tenascin OS=Homo sapiens GN=TNC	1521.780	2.3
1629.719	0.67	FQGPAGEPGEPGQTGPA	FQGPAGEP(1)GEP(1)GQTGPA	Collagen alpha-2(I) chain OS=Homo sapiens GN=COL1A2 PE=1 SV=7	1629.719	0.3

heatmap mapping of these colocalized peptides that there are regions of increased intensity that qualitatively differ from normal valves (Figure 35C, Table 10).

This technique shows the importance of considering the spatial localization of a proteome. While all 10 RIFD colocalized peptides were identified in both the normal and pCAVS age matched control samples (Table 10) – with no statistical difference in the mean intensity of these peptides across the tissue – there were specific areas of increased localization within the pCAVS samples that directly overlaps with RIFDs identified in a previous study (Chapter 3). This can be visualized in the representative images (Fig. 35C), as well as seen in maximum intensity quantification of two samples shown (Fig. 35D). Certain peptides show high maximum intensity with pCAVS' RIFD and relatively low intensity within normal valves, such as 785.3833 mz (COLα1(III), GLPGTGGPP^{ox}; 21.6% increase in maximum intensity from normal age-matched control), 1323.7799 m/z (COLα1(III), GPLGIAGITGARGLA; 43% increase) and 1480.7511 m/z (COLα2(I), GKEGPVGLP^{ox}GIDGRP^{ox}; 46% increase).

As expected, 6 out of the 10 RIFD colocalizing peptides were putatively identified to be derived from fibril collagens, (I, III, and V). However, 4 peptides were putatively identified from network-associated collagen α3(VI) as well as non-collagen proteins tenascin-c, lumican, and vimentin. The proteoglycan lumican has been previously explored for its role in limiting collagen fibrillogenesis [294-296], but may also play a role in increasing myocardial collagen production during pressure overload [297]. Small Leucine Rich Proteoglycans (SLRPs) such as lumican have been identified as having a critical role in spatiotemporal ECM remodeling in the developing mouse valve cusp [38, 298], however, its role in human valve disease remains unexplored. Interestingly, the ECM glycoprotein tenascin-c has been previously implicated endothelial function in healthy

140

valves, as well as in the progression of human aortic valve stenosis when found within deeper layers of the valve structure [299], similar to spatiotemporal patterns identified in this study.

Segmentation analysis was performed on these two age-matched samples to determine if there were unique proteomes associated with RIFD colocalized regions, as well as between age-matched healthy and diseased valvular tissues (Fig. 35E). This analysis showed that when considering both intensity and localization, there are collagen proteome clusters unique to previously identified RIFDs (purple, Fig. 35E). Similarly, the distal tip of the normal valve (Fig. 35E, yellow), which has been shown to under stronger hemodynamic forces and more actively remodeling, appears to share a similar proteome to the length of the age-matched pCAVS valve sample (Fig 35E, yellow).

Unexpectedly, a peptide from non-fibril type collagen VI (m/z 1211.6196; GGAVPIGIGIGNAD) was found to colocalize within regions of RIFDs and collagen fiber misalignment within the adolescent pCAVS valve studied above. This peptide was visualized within all AV samples as well (Fig. 36). Following the trend seen in the pCAVS valve sample above, this peptide was found to be abundant in regions previously identified as RIFDs as well as stained for collagen maturity via Herovici (Fig. 36, arrows). Colocalization analysis, applied to this spatial distribution within the valve cohort, putatively identified 21 other peptides that overlapped with regions of collagen maturity and RIFDs, similar to the 1211 m/z distribution shown in Fig. 36 (Table 11). Of these peptides, 33% (7 out of 21 identified peptides, Table 11) were also putatively identified to be from collagen VI, suggesting a role for collagen type VI in RIFD formation.

Collagen type VI is a unique member of the collagen family that forms a supramolecular assembly of beaded microfilaments within the ECM [300]. ColVI has been
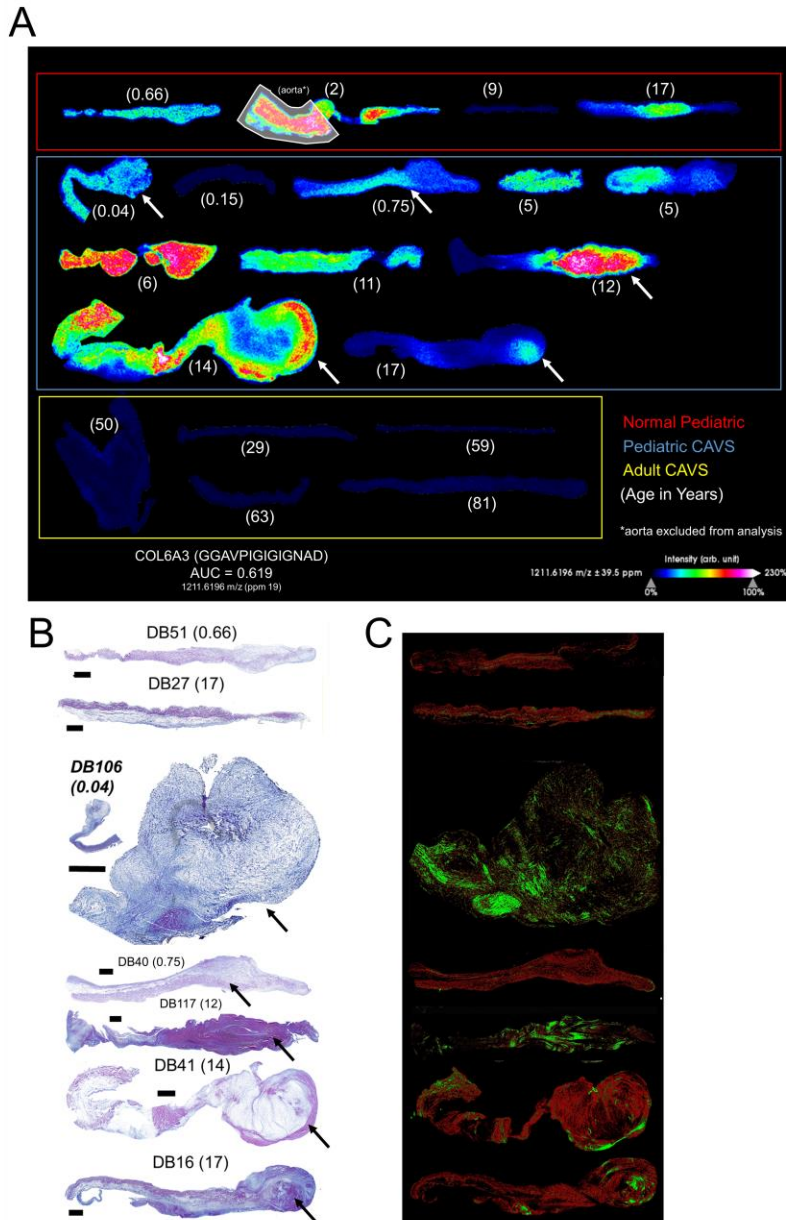
Figure 36: Distribution of COL6A3 peptide aligns with regions of mature collagen deposition and RIFDs in several pCAVS valves. A) Imaging data of a COL6A3 peptide found to colocalize with DB16 in Figure 35 (m/z 1211.620; GGAVPIGIGIGNAD). White arrows show RIFDs identified in B and C. B) Herovici stained serial sections of AVs studied in A. C) RIFD masques (see Chapter 3) of PSR stained serial sections of AVs studied in A.

Table 11: Putatively identified peptides that colocalize with COL6A3 peptide 1211 m/z. Colocalization analysis was done on all valve studied (Table 9). Colocalization threshold was 0.65.

m/z	Colocalization Score with 1211 mz	Peptide	HYP Probability Sequence (if modified)	Protein	(M+1H) Theorhetical	ppm
843.384	0.686	LVDYLDVGFDTTRVA		Collagen alpha-3(VI) chain	843.433	8.0
1001.509	0.731	PGKDGLNGLP	P(1)GKDGLNGLP(1)	Collagen alpha-1(I) chain	1001.495	14.6
1040.528	0.686	KKSQPPPPQ	KKSQP(0.946)P(0.967)P(0.043)P(0.043)Q	Collagen alpha-3(VI) chain	1040.542	13.8
1041.539	0.682	NTEFKNTRTNEKVELQE		Vimentin	1041.519	19.6
1115.534	0.707	LGGEGPGESEKVQQLEEQVQS		Emilin-1	1115.537	-3.3
1125.535	0.743	AVEAANYQDTIGRLQDEIQN		Vimentin	1125.546	-9.9
1211.620	1.000	GGAVPIGIGIGNAD		Collagen alpha-3(VI) chain	1211.643	-19.0
1242.582	0.752	GLKGNEGPPGPPG	GLKGNEGP(0.5)P(0.5)GP(0.5)P(0.5)G	Collagen alpha-1(V) chain	1242.564	14.0
1386.732	0.777	FRAAPLQGMLPGL		Collagen alpha-3(VI) chain	1386.756	17.8
1399.630	0.730	LGDLYEEmRE		Vimentin	1399.605	18.0
1438.714	0.682	GPPGHLTAALGDIMG		Collagen alpha-2(V) chain	1438.699	-9.9
1458.657	0.656	GPNGDAGRPGEPGLM	GPNGDAGRP(0.988)GEP(0.012)GLM	Collagen alpha-2(I) chain	1458.633	-16.8
1480.751	0.660	GKEGPVGLpGIDGRp		Collagen alpha-2(I) chain	1480.776	-16.7
1521.783	0.743	LTDLEPATEYTLR		Tenascin-C	1521.780	2.3
1609.756	0.673	IVDTVYEDGDSIQVG		Collagen alpha-3(VI) chain	1609.759	1.8
1623.869	0.668	SRAKRRGGGGHDALKG		Fibrillin-1	1623.895	15.6
1629.719	0.757	FQGPAGEPGEPGQTGPA	FQGPAGEP(1)GEP(1)GQTGPA	Collagen alpha-2(I) chain	1629.719	0.3
1772.810	0.725	GEIGLDGLDGEDGDKGLP		Collagen alpha-3(VI) chain	1772.818	4.6
1781.947	0.659	RLTLARRDDDPLNAR		Collagen alpha-2(VI) chain	1781.973	14.5
1829.893	0.653	MLSLGTKADTHDEILEG		Alpha-1-antitrypsin	1829.895	-1.1
1942.902	0.693	GLAGTAGEpGRDGNpGSDGLp		Collagen alpha-1(III) chain	1942.874	14.2

associated with roles as diverse and biomechanical stabilization to protecting against oxidative stress, depending on the tissue of origin [300]. In the heart, ColVI has been found to be increased in myocardial infarction mouse models, with a suggested role in cardiac remodeling post-infarction [301]. While the role of ColVI has been described in endocardial cushion development [302] and early VIC migration [303], its role in valve disease has not been explored. The MALDI-IMS studies outlined here do not necessary give mechanistic insight into the formation of RIFDs in pCAVS, but they do define molecular targets that should be explored in future studies.

5.3.5 ECM Profiling shows Developmental Regulation within Aortic Valves

With limited differences in pCAVS vs normal within the whole-tissue proteome, we explored developmental differences based on pediatric age categories defined by National Institute of Child and Human Development: Neonate (0-30d), Infant (1 mo – 2 yrs), young Child (2-6 yrs), Child (6-12 yrs), Adolescent (12-18 yrs). Our previous research (Chapter 3) has shown significant ECM regulation occurring in early periods of pediatric development (young pediatric, age 0-5 yrs) compared to later stages of pediatric development (older pediatric, age 6-18).

Segmentation analysis was done on all ECM peptides identified within the valve cohort to determine if unique peptide clusters exist between young pediatric, old pediatric, and adult patients, independent of disease (Fig. 37). Previous studies have shown a unique inflammatory and cell-signaling profile between pediatric and adult populations of AVS [31], however ECM profiling remained limited between these two pathologies. It is clear in the segmentation analysis shows that there ECM proteomes that are unique to adult fibrocalcific samples as compared to the pediatric cohort; however, differences between young and old pediatric AVs are more subtle (Fig. 37).
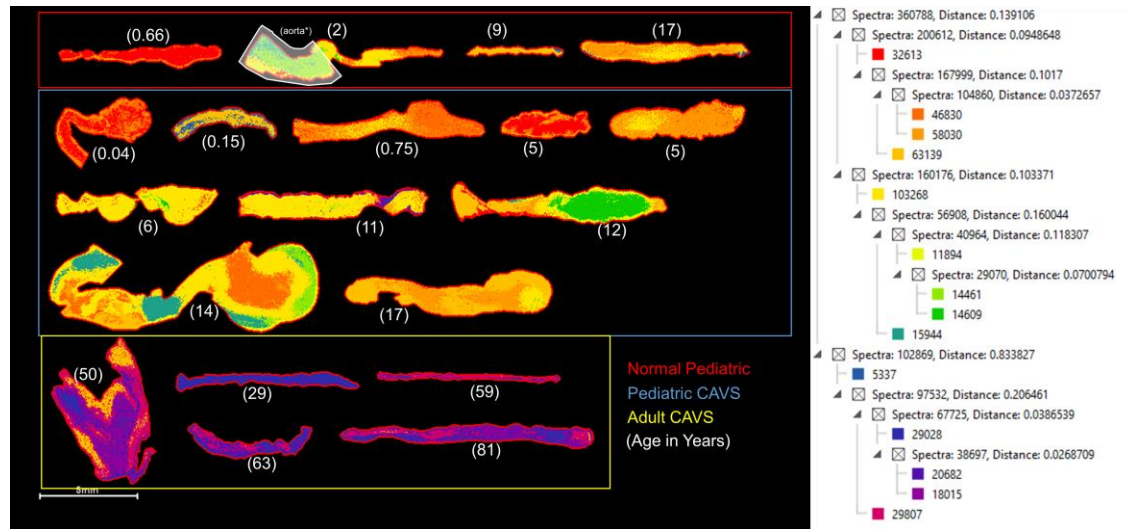
Figure 37: Segmentation analysis of the AV cohort on all peptides identified. Results show a unique proteome between adult CAVS samples (bottom, purple clusters) and pediatric samples (top, middle). Pediatric samples show similar proteome distributions, however RIFDs show unique clusters (green, light yellow).

Differential expression analysis was performed between young and old pediatric AVs via ROC-AUC. A total of 104 peptides were found with the generous threshold of 0.65 used within previous studies. Narrowing the threshold to 0.70 identified a total of 14 putative peptides to be differentially expressed between young and old pediatric AVs, data from which were used for further analysis (Table 12, Figure 38). A representative putative peptide from collagen α1(XVI) (m/z 1068.511, PGP^{ox}PGRGVQGP, AUC = 0.704; Note P^{ox} is a putative HYP site in need of confirmation) that is differentially expressed between pediatric age groups can be seen in Figure 38A. Interestingly, peptides that showed developmental regulation tended to show dissimilar distribution patterns to those correlation to RIFDs – this can be clearly seen by lack of distribution along the endothelial RIFDs seen in pCAVS SKU DB41 (age 14), and interstitial RIFDs seen in SKUs DB16 (pCAVS age 17) and DB117 (pCAVS age 12). Collagen α1(XVI) is a FACIT type collagen that aligns well with the fibrosa in healthy tri-layer valves (Fig. 38A, top). Interestingly, this FACIT collagen also aligns within regions highlighted by another FACIT collagen peptide, shown in Figure 34 within DB 119 (COLα1(XIV), pCAVS age 5).

To further show that these peptides identified via ROC-AUC analysis could unbiasedly differentiate between young and old pediatric patients independently of disease category, hierarchical clustering analysis was done (Fig. 38B). It can be seen here, with the exception of SKU DB43 (pCAVS age 0.15) and SKU DB18 (pCAVS age 6), these peptides can unbiasedly cluster pediatric patients by age category (Fig. 38B). Interestingly, the patient that was misclassified within the "older pediatric" cluster (SKU DB43, age 0.15), is a tricuspid pCAVS patient that was included in this study due to their severe stenosis. When reviewing the segmentation analysis in Figure 37, this patient has a similar proteome to the adult tricuspid fibrocalcific CAVS patients. Overall, certain

146

Table 12: ROC-AUC identified peptides to be differentially expressed between young (Age <6) pediatrics and old (Age ≥6) pediatrics. AUC threshold was >0.7.

m/z	ROC-AUC (Young vs. Old Pediatric)	Peptide	HYP Probability Sequence (if modified)	Protein	(M+1H) Theorhetical	ppm
1034.567	0.719	LSDAGITPLF		Collagen alpha-3(VI) chain	1034.556	-10.3
1056.579	0.725	LLVTEAPSKPITVTVEEQR		Basement Membrane Specific Heparan Sulfate Proteoglycan	1056.591	12.2
1068.511	0.704	PGPPGRGVQGP	P(0.333)GP(0.333)P(0.333)GRGVQGP	Collagen alpha-1(16) chain	1068.512	0.3
1163.568	0.770	LTVTGSSPDSLS		Tenascin X	1163.579	9.3
1259.649	0.709	AWASLPAEVLDS		TGFβ Induced Protein Ig-h3	1259.631	-13.6
1275.685	0.709	PTFRQLGTVQQ		Collagen alpha-3(VI) chain	1275.685	0.5
1316.673	0.702	GPKGEPGPAGPQGAP		Collagen alpha-1(II) chain	1316.659	-10.1
1359.669	0.729	LQAAEAIDDIPFG		P4HB	1359.679	7.6
1430.709	0.764	LGSQVGLMPGSVGPV	LGSQVGLMP(1)GSVGPV	Collagen alpha-2(V) chain	1430.736	18.5
1444.661	0.718	GLKGENGLPGENGAP	GLKGENGLP(1)GENGAP(1)	Collagen alpha-1(III) chain	1444.660	-0.6
1510.715	0.704	MFGGPGTASRPSSSR		Vimentin	1510.707	-5.2
1517.705	0.716	PPQEKAHDGGRYY		Collagen alpha-1(I) chain	1517.713	5.2
1715.777	0.707	FSPMLGEFVSETESR		Alpha Fibrinogen	1715.795	10.2
1762.866	0.722	VVQYSGTGQQRPERAS		Collagen alpha-1(VI) chain	1762.883	9.6
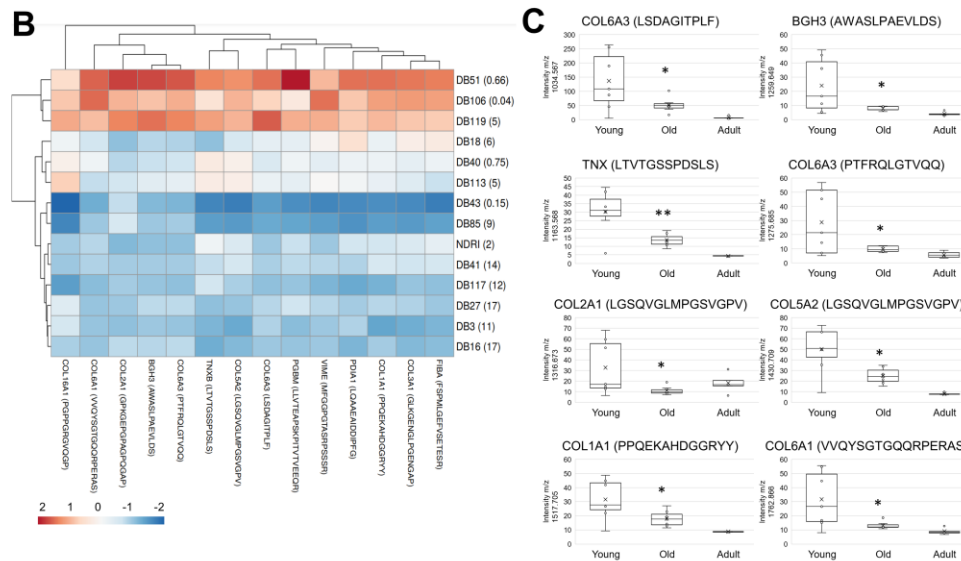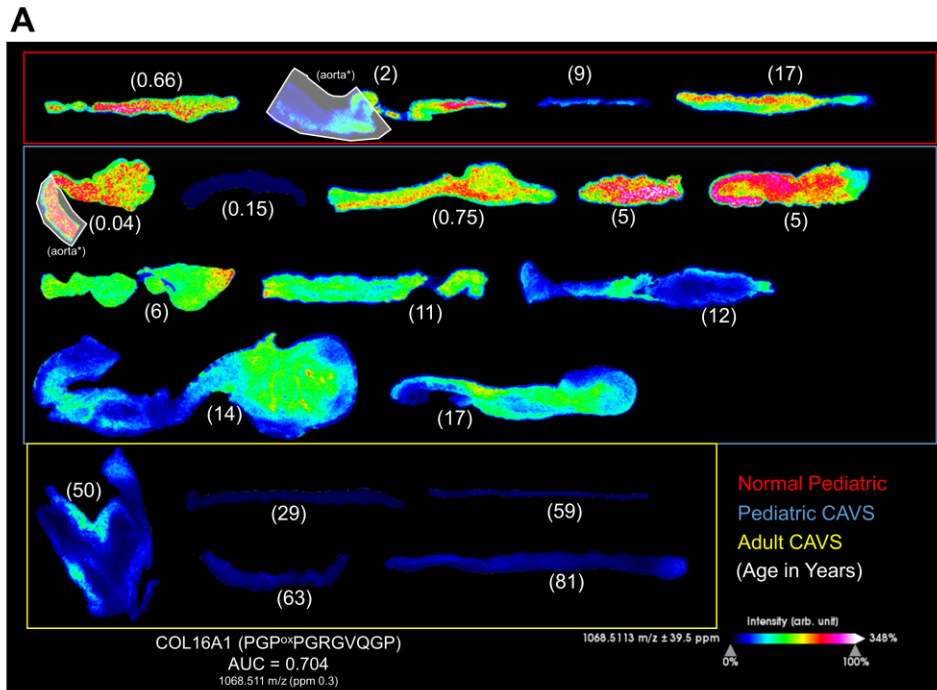
Figure 38: ECM Profiling shows Developmental Regulation within Aortic Valves. A) Representative image of a HYP containing collagen peptide (m/z 1068.511; COL16A1, PGPˣPGRGVQGP) that was identified to be differentially expressed between pediatric age groups, independent of disease. Note: HYP site requires confirmational proteomic studies. B) Hiearchical-clustering analysis of all peptides identified via ROC-AUC to be differentially expressed between pediatric patients (Table 12). These results show ROC-AUC identified peptides can unbiasedly cluster patients by pediatric age group. C) Boxplots of mean intensity for significantly differentially expressed peptides, as determined by Mann Whitney U-test (*p<0.05).

peptides (outlined in Fig. 38C) appear to be increased in the young pediatric population that decrease in expression as valve development progresses. One unexpected peptide of interest is m/z 1316.673 (COLα1(II), LGSQVGLMPGSVGPV). While collagen II is not the dominant fibril type collagen within cardiac tissues, there are early studies outlying its role in embryonic valve morphogenesis [304].

5.3.6 Conclusions

This Chapter outlines the application of MALDI-ECM-IMS to determine collagen sub-type regulation within localized regions of histologically defined collagen dysregulation. Similarly, large -omics datasets such as those acquired with this technique have the potential to unbiasedly classify valve samples dependent on pediatric fibrotic vs. adult fibrocalcific CAVS valve samples. However, more work needs to be done to investigate the subtle translational and post-translational regulation between normal pediatric and pCAVS AVs. This study shows that unique ECM peptides may be developmentally regulated within the aortic valve structure. Collagen subtypes within this study are known to interaction with proteoglycan families as well as elastin, as outlined above. This technique may be used together with multi-enzyme studies outlined in Chapter 4 to colocalize collagen subtypes directly with spatial regulated GAGs and elastin. Similarly, these studies lay the foundational work for those exploring cell-ECM interactions within AVs. These techniques that may be applied for future studies are outlined in detail within Chapter 7.

Defining unique peptides that correlate to RIFDs may aid in the discovery of molecular markers to be used clinically. Similar studies have been done targeting renal and myocardial, lung, and liver fibrosis via MRI, PET and CT imaging [250]. The long-term

goal of the studies outlined in this dissertation is to identify ECM biomarkers of pCAVS that may be targets for pharmacotherapeutic development to slow the disease progression. However, these same targets may be used to diagnose the disease before the onset of heart failure identified via irregular hemodynamics and electrophysiology, most commonly diagnosed by echocardiography and doppler [61]. Similarly, these ECM-targeted proteomics applications may be useful to correlate our finding here with on-tissue pCAVS profiles to future studies with serum-derived from patients, in order to develop minimally invasive diagnostics for the progression of fibrotic cardiac disease, potential before the onset of cardiac perturbances. Overall, this chapter outlines the value in localized proteomic studies of the ECM within valvular tissues.

Chapter 6: Evaluation of Therapeutic Collagen-Based Biomaterials in the Infarcted Mouse Heart by Extracellular Matrix Targeted MALDI Imaging Mass Spectrometry

This chapter outlines a proof-of-concept study using the developed ECM-targeted MALDI-IMS techniques towards biomaterial applications of fibrotic cardiac disease. In this study, we aimed to use MALDI-IMS to both 1) investigate the ability of this technique to distinguish between the spatial distribution of hydrogel injected collagen peptides as compared to endogenous mouse tissue; and 2) use MALDI-IMS and proteomics to explore the effects of therapeutic-based collagen hydrogels on endogenous remodeling of the infarcted mouse heart. The bulk of this chapter has been submitted as a manuscript in the Journal of the American Society for Mass Spectrometry and is under review at the time of submission of this dissertation.

6.1 Introduction

Collagen is a natural, degradable polymer found in the extracellular matrix (ECM) that is widely used in therapeutic biomaterial applications due to its biocompatibility, cell adhesion promotion, and cell permeability [305-307]. One application of biomaterials is in the treatment of myocardial infarction (MI), which if left untreated leads to the formation of non-contractile scar tissue and potentially heart failure [53, 55, 308, 309]. Collagen has been studied as a biomaterial for injectable hydrogels to repair heart tissue damage post-MI, with the goal of limiting scar formation [310]. A previous study took advantage of human collagen subtypes as a component of the injectable hydrogel [310]. However, recent literature suggests that peptides, as opposed to whole proteins, provide a promising therapeutic advantage, as full-length human collagen is difficult to synthesize and stabilize due to extensive post-translational modifications [311, 312]. For this reason, determining which peptides within the protein used in purified collagen protein hydrogels are most efficacious may contribute to more applicable therapeutics. Recent studies show that peptide-based biomaterials can mimic the function of their full-length protein counterparts,

are easier to produce, can be derived from human origin, reducing autoimmune effects, and can similarly contribute to structural cell-recognition motifs [313, 314].

Several imaging techniques have been developed over the years to analyze biomaterials in tissues. Fluorescence and MRI imaging techniques have been used to trace injected collagen *ex vivo* as well as *in vivo* at low penetrative depths [315, 316]. These techniques, however, require labeling of the injected material. Imaging Mass Spectrometry (IMS) can analyze the spatial distribution of molecules without labeling. Recent advances in this field have been applied to biomaterials research, using ionization techniques such as Secondary Ion MS (SIMS), Matrix Assisted Laser Desorption Ionization (MALDI), and Desorption Electrospray Ionozaion (DESI), amongst others [317]. These IMS techniques have been used to detect synthetic polymeric biomaterial and nanoparticles *in vitro* [317-320]. IMS is not only capable of analyzing the biomaterial itself, but also potential interactions with the treated tissue [321]. To date, however, the majority of studies have been on biomaterial surface analysis [317]. A soft-ionization technique, such as MALDI-IMS, is arguably one of the most appropriate methods for natural polymer detection *in situ* due to minimal fragmentation, allowing for more information from a complex substrate such as tissue.

MALDI-IMS is a robust technique that is able to identify endogenous or enzymatically derived peptides in tissue sections [322]. However, proteomics-based techniques to evaluate ECM-based biomaterial interactions in surrounding tissues have been limited due to poor detection of ECM proteins. This is due to their low abundance and inter- and intra-molecular crosslinking. Recently, our lab has developed a collagenase-based ECM-targeted MALDI-Imaging Mass Spectrometry (ECM-IMS) methodology that may be used sequentially with other enzymatic imaging strategies [39, 142, 145, 154-157]. In the current study, we utilize this method to elucidate the distribution

153

and therapeutic effects of collagen-based biomaterials on extracellular matrix remodeling in the infarcted heart, as well as identify potential therapeutic collagen peptides to be evaluated in future studies.

6.2 Materials & Methods
6.2.1 Materials and Chemicals

All solutions were prepared using double distilled or HPLC grade water, following all necessary safety and waste disposal regulations. Xylenes, 200 proof ethanol were purchased from Fisher Scientific (Pittsburgh, PA, USA). Acetonitrile, ammonium bicarbonate, calcium chloride, formic acid, and Trizma base were purchased from Sigma-Aldrich (St. Louis, MO, USA). PNGase F PRIME was purchased from N-Zyme scientific (Charleston, SC, USA). Collagenase type III (COLase3) (*C. histolyticum*) was purchased from Worthington Biochemical (Lakewood, NJ, USA).

6.2.2 Preparation and characterization of collagen hydrogel

Collagen hydrogels were prepared as previously described by McLaughlin et al.[310]. Brielfy, a 1% collagen solution was prepared by dissolving lyophilized recombinant human collagen type I or type III (rhCI and rhCIII, from Fibrogen) in 10 mL of ultra-pure ddH$_2$O. Chondroitin sulfate (CS; Wako), N-ethyl-N-(3-dimethylaminopropyl) carbodiimide (EDC) and N-hydroxysuccinimide (NHS) were added to produce a final mixture with a mass ratio of 1:4:0.5:0.3 for collagen:CS:NHS:EDC. Before the final step of the hydrogel preparation, after EDC/NHS crosslinkers have been added but before NaOH addition to a pH of 7.4, 20 µL of AlexaFluor 594-NHS conjugate (Thermofisher) was added to label the hydrogels (25 nmol of dye/gel). The materials were prepared on ice using an enclosed system that allows homogenous mixing.

154

6.2.3 Animal Experiments

All procedures were approved by the University of Ottawa Animal Care Committee and performed according to the National Institute of Health Guide for the Care and Use of Laboratory Animals. Myocardial infarction (MI) was induced in 8 to 9-week-old female C57BL/6 mice (Charles River) and treatment delivery was performed using an established protocol [323, 324]. Briefly, mice were anesthetized (2% isoflurane), intubated, and the heart was exposed via fourth intercostal thoracotomy. At 1-week post-MI (baseline), mice were randomly assigned to receive treatment of PBS (control), rhCI or rhCIII matrices, delivered in 5 equivolumetric intramyocardial injections (10μL each site, 50μL total) through a 25G needle using an ultrasound-guided closed-chest procedure. Mice were sacrificed by terminal anesthesia at 2 days post-treatment (9 days post-MI) and hearts were collected and frozen in OCT for histological sectioning.

6.2.4 Tissue Preparation and Histology

Frozen tissue sections of mouse hearts injected with AF594-labeled hydrogels or PBS (10 μm thick) were cut via cryostat. A section approximately 2.16 mm from the apex was used in the present study. Fresh frozen mouse heart tissue sections were fixed briefly in 4% paraformaldehyde and stained with DAPI counterstain (Sigma-Aldrich, St Louis, MO, USA). Sections were mounted with Dako Fluorescent mounting medium (Agilent Technologies, Santa Clara, CA, USA), coverslipped, and sealed with clear nail polish. High resolution digital captures were taken of IHC stained mouse heart sections before MALDI-IMS studies of the same slide. Slides are imaged using a Leica Aperio Versa slide scanner with the 20X objective for DAPI and AF594 signals ($\lambda_{excitation}$: 580nm; $\lambda_{emission}$: 625 nm).

For N-glycan and ECM peptide MALDI-IMS studies, FFPE tissues were prepared as previously described [154, 325]. Briefly, after staining, AF594-labeled hydrogel detection, and coverslip removal, tissues were cleared of potential remaining OCT and mounting media with the following washing steps: 1 min Xylene, 2x 1 min 100% ethanol, 1 min 95% ethanol, 1 min 70% ethanol, 2x 1 min HPLC water. Tissues were then antigen retrieved in Citraconic Buffer pH 3 and 10mM Tris pH 9 [154, 325]. Tissue sections were then digested with Collagenase Type III (COLase3) after deglycosylation with PNGaseF (N-Zyme Scientifics) for MALDI-IMS experiments [145, 155]. Enzyme solutions were sprayed with a TM Sprayer M3 (HTX Imaging, Chapel Hill, NC, USA) under the following parameters: 15 passes, crisscross pattern, 3.0 mm track spacing, velocity of 1200 mm/min, and a dry time of zero.

COLase3 treated samples were digested in ≥80% relative humidity at 37.5°C for 5 hours. Matrix was 7 mg/mL solution of alpha-cyano-4-hydroxycinnamic acid (CHCA) solution, prepared in 50% acetonitrile and 1.0% TFA, spiked with a standard of 200 femtomole/L [Glu1]-fibrinopeptide B human (GluFib) (Sigma-Aldrich, St Louis, MO, USA). CHCA automatic spray conditions included: 79°C, 10 psi, 70 µL/min, 1300 velocity, and 14 passes with a 2.5 mm offset. Slides for peptide imaging were rapidly dipped (<1 second) in cold 5mM ammonium phosphate and immediately dried in a desiccator.

6.2.5 MALDI-Imaging Mass Spectrometry

MALDI-IMS analysis was via a 7.0 Tesla solariX™ Legacy FT-ICR (Bruker Scientific, LLC) operated in positive ion broadband mode over m/z range 600-2500. Laser settings used were 200 shots/pixel with a 75 µm stepsize. A lock mass of 1570.6768 (GluFib peptide) was used. Images were visualized in FlexImaging v5.0 and analyzed using SCiLS (Bruker Scientific). All images shown are normalized to total ion current.

Spectra shown were analyzed using mMass version 5.5.0. A filter of 10 ppm mass error was used for this study. Target peptides were were further fragmented by on-tissue MALDI-MS/MS and analyzed for ion mobility to confirm post-translational modification site occupancy via CID on a timsTOF fleX as previously described (Bruker Scientific, LLC) [145].

6.2.6 Proteomic Tissue Preparation

Tissue was prepared as previously described [39]. Briefly, tissues were antigen retrieved and deglycosylated as described above. One slide with 6 serial sections per slide was used per treatment group. Tissue was scraped off the slide and ultrasonicated at 50% energy (Fisherbrand 120 sonic dismembrator; Fisher Scientific, Pittsburgh, PA, USA) for 2 min each in 10 mM ammonium bicarbonate 1 mM $CaCl_2$ (pH 7.4). Tissues were incubated with 2 µg of Collagenase Type III overnight and centrifuged to collect supernatant for proteomic analysis. Samples were purified by C18 STAGE tip (Pierce Biotechnology, Waltham, MA) according to manufacturer's protocol. STAGE-tip eluate was dried down via speed vac and resuspended in mobile phase A (HPLC water).

6.2.7 Proteomics

Peptides were analyzed data dependent acquisition on a timsTOF fleX equipped with a nano-HPLC (nano-Elute, Bruker Daltonics). Peptides were loaded onto a trap column and separate on a 75 µm x 25 cm classic pulled tip column (Aurora C18 1.6um particles) at 50°C. The gradient was from 2 to 80% solvent B over 105 min, where solvent A was HPLC water and solvent B was acetonitrile. Parallel accumulation serial fragmentation (PASEF) scan mode and TIMS were enabled in positive ion mode. TIMS accumulation time was fixed to 2 ms with a cycle time of 100 ms, covering a mass range of 100–1700 m/z and a $1/K_0$ range of 0.6-1.6 Vs/cm^2.

Data was searched using MSFragger with IonQuant [326] (v3.2; Fragpipe v15.0) against the mouse extracellular matrix database (downloaded February 26, 2021), a subset database of 2976 entries with keywords used (collagen, elastin, aggrecan, gelatin, osteonectin, perlecan, plasminogen, and fibronectin). Parameters included unspecified proteolytic enzyme, precursor mass tolerance of ± 20 ppm, and fragment mass tolerance ± 0.8 Da. Methionine oxidation, and proline hydroxylation were included as variable modifications. Proteins were identified with FDR ≤ 0.05 and at least two peptides. Scaffold v5 was used for protein and peptide level analyses.

6.2.8 Bioinformatics

Normalized peak intensities were evaluated by ANOVA and Mann Whitney U test, correcting for multiple comparisons (IBM SPSS Statistics, version 25). A Type I error probability of ≤0.1 was used to evaluate the significance of the result. For this proof of principle study, p-values of ≤0.1 are reported as trending to significance and p-values of ≤0.05 were used determine significant results. AUC p-values are reported as the maximal discriminative power at the centroid. Peaks reported as significantly regulated were identified via SCiLS (v. 2017a). Exported peak intensities are visualized as heatmaps after natural log transformation with MultiExperiment Viewer (http:/mev.tm4.org) [327].

6.2.9 Peptide synthesis

GRP^{ox}GEVGP^{ox}P, GRPGEVGP^{ox}P^{ox}, and GRP^{ox}GEVGPP^{ox} peptides were synthesized using the Liberty Blue (CEM) automated microwave peptide synthesizer (where P^{ox} is HYP). Fmoc protected amino acids were purchased from CEM. HYP were purchased from BACHEM. To 2-Chloro trityl resin (ProTideCl-TCP(Cl) resin, CEM), the first aminoacid was loaded under microwave (90ºC), DIEA (1M) and KI (0.125M) for 10 minutes with twice coupling. Next, Fmoc deprotection was carried out with 20% piperidine

at 90°C for 60s while standard coupling cycles using DIC/Oxyma Pure were run at 90°C for 240s. Peptides were cleaved from the resin and deprotected with 92.5/2.5/2.5/2.5% v/v TFA/TIS/EDT/H2O at 42°C for 30 minutes and then precipitated in -20°C diethyl ether. Crude peptides were dried under vacuum overnight and purified by RP-HLPC in a Waters 1525EF semi-preparative system with a 21.6x250 mm C18 column at 20 mL/min. Peptide purity and identity was confirmed via RP-UPLC-UV/MS in a Waters Acquity UPLC Xevo TQD using a 2.1x100 mm UPLC BEH C8 column. A purity of 95% was determined through UV peak analysis. The theorical monoisotopic mass for the 3 peptides is equal to 896.4 Da. For the peptide GRP^{ox}GEVGP^{ox}P mass spectrometry results gave the most abundant peaks of 449.3 m/z [M-2H$^+$] and 897.4 m/z [M-H$^+$] for an experimental mass of 896.4 Da. For the peptide GRPGEVGP^{ox}P^{ox} mass spectrometry results gave the most abundant peaks of 449.4 m/z [M-2H$^+$] and 897.6 m/z [M-H$^+$] for an experimental mass of 896.6 Da. For the peptide GRP^{ox}GEVGPP^{ox} mass spectrometry results gave the most abundant peaks of 449.3 m/z [M-2H$^+$] and 897.4 m/z [M-H$^+$] for an experimental mass of 896.4 Da (**Fig. 46**).

6.3 Results & Discussion
6.3.1 Study design and hydrogel region of interest analysis

In this study, mice with myocardial infarction (MI) were treated at 7 days post-MI with either a Collagen Type 1 (rhCI) or a Collagen Type 3 (rhCIII) hydrogel [310]. Two days after hydrogel treatment, mouse hearts were harvested, frozen, and sectioned for tandem histology and MALDI-IMS studies (**Fig. 39**). Injected human collagen hydrogels were fluorescently labeled prior to injection and analyzed via immunofluorescence. Microscopy based analysis of tissues identified the potential site of hydrogel injection as well as the infarcted region, the border zone (area immediately adjacent to the infarct),
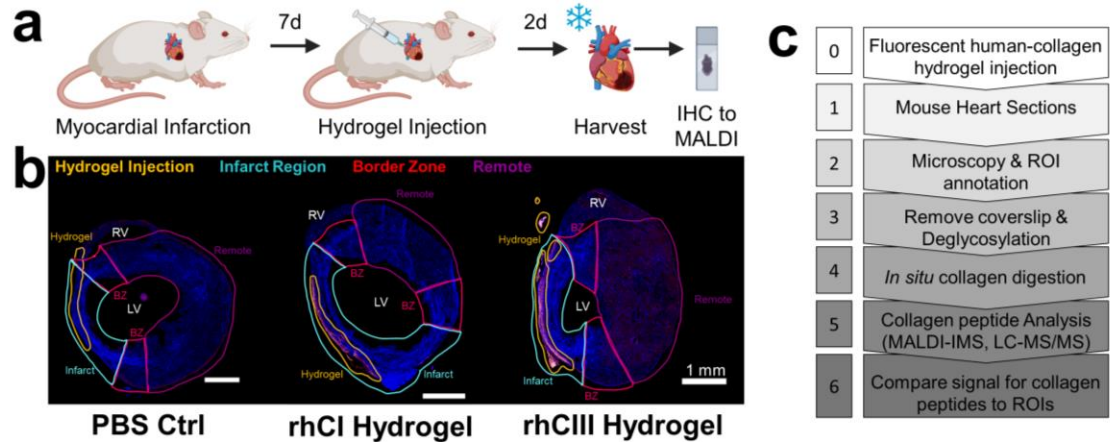
Figure 39: Mouse model study design and multimodal imaging mass spectrometry workflow. a. Timeline of mouse model. 9-week old mice were induced with myocardial infarction. 7-days post-surgery, collagen hydrogel or PBS control was injected into the left ventricle. 2-days post injection, hearts were harvested. **b.** Region of interest (ROI) annotation of heart sections in relation to fluorescently labeled human hydrogel signal. BZ: Border Zone; LV: Left Ventricle; RV: Right Ventricle. Scale bar shown is 1 mm. **c.** Simplified workflow of tandem high resolution fluorescent microscopy and collagenase-based MALDI-IMS and LC-MS/MS experiments.
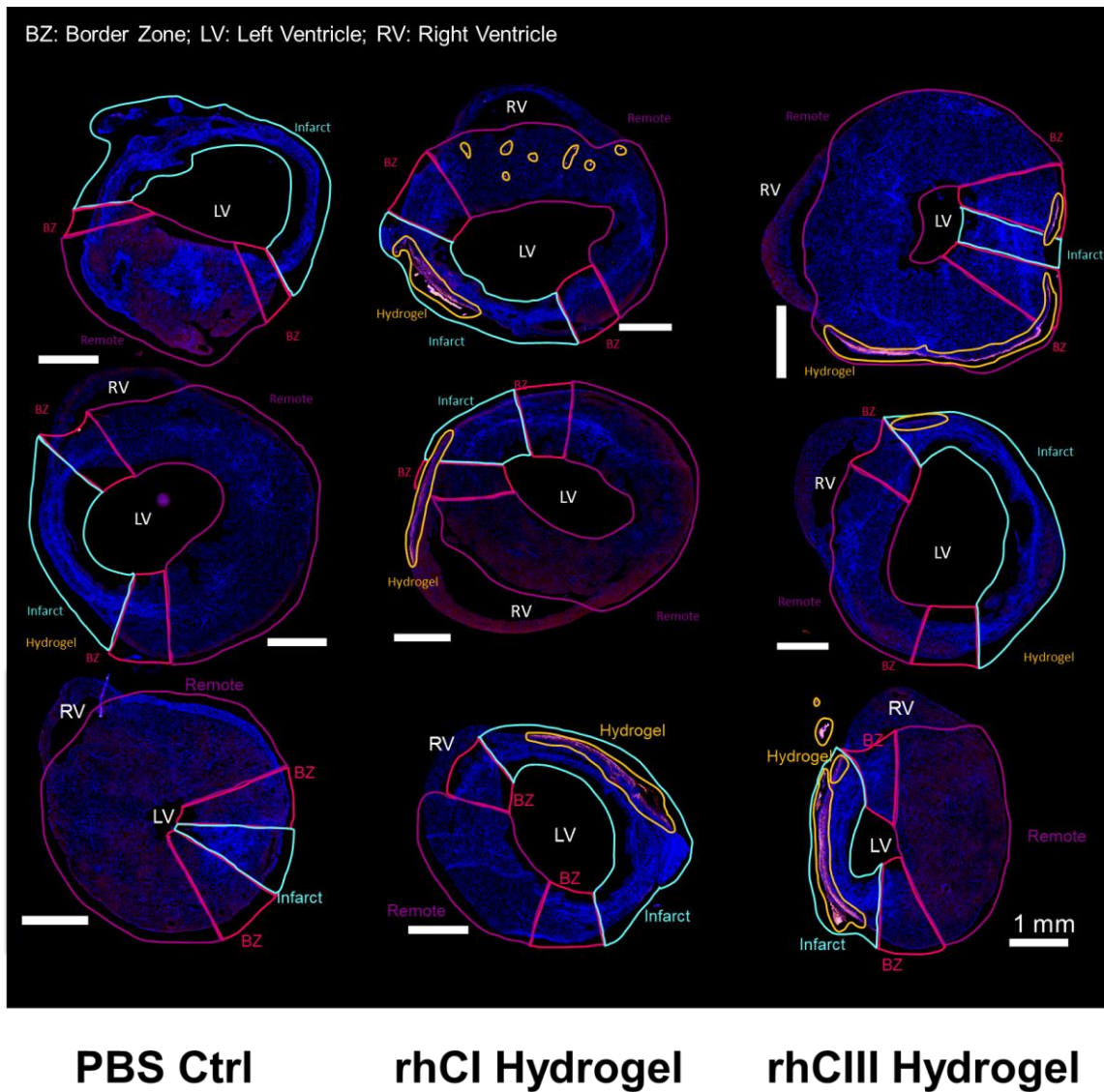
Figure 40: Representative sections with ROI annotations from all mice included in this study (n=3 per treatment group). All mice were confirmed to have a Left Ventricular Ejection Fraction of <50% for initial injury. representative annotated tissue section for each biological replicate shown across three patient categories: PBS injected control, rhCI hydrogel, and rhCIII hydrogel. Annotated regions include HIS (hydrogel injection site), Infarct (region of myocardial infarction, identified via previous studies (McLaughlin, 2019); BZ (border zone, region immediately adjacent to infarct), and remote (region furthest from infarct). LV: Left Ventricle. RV: Right Ventricle. Scale bar is 1 mm.

and the remote region (intact myocardium) (**Fig. 39-40**). These microscopy-based observations were used to create regions of interest (ROIs) for downstream MALDI-IMS analysis of collagen and other ECM peptides (ECM-IMS) (**Fig. 39c**). While downstream peak-picking was performed unbiased of microscopy-based observations, ROIs were used to further evaluate collagen-type peaks of interest in relation to hydrogel specificity.

6.3.2 Fibrillar collagen homology sequences are more abundant in hydrogel injection sites

A challenge of this study is that humans and mice have 93-94% homology between collagen sequences (for the collagen subtypes used for hydrogel injections: collagen α1(I), α2(I), and α1(III). To determine specificity of hydrogel-derived human collagen sequences, the localization capability of MALDI-IMS was leveraged with multiplexed histopathology-based studies in conjunction with on-tissue peptide sequencing via MALDI-MS/MS. Overall, 22 Collagen Type I putative peptides (9 COLα1(I), and 13 COLα2(I)) were identified; 11 of all collagen type I putative peptides identified contained sequences homologous between human and mouse (**Fig. 41a, Table 13**). Additionally, ECM-IMS analysis identified 18 human COLα1(III) peptides, with only 5 being homologous between human and mouse sequences (**Fig. 41a, Table 13**). Amongst these, pathological ROI analysis identified four collagen type I peaks that were differentially regulated in rhCI-injected hearts, specifically at the infarct ROI (**Table 13**). Similarly, two COLα1(III) peaks were differentially expressed between PBS-control and rhCIII-injected hearts (**Table 13**). Two representative images of Collagen Type 1 in rhCI hearts and COLα1(III) in rhCIII hearts are shown as compared to PBS injected controls (**Fig. 41b,d** respectively).

Figure 41: Human collagen peptides with mouse homology are more abundant in hydrogel injection sites. a. Total number of putative human peptide identifications from hydrogel injected tissues as a function of collagen subtype for collagens injected. **b.** Representative collagen type 1 peaks as visualized in rhCI injected hearts as compared to PBS controls. Average intensity levels measured between all samples studied are shown in **(c). d.** Representative collagen type 3a1 peaks as visualized in rhCIII injected hearts as compared to PBS controls. Average intensity levels measured between all samples studied are shown in **(e).** n=3. Six tissue sections were visualized for each biological replicate. Different representative samples are used to show reproducibility across n's.

Table 13: MALDI-IMS mapped human hydrogel peptides, showing both peptides that are unique to the human proteome as well as those that share mouse and human homology sequences. For those with human specific sequences, the corresponding mouse peptide and m/z is shown.

Protein	Sequence	HYP	Centroid [m/z]	Human + Mouse Homology/Isobaric	Human Specific	Corresponding Mouse m/z (Sequence)
COL3A1	GPPoxGPTGPG	+	752.3231			766.3730 (GPPGPTGPA)
COL3A1	LQGLPoxGTG	+	758.4520	+		758.4520 (LQGIPGTG)
COL3A1	GPPoxGLAGAPox	+	768.3922			798.3992 (GPPGTAGIP)
COL3A1	GPAGFPoxGAPox	+	802.3981	+		
COL3A1	GPPoxGINGSPox	+	827.4826			828.3482 (GPPGNNGSP)
COL3A1	GPPoxGTAGFPox	+	832.4206	+		
COL3A1	GPPoxGEPoxGQA	+	841.4255	+		
COL3A1	GPAGIPoxGFPox	+	844.4086		+	862.3764 (GPAGMPoxGFPox)
COL3A1	GPAGIPoxGFPox	+	844.4096			862.3764 (GPAGMPGFP)
COL3A1	GAPoxGFRGPA	+	845.4069		+	845.4264 (GPSGFRGPA)
COL1A2	GKEGPVGLPox	+	869.4550	+		
COL1A1	GRPoxGEAGLPox	+	885.4538	+		
COL1A1	GSPoxGFQGLPox	+	891.4158	+		
COL1A1	GRPoxGEVGPoxP	+	897.4448	+		
COL1A2	GERGVVGPQ		898.4464	+		
COL1A1	GQRGVVGLPox	+	898.5197	+		
COL1A2	GPPoxGFQGLPox	+	901.4262	+		
COL3A1	VAVGGLAGYPox	+	919.4372		+	
COL3A1	GQPoxGVMGFPox	+	921.4389			
COL1A2	GNIGPVGAAGAPox	+	996.4044		+	998.4901 (GNIGPTGAAGAP)
COL1A1	GPPoxSAGFDFS	+	997.4646		+	999.4054 (GPPSGGYDFS)
COL3A1	IAGITGARGLA		999.5115	+	+	999.5115 (IAGLTGARGLA)
COL1A2	GARGSDGSVGPV		1058.5198	+		
COL3A1	SGVAVGGLAGYPox	+	1063.5199		+	
COL3A1	GPLGIAGITGAR		1082.6426	+	+	1082.6426 (GPLGLAGITGAR)
COL3A1	GPoxPGTAGFPoxGSPox	+	1089.5523	+		
COL1A2	GSRGFPoxGADGVA	+	1106.4586	+		
COL1A2	GRTGEVGAVGPoxP	+	1112.5001		+	
COL1A1	GPPSAGFDFSF		1128.5681		+	1130.4789 (GPPSGGYDFSF)
COL1A2	FGYDGDFYR		1139.4483		+	1137.5000 (FGFEGDFYR)
COL3A1	GPLGIAGITGARG		1139.6670	+	+	1139.6670 (GPLGLAGITGARG)
COL1A1	GPPGPPSAGFDF		1145.4746		+	1147.5055 (GPPGPPSGGYDF)
COL1A2	GGGYDFGYDGDF		1269.5981		+	1267.4902 (GGGYDFGFEGDF)
COL1A1	GAVGPAGKDGEAGAQ		1284.5619	+		
COL1A2	GPoxKGEIGAVGNAGPA	+	1310.6298		+	1362.7012 (GPKGELGPVGNPGPA)
COL3A1	GPLGIAGITGARGLA		1323.8029	+	+	1323.8029 (GPLGLAGITGARGLA)
COL1A2	VSGGGYDFGYDGDF		1455.6838		+	1453.5907 (VSGGGYDFGFEGDF)
COL1A1	GPPSAGFDFSFLPQ		1466.7614		+	1468.6743 (GPPSGGYDFSFLPQ)
COL1A2	GPAGARGSDGSVGPVGPA		1508.7727	+		
COL1A2	GPDGNKGEPoxGVVGAVGTAGPS	+	1838.8609		+	1726.7991 (GPDGNKGEAGAVGAPGSAGAS)

Table 14: Significantly Differentially Expressed human hydrogel derived peptides (ROC AUC); infarct ROI comparisons.

Groups	ROI	Protein	Peptide	Centroid [m/z]	AUC
rhCI-Ctrl	Infarct	COL1A1	GRP^{ox}GEVGP^{ox}P	897.4448	0.605
rhCI-Ctrl	Infarct	COL1A2	GSRGFP^{ox}GADGVA	1106.4586	0.668
rhCI-Ctrl	Infarct	COL1A1	GPPSAGFDFSF	1128.5681	0.689
rhCI-Ctrl	Infarct	COL1A2	GPAGARGSDGSVGPVGPA	1508.7727	0.673
rhCIII-Ctrl	Infarct	COL3A1	GPP^{ox}GTAGFP^{ox}	832.4206	0.610
rhCIII-Ctrl	Infarct	COL3A1	GP^{ox}PGTAGFP^{ox}GSP^{ox}	1089.5523	0.671

Average intensity levels of peaks shown in representative images were quantified across all tissue sections studied (**Fig. 41c,e**). Overall, ROI annotation and differential intensity distributions were able to identify putative peptides corresponding to the site of hydrogel injections.

6.3.3 ECM-IMS identifies human-specific collagen sequences in hydrogel injected mouse hearts

An example of a significantly increased peptide identified that aligned uniquely to the collagen α1(I) human sequence is shown in Figure 3 (rhCI 1128.5681 m/z; GPPSAGFDFSF). ECM-IMS analysis was also able to identify the mouse peptide corresponding to this human sequence (1130.4789 m/z, +1.9108 m/z; GPPS**G**G**Y**DFSF) (**Fig. 42a-b**). As can be seen in Figure 3, the peak corresponding to the mouse peak is equally present in the PBS control and rhCI hydrogel tissue. However, the corresponding human specific peptide is significantly more abundant in the rhCI-injected heart (AUC at infarct 0.689, p-value 0.013). A similar result is seen for a COLα1(III) peptide sequence in the rhCIII-treated heart (AUC at infarct, 0.923, p-value 0.008) (**Fig. 42c-d**). Importantly, m/z 1128 and m/z 844 were not identified in the mouse-database identified peptides via LC-MS/MS (**Fig 43, Table 15**). Finding these human-proteome unique peptides provides further evidence of biomaterial localization via MALDI-ECM-IMS. While fluorescent label-based microscopy techniques may be able to identify the site of injection, ECM-IMS identifies unique peptides within the hydrogel that may be contributing to endogenous ECM remodeling and improved cardiac function, as seen in tandem studies on the same mice [310].
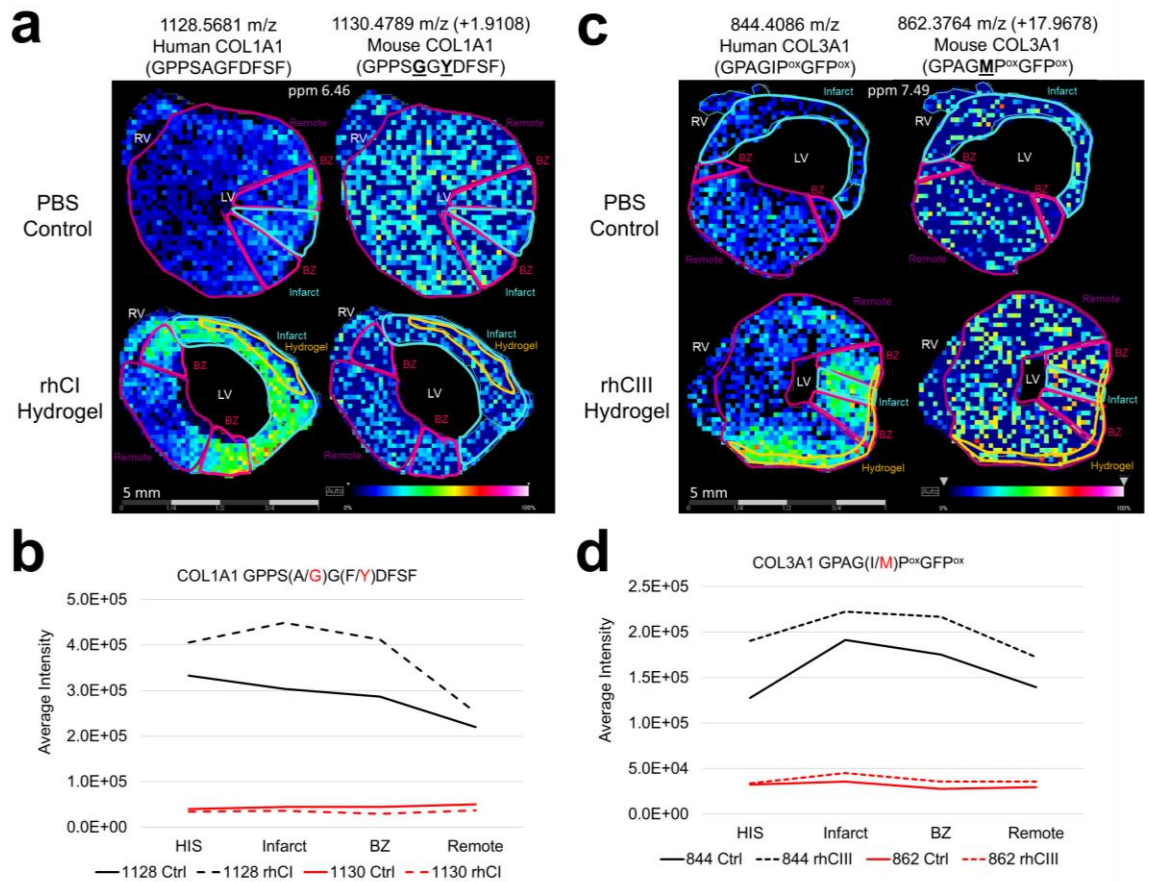
Figure 42: Collagen peptides unique to human proteome have differential distribution to corresponding mouse peptides. Species differentiating amino acids are underlined in bold within the sequence. **a.** Representative collagen type 1 peaks as visualized in rhCI injected hearts as compared to PBS controls are shown for the human-specific collagen sequence (left) and corresponding mouse sequence (right). Average intensity levels measured between all samples studied are shown in **(b). c.** Representative collagen type 3a1 peaks as visualized in rhCIII injected hearts as compared to PBS controls are shown for the human-specific collagen sequence (left) and corresponding mouse sequence (right). Average intensity levels measured between all samples studied are shown in **(d).** n=3. Six tissue sections were visualized for each biological replicate. Different representative samples are used to show reproducibility across n's. Note: Location of hydroxyproline (P^{ox}) are ambiguous and require further validation.
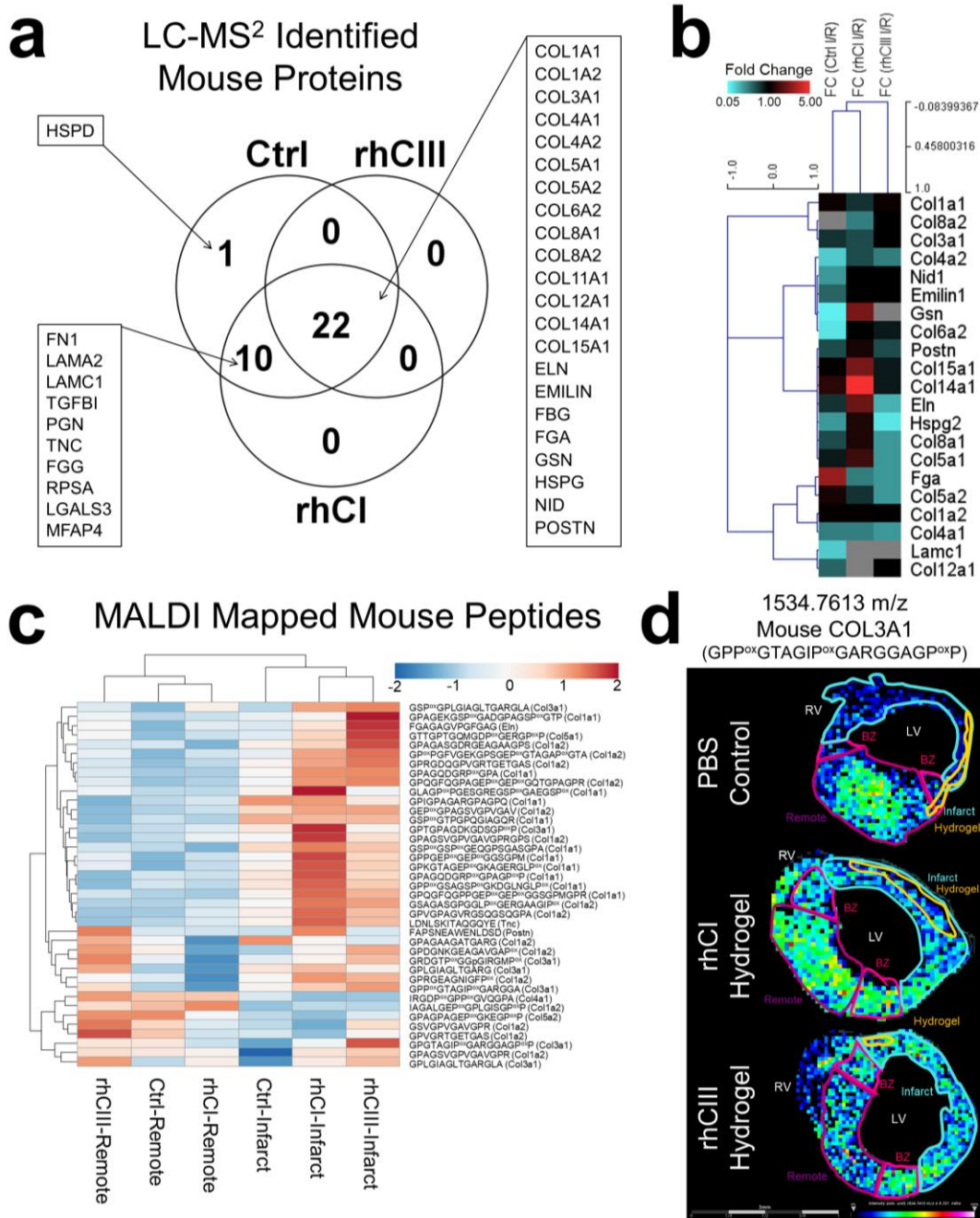
Figure 43: Collagen targeted proteomics investigates endogenous mouse ECM remodeling. **a.** Venn Diagram showing the number of proteins identified in PBS control, rhCI hydrogel, and rhCIII hydrogel samples. **b.** Hierarchical clustering of protein level Fold Change (Infarct/Remote) values for each treatment group. **c.** Hierarchical clustering of LC-MS/MS identified mouse peptides mapped via MALDI-IMS studies. ROI intensity for infarct and remote is shown for each treatment group. **d.** Representative image of a COL3A1 peptide that was differentially abundant in PBS Ctrl vs hydrogel treatment, mapped via MALDI-IMS.

168

Table 15: MALDI-mapped endogenous mouse ECM peptides identified via LC-MS/MS proteomics. *Mouse peptides that share homology sequences with human peptides (+) were mapped via MALDI-ECM-IMS, but were not used for the endogenous mouse differential expression experiments (**Fig. 4c**). Lowercase 'm' represents oxidation of Methionine.

Centroid [m/z]	Protein name	Alternate IDs	Peptide sequence	Human Homology*	Peptide identification probability	Discriminant Score	Hyperscore	Nextscore
1,013.51	Collagen alpha-2(I) chain	Col1a2	GPAGAAGATGARG		99.70%	4.96	23.1	14.1
1052.5848	Collagen alpha-2(I) chain	Col1a2	GSVGPVGAVGPR		99.70%	3.91	25.5	13.3
1064.5161	Elastin	Eln	FGAGAGVPGFGAG		99.60%	4.55	25.9	15.8
1082.6319	Collagen alpha-1(I) chain	Col1a1	IAGQRGVVGLP^{ox}	+	99.40%	3.07	25.5	14.6
1088.5332	Collagen alpha-2(I) chain	Col1a2	GPVGRTGETGAS		99.70%	4.49	23.5	12.6
1095.5181	Collagen alpha-1(I) chain	Col1a1	GPAGQDGRP^{ox}GPA		99.50%	4.37	22.3	18.6
1139.6534	Collagen alpha-1(III) chain	Col3a1	GPLGIAGLTGARG		99.70%	5.68	32.5	19.9
1154.6056	Collagen alpha-2(I) chain	Col1a2	GKEGPVGLP^{ox}GID	+	99.60%	4.27	24.5	16.8
1179.5577	Collagen alpha-1(I) chain	Col1a1	GARGQAGVmGFP^{ox}	+	98.90%	3.45	22.1	13.8
1187.5806	Collagen alpha-2(I) chain	Col1a2	GPRGEAGNIGFP^{ox}		99.70%	4.28	27.4	17.1
1229.5912	Collagen alpha-1(I) chain	Col1a1	GFP^{ox}GERGVQGPP^{ox}	+	98.30%	3.78	28.5	26.7
1231.5954	Gelsolin	Gsn	LVADENPFAQGA	+	99.70%	5.38	28.1	14.9
1266.6327	Collagen alpha-2(I) chain	Col1a2	GEP^{ox}GPAGSVGPVGAV		98.80%	3.62	27.8	27.8
1267.6393	Collagen alpha-1(III) chain	Col3a1	GPP^{ox}GTAGIP^{ox}GARGGA		98.40%	3.47	22.4	20.2
1277.6962	Collagen alpha-2(I) chain	Col1a2	GPAGSVGPVGAVGPR		99.40%	4.32	32.3	18
1283.6340	Collagen alpha-2(I) chain	Col1a2	GPAGARGSDGSVGPV	+	97.60%	3.77	24.2	15.1
1302.6916	Collagen alpha-1(I) chain	Col1a1	GPIGPAGARGPAGPQ		99.70%	6.91	32.5	15.1
1311.5968	Collagen alpha-1(I) chain	Col1a1	GPAGFAGPP^{ox}GADGQP	+	99.10%	2.94	27.1	27.1
1312.6131	Collagen alpha-2(I) chain	Col1a2	GPDGNKGEAGAVGAP^{ox}		97.10%	3.67	22.9	14.8
1323.7746	Collagen alpha-1(III) chain	Col3a1	GPLGIAGLTGARGLA		99.50%	4.99	24.2	16.3
1325.5973	Collagen alpha-1(III) chain	Col3a1	GPTGPAGDKGDSGP^{ox}P		97.80%	3.73	23.3	23.3
1349.6336	Collagen alpha-2(V) chain	Col5a2	GPAGPAGEP^{ox}GKEGP^{ox}P		99.70%	4.83	23.7	23.7
1349.6812	Collagen alpha-1(IV) chain	Col4a1	IRGDP^{ox}GPP^{ox}GVQGPA		99.00%	4.2	30.8	26.5
1354.5584	Collagen alpha-1(I) chain	Col1a1	GPPGEP^{ox}GEP^{ox}GGSGPM		99.70%	5.17	32.8	28.2
1362.6401	Collagen alpha-1(I) chain	Col1a1	GPAGQDGRP^{ox}GPAGP^{ox}P		99.10%	4.41	25.4	25.4
1383.6689	Collagen alpha-2(I) chain	Col1a2	GLP^{ox}GADGRAGVMGP^{ox}P	+	99.50%	4.52	27.6	27.6
1395.6979	Collagen alpha-1(I) chain	Col1a1	GSP^{ox}GTPGPQGIAGQR		99.70%	5.37	26.7	17.7
1399.6638	Collagen alpha-2(I) chain	Col1a2	GLP^{ox}GADGRAGVmGP^{ox}P	+	99.70%	6.07	27.8	27.8
1400.6444	Collagen alpha-2(V) chain	Col5a2	GPNGEQGSAGIP^{ox}GPF	+	99.70%	3.36	22.5	17.4
1407.7594	Collagen alpha-2(I) chain	Col1a2	GPRGEVGLP^{ox}GLSGPV	+	99.70%	4.13	34.9	22.2
1421.6481	Collagen alpha-2(I) chain	Col1a2	GmTGFP^{ox}GAAGRTGP^{ox}P	+	97.90%	3.41	19.4	19.4
1442.7060	Collagen alpha-1(I) chain	Col1a1	GLQGMP^{ox}GERGAAGLP^{ox}	+	98.90%	4	25.9	21.4
1472.6915	Collagen alpha-1(III) chain	Col3a1	GRDGTP^{ox}GGP^{ox}GIRGMP^{ox}		99.70%	5.37	26.8	24.7
1484.6726	Collagen alpha-2(I) chain	Col1a2	GPAGASGDRGEAGAAGPS		99.70%	7.06	34.4	14.3
1508.7454	Collagen alpha-2(I) chain	Col1a2	GPAGARGSDGSVGPVGPA	+	99.60%	4.9	37.3	20.7
1518.8025	Collagen alpha-2(I) chain	Col1a2	GPAGSVGPVGAVGPRGPS		99.70%	6.86	29.4	15.6
1524.7768	Collagen alpha-2(I) chain	Col1a2	GAAGATGARGLVGEP^{ox}GPA	+	99.70%	8.82	44.5	39.6
1528.6513	Collagen alpha-1(I) chain	Col1a1	GSP^{ox}GSP^{ox}GEQGPSGASGPA		99.70%	5.43	33.3	24.4
1534.7613	Collagen alpha-1(III) chain	Col3a1	GPP^{ox}GTAGIP^{ox}GARGGAGP^{ox}P		99.70%	6.27	32.1	32.1
1534.8116	Collagen alpha-2(I) chain	Col1a2	IAGALGEP^{ox}GPLGISGP^{ox}P		99.70%	4.83	44.9	42.4
1566.7035	Collagen alpha-1(I) chain	Col1a1	GPP^{ox}GP^{ox}AGEKGSP^{ox}GADGPA	+	98.90%	3.38	25.2	22.9
1578.7985	Collagen alpha-2(I) chain	Col1a2	GPVGPAGVRGSQGSQGPA		97.20%	2.79	17.2	11.1
1579.7964	Tenascin	Tnc	LDNLSKITAQGQYE		99.70%	10.5	34.7	13.2
1580.8759	Collagen alpha-1(III) chain	Col3a1	GSP^{ox}GPLGIAGLTGARGLA		99.20%	4.25	22.7	22.7
1584.7327	Collagen alpha-1(III) chain	Col3a1	GSP^{ox}GGKGEMGPAGIP^{ox}GAP^{ox}	+	97.50%	3.49	26.3	24.5
1585.7720	Collagen alpha-1(I) chain	Col1a1	GANGAP^{ox}GIAGAP^{ox}GFP^{ox}GAR	+	99.70%	3.8	24.2	16.4
1594.6656	Periostin	Postn	FAPSNEAWENLDSD		99.70%	7.46	33	16.4
1625.7770	Collagen alpha-1(I) chain	Col1a1	GPP^{ox}GSAGSP^{ox}GKDGLNGLP^{ox}		98.00%	3.71	24.3	22.1
1644.7140	Collagen alpha-2(I) chain	Col1a2	FQGPAGEP^{ox}GEP^{ox}GQTGP^{ox}A	+	99.70%	4.79	24.7	23
1672.7752	Collagen alpha-2(I) chain	Col1a2	GPP^{ox}GMTGFP^{ox}GAAGRTGP^{ox}P	+	99.70%	5.14	24.4	24.4
1674.9177	Collagen alpha-1(V) chain	Col5a1	GPP^{ox}GEVIQPLPIQASR	+	99.70%	5.87	28.1	25.9
1698.8157	Collagen alpha-2(I) chain	Col1a2	GPRGDQGPVGRTGETGAS		99.00%	4.49	20.6	11.6
1699.8184	Collagen alpha-2(I) chain	Col1a2	GSRGLP^{ox}GADGRAGVmGP^{ox}P	+	99.70%	5.25	27.1	27.1
1710.8774	Collagen alpha-1(I) chain	Col1a1	GPKGTAGEP^{ox}GKAGERGLP^{ox}		99.70%	8.41	33	16.9
1743.7608	Collagen alpha-1(V) chain	Col5a1	GTTGPTGQMGDP^{ox}GERGP^{ox}P		99.70%	4.4	20.7	20.7
1767.8624	Collagen alpha-2(I) chain	Col1a2	GSAGASGPGGLP^{ox}GERGAAGIP^{ox}		99.70%	5.26	31.4	22.2
1795.8098	Collagen alpha-1(I) chain	Col1a1	GPAGEKGSP^{ox}GADGPAGSP^{ox}GTP		99.70%	4.95	24.7	24.7
1908.8939	Collagen alpha-1(I) chain	Col1a1	GEAGKP^{ox}GEQGVPGDLGAP^{ox}GPS	+	99.10%	4	26.9	26.9
1913.8475	Collagen alpha-1(I) chain	Col1a1	GLAGP^{ox}PGESGREGSP^{ox}GAEGSP^{ox}		98.40%	2.73	17.7	17.7
2142.9943	Collagen alpha-2(I) chain	Col1a2	GP^{ox}PGFVGEKGPSGEP^{ox}GTAGAP^{ox}GTA		99.70%	8.73	34.9	34.9
2278.0489	Collagen alpha-2(I) chain	Col1a2	GPQGFQGPAGEP^{ox}GEP^{ox}GQTGPAGPR		98.80%	3.59	39.9	32.8
2279.0152	Collagen alpha-1(I) chain	Col1a1	GPQGFQGPPGEP^{ox}GEP^{ox}GGSGPMGPR		99.00%	3.18	37.6	29

6.3.4 On-tissue MALDI tandem MS peptide sequencing provides evidence towards identifications and PTM site occupancy

Within the differentially regulated COLα1(I) peptides identified, one peptide had potential for differential HYP sites. HYP is a post-translational modification necessary for collagen triple helix structural stability. The putative HYP containing peptide, with a COLα1(I) peak at m/z 897.4448 (GRP^{ox}GEVGP^{ox}P, where P^{ox} is HYP; AUC = 0.686, p-value 0.018); this peptide has one hydroxylated proline, with three potential variants at isobaric peaks. To identify fragments associated with each HYP variant, on-tissue fragmentation was performed MALDI MS/MS to identify specific fragments relating to each variant (**Fig. 44a-b**). On-tissue, the primary HYP variant identified was in proline positions 1 and 2 (1,2; GRP^{ox}GEVGP^{ox}P), with 17 unique fragment peaks out of the 30 peaks identified. However, this experiment showed a mix of peptide variants, with 1,3 and 2,3 variants also being identified (**Fig. 44b**)

HYP site occupancy in the hydrogel-derived 897 m/z peptide were putatively identified but were investigated further using synthesize peptide standards (**Fig. 44c-e**). The three synthesized peptide variant standards were also investigated via trapped ion mobility, to distinguish the three isoforms of the 897 m/z peptide by their collisional cross-section (**Fig. 44f**). An additional unmodified COLα2(I) peptide m/z 1508.7727 (GPAGARGSDGSVGPVGPA; AUC 0.690), was also targeted for on-tissue fragmentation (**Fig. 45**). These preliminary results have tentatively identified putative peptides, as validated by on-tissue MALDI-MS/MS, that may be promising candidates for use in developing therapeutic peptide-based biomaterials.

a.

HYP (Pox) Position 1,2	HYP (Pox) Position 1,3	HYP (Pox) Position 2,3	b	897.4425	y	HYP (Pox) Position 1,2	HYP (Pox) Position 1,3	HYP (Pox) Position 2,3
--	--	--	1	G	9	--	--	--
214.130	214.130	214.130	2	R	8	840.421	840.421	840.421
327.178	327.178	311.183	3	P^1	7	684.320	684.320	684.320
384.200	384.199	368.204	4	G	6	571.272	571.272	587.267
513.242	513.242	497.247	5	E	5	514.251	514.251	530.246
612.310	612.310	596.315	6	V	4	385.208	385.208	401.203
669.332	669.332	653.337	7	G	3	286.140	286.140	302.135
782.380	766.384	766.384	8	P^2	2	229.118	229.118	245.113
--	--	--	9	P^3	1	116.071	132.066	132.066

Figure 44: Supplementary Figure S2. On-tissue MALDI-IMS provides evidence of peptide sequence validation and hydroxyproline site occupancy. a. Table showing potential fragment ion m/z depending on hydroxyproline site localization positions of P1-P2, P2-P3, or P1-P3. **b.** Annotated MALDI-MS/MS spectra produced by CID fragmentation on tissue. Identified b (blue) and y (red) ions are shown. Precursor ion is 897.4425 m/z, corresponding to a hydroxyproline containing COL1A1 peptide. P#: observed site of HYP (Pox) positions. There are 2 potential Pox sites out of 3 available prolines within the sequence. **c-e**. Annotated MALDI-MS/MS spectra produced by CID fragmentation of synthesized peptide standards of the three potential HYP site localizations (**Supp. Fig S4**). **f**. Ion Mobility study of the three synthesized peptides standards shown in **c-e** (and **Supp. Fig. S4**). An additional study was done of the three combined standards spotted ("cocktail") as well as on-target summed acquisition of the three standards spotted separately. 600 shots were taken for each acquisition.
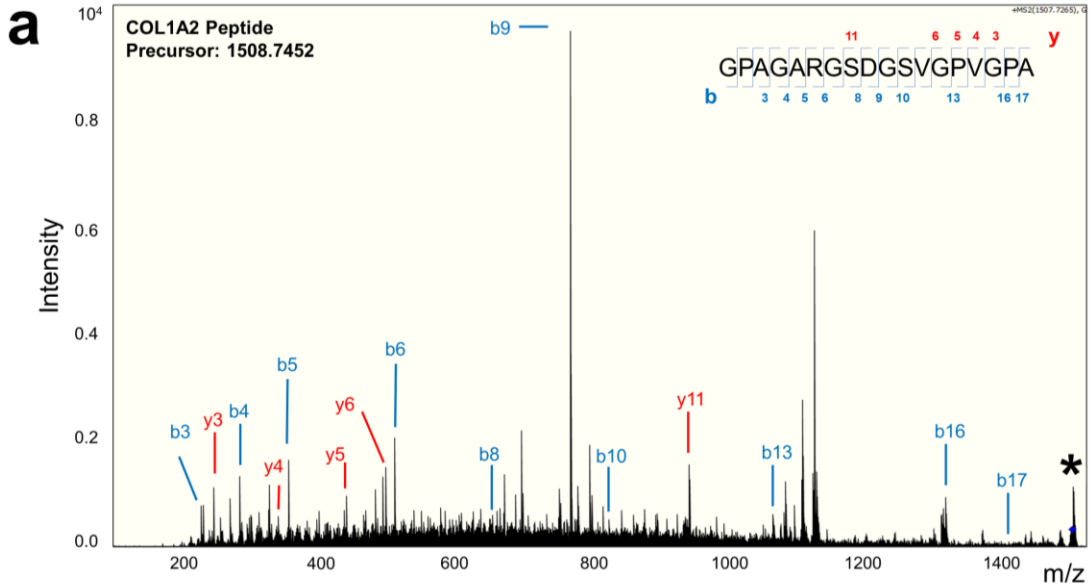
Figure 45: On-tissue MALDI-IMS provides evidence of peptide sequence validation and hydroxyproline site occupancy. a. Annotated MALDI-MS/MS spectra produced by CID fragmentation. Identified b (blue) and y (red) ions are shown. Precursor ion is 1508.7452 m/z, corresponding to an unmodified COL1A2 peptide.
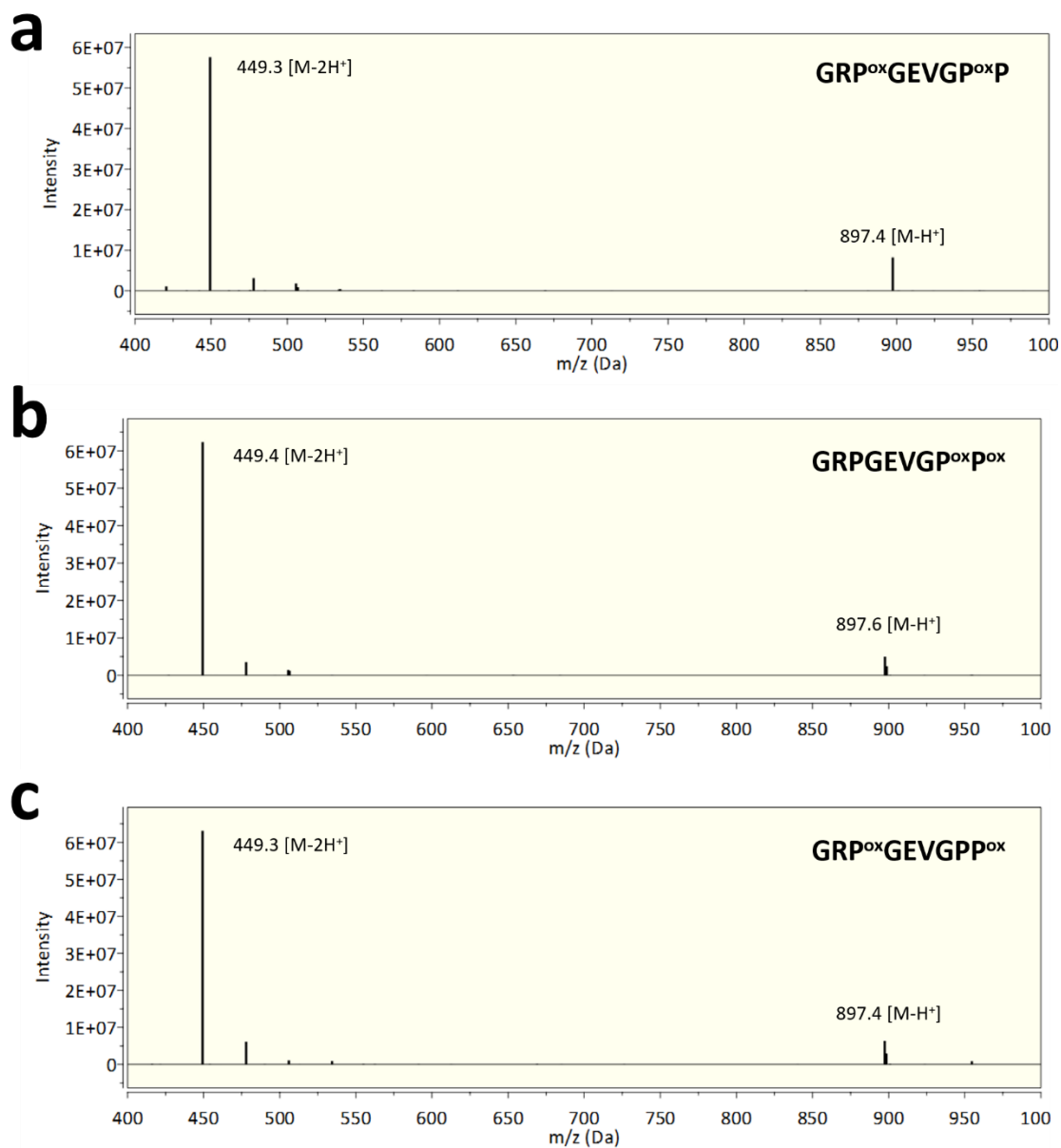
Figure 46: Confirmation of the synthesized peptide mass. a. Mass Spectrometry data of the synthesized peptide GRP^{ox}GEVGP^{ox}P, **b.** synthesized peptide GRPGEVGP^{ox}P^{ox}, and **c.** synthesized peptide GRP^{ox}GEVGPP^{ox}. Mass Spectrometry analysis was performed in a Waters ACQUITY UPLC XEVO TQD with a column 2.1x100 mm BEH C8, and a flow rate of 0.5 mL/min, a gradient of 2% to 95% of Acetonitrile in 9 minutes, and constant 0.1% of Formic Acid.

6.3.5 Collagen-based biomaterials effects on endogenous mouse ECM remodeling

To further identify endogenous mouse ECM proteins were differentially regulated with hydrogel treatment, we performed parallel chromatographic proteomic experiments on macro dissected regions, infarct and remote. In these studies, created mouse ECM databases were used to earmark endogenous mouse peptides in serial sections of tissue used in the ECM-IMS studies. A total of 33 proteins were identified, with 42 percent (14 out of 33) proteins being collagen subtypes, varied across families of fibril, network-associated, FACIT (fibril-associated collagen with interrupted triple helices) and multiplexin (**Fig. 43a-b, Fig. 44, Table 15**). Peptides putatively identified from non-collagen type proteins were implicated in pathways related to collagen biosynthesis and chain trimerization, GAG biosynthesis, and ECM degradation (**Supplemental Table 17**). Proteins were investigated as a function of fold change between each treatment's Infarct ROI vs. Remote ROI (**Fig. 43b**).

These proteomic experiments were then used to create a mouse ECM peptide database to apply to the MALDI-IMS dataset. Of the 62 mouse peptides mapped in the MALDI dataset, 39 peptides contained sequences unique to mouse and were used for further analysis (**Fig. 43c-d, Table 17**). Infarcted and Remote regions show unique unbiased clustering based on ECM peptide regulation (**Fig. 43c**). Within the infarcted region, rhCI and rhCIII hydrogel treated mice show similar endogenous peptide expression as compared to PBS treated control mice (**Fig. 43c**). Of these 39 endogenous mouse peptides, 8 were found to be differentially regulated amongst treatment groups (**Table 14**). **Figure 43d** shows a representative image of one of these peptides (m/z 1534.7613; COLα1(III) GPP^{ox}GTAGIP^{ox}GARGGAGP^{ox}P) via MALDI-IMS mapping. Here, unique spatial distribution of this endogenous mouse peptide is seen as
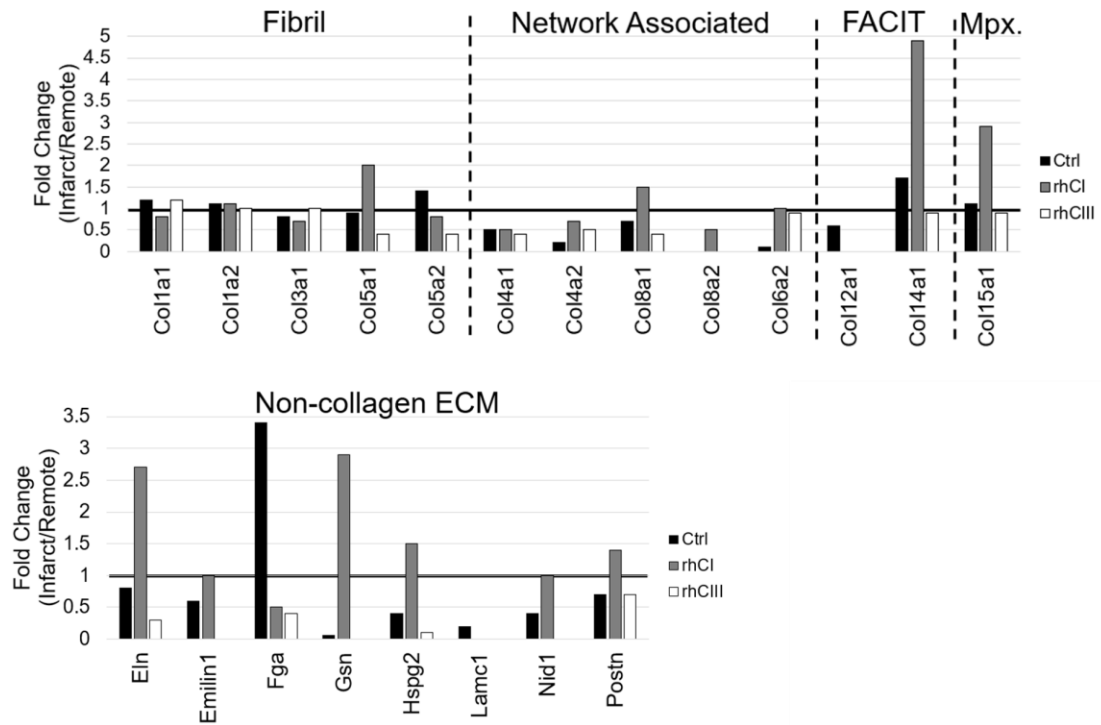
Figure 47: Protein Fold Change intensity values of Infarct/Remote ROIs for each treatment group (PBS control, rhCI hydrogel, rhCIII hydrogel). Raw values can be seen in **Table 16**. Proteins are organized by collagen subtype (FACIT: Fibril associated collagen with interrupted triple helices; Mpx: Multiplexin) and non-collagen proteins.

Table 16: Proteins identified via LC-MS/MS analysis on infarcted and remote regions of tissue for PBS Ctrl, rhCI hydrogel, and rhCIII hydrogel treated samples. Protein level Fold Change values (Infarct/Remote) were used to create hierarchical cluster in Fig 4b, with the exception of those with INF (infinity) values. Proteins were identified with a minimum of 2 peptides and a protein threshold of 99% with less than 1% FDR.

Bio View/Identified Proteins (33)	Accession Number	Alternate ID	Molecular Weight	Fold Change by Sample (Ctrl I/R)	Fold Change by Sample (rhCI I/R)	Fold Change by Sample (rhCIII I/R)	Total Spectral Count Ctrl_Infarct	Ctrl_Remote	rhCIII_Infarct	rhCIII_Remote	rhCI_Infarct	rhCI_Remote
40S ribosomal protein SA OS=Mus musculus OX=10090 GN=Rpsa PE=1 SV=4	P14206	Rpsa	33 kDa	0	INF	INF		2	2		1	
60 kDa heat shock protein, mitochondrial OS=Mus musculus OX=10090 GN=Hspd1 PE=1 SV=1	P63038 (+1)	Hspd1	61 kDa	0	INF	INF		2	2		7	
Basement membrane-specific heparan sulfate proteoglycan core protein OS=Mus musculus OX=10090 GN=Hspg2 PE=1 SV=1	Q05793	Hspg2	398 kDa	0.4	1.5	0.1	6	8	1	6	11	7
Biglycan OS=Mus musculus OX=10090 GN=Bgn PE=1 SV=1	P28653	Bgn	42 kDa	0	INF	INF	0	1	1		2	
Collagen alpha-1(I) chain OS=Mus musculus OX=10090 GN=Col1a1 PE=1 SV=4	P11087	Col1a1	138 kDa	1.2	0.8	1.2	354	165	287	211	236	275
Collagen alpha-1(III) chain OS=Mus musculus OX=10090 GN=Col3a1 PE=1 SV=4	P08121	Col3a1	139 kDa	0.8	0.7	1	105	75	110	97	72	107
Collagen alpha-1(IV) chain OS=Mus musculus OX=10090 GN=Col4a1 PE=1 SV=4	P02463	Col4a1	161 kDa	0.5	0.5	0.4	9	11	7	14	8	16
Collagen alpha-1(V) chain OS=Mus musculus OX=10090 GN=Col5a1 PE=1 SV=2	O88207 (+1)	Col5a1	184 kDa	0.9	2	0.4	14	9	4	9	12	6
Collagen alpha-1(VIII) chain OS=Mus musculus OX=10090 GN=Col8a1 PE=1 SV=3	Q00780	Col8a1	74 kDa	0.7	1.5	0.4	9	7	4	10	9	6
Collagen alpha-1(IX) chain OS=Mus musculus OX=10090 GN=Col11a1 PE=1 SV=2	Q61245 (+1)	Col11a1	181 kDa	INF	INF	INF	3		0		2	0
Collagen alpha-1(XII) chain OS=Mus musculus OX=10090 GN=Col12a1 PE=2 SV=3	Q60847 (+4)	Col12a1	340 kDa	0.6	INF	0	2	2	1	1	3	0
Collagen alpha-1(XIV) chain OS=Mus musculus OX=10090 GN=Col14a1 PE=1 SV=2	Q80X19 (+1)	Col14a1	193 kDa	1.7	4.9	0.9	3	1	1	1	5	1
Collagen alpha-1(XV) chain OS=Mus musculus OX=10090 GN=Col15a1 PE=1 SV=2	O35206	Col15a1	140 kDa	1.1	2.9	0.9	2	1	1	1	3	1
Collagen alpha-2(I) chain OS=Mus musculus OX=10090 GN=Col1a2 PE=1 SV=2	Q01149	Col1a2	130 kDa	1.1	1.1	1	506	256	367	328	347	313
Collagen alpha-2(IV) chain OS=Mus musculus OX=10090 GN=Col4a2 PE=1 SV=4	P08122	Col4a2	167 kDa	0.2	0.7	0.5	3	9	3	5	7	10
Collagen alpha-2(V) chain OS=Mus musculus OX=10090 GN=Col5a2 PE=1 SV=1	Q3U962	Col5a2	145 kDa	1.4	0.8	0.4	17	7	4	9	12	14
Collagen alpha-2(VI) chain OS=Mus musculus OX=10090 GN=Col6a2 PE=1 SV=3	Q02788	Col6a2	110 kDa	0.1	1	0.9	1	4	1	1	1	1
Collagen alpha-2(VIII) chain OS=Mus musculus OX=10090 GN=Col8a2 PE=2 SV=2	P25318	Col8a2	67 kDa	INF	0.5	0	4		0		1	2
EMILIN-1 OS=Mus musculus OX=10090 GN=Emilin1 PE=1 SV=1	Q99K41	Emilin1	108 kDa	0.6	0.5	1	2	2	2	1	1	2
Elastin OS=Mus musculus OX=10090 GN=Eln PE=1 SV=2	P54320	Eln	72 kDa	0.8	2.7	0.3	32	23	4	13	30	11
Fibrinogen alpha chain OS=Mus musculus OX=10090 GN=Fga PE=1 SV=1	E9PV24 (+1)	Fga	87 kDa	3.4	0.5	0.4	6	1	1	2	1	2
Fibrinogen beta chain OS=Mus musculus OX=10090 GN=Fgb PE=1 SV=1	Q8K0E8	Fgb	55 kDa	INF	INF	INF	2		0	0	1	
Fibrinogen gamma chain OS=Mus musculus OX=10090 GN=Fgg PE=1 SV=1	Q8VCM7	Fgg	49 kDa	INF	INF	INF				3	3	
Fibronectin OS=Mus musculus OX=10090 GN=Fn1 PE=1 SV=4	P11276	Fn1	273 kDa	INF	INF	INF	1				9	
Galectin-3 OS=Mus musculus OX=10090 GN=Lgals3 PE=1 SV=3	P16110	Lgals3	28 kDa	INF	INF	INF	1				2	
Gelsolin OS=Mus musculus OX=10090 GN=Gsn PE=1 SV=3	P13020 (+1)	Gsn	86 kDa	0.06	2.9	INF	1	9	0		3	1
Laminin subunit alpha-2 OS=Mus musculus OX=10090 GN=Lama2 PE=1 SV=2	Q60675	Lama2	344 kDa	INF	INF	INF		4			1	
Laminin subunit gamma-1 OS=Mus musculus OX=10090 GN=Lamc1 PE=1 SV=2	P02468	Lamc1	177 kDa	0.2	INF	INF	1	3			1	
Microfibril-associated glycoprotein 4 OS=Mus musculus OX=10090 GN=Mfap4 PE=1 SV=1	Q9D1H9 (+1)	Mfap4	29 kDa	INF	INF	INF	2				1	
Nidogen-1 OS=Mus musculus OX=10090 GN=Nid1 PE=1 SV=2	P10493	Nid1	137 kDa	0.4	1	0	2	3			1	
Periostin OS=Mus musculus OX=10090 GN=Postn PE=1 SV=2	Q62009 (+4)	Postn	93 kDa	0.7	1.4	0.7	13	11	3	4	10	7
Tenascin OS=Mus musculus OX=10090 GN=Tnc PE=1 SV=1	Q80YX1 (+4)	Tnc	232 kDa	INF	INF	INF	2				2	
Transforming growth factor-beta-induced protein ig-h3 OS=Mus musculus OX=10090 GN=Tgfbi PE=1 SV=1	P82198	Tgfbi	75 kDa	INF	INF	INF	0				2	

Table 17: Pathway annotations for non-collagen type proteins identified in LC-MS/MS experiments. Pathways were annotated in Scaffold v5 via reactome.org

Pathway	% of Displayed Proteins			Protein Accession Numbers
	Ctrl	rhCI	rhCIII	
Chondroitin sulfate biosynthesis	3.03	3.13	0.00	P28653
Collagen biosynthesis and modifying enzymes	42.42	43.75	63.64	P25318, Q61245
Collagen chain trimerization	42.42	43.75	63.64	P25318, Q61245
Degradation of the extracellular matrix	12.12	12.50	13.64	P54320, Q05793, P11276, P10493
Dermatan sulfate biosynthesis	3.03	3.13	0.00	P28653
ECM proteoglycans	30.30	31.25	31.82	Q05793, P11276, P28653, Q80YX1
Fibronectin matrix formation	3.03	3.13	0.00	P11276
Non-integrin membrane-ECM interactions	30.30	31.25	40.91	Q05793, P11276, Q61245

Table 18: Significantly Differentially Expressed Endogenous Mouse Peptides (ROC AUC); whole heart and infarct ROI comparisons. AUC thresholds of this study were 0.6.

Centroid [m/z]	ppm	Alternate IDs	Peptide sequence	Ctrl-rhCl AUC whole heart	Ctrl-rhClll AUC whole heart	rhCl-rhClll AUC whole heart	Ctrl-rhCl AUC at Infarct	Ctrl-rhClll AUC at Infarct	rhCl-rhClll AUC at Infarct
1088.5332	7.83	Col1a2	GPVGRTGETGAS	**0.651**	0.532	**0.618**	0.508	0.550	0.548
1187.5806	7.42	Col1a2	GPRGEAGNIGFPox	**0.600**	0.505	**0.608**	0.547	0.530	0.517
1302.6916	12.14	Col1a1	GPIGPAGARGPAGPQ	**0.630**	0.543	**0.619**	0.536	0.566	**0.748**
1349.6466	15.72	Col5a2	GPAGPAGEPoxGKEGPoxP	**0.683**	0.549	**0.628**	0.527	0.517	0.544
1534.7613	14.11	Col3a1	GPPoxGTAGIPoxGARGGAGPoxP	0.406	0.584	**0.662**	**0.600**	**0.800**	**0.710**
1698.8173	11.30	Col1a2	GPRGDQGPVGRTGETGAS	0.499	0.574	0.571	**0.610**	**0.744**	0.580
1743.7608	5.50	Col5a1	GTTGPTGQMGDPoxGERGPoxP	0.528	0.576	0.547	0.580	**0.680**	**0.607**
2142.9943	12.49	Col1a2	GPoxPGFVGEKGPSGEPoxGTAGAPoxGTA	0.539	0.564	0.526	**0.657**	**0.674**	0.543

compared to hydrogel distribution in previous figures. Interestingly, this COL3A1 peptide appears to be localized only to healthy remote tissue in PBS treated control, while being more homogenously distributed in hydrogel treated samples. Together, these studies show the utility of MALDI-IMS to localize both human hydrogel-specific peptides and endogenous mouse extracellular matrix peptides within a site of therapeutic biomaterial injection.

Chapter 7: Conclusions and Future Directions

7.1 Conclusions & Limitations

While ECM dysregulation in CAVS has been identified in the past, no approach to date has effectively elucidated dysregulation in specific collagen subtypes or collagen PTMs in pediatric end-stage CAVS. The majority of CAVS studies have involved adult end-stage fibrocalcific tissue samples, not pediatric end-stage caused by rapid ECM deposition. Current studies rely primarily on transcriptional analysis, such as qPCR and RNA-Seq, the results of which are not necessarily relevant to the translational level. On the protein level, collagen assays, such as the hydroxyproline assay, only measure total insoluble collagen content, not HYP levels or collagen subtypes directly. Immunohistochemical analysis, while translational, is limited to measuring only a few collagen types per tissue, and colocalization with prolyl-4-hydroxylase antibodies cannot map to the peptide level. Accordingly, there remains a critical need to provide in-depth characterization of valvular development and disease to inform therapeutic interventions.

In a recent editorial comment on this point, Atkins et. al. discuss the need for in-depth characterization of clinically relevant human valvular tissues samples [328]. They suggest the need for large-scale molecular screening that take advantage of multi-omic technologies. Further, the group references a recent study by Schlotter et. al. that takes advantage of localized proteomic analysis to use the "normal adjacent" tissue within a diseased valve as a control, due to the clinical lack of phenotypically normal samples [131]. Accordingly, the field of valve disease is shifting the paradigm from characterization towards a mechanistic understanding of the structure-function relationship of valve pathology in CAVS.

To address this need, this dissertation outlines the use of a novel mass spectrometry-based methodology to report on expression levels and spatial localization of dozens of collagens and other ECM proteins and peptides, as well as PTMs, from human

valve tissue sections. By identifying not only collagen subtypes, but also the specific sites of their differential HYP levels and the location where they are deposited within the tissue, we aimed to detect innovative targets for pharmacotherapeutics that may slow the progression of pediatric valvular fibrosis in CAVS.

The completion of Specific Aim 1 (Chapter 3) found via histopathological approaches that human pCAVS aortic valves have a unique tissue-associated collagen signature at end-stage: 1) the collagen-rich fibrosa layer is mixed and undefined; 2) collagen deposition rate increases by 56% per year of age compared to normal AV development; 3) there are dysregulated regions of immature collagen production; 4) collagen fibers misalign relative to the endothelium; and most notably 5) there are regions of high-density collagen fiber "plaques." From these data, we hypothesized that translational regulation of collagen sub-types would differ in pCAVS tissues. To test this hypothesis, chromatographic-based proteomics approaches were used in Specific Aim 2. Interestingly, this data showed a reduction in non-fibril-type collagens associated with healthy endothelium, such as multiplexins (α1(XVIII)), network forming (α1(IV), α2(IV)), and FACIT-type collagens (α1(XIV), α1(XVI)), while fibrillogenesis-associated collagens (α1(V)) and chaperones (SPARC) were upregulated. Interestingly, but not unexpectedly, we found post-translational regulation of these collagen sub-types differed as well. We identified that collagen hydroxyproline (HYP), a post-translational modification (PTM) necessary for stabilizing the collagen triple helix, is significantly decreased in pCAVS. Further, the sites of HYP loss in collagens α1(I) and α1(III) in pCAVS aligned with regions of glycoprotein VI and integrin binding, which require HYP within the sequence. This suggests an influence of HYP in pCAVS on cell-ECM interactions.

The studies outlined in Specific Aim 1 and Specific Aim 2 (Chapter 3) were the first to identify a tissue associated collagen signature unique to pediatric end-stage aortic valve stenosis, which includes highly localized regions of dense and misaligned collagen fibers within the valve structure. Additionally, this is the first quantitative and structural report of collagen hydroxyproline, or HYP, in valve development and disease. These data establish the groundwork for future studies examining the spatial regulation of collagen HYP within valvular structures and in relation to signaling factors driving collagen organization and deposition in pCAVS.

Specific Aim 3 aimed to correlate the spatial distribution of these deregulated collagen subtypes and PTMs relative to structural abnormalities identified via histopathology. However, further method development needed to be performed on our established MALDI-ECM-IM techniques to sufficiently access fibrotic valvular tissues. These developed methods, outlined in Chapter 4, detailed the serial application of Chondroitinase ABC, PNGaseF, Elastase, and Collagenase Type III, along with specific washing steps, in order to improve enzymatic access of the extracellular matrisome. This technique allowed for the mapping of the complex ECM from the same 5 µm tissue section. Here, one tissue section was evaluated for 1) pathology via histology 2) CS GAGs, 3) N-glycans, 4) elastin, and 5) collagens and other ECM peptides. Multimodal ECM studies such as these are particularly useful on human valvular studies, where patient samples may be limited. We found that the removal of non-collagen ECM components improved enzymatic access of collagenase-derived peptides by as much as 40% per peptide. Additionally, there was an 82% increase in total number of collagenase peptides identified after serial removal of GAGs, N-glycans, and elastin, as compared to collagenase alone. Successful completion of these method-development studies (Chapter

4) allowed for us to use MALDI-ECM-IMS to probe the structure-function relationship of the extracellular matrisome in pCAVS (Specific Aim 3, Chapter 5).

Chapter 5 outlines the results of our spatiotemporal mapping of collagen peptides across a cohort of normal pediatric, pediatric CAVS, and adult fibrocalcific CAVS tissues. Specific Aim 3 initially set out to test the hypothesis that there is differential HYP regulation on collagen peptides correlated to valve structure in pCAVS. While HYP containing collagen peptides were not found to have significantly different distribution within the valves structure compared to normal tissues, we did identify collagen subtype regulation as correlated to histopathologically defined regions of ECM dysregulation. Primarily, multiple peptides from collagen VI were found to localized with regions of increased fiber density. This study outlines the role of a collagen subtype, currently understudied past ages of embryonic valvular cushion development, within fibrotic valve disease. Additionally, this study outlines potential collagen and other ECM peptides that appear to have developmentally based regulation, independent of disease status. And finally, consistent with previous literature, we find a unique collagen proteome associated with fibrocalcific adult CAVS as compared to pediatric samples.

In studies described is Chapter 6, this dissertation expands upon the initially set-after Specific Aims to outline novel applications of our developed MALDI-ECM-IMS methods towards cardiovascular biomaterial characterization. ECM-IMS of collagen-based biomaterial therapeutics enabled complex protein and PTM expression data analysis, which were localized to surrounding pathological regions and within the biomaterial injection site (Chapter 6). The use of MALDI-IMS in this study was able to localize and identify peptides within hydrogel injected tissues, as well as identify potential endogenously differentiated extracellular matrix proteins. While this study focused on

imaging of the collagenous component of the injected biomaterials, glycosaminoglycans such as chondroitin sulfate (also within the hydrogel studied, Chapter 6) and recombinant elastin proteins are other common components of hydrogels that could potential be examined using the methods outlined in Chapter 6. Serial-enzyme ECM-targeted strategies used on-tissue may be beneficial to better understand therapeutic mechanisms of complex hydrogel mixtures [145]. These and future studies may provide evidence and insight for which hydrogel-derived peptides are most efficacious at promoting healing in the initial wound environment before therapeutic hydrogel degradation.

One limitation of our pCAVS study (Chapters 3 and 5) was the sample size of the cohort. Pediatric tissues inherently are difficult to obtain with a past national average of only 40% of families consenting for tissue use and donation [329]. Actual figures in specific regions may be lower[330]. This limitation similarly effects pediatric human aortic valve interstitial cell studies, as these require fresh samples for immediate cell isolation [331, 332] as opposed to the resected valves that are available through tissue banks. These limitations also prevented in-depth population studies of the cohort, including influences of gender, ethnicity, and socioeconomic status. Nevertheless, this is the largest collagen study to date on valve tissue with pediatric end-stage aortic valve stenosis. Future investigations to extend studies from this small clinically-relevant cohort will be critical to understanding how developmental timing of valvular interstitial cell signaling influences spatial distribution of collagen fiber production.

Overall, this dissertation used novel ECM targeted mass spectrometry techniques in order to elucidate the roll of collagen translation and post-translational regulation in pCAVS, with potential application to therapeutic biomaterials. By identifying specific collagen type peptides with deregulated HYP levels in CAVS, we will lay the groundwork

in new studies on signaling factors driving collagen organization and deposition in CAVS as well as other fibrotic diseases, driving novel anti-fibrotic pharmaco-therapeutic development. We anticipate that this data will inform functional testing of cell-based mechanisms regulating collagen HYP, the generation of new mouse models of valve disease, and improvements in the development of collagen biomaterials used in *in vitro* valve disease models and bioengineered valve replacements.

7.2 Future Directions

Many findings in this thesis lay the groundwork for mechanistic studies examining the functional implications of translational and post-translational regulation of the extracellular matrisome in pediatric CAVS. A major advantage of working with formalin-fixed paraffin embedded tissue samples is the ability to collect clinically relevant, human tissue samples from continuously expanding biorepositories, as done in this dissertation work. A limitation, however, is the static nature of fixed tissue, which hinders dynamic mechanistic studies. Potential future studies building upon our findings are discussed in this subchapter.

Our quantitative proteomic studies were able to map the collagen PTM HYP to cell-binding domains within the collagen sequences, however the role of ECM signaling was not investigated directly. The ECM has been shown to regulate signaling in three main ways that may be explored in future studies: 1) matricellular signaling, via cell surface receptors; 2) matricrine signaling, where the ECM serves as a reservoir for growth factors; and 3) mechanical signaling, where ECM affects stiffness, strain, and other biomechanical factors [42, 96]. Studies advancing our work beyond characterization towards ECM-signaling regulated mechanisms are outlined below.

Chapter 3 elucidates the potential role of matricellular signaling in pCAVS that could be explored. In a healthy valve, VECs form a barrier between interstitial collagen and circulating factors. However, as mentioned in Chapter 1, CAVS is associated with endothelial barrier dysfunction [333]. This potentially may lead to increased exposure of interstitial collagen subtypes that are capable of binding to platelets and subsequence thrombus deposition. We found that motifs of glycoprotein VI binding in primarily fibril type collagens showed a reduction of HYP, suggesting the potential for reduced glycoprotein

VI binding. While unexplored in pediatric cases, It has been reported that adult patients with AVS have decreased platelet function and aggregation; however the role of HYP content has not been explored as a potential mechanism directly [248]. Based on our research, investigating the role of collagen hydroxyproline and glycoprotein VI binding in pCAVS may be of value. Similarly, our studies find a reduction in HYP in domains of fibril type collagen reported to bind to integrins. Integrin α2β1 has been mostly shown to affect platelet aggregation and mast cell functions [246, 334]. Interestingly, mast and inflammatory cell infiltration is seen in adult CAVS [335-339] but is unexplored or unseen in pediatric cases [31]. Additional experiments may incorporate our findings of HYP reduction in integrin binding motifs with the impact on integrin signaling and immune cell infiltration.

Future studies may build upon our finding of differential localization of collagen HYPs site in CAVS to determine potential mechanisms of this reduction. Essential co-factors that regulate collagen HYP include iron, oxygen, and ascorbic acid, along with nutritional status and oxidative stress [69, 234, 340]. Wu et. al. recently found that ascorbic acid promoted quiescence in VICs [341]. Interestingly, organized and aligned deposition of collagens I and III were promoted. These studies were performed in 3D hydrogel cultures of porcine VICs and may further suggest a difference between "good" and "bad" ECM deposition in the context of valve disease [341]. Similar studies may be done in freshly isolated pediatric VICs. An alternative avenue to measure mechanisms of decreased HYP in pCAVS may be to explore other essential co-factors as well as the role of prolyl hydroxylases.

While not outlined in this dissertation, co-authored works within the Angel Lab investigated other collagen post-translational modifications involved in matricellular

signaling, such as N-linked glycosylation [114]. Within this work, we examined the relative abundance and localization of N-linked glycans within the pCAVS cohort (Appendix D-E). We found that pCAVS valve demonstrated a primarily core-fucosylated phenotype. Within normal valve samples, core-fucose N-glycans aligned with the GAG-rich spongiosa, however this layer-specific architecture is lost in pCAVS. Interestingly, core-fucose N-glycans have been associated with TGFβ signaling, with a reduction in core-fucosylation shown to attenuate renal fibrosis [342, 343]. This has yet to be explored in valvular disease. These data, along with recent literature, is suggestive of the need for further matricrine signaling focused research in pCAVS.

As suggested via extracellular localization studies outlined in Chapter 5, known hemodynamic-biomechanical signaling may have a potential localized role in matrix remodeling. Additionally, our histopathological studies show an increase in immature collagen localized regulation in pCAVS as well as an increase in regions of dense collagen fibers (**Chapter 3; Figure 8-9**). Further, this dissertation showed that pCAVS can be characterized by collagen fiber misalignment relative to the endothelium (**Chapter 3, Figure 10**). These suggest the need for future studies in the role of biomechanical signaling — as well as MMPs and TIMPs — on collagen deposition, degradation, and alignment in pCAVS, as our findings are suggestive of active collagen remodeling. Interesting work is being done on the role of MMPs, TIMPs, and matrix remodeling in the context of cardiac fibrosis by the Richardson Lab. Their group uses systems-based approaches to study localized regional heterogeneity of collagen orientation within the cardiac structure, as well as mechanical signaling induced remodeling regulation [344, 345]. Similar systems studies may be done to translate this work to our findings in collagen

alignment heterogeneity in valvular disease, as a function of hemodynamic induced mechanical strain.

Independent of valvular biology, this dissertation outlines MALDI-IMS methods that have promising applications in ECM biology and biomaterials. An advantage of the multi-enzyme ECM-targeting strategy outlined in Chapter 4 is that multiple analytes can be mapped to the same spatial coordinates which synergistically increases molecular information obtained from a single tissue section. Our work has shown that serial application of these enzymes does not impair the quality of the signal of the following enzyme, and it some cases it improves it. This workflow on a single tissue section allows for deep tissue mining of the extracellular matrix as well as colocalization and correlation studies between analytes. Work by Heijs et al described an elegant bioinformatic approach to colocalize N-glycan tissue maps to tryptic glycopeptide mapping [13]. A similar technique could be used in this current study not only for collagenase and elastin peptides but also for N-glycans and CS GAGs.

Multi-enzyme studies targeting GAGs as developed in this dissertation (Chapter 4) may be useful in elucidated the role of matricrine signaling in CAVS. Chondroitin Sulfate GAGs have been shown to increase bioavailability of latent TGFβ in smooth muscle cells, while heparan sulfate GAGs have been reported to increase Fibroblast Growth Factor signaling [96, 346, 347]. This has yet to be explored in valvular development or disease. However, proteoglycans biglycan and decorin have been associated with increasing TGFβ and other growth factors in valves, which resulted in increased calcification [348]. Interestingly, TGFβ has also been implicated in valvular EndMT [5], although the role of surrounding ECM has not been elucidated.

Additionally, serial enzyme methods developed here may have advantages for proteoglycan-peptide analysis. For example, digestions with chondroitinase ABC leaves behind a disaccharide and linker tetrasaccharide attached to the core protein that is later cleaved with COLase3 [36]. This unsaturated linker could be used in future studies to determine potential GAG-linker sites on identified CS-proteoglycan peptides (e.g., decorin, biglycan) [27]. While currently unexplored, this same linker-tracking methodology may be applicable with heparan sulfate proteoglycans and hyalectan proteoglycans, which are also detected via our COLase3 digest methodology.

Similarly, research done in this dissertation may inform strategies for imaging of COLase3-produced glycopeptides. Previous studies have shown that PNGase F digestion combined with ^{18}O water may be used to demark occupied sites of N-glycosylation on a tryptic glycopeptide [37]. For ECM analysis, this strategy combines PNGase F digestion in ^{18}O water followed by COLase3 to understand site occupancy of ECM glycopeptides. An additional strategy incorporates another enzyme, endoglycosidase F3, into this workflow. Endoglycosidase F3, which cleaves N-glycans directly above the core fucose-N-acetylglucasamine structure, creates an effective tag for core fucosylated N-glycopeptides [38, 39]. While not yet applied to glycopeptide imaging studies, this mass shift has shown to be a trackable linker in glycopeptide LC-MS/MS workflows [38].

Future work may be done to use multi-enzyme MALDI-IMS techniques developed in this dissertation to probe cell-ECM interactions on-tissue. Our preliminary proteomics studies show that HYP is not only reduced in pCAVS but is specifically reduced in collagen domains critical to cell-ECM binding (**Fig. 13**). The healthy AV is comprised of two cell types: valvular interstitial cells (VICs) and valvular endothelial cells (VECs). VIC activation is known to play a role in ECM disorganization in both adult FAVS and pediatric CAVS[31,

32]. Similarly, VEC dysfunction is well established in adult CAVS but underexplored in pCAVS. Published studies show an increase in collagen 2 and collagen 10 in calcified adult valves, along with osteochondrogenic markers such as p-SMAD 1/5/8 and Runx2[31]. However, the field recognizes a distinct cell activation profile between pCAVS and FAVS[31]. While activation markers specific to pCAVS have been identified[31], no work has been done to define the relationship between cell activation and surrounding ECM deposition in pCAVS.

Our lab has shown a decrease in endothelial-derived collagen peptides and, in contrast, an increase in fibril-type and fibrillogenesis-associated collagen peptides in pCAVS (Chapter 3, **Fig. 13**). Interestingly, chaperone SPARC – found be associated with increasing collagen fibrillogenesis, pro-collagen post-translational regulation and reduced collagen-integrin binding – was also enriched in pCAVS. (Chapter 3, **Fig. 14**). Further, HYP sites in SPARC binding motifs are maintained in pCAVS (Chapter 3, **Fig. 13**). All of these data suggest that there may be distinct cellular markers, such as SPARC, that correlate to localized ECM regulation.

One method to explore this is histology directed MALDI-IMS [349]. A representative workflow of this method is outlined in **Figure 48**. In this method, immunohistochemistry staining is done on-tissue to identify positively and negatively stained cells of interest. Then, high resolution scans can be taken to capture the histological profile and define regions of interest (ROIs) corresponding to positively and negatively stained cells. Tissues will then be taken through the MALDI-IMS protocol with ROIs targeted to identify each cell's corresponding ECM niche by identifying modified and unmodified ECM peptides. Preliminary data shows that this method can be used to identify

differentially distributed HYP containing collagen peptides between cell markers, such as PTEN in breast pathologies [350].

Relevent to these studies, histology direct MALDI-IMS could be used to identify the distinct molecular profiles of differentially activated VICs. Similarly, the relative ECM deposited by VECs and VICs could be characterized to identify molecular mechanisms of valve development and failure. These methods could be used during various stages of valvular development to determine the role of EndMT in ECM deposition and dysregulation [289, 351]. Using the multi-modal MALDI-IMS methods developed in this dissertation, the glycosaminoglycome and N-glycome of these cells could be explored, in addition to the collagen proteome.

Another potential avenue is to advance these histology-directed techniques on-tissue towards cell culture models. Recent advances have been made to single-cell and cell population IMS applications within cell culture conditions [352-355]. While several cell culture models exist for adult fibrocalcific AVS [356-361], there is a not a relevant model to pediatric CAVS beyond fresh isolation [331, 362]. A strategy to study the role of HYP in a dynamic mechanistic context could be to knock-down prolyl-4-hydroxylase in VICs, reducing HYP-modified collagen deposition in culture. MALDI-IMS and IHC can correlate HYP modification to molecular markers of interest, such as SPARC (as identified in Chapter 4; **Figure 15**) as well as cell activation, proliferation, and migration, compared to normal cells plated on unmodified collagen. Similarly, single-cell MALDI-IMS studies may be appropriate to studies of VICs and VECs in culture – potentially as a function of co- vs. mono-culture [15, 16, 363], layer specific architecture [131, 361], fluid dynamics [16, 29, 34, 364-368], or alignment [369-371].

Finally, Chapter 7 outlined the application of using our ECM targeted MALDI-IMS techniques to differentially localize species-specific collagen sequences, as applied to human-derived collagen hydrogel injected into mouse myocardium in vivo. This study also outlined the application of MALDI-ECM-IMS to student endogenous ECM remodeling as a function of therapeutic biomaterials. These techniques have the potential to be applied in valvular pathologies and bioengineered solutions. Blum et al recently called for mechanistic studies of tissue engineered heart valves [372]. They comment on the current need for improved tissue engineered heart valves (TEHV) for pediatric patients, due to high incidents of failure in pediatric patients with few studies on mechanism [373-375]. While advancements in valve regeneration have been made, few studies characterize the role of ECM in TEHV failure or regenerative capacity [373]. MALDI-ECM-IMS may be used to study ECM remodeling within TEHV in a species-targeted manner, similar to the work outlined in Chapter 6. For example, while decellularized porcine and sheep TEHVs may be investigated for cell infiltrate, it is difficult to elucidate collagen-subtype regulation and post-translational regulation as a function of scaffold vs. infiltrate remodeling. Along with further clinical characterization, we hope MALDI-ECM-IMS applications outlined in this study elucidate mechanisms of failure and inform better bioengineered solutions towards the development of regenerative TEHV for pCAVS patients.
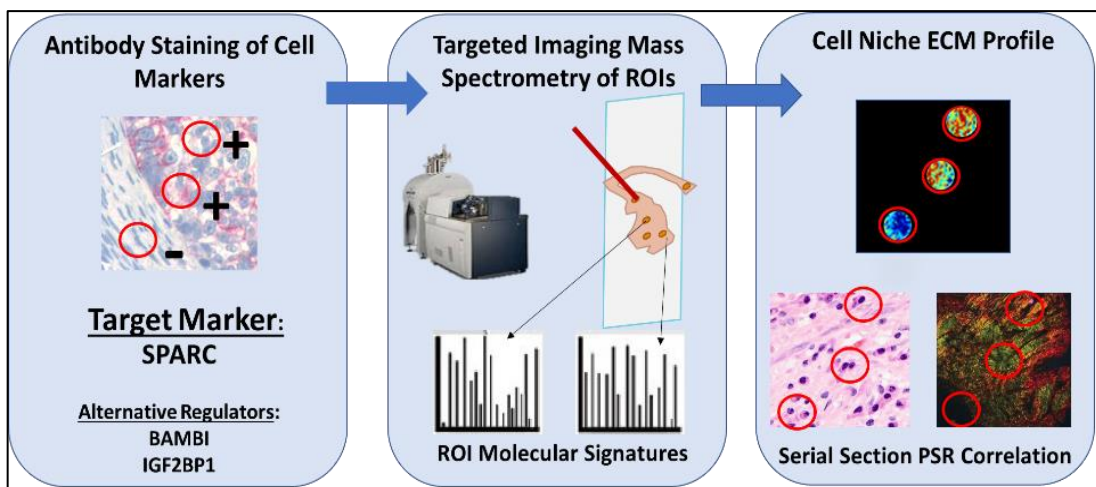
Figure 48: Histology-directed MALDI-IMS workflow. IHC analysis of cell markers will identify regions of interest (ROIs). The same tissue section will be taken through COLase3 MALDI-IMS to identify the molecular ECM signature of each ROI identified, which can be compared to acquired ECM histopathology.

Appendices
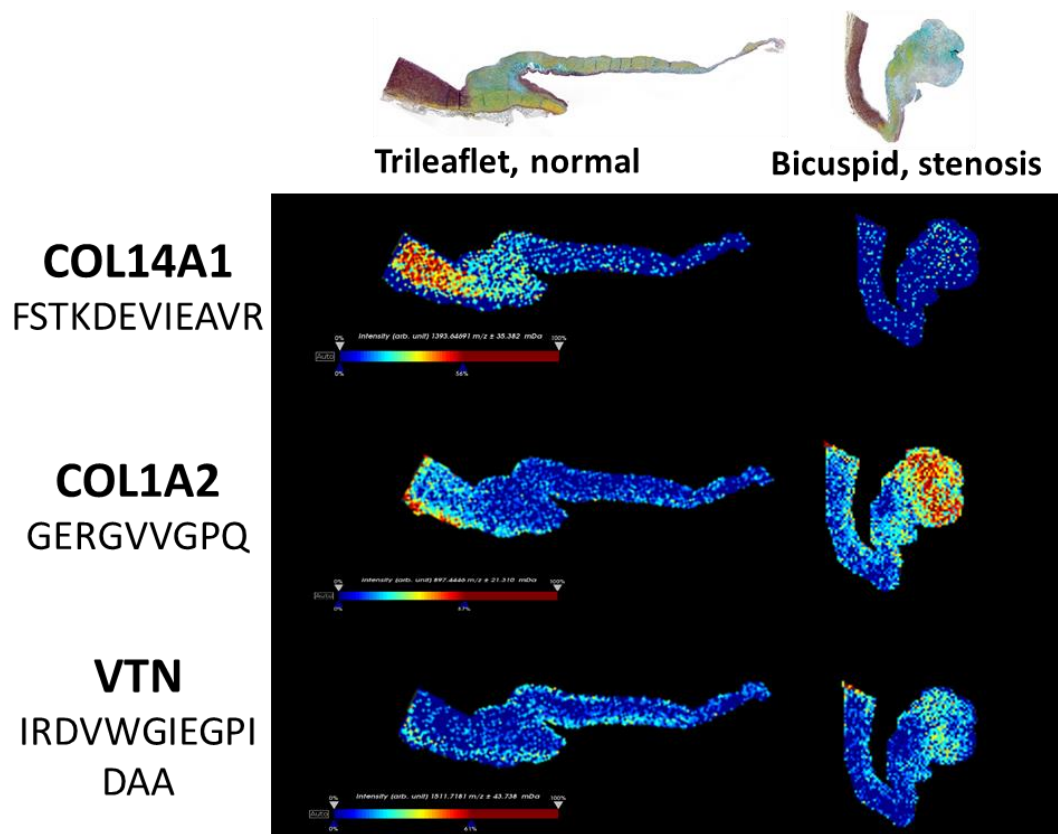
Appendix A: Representative image of unoptimized MALDI-ECM-IMS analysis on aortic valve tissue sections. A total of 20 putative peptides were identified from this dataset. Once optimized, this method identifies over ~150 putative peptides per tissue.
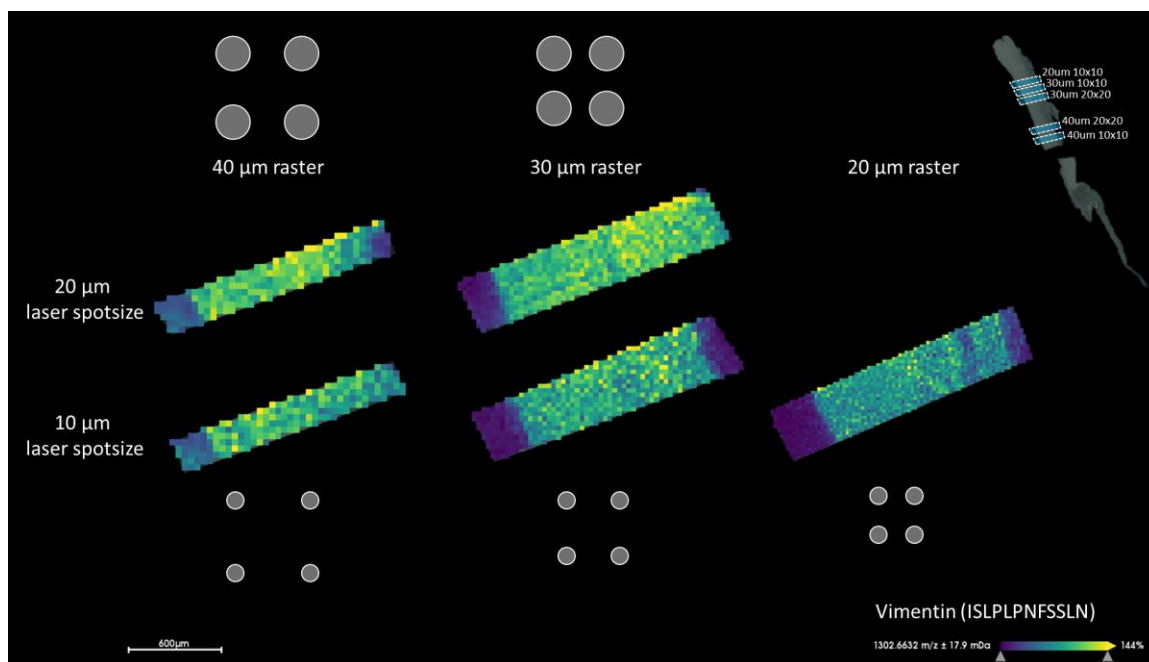
Appendix B: Laser spot size studies (timsTOF fleX, Bruker LLC). Method development study to optimize the laser spot size and raster for signal intensity
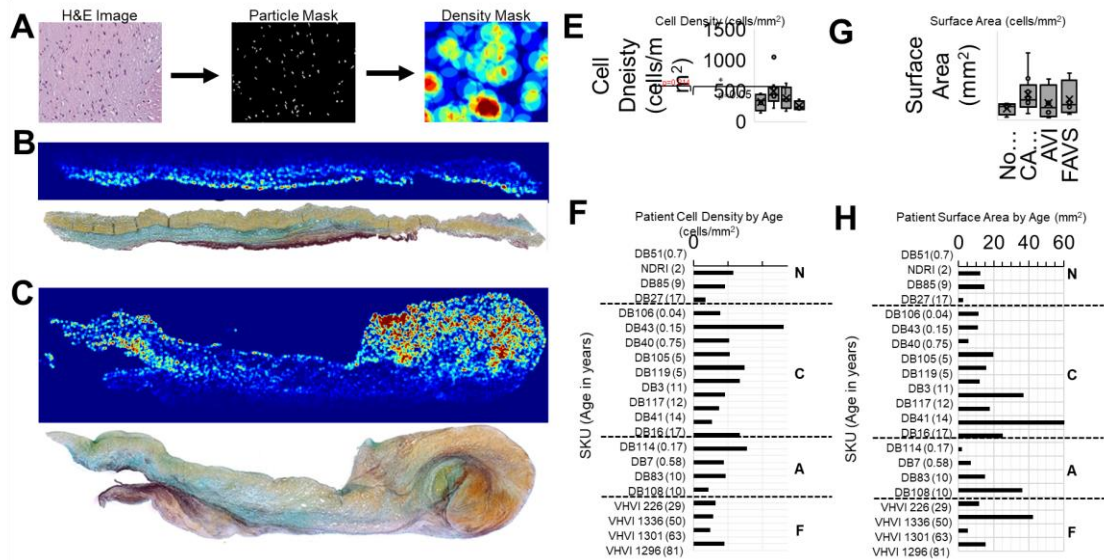
Appendix D: Pediatric CAVS valves have high cell density in regions of elastin mixing and high total surface area. A. Cell density mask workflow, created in ImageJ. **B.** Cell density mask of SKU DB27 with corresponding Movat's Pentachrome staining. **C.** Cell density mask of SKU DB16 with corresponding Movat's Pentachrome staining. **E.** Boxplot of cell density measurements across the valve cohort (in cells/mm^2). **F.** Patient specific cell density measurements (in cells/mm^2) organized by patient category and patient age. *$P<0.05$, Mann-Whitney U test. **G.** Boxplot of cross sectional (CS) surface area measurements across the valve cohort (in mm^2). **F.** Patient specific CS surface area measurements (in mm^2) organized by patient category and patient age.
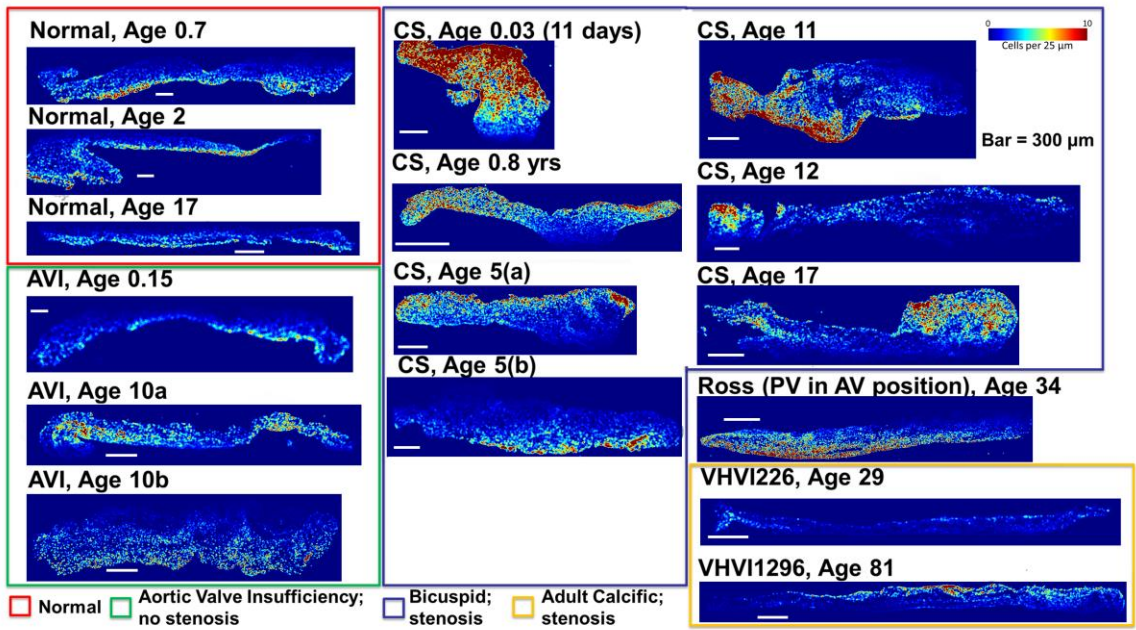
Appendix E: Cell density study images of all valves used for quantification in Appendix E.

References

1. Combs MD, Yutzey KE. Heart valve development: regulatory networks in development and disease. Circulation research. 2009;105:408-21. doi: 10.1161/CIRCRESAHA.109.201566. PubMed PMID: 19713546.
2. Aikawa E, Whittaker P, Farber M, Mendelson K, Padera RF, Aikawa M, Schoen FJ. Human semilunar cardiac valve remodeling by activated cells from fetus to adult: Implications for postnatal adaptation, pathology, and tissue engineering. Circulation. 2006;113:1344-52. doi: 10.1161/CIRCULATIONAHA.105.591768. PubMed PMID: 16534030.
3. Schoen FJ, Gotlieb AI. Heart valve health, disease, replacement, and repair: a 25-year cardiovascular pathology perspective. Cardiovascular Pathology. 2016;25:341-52. doi: 10.1016/j.carpath.2016.05.002. PubMed PMID: 27242130.
4. Schoen FJ. Evolving concepts of cardiac valve dynamics: The continuum of development, functional structure, pathobiology, and tissue engineering. Circulation. 2008;118:1864-80. doi: 10.1161/CIRCULATIONAHA.108.805911. PubMed PMID: 18955677.
5. Bischoff J. Endothelial-to-Mesenchymal Transition. Circulation research. 2019;124:1163-5. doi: 10.1161/CIRCRESAHA.119.314813. PubMed PMID: 30973806.
6. Eisenberg LM, Markwald RR. Molecular regulation of atrioventricular valvuloseptal morphogenesis. Circulation Research. 1995;77:1-6. doi: 10.1161/01.RES.77.1.1. PubMed PMID: 7788867.
7. Markwald RR FT, Manasek FJ. Structural Development of Endocardial Cushions. The American Journal of Anatomy. 1977;148:85-119.
8. Hinton RB, Lincoln J, Deutsch GH, Osinska H, Manning PB, Benson DW, Yutzey KE. Extracellular matrix remodeling and organization in developing and diseased aortic valves. Circulation Research. 2006;98:1431-8. doi: 10.1161/01.RES.0000224114.65109.4e. PubMed PMID: 16645142.
9. Tao G, Kotick JD, Lincoln J, Gao G, Kotick JD, Lincoln J. Heart Valve Development, Maintenance, and Disease: The role of endothelial cells. Current Topics in Developmental Biology. 2012;100:203-32. doi: 10.1016/B978-0-12-387786-4.00006-3. PubMed PMID: 22449845.
10. Butcher JT, Mahler GJ, Hockaday LA. Aortic valve disease and treatment: The need for naturally engineered solutions. Advanced Drug Delivery Reviews. 2011;63:242-68. doi: 10.1016/j.addr.2011.01.008. PubMed PMID: 21281685.
11. The emerging role of valve interstitial cell phenotypes in regulating heart valve pathobiology, (2007).
12. Wyss K, Yip CYY, Mirzaei Z, Jin X, Chen JH, Simmons CA. The elastic properties of valve interstitial cells undergoing pathological differentiation. Journal of Biomechanics. 2012;45:882-7. doi: 10.1016/j.jbiomech.2011.11.030. PubMed PMID: 22189247.
13. Hulin A, Hortells L, Gomez-Stallons MV, O'Donnell A, Chetal K, Adam M, Lancellotti P, Oury C, Potter SS, Salomonis N, Yutzey KE. Maturation of heart valve cell populations during postnatal remodeling. Development (Cambridge). 2019;146. doi: 10.1242/dev.173047. PubMed PMID: 30796046.
14. Ma H, Killaars AR, DelRio FW, Yang C, Anseth KS. Myofibroblastic activation of valvular interstitial cells is modulated by spatial variations in matrix elasticity and

its organization. Biomaterials. 2017;131:131-44. doi: 10.1016/j.biomaterials.2017.03.040. PubMed PMID: 28390245.

15. Hjortnaes J, Shapero K, Goettsch C, Hutcheson JD, Keegan J, Kluin J, Mayer JE, Bischoff J, Aikawa E. Valvular interstitial cells suppress calcification of valvular endothelial cells. Atherosclerosis. 2015;242:251-60. doi: 10.1016/j.atherosclerosis.2015.07.008. PubMed PMID: 26232165.

16. Butcher JT, Nerem RM. Valvular Endothelial Cells Regulate the Phenotype of Interstitial Cells in Co-culture: Effects of Steady Shear Stress. Tissue Engineering. 2006. doi: 10.1089/ten.2006.12.905.

17. Shapero K, Wylie-Sears J, Levine RA, Mayer JE, Bischoff J. Reciprocal interactions between mitral valve endothelial and interstitial cells reduce endothelial-to-mesenchymal transition and myofibroblastic activation. Journal of Molecular and Cellular Cardiology. 2015;80:175-85. doi: 10.1016/j.yjmcc.2015.01.006. PubMed PMID: 25633835.

18. Jain R, Yuan L, Epstein JA. Cardiac neural crest orchestrates remodeling and functional maturation of mouse semilunar valves. J Clin Invest. 2011;121. doi: 10.1172/JCI44244.

19. Kirby ML, Gale TF, Stewart DE. Neural crest cells contribute to normal aorticopulmonary septation. Science. 1983;220:1059-61. doi: 10.1126/science.6844926. PubMed PMID: 6844926.

20. Leatherbury L, Gauldin HE, Waldo K, Kirby ML, Cardiology P. Microcinephotography of the Developing Heart in Neural Crest-Ablated Chick Embryos.

21. Huang Y, Xu K, Zhou T, Zhu P, Dong N, Shi J. Comparison of Rapidly Proliferating, Multipotent Aortic Valve-Derived Stromal Cells and Valve Interstitial Cells in the Human Aortic Valve. Stem Cells International. 2019;2019. doi: 10.1155/2019/7671638.

22. Peacock JD, Lu Y, Koch M, Kadler KE, Lincoln J. Temporal and spatial expression of collagens during murine atrioventricular heart valve development and maintenance. Developmental Dynamics. 2008;237:3051-8. doi: 10.1002/dvdy.21719. PubMed PMID: 18816857.

23. Amofa D, Hulin A, Nakada Y, Sadek HA, Yutzey KE. Hypoxia promotes primitive glycosaminoglycan-rich extracellular matrix composition in developing heart valves. Am J Physiol Heart Circ Physiol. 2017;313:1143-54. doi: 10.1152/ajpheart.00209.2017.

24. Hoffman JIE, Kaplan S, Liberthson RR. Prevalence of congenital heart disease. American Heart Journal. 2004;147:425-39. doi: 10.1016/j.ahj.2003.05.003. PubMed PMID: 14999190.

25. Mathieu P, Bossé Y, Huggins GS, Della Corte A, Pibarot P, Michelena HI, Limongelli G, Boulanger M-C, Evangelista A, Bédard E, Citro R, Body SC, Nemer M, Schoen FJ, Corte AD, Pibarot P, Michelena HI, Limongelli G, Boulanger M-C, Evangelista A, Bédard E, Citro R, Body SC, Nemer M, Schoen FJ. The pathology and pathobiology of the bicuspid aortic valve: state of the art and novel research perspectives. The Journal of Pathology: Clinical Research. 2015;1:195-206. doi: 10.1002/cjp2.21. PubMed PMID: 27499904.

26. Hinton RB, Yutzey KE. Heart Valve Structure and Function in Development and Disease. Annual review of physiology. 2011;73:29. doi: 10.1146/ANNUREV-PHYSIOL-012110-142145. PubMed PMID: 20809794.

27. Garg V, Muth AN, Ransom JF, Schluterman MK, Barnes R, King IN, Grossfeld PD, Srivastava D. Mutations in NOTCH1 cause aortic valve disease. Nature. 2005;437:270-4. doi: 10.1038/nature03940. PubMed PMID: 16025100.

28. The science of BAV aortopathy, (2020).

29. Butcher JT, Tressel S, Johnson T, Turner D, Sorescu G, Jo H, Nerem RM. Transcriptional profiles of valvular and vascular endothelial cells reveal phenotypic differences: Influence of shear stress. Arteriosclerosis, Thrombosis, and Vascular Biology. 2006;26:69-77. doi: 10.1161/01.ATV.0000196624.70507.0d. PubMed PMID: 16293796.

30. Gharibeh L, Komati H, Bossé Y, Boodhwani M, Heydarpour M, Fortier M, Hassanzadeh R, Ngu J, Mathieu P, Body SC, Nemer M. GATA6 Regulates Aortic Valve Remodeling, and Its Haploinsufficiency Leads to Right-Left Type Bicuspid Aortic Valve. Circulation. 2018. doi: 10.1161/CIRCULATIONAHA.117.029506. PubMed PMID: 29567669.

31. Wirrig EE, Hinton RB, Yutzey KE. Differential expression of cartilage and bone-related proteins in pediatric and adult diseased aortic valves. Journal of Molecular and Cellular Cardiology. 2011;50:561-9. doi: 10.1016/j.yjmcc.2010.12.005. PubMed PMID: 21163264.

32. Ho SY. Structure and anatomy of the aortic root. European Journal of Echocardiography. 2009;10. doi: 10.1093/ejechocard/jen243. PubMed PMID: 19131496.

33. Butany Paul Fedak JW, Verma S, David TE, Leask RL. Clinical and Pathophysiological Implications of a Bicuspid Aortic Valve2002. doi: 10.1161/01.CIR.0000027905.26586.E8.

34. Atkins SK, Sucosky P. Etiology of bicuspid aortic valve disease: Focus on hemodynamics. World journal of cardiology. 2014;6:1227-33. doi: 10.4330/wjc.v6.i12.1227. PubMed PMID: 25548612.

35. Fernandes SM, Khairy P, Sanders SP, Colan SD. Bicuspid Aortic Valve Morphology and Interventions in the Young. Journal of the American College of Cardiology. 2007;49:2211-4. doi: 10.1016/j.jacc.2007.01.090. PubMed PMID: 17543642.

36. Hutson HN, Marohl T, Anderson M, Eliceiri K, Campagnola P, Masters KS. Calcific Aortic Valve Disease Is Associated with Layer-Specific Alterations in Collagen Architecture. PLOS ONE. 2016;11:e0163858. doi: 10.1371/journal.pone.0163858.

37. Perrotta I, Russo E, Camastra C, Filice G, Di Mizio G, Colosimo F, Ricci P, Tripepi S, Amorosi A, Triumbari F, Donato G. New evidence for a critical role of elastin in calcification of native heart valves: Immunohistochemical and ultrastructural study with literature review. Histopathology. 2011;59:504-13. doi: 10.1111/j.1365-2559.2011.03977.x. PubMed PMID: 22034890.

38. Vito AD, Donato A, Presta I, Mancuso T, Brunetti FS, Mastroroberto P, Amorosi A, Malara N, Donato G, Di Vito A, Donato A, Presta I, Mancuso T, Brunetti FS, Mastroroberto P, Amorosi A, Malara N, Donato G. Extracellular Matrix in Calcific Aortic Valve Disease: Architecture, Dynamic and Perspectives. International Journal of Molecular Sciences. 2021;22:913. doi: 10.3390/ijms22020913. PubMed PMID: 33477599.

39. Clift CL, Su YR, Bichell D, Jensen Smith HC, Bethard JR, Norris-Caneda K, Comte-Walters S, Ball LE, Hollingsworth MA, Mehta AS, Drake RR, Angel PM. Collagen fiber regulation in human pediatric aortic valve development and disease. Scientific Reports. 2021;11:9751. doi: 10.1038/s41598-021-89164-w.

40. Weston MW, LaBorde DV, Yoganathan AP. Estimation of the Shear Stress on the Surface of an Aortic Valve Leaflet. Annals of Biomedical Engineering. 1999;27:572-9. doi: 10.1114/1.199. PubMed PMID: 10468241.

41. Arjunon S, Rathan S, Jo H, Yoganathan AP. Aortic valve: mechanical environment and mechanobiology. Annals of biomedical engineering. 2013;41:1331-46. doi: 10.1007/s10439-013-0785-7. PubMed PMID: 23515935.

42. Kodigepalli KM, Thatcher K, West T, Howsmon DP, Schoen FJ, Sacks MS, Breuer CK, Lincoln J. Biology and biomechanics of the heart valve extracellular matrix. Journal of Cardiovascular Development and Disease. 2020;7:1-22. doi: 10.3390/jcdd7040057.

43. Mead TJ, Yutzey KE. Notch pathway regulation of neural crest cell development in vivo. Developmental Dynamics. 2012;241:376-89. doi: 10.1002/dvdy.23717.

44. Lincoln J, Alfieri CM, Yutzey KE. BMP and FGF regulatory pathways control cell lineage diversification of heart valve precursor cells. Developmental Biology. 2006;292:290-302. doi: 10.1016/J.YDBIO.2005.12.042.

45. Alfieri CM, Cheek J, Chakraborty S, Yutzey KE. Wnt signaling in heart valve development and osteogenic gene induction. Developmental Biology. 2010;338:127-35. doi: 10.1016/J.YDBIO.2009.11.030.

46. Sun L, Chandra S, Sucosky P. Ex Vivo Evidence for the Contribution of Hemodynamic Shear Stress Abnormalities to the Early Pathogenesis of Calcific Bicuspid Aortic Valve Disease. PLoS ONE. 2012;7:e48843. PubMed PMID: 23119099.

47. Butcher JT, Simmons CA, Warnock JN. Review: Mechanobiology fo the Aortic Heart Valve. The Journal of heart valve disease. 2008;17:62-73. PubMed PMID: 18365571.

48. Ku C-HH, Johnson PH, Batten P, Sarathchandra P, Chambers RC, Taylor PM, Yacoub MH, Chester AH. Collagen synthesis by mesenchymal stem cells and aortic valve interstitial cells in response to mechanical stretch. Cardiovascular Research. 2006;71:548-56. doi: 10.1016/j.cardiores.2006.03.022. PubMed PMID: 16740254.

49. Steitz SA, Speer MY, McKee MD, Liaw L, Almeida M, Yang H, Giachelli CM. Osteopontin inhibits mineral deposition and promotes regression of ectopic calcification. American Journal of Pathology. 2002;161:2035-46. doi: 10.1016/S0002-9440(10)64482-3. PubMed PMID: 12466120.

50. Bogdanova M, Kostina A, Zihlavnikova Enayati K, Zabirnyk A, Malashicheva A, Stensløkken K-O, Sullivan GJ, Kaljusto M-L, Kvitting J-P, Kostareva A, Vaage J, Rutkovskiy A. Inflammation and Mechanical Stress Stimulate Osteogenic Differentiation of Human Aortic Valve Interstitial Cells. Frontiers in physiology. 2018;9:1635. doi: 10.3389/fphys.2018.01635. PubMed PMID: 30524301.

51. Francis Stuart SD, De Jesus NM, Lindsey ML, Ripplinger CM. The crossroads of inflammation, fibrosis, and arrhythmia following myocardial infarction. Journal of Molecular and Cellular Cardiology. 2016;91:114-22. doi: 10.1016/j.yjmcc.2015.12.024. PubMed PMID: 26739214.

52. Talman V, Ruskoaho H. Cardiac fibrosis in myocardial infarction-from repair and remodeling to regeneration. doi: 10.1007/s00441-016-2431-9.

53. Venugopal JR, Prabhakaran MP, Mukherjee S, Ravichandran R, Dan K, Ramakrishna S. Biomaterial strategies for alleviation of myocardial infarction. Journal of the Royal Society Interface. 2012;9:1-19. doi: 10.1098/rsif.2011.0301. PubMed PMID: 21900319.

54. McLaughlin S, McNeill B, Podrebarac J, Hosoyama K, Sedlakova V, Cron G, Smyth D, Seymour R, Goel K, Liang W, Rayner KJ, Ruel M, Suuronen EJ, Alarcon EI. Injectable human recombinant collagen matrices limit adverse remodeling and improve cardiac function after myocardial infarction. Nature Communications. 2019;10. doi: 10.1038/s41467-019-12748-8. PubMed PMID: 31653830.

55. Ungerleider JL, Christman KL. Concise Review: Injectable Biomaterials for the Treatment of Myocardial Infarction and Peripheral Artery Disease: Translational Challenges and Progress. STEM CELLS Translational Medicine. 2014;3:1090-9. doi: 10.5966/sctm.2014-0049. PubMed PMID: 25015641.

56. Zhang BL, Bianco RW, Schoen FJ. Preclinical Assessment of Cardiac Valve Substitutes: Current Status and Considerations for Engineered Tissue Heart Valves. Frontiers in Cardiovascular Medicine. 2019;6:1-9. doi: 10.3389/fcvm.2019.00072.

57. Sharabiani MTA, Dorobantu DM, Mahani AS, Turner M, Peter Tometzki AJ, Angelini GD, Parry AJ, Caputo M, Stoica SC. Aortic Valve Replacement and the Ross Operation in Children and Young Adults. Journal of the American College of Cardiology. 2016;67:2858-70. doi: 10.1016/j.jacc.2016.04.021. PubMed PMID: 27311525.

58. Schoen FJ. Heart valve tissue engineering: quo vadis? doi: 10.1016/j.copbio.2011.01.004.

59. Siebelink MJ, Albers MJIJIJ, Roodbol PF, Van De Wiel HBMM. Key factors in paediatric organ and tissue donation: An overview of literature in a chronological working model. Transplant International. 2012;25:265-71. doi: 10.1111/j.1432-2277.2011.01407.x.

60. Grocott-Mason R, Lund O, Elwidaa H, Mazhar R, Chandrasakeran V, Mitchell AG, Ilsley C, Khaghani A, Rees A, Yacoub M. Long-term results after aortic valve replacement in patients with congestive heart failure. Homografts vs prosthetic valves. European Heart Journal. 2000;21:1698-707. doi: 10.1053/euhj.1999.2040.

61. Saiki H, Senzaki H. Congenital Aortic Stenosis in Children. Calcific Aortic Valve Disease: InTech; 2013.

62. Bouhout I, Ba PS, El-Hamamsy I, Poirier N. Aortic Valve Interventions in Pediatric Patients. Seminars in Thoracic and Cardiovascular Surgery. 2018. doi: 10.1053/J.SEMTCVS.2018.10.009.

63. Takkenberg JJM, Klieverik LMA, Schoof PH, Van Suylen RJ, Van Herwerden LA, Zondervan PE, Roos-Hesselink JW, Eijkemans MJC, Yacoub MH, Bogers AJJC. The Ross procedure: A systematic review and meta-analysis. Circulation. 2009;119:222-8. doi: 10.1161/CIRCULATIONAHA.107.726349. PubMed PMID: 19118260.

64. Ikhumetse JD, Konduri S, Warnock JN, Xing Y, Yoganathand AP. Cyclic aortic pressure affects the biological properties of porcine pulmonary valve leaflets. The Journal of heart valve disease. 2006. PubMed PMID: 16607914.

65. Angel PM, Nusinow D, Brown CB, Violette K, Barnett JV, Zhang B, Baldwin HS, Caprioloi RM. Networked-based characterization of extracellular matrix proteins from adult mouse pulmonary and aortic valves. Journal of proteome research. 2011;10:812-23. doi: 10.1021/pr1009806. PubMed PMID: 21133377.

66. Ricard-Blum S, Ruggiero F. The collagen superfamily: From the extracellular matrix to the cell membrane. Pathologie Biologie. 2005;53:430-42. doi: 10.1016/j.patbio.2004.12.024. PubMed PMID: 16085121.

67. Ricard-Blum S. The Collagen Family2011;3. PubMed PMID: 21421911.

68. Gordon MK, Hahn RA. Collagens. Cell and Tissue Research. 2010;339:247-57. doi: 10.1007/s00441-009-0844-4.

69. Shoulders MD, Raines RT. Collagen Structure and Stability. Annual Review of Biochemistry. 2009;78:929-58. doi: 10.1146/annurev.biochem.77.032207.120833. PubMed PMID: 19344236.

70. Hohenester E, Engel J. Domain structure and organisation in extracellular matrix proteins. Matrix Biology. 2002;21:115128.

71. Fichard As, Kleman J-P, Ruggiero F. Another Look at Collagen V and XI Molecules. Matrix Biology. 1994;14:515-31.

72. Kadler KE, Baldock C, Bella J, Boot-Handford RP. Collagens at a glance. Journal of Cell Science. 2007;120:1955-8. doi: 10.1242/jcs.03453.

73. Bruckner-Tuderman L, Von Der Mark K, Pihlajaniemi T, Unsicker K. Cell interactions with the extracellular matrix. Cell and Tissue Research. 2010;339:1-5. doi: 10.1007/s00441-009-0891-x.

74. Banyard J, Bao L, Zetter BR. Type XXIII Collagen, a New Transmembrane Collagen Identified in Metastatic Tumor Cells*2003. doi: 10.1074/jbc.M210616200.

75. Kivirikko KI, Myllyharju J. Proty[4-Hydroxytases and their Protein DisuLfide Isomerase Subunit1998.

76. Myllyharju J. Prolyl 4-hydroxylases, the key enzymes of collagen biosynthesis. Matrix Biology. 2003;22:15-24.

77. Myllyharju J, Kivirikko KI. Collagens, modifying enzymes and their mutations in humans, flies and worms. Trends in Genetics. 2004;20:33-43. doi: 10.1016/j.tig.2003.11.004. PubMed PMID: 14698617.

78. Myllyharju J, Kivirikko KI. Collagens and collagen-related diseases. Annals of Medicine. 2001;33:7-21. doi: 10.3109/07853890109002055.

79. Prockop D, Sieron AL, Li S-W. Procollagen N-Proteinase and Procollagen C-Proteinase. Two Unusual Metattoproteinases that are Essentia for Procollagen Processing Probably Have Important Roles in Development and Celt Signaling1998.

80. Kagan HM, Li W. Lysyl Oxidase: Properties, Specificity, and Biological Roles Inside and Outside of the Cell. Journal of Cellular Biochemistry. 2003;88:660-72. doi: 10.1002/jcb.10413.

81. Krane SM. The importance of proline residues in the structure, stability and susceptibility to proteolytic degradation of collagens. Amino Acids. 2008;35:703-10. doi: 10.1007/s00726-008-0073-2. PubMed PMID: 18431533.

82. Yamauchi M, Sricholpech M. Lysine post-translational modifications of collagen. Essays in Biochemistry. 2012;52:113-33. doi: 10.1042/BSE0520113. PubMed PMID: 22708567.

83. Bella J, Brodsky B, Bermanl HM. Hydration structure of a collagen peptide.

84. Vitagliano L, Berisio R, Mazzarella L, Zagari A. Structural Bases of Collagen Stabilization Induced by Proline Hydroxylation2001;58:459-64.

85. Prolyl 4-hydroxylase, (2010).

86. Schmelzer CEH, Nagel MBM, Dziomba S, Merkher Y, Sivan SS, Heinz A. Prolyl hydroxylation in elastin is not random. Biochimica et Biophysica Acta (BBA) - General Subjects. 2016;1860:2169-77. doi: 10.1016/J.BBAGEN.2016.05.013.

87. Humphries JD, Byron A, Humphries MJ. Integrin ligands at a glance. Journal of Cell Science. 2006;119:3901-3. PubMed PMID: 16988024.

88. Xu Y, Gurusiddappa S, Rich RL, Owens RT, Keene DR, Mayne R, Höök A, Höök M. Multiple binding sites in collagen type I for the integrins α1β1 and α2β1. Journal of Biological Chemistry. 2000;275:38981-9. doi: 10.1074/jbc.M007668200.

89. Sipilä KH, Drushinin K, Rappu P, Jokinen J, Salminen TA, Salo AM, Käpylä J, Myllyharju J, Heino J. Proline hydroxylation in collagen supports integrin binding by two distinct mechanisms. The Journal of biological chemistry. 2018;293:7645-58. doi: 10.1074/jbc.RA118.002200. PubMed PMID: 29615493.

90. Leitinger B, Hohenester E. Mammalian collagen receptors. Matrix Biology. 2007;26:146-55. doi: 10.1016/j.matbio.2006.10.007.

91. Flynn LA, Blissett AR, Calomeni EP, Agarwal G. Inhibition of Collagen Fibrillogenesis by Cells Expressing Soluble Extracellular Domains of DDR1 and DDR2. Journal of Molecular Biology. 2009;395:533-43. doi: 10.1016/j.jmb.2009.10.073.

92. Lebbink RJ, de Ruiter T, Adelmeijer J, Brenkman AB, van Helvoort JM, Koch M, Farndale RW, Lisman T, Sonnenberg A, Lenting PJ, Meyaard L. Collagens are functional, high affinity ligands for the inhibitory immune receptor LAIR-1. Journal of Experimental Medicine. 2006;203:1419-25. doi: 10.1084/JEM.20052554.

93. Farndale RW, Lisman T, Bihan D, Hamaia S, Smerling CS, Pugh N, Konitsiotis A, Leitinger B, De Groot PG, Jarvis GE, Raynal N. Cell-collagen interactions: The use of peptide Toolkits to investigate collagen-receptor interactions. Biochemical Society Transactions. 2008;36:241-50. doi: 10.1042/BST0360241.

94. Wiltz D, Arevalos CA, Balaoing LR, Blancas AA, Sapp MC, Zhang X, Grande-Allen KJ. Extracellular Matrix Organization, Structure, and Function. In: Aikawa E, editor. Calcific Aortic Valve Disease2012. p. 1-15.

95. Evolving concepts of cardiac valve dynamics: The continuum of development, functional structure, pathobiology, and tissue engineering, (2008).

96. Chen JH, Simmons CA. Cell-matrix interactions in the pathobiology of calcific aortic valve disease: Critical roles for matricellular, matricrine, and matrix mechanics cues. Circulation Research. 2011;108:1510-24. doi: 10.1161/CIRCRESAHA.110.234237. PubMed PMID: 21659654.

97. Aggrecan in Cardiovascular Development and Disease, (2020).

98. Granath C, Noren H, Björck H, Simon N, Olesen K, Rodin S, Grinnemo KH, Österholm C. Characterization of Laminins in Healthy Human Aortic Valves and a Modified Decellularized Rat Scaffold. BioResearch Open Access. 2020;9:269-78. doi: 10.1089/biores.2020.0018.

99. The many facets of the matricelluar protein periostin during cardiac development, remodeling, and pathophysiology, (2009).

100. Conway SJ, Doetschman T, Azhar M. The Inter-Relationship of Periostin, TGFβ, and BMP in Heart Valve Development and Valvular Heart Diseases. Review TheScientificWorldJOURNAL. 2011;11. doi: 10.1100/tsw.2011.132.

101. Wilton E, Bland M, Thompson M, Jahangiri M. Work in progress report - Valves: Matrix metalloproteinase expression in the ascending aorta and aortic valve. Interactive Cardiovascular and Thoracic Surgery. 2008;7:37-40. doi: 10.1510/icvts.2007.163311. PubMed PMID: 18025061.

102. Fondard O, Detaint D, Iung B, Choqueux C, Adle-Biassette H, Jarraya M, Hvass U, Couetil J-P, Henin D, Michel J-B, Vahanian A, Jacob M-P. Extracellular matrix remodelling in human aortic valve disease: the role of matrix metalloproteinases and their tissue inhibitors. European Heart Journal. 2005;26:1333-41. doi: 10.1093/eurheartj/ehi248.

103. Korossis S. Structure-Function Relationship of Heart Valves in Health and Disease. Structural Insufficiency Anomalies in Cardiac Valves: InTech; 2018.

104. Filova E, Burdikova Z, Stankova L, Hadraba D, Svindrych Z, Schornik D, Bacakova L, Chlup H, Gultova E, Vesely J, Horny L, Zitny R, Straka F, Pirk J. Collagen structures in pericardium and aortic heart valves and their significance for tissue engineering2013.

105. Gu J, Lu Y, Deng M, Qiu M, Tian Y, Ji Y, Zong P, Shao Y, Zheng R, Zhou B, Sun W, Kong X. Inhibition of acetylation of histones 3 and 4 attenuates aortic valve calcification. Experimental and Molecular Medicine. 2019;51:1-14. doi: 10.1038/s12276-019-0272-9. PubMed PMID: 31292436.

106. Regulation of metabolism by mitochondrial enzyme acetylation in cardiac ischemia-reperfusion injury, (2020).

107. Wang SB, Venkatraman V, Crowgey EL, Liu T, Fu Z, Holewinski R, Ranek M, Kass DA, O'Rourke B, Van Eyk JE. Protein S-Nitrosylation Controls Glycogen Synthase Kinase 3β Function Independent of Its Phosphorylation State. Circulation Research. 2018;122:1517-31. doi: 10.1161/CIRCRESAHA.118.312789. PubMed PMID: 29563102.

108. Lal H, Ahmad F, Zhou J, Yu JE, Vagnozzi RJ, Guo Y, Yu D, Tsai EJ, Woodgett J, Gao E, Force T. Cardiac fibroblast glycogen synthase kinase-3β regulates ventricular remodeling and dysfunction in ischemic heart. Circulation. 2014;130:419-30. doi: 10.1161/CIRCULATIONAHA.113.008364. PubMed PMID: 24899689.

109. Majumdar U, Manivannan S, Basu M, Ueyama Y, Blaser MC, Cameron E, McDermott MR, Lincoln J, Cole SE, Wood S, Aikawa E, Lilly B, Garg V. Nitric oxide prevents aortic valve calcification by S-nitrosylation of USP9X to activate NOTCH signaling. Science Advances. 2021;7. doi: 10.1126/sciadv.abe3706. PubMed PMID: 33547080.

110. Li J, Johnson JA, Su H. Ubiquitin and ubiquitin-like proteins in cardiac disease and protection. Current Drug Targets. 2018;19:989-1002. doi: 10.2174/1389450117666151209114608. PubMed PMID: 26648080.

111. Grosche J, Meißner J, Eble JA. More than a syllable in fib-ROS-is: The role of ROS on the fibrotic extracellular matrix and on cellular contacts. Molecular Aspects of Medicine. 2018:0-1. doi: 10.1016/j.mam.2018.03.005.

112. Risteli M, Ruotsalainen H, Salo AM, Sormunen R, Sipilä L, Baker NL, Lamandé SR, Vimpari-Kauppinen L, Myllylä R. Reduction of lysyl hydroxylase 3 causes deleterious changes in the deposition and organization of extracellular matrix. Journal of Biological Chemistry. 2009;284:28204-11. doi: 10.1074/jbc.M109.038190. PubMed PMID: 19696018.

113. Proteoglycan form and function: A comprehensive nomenclature of proteoglycans, (2015).

114. Angel PM, Drake RR, Park Y, Clift CL, West C, Berkhiser S, Hardiman G, Mehta AS, Bichell D, Su YR. Spatial N-glycomics of the human aortic valve in development and pediatric endstage congenital aortic valve stenosis. Journal of Molecular and Cellular Cardiology. 2021;154:6-20. doi: 10.1016/j.yjmcc.2021.01.001.

115. Ohtsubo K, Marth JD. Glycosylation in cellular mechanisms of health and disease. Cell. 2006;126:855-67. doi: 10.1016/j.cell.2006.08.019.

116. Redox-mediated post-translational modifications of proteolytic enzymes and their role in protease functioning, (2020).

117. Raghunath M. Delayed Triple Helix Formation of Mutant Collagen from Patients with Osteogenesis Imperfecta. J Mol Biol. 1994.

118. Gjaltema RAF, Bank RA. Molecular insights into prolyl and lysyl hydroxylation of fibrillar collagens in health and disease. Critical Reviews in Biochemistry and Molecular Biology. 2016;52:74-95. doi: 10.1080/10409238.2016.1269716.

119. Peterkofsky B. Ascorbate requirement for hydroxylation and secretion of procollagen: relationship to inhibition of collagen synthesis in scurvy. The American Journal of Clinical Nutrition. 1991;54:1135S-40S. doi: 10.1093/ajcn/54.6.1135s.

120. Zhou T, Erber L, Liu B, Gao Y, Ruan H-B, Chen Y. Proteomic analysis reveals diverse proline hydroxylation-mediated oxygen-sensing cellular pathways in cancer cells. Oncotarget. 2016;7:79154-69. doi: 10.18632/oncotarget.12632. PubMed PMID: 27764789.

121. Chen Y, Guo H, Terajima M, Banerjee P, Liu X, Yu J, Momin AA, Katayama H, Hanash SM, Burns AR, Fields GB, Yamauchi M, Kurie JM. Lysyl hydroxylase 2 is secreted by tumor cells and can modify collagen in the extracellular space. Journal of Biological Chemistry. 2016;291:25799-808. doi: 10.1074/jbc.M116.759803. PubMed PMID: 27803159.

122. Kamel M, Wagih M, Kilic GS, Diaz-Arrastia CR, Baraka MA, Salama SA, Diaz-Arrastia CR, Kamel M, Salama SA, Wagih M, Kilic GS. Overhydroxylation of Lysine of Collagen Increases Uterine Fibroids Proliferation: Roles of Lysyl Hydroxylases, Lysyl Oxidases, and Matrix Metalloproteinases. BioMed Research International. 2017;2017:1-13. doi: 10.1155/2017/5316845.

123. Drug penetration in solid tumours, (2006).

124. Singha NC, Nekoroski T, Zhao C, Symons R, Jiang P, Frost GI, Huang Z, Shepard HM. Tumor-Associated Hyaluronan Limits Efficacy of Monoclonal Antibody Therapy. Molecular Cancer Therapeutics. 2014;14:523-32. doi: 10.1158/1535-7163.mct-14-0580. PubMed PMID: 25512619.

125. Myasoedova VA, Ravani AL, Frigerio B, Valerio V, Moschetta D, Songia P, Poggio P. Novel pharmacological targets for calcific aortic valve disease: Prevention and treatments. Pharmacological Research. 2018;136:74-82. doi: 10.1016/J.PHRS.2018.08.020.

126. Walraven M, Hinz B. Therapeutic approaches to control tissue repair and fibrosis: Extracellular matrix as a game changer. Matrix Biology. 2018;71-72:205-24. doi: 10.1016/j.matbio.2018.02.020. PubMed PMID: 29499355.

127. Noble PW, Albera C, Bradford WZ, Costabel U, Glassberg MK, Kardatzke D, King TE, Lancaster L, Sahn SA, Szwarcberg J, Valeyre D, du Bois RM. Pirfenidone in patients with idiopathic pulmonary fibrosis (CAPACITY): Two randomised trials. The Lancet. 2011;377:1760-9. doi: 10.1016/S0140-6736(11)60405-4.

128. Knüppel L, Ishikawa Y, Aichler M, Heinzelmann K, Hatz R, Behr J, Walch A, Bächinger HP, Eickelberg O, Staab-Weijnitz CA. A Novel Antifibrotic Mechanism of Nintedanib and Pirfenidone. Inhibition of Collagen Fibril Assembly. American Journal of Respiratory Cell and Molecular Biology. 2017;57:77-90. doi: 10.1165/rcmb.2016-0217OC.

129. Collagen Prolyl 4-Hydroxylase as a Therapeutic Target, (2018).

130. Brioschi M, Baetta R, Ghilardi S, Gianazza E, Guarino A, Parolari A, Polvani G, Tremoli E, Banfi C. Normal human mitral valve proteome: A preliminary investigation by gel-based and gel-free proteomic approaches. Electrophoresis. 2016;37:2633-43. doi: 10.1002/elps.201600081. PubMed PMID: 27450324.

131. Schlotter F, halu A, goto S, Blaser mC, body SC, Lee lH, higashi H, delaughter DM, hutcheson JD, vyas P, Pham t, rogers MA, sharma A, Seidman CECE, Loscalzo j, seidman JGjG, Aikawa MM, Singh SA, Aikawa E. Spatiotemporal multi-omics mapping generates a molecular atlas of the aortic valve and reveals networks driving disease. Circulation. 2018;138:377-93. doi: 10.1161/CIRCULATIONAHA.117.032291.

132. Gil-Dones F, Martin-Rojas T, Lopez-Almodovar LF, de la Cuesta F, Darde VM, Alvarez-Llamas G, Juarez-Tosina R, Barroso G, Vivanco F, Padial LR, Barderas MG. Valvular aortic Stenosis: A proteomic insight. Clinical Medicine Insights: Cardiology. 2010;4:1-7. doi: 10.4137/cmc.s3884.

133. Martín-Rojas T, Gil-Dones F, Lopez-Almodovar LF, Padial LR, Vivanco F, Barderas MG. Proteomic profile of human aortic stenosis: Insights into the degenerative process. Journal of Proteome Research. 2012;11:1537-50. doi: 10.1021/pr2005692. PubMed PMID: 22276806.

134. Martin-Rojas T, Mourino-Alvarez L, Alonso-Orgaz S, Rosello-Lleti E, Calvo E, Lopez-Almodovar LF, Rivera M, Padial LR, Lopez J-A, Cuesta Fdl, Barderas MG. iTRAQ proteomic analysis of extracellular matrix remodeling in aortic valve disease. Scientific Reports. 2015;5:17290. doi: 10.1038/srep17290.

135. Bouchareb R, Guauque-Olarte S, Snider J, Zaminski D, Anyanwu A, Stelzer P, Lebeche D. Proteomic Architecture of Valvular Extracellular Matrix: FNDC1 and MXRA5 Are New Biomarkers of Aortic Stenosis. JACC: Basic to Translational Science. 2021;6:25-39. doi: 10.1016/j.jacbts.2020.11.008.

136. Syedain ZH, Haynie B, Johnson SL, Lahti M, Berry J, Carney JP, Li J, Hill RC, Hansen KC, Thrivikraman G, Bianco R, Tranquillo RT. Pediatric tri-tube valved conduits made from fibroblast-produced extracellular matrix evaluated over 52 weeks in growing lambs. Science Translational Medicine. 2021;13:7225. doi: 10.1126/scitranslmed.abb7225. PubMed PMID: 33731437.

137. McCabe MC, Schmitt LR, Hill RC, Dzieciatkowska M, Maslanka M, Daamen WF, van Kuppevelt TH, Hof DJ, Hansen KC. Evaluation and Refinement of Sample Preparation Methods for Extracellular Matrix Proteome Coverage. Molecular & Cellular Proteomics. 2021;20:100079. doi: 10.1016/j.mcpro.2021.100079.

138. Naba A, Clauser KR, Ding H, Whittaker CA, Carr SA, Hynes RO. The extracellular matrix: Tools and insights for the "omics" era. Matrix Biology. 2016;49:10-24. doi: 10.1016/J.MATBIO.2015.06.003.

139. Naba A, Pearce OMT, Rosario AD, Ma D, Ding H, Rajeeve V, Cutillas PR, Balkwill FR, Hynes RO. Characterization of the Extracellular Matrix of Normal and Diseased Tissues Using Proteomics. Journal of Proteome Research. 2017;16:17. doi: 10.1021/acs.jproteome.7b00191.

140. Naba A, Clauser KR, Hynes RO. Enrichment of Extracellular Matrix Proteins from Tissues and Digestion into Peptides for Mass Spectrometry Analysis. Journal of visualized experiments : JoVE. 2015:e53057. doi: 10.3791/53057. PubMed PMID: 26273955.

141. Angel PM, Comte-Walters S, Ball LE, Talbot K, Brockbank KGM, Mehta AS, Drake RR. Mapping Extracellular Matrix Proteins in Formalin-Fixed, Paraffin-embedded Tissues by MALDI Imaging Mass Spectrometry. Journal of Proteome Research. 2018;17(1):635-46. PMID: 29161047.

142. Angel PM, Bruner E, Bethard J, Clift CL, Ball L, Drake RR, Feghali-Bostwick C. Extracellular matrix alterations in low-grade lung adenocarcinoma compared with

normal lung tissue by imaging mass spectrometry. Journal of Mass Spectrometry. 2020;55. doi: 10.1002/jms.4450. PubMed PMID: 31654589.

143. Angel PM, Schwamborn K, Comte-Walters S, Clift C, Ball LE, Mehta AS, Drake RR. Extracellular Matrix Imaging of Breast Tissue Pathologies by MALDI Imaging Mass Spectrometry. Proteomics Clinical Applications. 2019;13(1).

144. Angel PM, Spruill L, Jefferson M, Bethard JB, Ball LE, Hughes-Halbert C, Drake RR. Zonal Regulation of Collagen Types and Post-Translational Modifications In Prostatic Benign and Cancer Tissues By Imaging Mass Spectrometry. The Prostate. 2020;In press.

145. Clift CL, Drake RR, Mehta A, Angel PM. Multiplexed imaging mass spectrometry of the extracellular matrix using serial enzyme digests from formalin-fixed paraffin-embedded tissue sections. Analytical and Bioanalytical Chemistry 2020. 2020:1-11. doi: 10.1007/S00216-020-03047-Z.

146. Duarte AS, Correia A, Esteves AC. Bacterial collagenases – A review. Critical Reviews in Microbiology. 2016;42:106-26. doi: 10.3109/1040841X.2014.904270.

147. Egerstedt A, Berntsson J, Smith ML, Gidlöf O, Nilsson R, Benson M, Wells QS, Celik S, Lejonberg C, Farrell L, Sinha S, Shen D, Lundgren J, Rådegran G, Ngo D, Engström G, Yang Q, Wang TJ, Gerszten RE, Smith JG. Profiling of the plasma proteome across different stages of human heart failure. Nature Communications. 2019;10:1-13. doi: 10.1038/s41467-019-13306-y. PubMed PMID: 31862877.

148. McDonald K, Glezeva N, Collier P, O'Reilly J, O'Connell E, Tea I, Russell-Hallinan A, Tonry C, Pennington S, Gallagher J, Ledwidge M, Baugh J, Watson CJ. Tetranectin, a potential novel diagnostic biomarker of heart failure, is expressed within the myocardium and associates with cardiac fibrosis. Scientific Reports. 2020;10:1-12. doi: 10.1038/s41598-020-64558-4. PubMed PMID: 32371911.

149. Landi C, Bergantini L, Cameli P, d'Alessandro M, Carleo A, Shaba E, Rottoli P, Bini L, Bargagli E. Idiopathic Pulmonary Fibrosis Serum proteomic analysis before and after nintedanib therapy. Scientific Reports. 2020;10:1-9. doi: 10.1038/s41598-020-66296-z. PubMed PMID: 32523095.

150. Cheung KJ, Tilleman K, Deforce D, Colle I, Van Vlierberghe H. The HCV serum proteome: a search for fibrosis protein markers. Journal of Viral Hepatitis. 2009;16:418-29. doi: 10.1111/j.1365-2893.2009.01083.x.

151. Proteomic analysis of the cardiac extracellular matrix: clinical research applications, (2018).

152. Aikawa E, Blaser MC, Kraler S, Lüscher TF. AORTIC VALVE DISEASE REVIEW SERIES Multi-Omics Approaches to Define Calcific Aortic Valve Disease Pathogenesis. Circulation Research. 2021;128:1371-97. doi: 10.1161/CIRCRESAHA.120.317979.

153. Chester AH, Grande-Allen KJ. Which Biological Properties of Heart Valves Are Relevant to Tissue Engineering?2020;7:63. doi: 10.3389/fcvm.2020.00063.

154. Angel PM, Comte-Walters S, Ball LE, Talbot K, Mehta AS, Brockbank KGMM, Drake RR. Mapping Extracellular Matrix Proteins in Formalin-Fixed, Paraffin-Embedded Tissues by MALDI Imaging Mass Spectrometry. Journal of Proteome Research. 2018;17:635-46. doi: 10.1021/acs.jproteome.7b00713.

155. Clift CL, Mehta A, Drake RR, Angel PM. Multiplexed Imaging Mass Spectrometry of Histological Staining, N-glycan and Extracellular Matrix from One Tissue Section: A Tool for Fibrosis Research2019.

156. Angel PM, Schwamborn K, Comte-Walters S, Clift CL, Ball LE, Mehta AS, Drake RR. Extracellular Matrix Imaging of Breast Tissue Pathologies by MALDI Imaging

Mass Spectrometry. PROTEOMICS - Clinical Applications. 2018;1700152:1700152. doi: 10.1002/prca.201700152.

157. Angel PM, Spruill L, Jefferson M, Bethard JR, Ball LE, Hughes-Halbert C, Drake RR. Zonal regulation of collagen-type proteins and posttranslational modifications in prostatic benign and cancer tissues by imaging mass spectrometry. The Prostate. 2020;80:1071-86. doi: 10.1002/pros.24031.

158. Angel PM, Baldwin HS, Gottlieb Sen D, Su YR, Mayer JE, Bichell D, Drake RR. Advances in MALDI imaging mass spectrometry of proteins in cardiac tissue, including the heart valve. Biochimica et Biophysica Acta - Proteins and Proteomics. 2017;1865:927-35. doi: 10.1016/j.bbapap.2017.03.009. PubMed PMID: 28341601.

159. Mourino-Alvarez L, Iloro I, De La Cuesta F, Azkargorta M, Sastre-Oliva T, Escobes I, Lopez-Almodovar LF, Sanchez PL, Urreta H, Fernandez-Aviles F, Pinto A, Padial LR, Akerström F, Elortza F, Barderas MG. MALDI-Imaging Mass Spectrometry: a step forward in the anatomopathological characterization of stenotic aortic valve tissue OPEN. Nature Publishing Group. 2016. doi: 10.1038/srep27106.

160. Lim J, Aguilan JT, Sellers RS, Nagajyothi F, Weiss LM, Angeletti RH, Bortnick AE. Lipid mass spectrometry imaging and proteomic analysis of severe aortic stenosis. Journal of Molecular Histology. 2020;51:559-71. doi: 10.1007/s10735-020-09905-5. PubMed PMID: 32794037.

161. Angel PM, Bayoumi AS, Hinton RB, Su YR, Bichell D, Mayer JE, Baldwin HS, Caprioloi RM, Ru Su Y, Scott Baldwin H. MALDI-IMS as a lipidomic Approach to Heart Valve Research2016;25:240-52. PubMed PMID: 27989075.

162. Chaurand P, Cornett DS, Angel PM, Caprioli RM. From whole-body sections down to cellular level, multiscale imaging of phospholipids by MALDI mass spectrometry. Molecular and Cellular Proteomics. 2011;10. doi: 10.1074/mcp.O110.004259. PubMed PMID: 20736411.

163. Atkins SK, Singh SA, Aikawa E. Calcific Aortic Valve Disease "Omics" Is Timely, But Are We Looking Too Late? JACC: Basic to Translational Science. 2020;5:1178-80. doi: 10.1016/j.jacbts.2020.11.001.

164. Nkomo VT, Gardin JM, Skelton TN, Gottdiener JS, Scott CG, Enriquez-Sarano M. Burden of valvular heart diseases: a population-based study. The Lancet. 2006;368:1005-11. doi: 10.1016/S0140-6736(06)69208-8.

165. Tsamis A, Krawiec JT, Vorp DA. Elastin and collagen fibre microstructure of the human aorta in ageing and disease: A review2013;10:20121004-. doi: 10.1098/rsif.2012.1004. PubMed PMID: 23536538.

166. Hanson KP, Jung JP, Tran QA, Hsu S-PP, Iida R, Ajeti V, Campagnola PJ, Eliceiri KW, Squirrell JM, Lyons GE, Ogle BM. Spatial and temporal analysis of extracellular matrix proteins in the developing murine heart: a blueprint for regeneration. Tissue engineering Part A. 2013;19:1132-43. doi: 10.1089/ten.TEA.2012.0316. PubMed PMID: 23273220.

167. Gilkes DM, Bajpai S, Chaturvedi P, Wirtz D, Semenza GL. Hypoxia-inducible factor 1 (HIF-1) promotes extracellular matrix remodeling under hypoxic conditions by inducing P4HA1, P4HA2, and PLOD2 expression in fibroblasts. The Journal of biological chemistry. 2013;288:10819-29. doi: 10.1074/jbc.M112.442939. PubMed PMID: 23423382.

168. Gilkes DM, Chaturvedi P, Bajpai S, Wong CC-L, Wei H, Pitcairn S, Hubbi ME, Wirtz D, Semenza GL. Collagen Prolyl Hydroxylases are Essential for Breast

Cancer Metastasis. Cancer research. 2013;73:3285. doi: 10.1158/0008-5472.CAN-12-3963. PubMed PMID: 23539444.

169. Yang C, Park AC, Davis NA, Russell JD, Kim B, Brand DD, Lawrence MJ, Ge Y, Westphall MS, Coon JJ, Greenspan DS. Comprehensive mass spectrometric mapping of the hydroxylated amino acid residues of the α1(V) collagen chain. Journal of Biological Chemistry. 2012;287:40598-610. doi: 10.1074/jbc.M112.406850. PubMed PMID: 23060441.

170. Choi B, Lee SRS, Kim SM, Lee EJ, Lee SRS, Kim DH, Jang JY, Kang SW, Lee KU, Chang EJ, Song JK. Dipeptidyl peptidase-4 induces aortic valve calcifcation by inhibiting insulin-like growth factor-1 signaling in valvular interstitial cells. Circulation. 2017;135:1935-50. doi: 10.1161/CIRCULATIONAHA.116.024270. PubMed PMID: 28179397.

171. Aikawa E, Libby P. A rock and a hard place chiseling away at the multiple mechanisms of aortic stenosis. Circulation. 2017;135:1951-5. doi: 10.1161/CIRCULATIONAHA.117.027776. PubMed PMID: 28507250.

172. Kirklin JW, Kouchoukos NT. Cardiac surgery: congenital aortic stenosis1993:1195-237. Epub 2.

173. d'Arcy JL, Prendergast BD, Chambers JB, Ray SG, Bridgewater B. Valvular Heart Disease: The Next Cardiac Epidemic. British Medical Journal. 2010;97:91-3.

174. Levay AK, Peacock JD, Lu Y, Koch M, Hinton RB, Kadler KE, Lincoln J. Scleraxis Is Required for Cell Lineage Differentiation and Extracellular Matrix Remodeling During Murine Heart Valve Formation In Vivo. Circulation Research. 2008;103:948-56. doi: 10.1161/CIRCRESAHA.108.177238.

175. Aikawa E, Whittaker P, Farber M, Mendelson K, Padera RF, Aikawa M, Schoen FJ. Human semilunar cardiac valve remodeling by activated cells from fetus to adult: implications for postnatal adaptation, pathology, and tissue engineering. Circulation. 2006;113(10):1344-52. Epub 2006/03/15. doi: 10.1161/CIRCULATIONAHA.105.591768. PubMed PMID: 16534030.

176. Tsamis A, Krawiec JT, Vorp DA. Elastin and collagen fibre microstructure of the human aorta in ageing and disease: a review. Journal of The Royal Society Interface. 2013;10:20121004-. doi: 10.1098/rsif.2012.1004.

177. Joyce EM, Liao J, Schoen FJ, Mayer JE, Sacks MS. Functional Collagen Fiber Architecture of the Pulmonary Heart Valve Cusp. The Annals of Thoracic Surgery. 2009;87(4):1240-9.

178. Schoen FJ. Evolving concepts of cardiac valve dynamics: the continuum of development, functional structure, pathobiology, and tissue engineering. Circulation. 2008;118(18):1864-80. PMID:18955677.

179. Oomen PJA, Loerakker S, Van Geemen D, Neggers J, Goumans MJ, Van Den Bogaerdt AJ, Bogers A, Bouten CVC, Baaijens FPT. Age-dependent changes of stress and strain in the human heart valve and their relation with collagen remodeling. Acta Biomaterialia. 2016;29:161-9.

180. Peacock JD, Lu Y, Koch M, Kadler KE, Lincoln J. Temporal and spatial expression of collagens during murine atrioventricular heart valve development and maintenance. Developmental Dynamics. 2008;237(10):3051-8.

181. Aikawa E, Whittaker P, Farber M, Mendelson K, Padera RF, Aikawa M, Schoen FJ. Human Semilunar Cardiac Valve Remodeling by Activated Cells From Fetus to Adult: Implications for Postnatal Adaptation, Pathology, and Tissue Engineering. Circulation. 2006;113(10):1344-52. PMID:16534030.

182. Lockhart M, Wirrig E, Phelps A, Wessels A. Extracellular matrix and heart development. Birth Defects Research Part A: Clinical and Molecular Teratology. 2011;91(6):535-50.

183. Wirrig EE, Hinton RB, Yutzey KE. Differential expression of cartilage and bone-related proteins in pediatric and adult diseased aortic valves. Journal of Molecular and Cellular Cardiology. 2011;50(3):561-9. PMID:21163264, PMCID: PMC3035730.

184. Hinton Jr RB, Lincoln J, Deutsch GH, Osinska H, Manning PB, Benson DW, Yutzey KE. Extracellular matrix remodeling and organization in developing and diseased aortic valves. Circulation Research. 2006;98(11):1431-8. PMID:16645142.

185. Hutson HN, Marohl T, Anderson M, Eliceiri K, Campagnola P, Masters KS. Calcific aortic valve disease is associated with layer-specific alterations in collagen architecture. PloS One. 2016;11(9).

186. Eriksen HA, Satta J, Risteli J, Veijola M, Väre P, Soini Y. Type I and type III collagen synthesis and composition in the valve matrix in aortic valve stenosis. Atherosclerosis. 2006;189(1):91-8.

187. Podlesnikar T, Delgado V, Bax JJ. Cardiovascular magnetic resonance imaging to assess myocardial fibrosis in valvular heart disease. The International Journal of Cardiovascular Imaging. 2018;34(1):97-112.

188. Pinkert MA, Hortensius RA, Ogle BM, Eliceiri KW. Imaging the Cardiac Extracellular Matrix. Cardiac Extracellular Matrix: Springer; 2018. p. 21-44.

189. Angel PM, Bruner E, Clift CL, Bethard JB, Ball LE, Drake RR, Feghali-Bostwick C. Extracellular Matrix Alterations in Low Grade Lung Adenocarcinoma Compared to Normal Lung Tissue by Imaging Mass Spectrometry. Journal of Mass Spectrometry. 2019;In press.

190. Williams K, Thomson D, Seto I, Contopoulos-Ioannidis DG, Ioannidis JPA, Curtis S, Constantin E, Batmanabane G, Hartling L, Klassen T, Offringa M. Standard 6: Age groups for pediatric trials. Pediatrics. 2012;129:S153-S60. doi: 10.1542/peds.2012-0055I. PubMed PMID: 22661762.

191. Collins TJ. ImageJ for microscopy. Biotechniques. 2007;43(1 Suppl):25-30. PMID: 17936939.

192. Bredfeldt JS, Liu Y, Pehlke CA, Conklin MW, Szulczewski JM, Inman DR, Keely PJ, Nowak RD, Mackie TR, Eliceiri KW. Computational segmentation of collagen fibers from second-harmonic generation images of breast cancer. Journal of Biomedical Optics. 2014;19(1):016007.

193. Sprung RW, Brock JWC, Tanksley JP, Li M, Washington MK, Slebos RJC, Liebler DC. Equivalence of protein inventories obtained from formalin-fixed paraffin-embedded and frozen tissue in multidimensional liquid chromatography-tandem mass spectrometry shotgun proteomic analysis. Molecular & Cellular Proteomics. 2009;8(8):1988-98. PMCID: PMC2722776.

194. Rappsilber J, Ishihama Y, Mann M. Stop and go extraction tips for matrix-assisted laser desorption/ionization, nanoelectrospray, and LC/MS sample pretreatment in proteomics. Analytical Chemistry. 2003;75(3):663-70.

195. Tyanova S, Temu T, Cox J. The MaxQuant computational platform for mass spectrometry-based shotgun proteomics. Nature Protocols. 2016;11(12):2301-19.

196. Tyanova S, Temu T, Sinitcyn P, Carlson A, Hein MY, Geiger T, Mann M, Cox J. The Perseus computational platform for comprehensive analysis of (prote) omics data. Nature methods. 2016;13(9):731.

197. Ashburner M, Ball CA, Blake JA, Botstein D, Butler H, Cherry JM, Davis AP, Dolinski K, Dwight SS, Eppig JT. Gene ontology: tool for the unification of biology. Nature Genetics. 2000;25(1):25-9.
198. Gene Ontology C. The gene ontology resource: 20 years and still GOing strong. Nucleic Acids Research. 2019;47(D1):D330-D8.
199. Mi H, Muruganujan A, Ebert D, Huang X, Thomas PD. PANTHER version 14: more genomes, a new PANTHER GO-slim and improvements in enrichment analysis tools. Nucleic Acids Research. 2019;47(D1):D419-D26.
200. Saeed AIB, N. K.; Braisted, J. C.; Liang, W.; Sharov, V.; Howe, E. A.; Li, J.; Thiagarajan, M.; White, J. A.; Quackenbush, J.,. TM4 Microarray Software Suite. . Methods in Enzymology 2006;411:134-93; PMCID: PMID: 16939790.
201. Su YR, Linton MF, Fazio S. Rapid quantification of murine ABC mRNAs by real time reverse transcriptase-polymerase chain reaction. Journal of Lipid Research. 2002;43:2180-7. doi: 10.1194/jlr.D200020-JLR200. PubMed PMID: 12454281.
202. Bustin SA, Benes V, Garson JA, Hellemans J, Huggett J, Kubista M, Mueller R, Nolan T, Pfaffl MW, Shipley GL, Vandesompele J, Wittwer CT. The MIQE Guidelines: Minimum Information for Publication of Quantitative Real-Time PCR Experiments. Clinical Chemistry. 2009;55:611-22. doi: 10.1373/clinchem.2008.112797.
203. Angel PM, Comte-Walters S, Ball LE, Talbot K, Mehta A, Brockbank KGM, Drake RR. Mapping Extracellular Matrix Proteins in Formalin-Fixed, Paraffin-Embedded Tissues by MALDI Imaging Mass Spectrometry. Journal of Proteome Research. 2018. doi: 10.1021/acs.jproteome.7b00713.
204. Wirrig EE, Hinton RB, Yutzey KE. Differential expression of cartilage and bone-realted proteins in pediatric and adult diseased aortic valves. J Mol Cell Cardiol. 2012;50:561-9. doi: 10.1016/j.yjmcc.2010.12.005.
205. Herovici. A polychrome stain for differentiating precollagen from collagen. Stain Technology. 1963;38:204-6.
206. Fidler AL, Boudko SP, Rokas A, Hudson BG. The triple helix of collagens - An ancient protein structure that enabled animal multicellularity and tissue evolution. Journal of Cell Science. 2018;131. doi: 10.1242/jcs.203950. PubMed PMID: 29632050.
207. Farndale RW. Collagen-binding proteins: Insights from the Collagen toolkits. Essays in Biochemistry. 2019;63:337-48. doi: 10.1042/EBC20180070.
208. Sipila KH, Drushinin K, Rappu P, Johanna J, Salminen TA, Salo AM, Kapyla J, Myllyharju J, Heino J. Proline hydroxylation in collagen supports integrin binding by two distinct mechanisms. J Biol Chem. 2018;293(20):7645-58.
209. Carolina G-C, Esther R-L, Ana O, Estefanı́a Tn, Carlos TJ, Luis Mn-D, Ramo´n Gl-JJ, Francisca L, Manuel Ps, Miguel R. New Altered Non-Fibrillar Collagens in Human Dilated Cardiomyopathy: Role in the Remodeling Process. PLOS one. 2016;11(12).
210. Skonier J, Bennett K, Rothwell V, Kosowski S, Plowman G, Wallace P, Edelhoff S, Disteche C, Neubauer M, Marquardt H. βig-h3: a transforming growth factor-β-responsive gene encoding a secreted protein that inhibits cell attachment in vitro and suppresses the growth of CHO cells in nude mice. DNA and Cell Biology. 1994;13(6):571-84.
211. Roberts AB, McCune BK, Sporn MB. TGF-beta: Regulation of extracllular matrix. Kidney International. 1992;41:557-9.

212. Kuroda N MM, Tawara I, Tsuboi J, Yoneda M, Nishikawa K, Kageyama Y, Hachiya K, Ohishi K, Miwi H, Yamada R, Hamada Y, Tanaka K, Kato T, Takei Y, Katayama N. Infiltrating CCR2+ monocytes and their progenies, fibrocytes, contribute to colon fibrosis by inhibiting collagen degradation through the production of TIMP-1. Nature Scientific Reports. 2019;9(8568).

213. Ling M LA. Novel approach to inhibiting chemokine function. EMBO Mol Med. 2011;3(9):510-2. doi: 10.1002/emmm.201100161; PMCID: PMC3377098.

214. Lin Z, Gao C, Ning Y, He X, Wu W, Chen Y-G. The pseudoreceptor BMP and activin membrane-bound inhibitor positively modulates Wnt/β-catenin signaling. Journal of Biological Chemistry. 2008;283(48):33053-8.

215. Onichtchouk D, Chen Y-G, Dosch R, Gawantka V, Delius H, Massague J, Niehrs C. Silencing of TGF-β signalling by the pseudoreceptor BAMBI. Nature. 1999;401(6752):480-5.

216. Yan X, Lin Z, Chen F, Zhao X, Chen H, Ning Y, Chen Y-G. Human BAMBI cooperates with Smad7 to inhibit transforming growth factor-β signaling. Journal of Biological Chemistry. 2009;284(44):30097-104.

217. Villar AV, García R, Llano M, Cobo M, Merino D, Lantero A, Tramullas M, Hurlé JM, Hurlé MA, Nistal JF. BAMBI (BMP and activin membrane-bound inhibitor) protects the murine heart from pressure-overload biomechanical stress by restraining TGF-β signaling. Biochimica et Biophysica Acta - Molecular Basis of Disease. 2013;1832:323-35. doi: 10.1016/j.bbadis.2012.11.007.

218. Krä Mer A, Green J, Pollard J, Tugendreich S. Systems biology Causal analysis approaches in Ingenuity Pathway Analysis2014:1-8. doi: 10.1093/bioinformatics/btt703.

219. Wirrig EE, Yutzey KE. Conserved transcriptional regulatory mechanisms in aortic valve development and disease. Arteriosclerosis, Thrombosis, and Vascular Biology. 2014;34(4):737-41.

220. Nordquist E, LaHaye S, Nagel C, Lincoln J. Postnatal and Adult Aortic Heart Valves Have Distinctive Transcriptional Profiles Associated With Valve Tissue Growth and Maintenance Respectively. Frontiers in Cardiovascular Medicine. 2018;5:30.PMCID: PMC5928323.

221. Lincoln J, Garg V. Etiology of Valvular Heart Disease. Circulation Journal. 2014;78(8):1801-7. PMID: 24998280.

222. Hinton RB. Genetics of Bicuspid Aortic Valve and Calcific Aortic Valve Disease. 2013. In: Calcific Aortic Valve Disease [Internet]. Rijeka, Croatia: InTech , Europe; [Chapter 7. 173-203. http://dx.doi.org/10.5772/55506].

223. Lewin MB, Otto CM. The bicuspid aortic valve: adverse outcomes from infancy to old age. Circulation. 2005;111(7):832-4.

224. Hinton RB, Martin LJ, Rame-Gowda S, Tabangin ME, Cripe LH, Benson DW. Hypoplastic left heart syndrome links to chromosomes 10q and 6q and is genetically related to bicuspid aortic valve. Journal of the American College of Cardiology. 2009;53(12):1065.

225. Martin LJ, Ramachandran V, Cripe LH, Hinton RB, Andelfinger G, Tabangin M, Shooner K, Keddache M, Benson DW. Evidence in favor of linkage to human chromosomal regions 18q, 5q and 13q for bicuspid aortic valve and associated cardiovascular malformations. Human Genetics. 2007;121(2):275-84. PMID:17203300.

226. Hitz MP, Brand T, Andelfinger G. Genetic regulation of heart valve development: Clinical implications. Aswan Heart Centre Science & Practice Series. 2011;2011(9):DOI: http://dx.doi.org/10.5339/ahcsps.2011.09.

227. Simard L, Côté N, Dagenais F, Mathieu P, Couture C, Trahan S, Bossé Y, Mohammadi S, Pagé S, Joubert P, Clavel MA. Sex-related discordance between aortic valve calcification and hemodynamic severity of aortic stenosis. Circulation Research. 2017;120:681-91. doi: 10.1161/CIRCRESAHA.116.309306. PubMed PMID: 27879282.

228. Voisine M, Hervault M, Shen M, Boilard A-J, Filion B, Rosa M, Bossé Y, Mathieu P, Côté N, Clavel M-A. Age, Sex, and Valve Phenotype Differences in Fibro-Calcific Remodeling of Calcified Aortic Valve2020. doi: 10.1161/JAHA.119.015610.

229. Henaine R, Roubertie F, Vergnat M, Ninet J. Valve replacement in children: A challenge for a whole life. Archives of Cardiovascular Disease. 2012;105(10):517-28. PMID:23062483.

230. Sharabiani MTA, Dorobantu DM, Mahani AS, Turner M, Tometzki AJP, Angelini GD, Parry AJ, Caputo M, Stoica SC. Aortic valve replacement and the Ross operation in children and young adults. Journal of the American College of Cardiology. 2016;67(24):2858-70.

231. Myllyharju J, Kivirikko KI. Collagens, modifying enzymes and their mutations in humans, flies and worms. TRENDS in Genetics. 2004;20(1):33-43.PMID: 14698617.

232. Bella J. Collagen structure: new tricks from a very old dog. Biochemical Journal. 2016;473(8):1001-25.PMID: 27060106.

233. Krane SM. The importance of proline residues in the structure, stability and susceptibility to proteolytic degradation of collagens. Amino Acids. 2008;35(4):703-10. PMID: 18431533.

234. Wedemeyer WJ, Welker E, Scheraga HA. Proline cis− trans isomerization and protein folding. Biochemistry. 2002;41(50):14637-44. PMID: 12475212.

235. Tang L, Zeng J, Geng P, Fang C, Wang Y, Sun M, Wang C, Wang J, Yin P, Hu C. Global Metabolic Profiling Identifies a Pivotal Role of Proline and Hydroxyproline Metabolism in Supporting Hypoxic Response in Hepatocellular Carcinoma. Clinical Cancer Research. 2018;24(2):474-85.PMID: 29084919.

236. Gorres KL, Raines RT. Prolyl 4-hydroxylase. Critical Reviews in Biochemistry and Molecular Biology. 2010;45(2):106-24. PMCID: PMC2841224.

237. Annunen P, Autio-Harmainen H, Kivirikko KI. The novel type II prolyl 4-hydroxylase is the main enzyme form in chondrocytes and capillary endothelial cells, whereas the type I enzyme predominates in most cells. J Biol Chem. 1998;273(11):5989-92. PMID: 9497309.

238. Hamaia S, Farndale RW. Integrin recognition motifs in the human collagens. Advances in Experimental Medicine and Biology. 2014;819:127-42.

239. Ilamaran M, Janeena A, Valappil S, Ramudu KN, Shanmugam G, Niraikulam A. A self-assembly and higher order structure forming triple helical protein as a novel biomaterial for cell proliferation. Biomaterials Science. 2019;7(5):2191-9.

240. Davidenko N, Hamaia S, Bax DV, Malcor J-D, Schuster CF, Gullberg D, Farndale RW, Best SM, Cameron RE. Selecting the correct cellular model for assessing of the biological response of collagen-based biomaterials. Acta Biomaterialia. 2018;65:88-101. PMID: 25023172.

241. Leitinger B. Molecular analysis of collagen binding by the human discoidin domain receptors, DDR1 and DDR2 identification of collagen binding sites in DDR2. J Biol Chem. 2003;278(19):16761-9.
242. Sipilä KH, Drushinin K, Rappu P, Jokinen J, Salminen TA, Salo AM, Käpylä J, Myllyharju J, Heino J. Proline hydroxylation in collagen supports integrin binding by two distinct mechanisms. J Biol Chem. 2018;293(20):7645-58. PMCID: PMC5961056.
243. Ilamaran M, Janeena A, Valappil S, Ramudu KN, Shanmugam G, Niraikulam A. A self-assembly and higher order structure forming triple helical protein as a novel biomaterial for cell proliferation. Biomaterials Science. 2019;7(5):2191-9. PMID: 30900708.
244. Hamaia S, Farndale RW. Integrin recognition motifs in the human collagens. I Domain Integrins: Springer; 2014. p. 127-42. PMID: 25023172.
245. Wasinski B, Sohail A, Bonfil RD, Kim S, Saliganan A, Polin L, Bouhamdan M, Kim H-RC, Prunotto M, Fridman R. Discoidin Domain Receptors, DDR1b and DDR2, Promote Tumour Growth within Collagen but DDR1b Suppresses Experimental Lung Metastasis in HT1080 Xenografts. Scientific Reports. 2020;10(1):1-21.
246. Zeltz C, Gullberg D. The integrin-collagen connection - a glue for tissue repair? Journal of Cell Science. 2016;129:653-64. doi: 10.1242/jcs.180992.
247. Miura Y, Takahashi T, Jung SM, Moroi M. Analysis of the interaction of platelet collagen receptor glycoprotein VI (GPVI) with collagen: A dimeric form of GPVI, but not the monomeric form, shows affinity to fibrous collagen. Journal of Biological Chemistry. 2002;277:46197-204. doi: 10.1074/jbc.M204029200.
248. O'Brien JR, Etherington MD, Brant J, Watkins J. Decreased platelet function in aortic valve stenosis: High shear platelet activation then inactivation. Heart. 1995;74:641-4. doi: 10.1136/hrt.74.6.641.
249. Leeming DJ, Karsdal MA. Type V Collagen2016. doi: 10.1016/B978-0-12-809847-9.00005-2.
250. Molecular imaging of fibrosis: Recent advances and future directions, (2019).
251. Riley H, Bradshaw A. The Influence of the Extracellualr Matrix in Inflammation: Findings from the SPARC null mouse. The Anatomical Record. 2019;303(6):1624-9. doi: 10.1002/ar.24133.
252. Armstrong EJ, Bischoff J, Deutsch GH, Osinska H, Manning PB, Benson DW, Yutzey KE. Heart Valve Development: Endothelial Cell Signaling and Differentiation. Circulation Research. 2004;95:459-70. doi: 10.1161/01.RES.0000141146.95728.da. PubMed PMID: 15345668.
253. Rabkin-Aikawa E, Farber M, Aikawa M, Schoen FJ. Dynamic and reversible changes of interstitial cell phenotype during remodeling of cardiac valves2004.
254. Angel PM, Mehta A, Norris-Caneda K, Drake RR. MALDI Imaging Mass Spectrometry of N-glycans and Tryptic Peptides from the Same Formalin-Fixed, Paraffin-Embedded Tissue Section. Methods in Molecular Biology: Humana Press Inc.; 2018. p. 225-41.
255. Cox TR, Erler JT. Remodeling and homeostasis of the extracellular matrix: implications for fibrotic diseases and cancer. Disease Models & Mechanisms. 2011;4:165-78. doi: 10.1242/dmm.004077. PubMed PMID: 21324931.
256. Cardiac fibroblasts, fibrosis and extracellular matrix remodeling in heart disease, (2012).
257. MALDI imaging mass spectrometry — From bench to bedside, (2017).

258. West CA, Wang M, Herrera H, Liang H, Black A, Angel PM, Drake RR, Mehta AS. N-Linked Glycan Branching and Fucosylation Are Increased Directly in Hcc Tissue As Determined through in Situ Glycan Imaging. Journal of Proteome Research. 2018;17:3454-62. doi: 10.1021/acs.jproteome.8b00323.

259. Drake RR, West CA, Mehta AS, Angel PM. MALDI Mass Spectrometry Imaging of N-Linked Glycans in Tissues. Springer, Singapore; 2018. p. 59-76.

260. Powers TW, Neely BA, Shao Y, Tang H, Troyer DA, Mehta AS, Haab BB, Drake RR. MALDI imaging mass spectrometry profiling of N-glycans in formalin-fixed paraffin embedded clinical tissue blocks and tissue microarrays. PLoS ONE. 2014;9:106255. doi: 10.1371/journal.pone.0106255. PubMed PMID: 25184632.

261. Angel PM, Caprioli RM. Matrix-assisted laser desorption ionization imaging mass spectrometry: In situ molecular mapping. Biochemistry. 2013;52:3818-28. doi: 10.1021/bi301519p. PubMed PMID: 23259809.

262. Angel PM, Mehta A, Norris-Caneda K, Drake RR. MALDI Imaging Mass Spectrometry of N-glycans and Tryptic Peptides from the Same Formalin-Fixed, Paraffin-Embedded Tissue Section.2018;1788:225-41. doi: 10.1007/7651_2017_81. PubMed PMID: 29058228.

263. Norris JL, Caprioli RM. Analysis of Tissue Specimens by Matrix-Assisted Laser Desorption/Ionization Imaging Mass Spectrometry in Biological and Clinical Research. Chemical Reviews. 2013;113:2309-42. doi: 10.1021/cr3004295.

264. Frantz C, Stewart KM, Weaver VM. The extracellular matrix at a glance. Journal of Cell Science. 2010;123:4195-200. doi: 10.1242/jcs.023820.

265. Proteoglycans: From structural compounds to signaling molecules, (2010).

266. Sethi MK, Downs M, Zaia J. Serial in-solution digestion protocol for mass spectrometry-based glycomics and proteomics analysis. Molecular Omics. 2020. doi: 10.1039/d0mo00019a.

267. Ruhaak LR, Xu G, Li Q, Goonatilleke E, Lebrilla CB. Mass Spectrometry Approaches to Glycomic and Glycoproteomic Analyses. Chemical Reviews. 2018;118:7886-930. doi: 10.1021/acs.chemrev.7b00732.

268. Raghunathan R, Sethi MK, Zaia J. On-slide tissue digestion for mass spectrometry based glycomic and proteomic profiling. MethodsX. 2019;6:2329-47. doi: 10.1016/j.mex.2019.09.029.

269. Gessela M, Spraggins JM, Voziyanb P, Hudsonb BG, Caprioli RM. Decellularization of intact tissue enables MALDI imaging mass spectrometry analysis of the extracellular matrix. J Mass Spectrom. 2015;50:1288-93. doi: 10.1016/j.physbeh.2017.03.040.

270. Heijs B, Holst S, Briaire-De Bruijn IH, Van Pelt GW, De Ru AH, Van Veelen PA, Drake RR, Mehta AS, Mesker WE, Tollenaar RA, Boveé JVMG, Wuhrer M, Mcdonnell LA. Multimodal Mass Spectrometry Imaging of N-Glycans and Proteins from the Same Tissue Section2016. doi: 10.1021/acs.analchem.6b01739.

271. Aichler M, Kunzke T, Buck A, Sun N, Ackermann M, Jonigk D, Gaumann A, Walch A. Molecular similarities and differences from human pulmonary fibrosis and corresponding mouse model: MALDI imaging mass spectrometry in comparative medicine. Laboratory Investigation. 2018;98:141-9. doi: 10.1038/labinvest.2017.110.

272. Ceroni A, Maass K, Geyer H, Geyer R, Dell A, Haslam SM. GlycoWorkbench: A tool for the computer-assisted annotation of mass spectra of glycans. Journal of Proteome Research. 2008;7:1650-9. doi: 10.1021/pr7008252. PubMed PMID: 18311910.

273. Protein analysis by shotgun/bottom-up proteomics, (2013).

274. Zhao RR, Ackers-Johnson M, Stenzig J, Chen C, Ding T, Zhou Y, Wang P, Ng SL, Li PY, Teo G, Rudd PM, Fawcett JW, Foo RSY. Targeting Chondroitin Sulfate Glycosaminoglycans to Treat Cardiac Fibrosis in Pathological Remodeling. Circulation. 2018;137:2497-513. doi: 10.1161/CIRCULATIONAHA.117.030353. PubMed PMID: 29371215.

275. Westergren-Thorsson G, Hedstrom U, Nybom A, Tykesson E, Ahrman E, Hornfelt M, Maccarana M, van Kuppevelt TH, Dellgren G, Wildt M, Zhou X-H, Eriksson L, Bjermer L, Hallgren O. Increased deposition of glycosaminoglycans and altered structure of heparan sulfate in idiopathic pulmonary fibrosis. International Journal of Biochemistry and Cell Biology. 2017;83:27-38. doi: 10.1016/j.biocel.2016.12.005.

276. Guo S, Xue C, Li G, Zhao X, Wang Y, Xu J. Serum Levels of Glycosaminoglycans and Chondroitin Sulfate/Hyaluronic Acid Disaccharides as Diagnostic Markers for Liver Diseases. Journal of Carbohydrate Chemistry. 2015;34:55-69. doi: 10.1080/07328303.2015.1008518.

277. Glycosaminoglycan glycomics using mass spectrometry, (2013).

278. Turiák L, Tóth G, Ozohanics O, Révész Á, Ács A, Vékey K, Zaia J, Drahos L. Sensitive method for glycosaminoglycan analysis of tissue sections. Journal of Chromatography A. 2018;1544:41-8. doi: 10.1016/j.chroma.2018.02.034. PubMed PMID: 29506752.

279. History and overview of antigen retrieval: Methodologies and critical aspects, (2002).

280. Magangane PS, Khumalo NP, Adeola HA. The effect of antigen retrieval buffers on MALDI mass spectrometry imaging of peptide profiles in skin FFPE tissue. Journal of Interdisciplinary Histopathology. 2018;6:26-32. doi: 10.5455/jihp.20180528101354.

281. Klein JA, Meng L, Zaia J. SUPPLEMENTAL DATA: Deep sequencing of complex proteoglycans: a novel strategy for high coverage and site-specific identification of glycosaminoglycan-linked peptides. Molecular and Cellular Proteomics. 2018;17:1578-90. doi: 10.1074/mcp.RA118.000766.

282. Smirnov IP, Zhu X, Taylor T, Huang Y, Ross P, Papayanopoulos IA, Martin SA, Pappin DJ. Suppression of α-cyano-4-hydroxycinnamic acid matrix clusters and reduction of chemical noise in MALDI-TOF mass spectrometry. Analytical Chemistry. 2004;76:2958-65. doi: 10.1021/ac035331j.

283. Wei J, Wu J, Tang Y, Ridgeway ME, Park MA, Costello CE, Zaia J, Lin C. Characterization and Quantification of Highly Sulfated Glycosaminoglycan Isomers by Gated-Trapped Ion Mobility Spectrometry Negative Electron Transfer Dissociation MS/MS. Analytical Chemistry. 2019;91:2994-3001. doi: 10.1021/acs.analchem.8b05283.

284. Miller RL, Guimond SE, Schwörer R, Zubkova OV, Tyler PC, Xu Y, Liu J, Chopra P, Boons GJ, Grabarics M, Manz C, Hofmann J, Karlsson NG, Turnbull JE, Struwe WB, Pagel K. Shotgun ion mobility mass spectrometry sequencing of heparan sulfate saccharides. Nature Communications. 2020;11. doi: 10.1038/s41467-020-15284-y. PubMed PMID: 32198425.

285. Stephens EH, Saltarrelli JG, Baggett LS, Nandi I, Kuo JJ, Davis AR, Olmsted-Davis EA, Reardon MJ, Morrisett JD, Grande-Allen KJ. Differential proteoglycan and hyaluronan distribution in calcified aortic valves. Cardiovascular Pathology. 2011;20:334-42. doi: 10.1016/j.carpath.2010.10.002.

286. Itabashi T, Harata S, Endo M, Takagaki K, Yukawa M, Ueyama K, Toh S. Interaction Between Proteoglycans and α-Elastin in Construction of Extracellular Matrix of Human Yellow Ligament. Connective Tissue Research. 2005;46:67-73. doi: 10.1080/03008200590954078.

287. Fornieri C, Baccarani-Contri M, Quaglino D, Pasquali-Ronchetti I. Lysyl oxidase activity and elastinglycosaminoglycan interactions in growing chick and rat aortas. - Fornieri et al.pdf. Journal of Cell Biology. 1987;105:1463-9.

288. Reinboth B, Hanssen E, Cleary EG, Gibson MA. Molecular interactions of biglycan and decorin with elastic fiber components: Biglycan forms a ternary complex with tropoelastin and microfibril-associated glycoprotein 1. Journal of Biological Chemistry. 2002;277:3950-7. doi: 10.1074/jbc.M109540200.

289. Biology and biomechanics of the heart valve extracellular matrix, (2020).

290. Pilecki B, Holm AT, Schlosser A, Moeller JB, Wohl AP, Zuk AV, Heumüller SE, Wallis R, Moestrup SK, Sengle G, Holmskov U, Sorensen GL. Characterization of Microfibrillar-associated Protein 4 (MFAP4) as a Tropoelastin- and Fibrillin-binding Protein Involved in Elastic Fiber Formation *. Journal of Biological Chemistry. 2016;291:1103-14. doi: 10.1074/JBC.M115.681775. PubMed PMID: 26601954.

291. Yin X, Wanga S, Fellows AL, Barallobre-Barreiro J, Lu R, Davaapil H, Franken R, Fava M, Baig F, Skroblin P, Xing Q, Koolbergen DR, Groenink M, Zwinderman AH, Balm R, de Vries CJM, Mulder BJM, Viner R, Jahangiri M, Reinhardt DP, Sinha S, Waard Vd, Mayr M, Yin (殷晓科) X, Wanga S, Fellows AL, Barallobre-Barreiro J, Lu R, Davaapil H, Franken R, Fava M, Baig F, Skroblin P, Xing Q, Koolbergen DR, Groenink M, Zwinderman AH, Balm R, de Vries CJM, Mulder BJM, Viner R, Jahangiri M, Reinhardt DP, Sinha S, de Waard V, Mayr M. Glycoproteomic Analysis of the Aortic Extracellular Matrix in Marfan Patients. Arteriosclerosis, Thrombosis, and Vascular Biology. 2019;39:1859-73. doi: 10.1161/ATVBAHA.118.312175.

292. Itoh A, Nonaka Y, Ogawa T, Nakamura T, Nishi N. Small leucine-rich repeat proteoglycans associated with mature insoluble elastin serve as binding sites for galectins. Bioscience, Biotechnology, and Biochemistry. 2017;81:2098-104. doi: 10.1080/09168451.2017.1374828.

293. Dey P. Basic and Advanced Laboratory Techniques in Histopathology and Cytology2018:275. doi: 10.1007/978-981-10-8252-8.

294. Chakravarti S, Magnuson T, Lass JH, Jepsen KJ, LaMantia C, Carroll H. Lumican Regulates Collagen Fibril Assembly: Skin Fragility and Corneal Opacity in the Absence of Lumican. The Journal of Cell Biology. 1998;141:1277. doi: 10.1083/JCB.141.5.1277. PubMed PMID: 9606218.

295. Kafienah W, Cheung FL, Sims T, Martin I, Miot S, Ruhland CV, Roughley PJ, Hollander AP. Lumican inhibits collagen deposition in tissue engineered cartilage ☆2008. doi: 10.1016/j.matbio.2008.04.002.

296. Geng Y, Mcquillan D, Roughley PJ. SLRP interaction can protect collagen fibrils from cleavage by collagenases2006. doi: 10.1016/j.matbio.2006.08.259.

297. Mohammadzadeh N, Lunde IG, Andenæs K, Strand ME, Aronsen JM, Skrbic B, Marstein HS, Bandlien C, Nygård S, Gorham J, Sjaastad I, Chakravarti S, Christensen G, Engebretsen KVT, Tønnessen T. The extracellular matrix proteoglycan lumican improves survival and counteracts cardiac dilatation and failure in mice subjected to pressure overload. Scientific Reports 2019 9:1. 2019;9:1-13. doi: 10.1038/s41598-019-45651-9.

298. Dupuis LE, Kern CB. Small Leucine Rich Proteoglycans Exhibit Unique Spatiotemporal Expression Profiles During Cardiac Valve Development. Developmental dynamics : an official publication of the American Association of Anatomists. 2014;243:601. doi: 10.1002/DVDY.24100. PubMed PMID: 24272803.

299. Satta J, Melkko J, Pöllänen R, Tuukkanen J, Pääkkö P, Ohtonen P, Mennander A, Soini Y. Progression of human aortic valve stenosis is associated with tenascin-C expression. Journal of the American College of Cardiology. 2002;39:96-101. doi: 10.1016/S0735-1097(01)01705-3.

300. Cescon M, Gattazzo F, Chen P, Bonaldo P. Collagen VI at a glance. Journal of Cell Science. 2015;128:3525-31. doi: 10.1242/JCS.169748.

301. Luther DJ, Thodeti CK, Shamhart PE, Adapala RK, Hodnichak C, Weihrauch D, Bonaldo P, Chilian WM, Meszaros JG. Absence of Type VI Collagen Paradoxically Improves Cardiac Function, Structure, and Remodeling After Myocardial Infarction. Circulation Research. 2012;110:851-6. doi: 10.1161/CIRCRESAHA.111.252734.

302. Gittenberger-De Groot AC, Bartram U, Oosthoek PW, Bartelings MM, Hogers B, Poelmann RE, Jongewaard IN, Klewer SE. Collagen Type VI Expression during Cardiac Development and in Human Fetuses with Trisomy 21. Anatomical Record - Part A Discoveries in Molecular, Cellular, and Evolutionary Biology. 2003;275:1109-16. doi: 10.1002/AR.A.10126.

303. Klewer SE, Krob SL, Kolker SJ, Kitten GT. Expression of Type VI Collagen in the Developing Mouse Heart. Developmental Dynamics. 1998;211:248-55.

304. Swiderski RE, Daniels KJ, Jensen KL, Solursh M. Type II collagen is transiently expressed during avian cardiac valve morphogenesis. Developmental Dynamics. 1994;200:294-304. doi: 10.1002/AJA.1002000404.

305. Chattopadhyay S, Raines RT. Review collagen-based biomaterials for wound healing. Biopolymers. 2014;101:821-33. doi: 10.1002/bip.22486. PubMed PMID: 24633807.

306. Collagen tissue engineering: Development of novel biomaterials and applications, (2008).

307. Parenteau-Bareil R, Gauvin R, Berthod F. Collagen-based biomaterials for tissue engineering applications. Materials. 2010;3:1863-87. doi: 10.3390/ma3031863.

308. Rane AA, Christman KL. Biomaterials for the treatment of myocardial infarction: A 5-year update. Journal of the American College of Cardiology. 2011;58:2615-29. doi: 10.1016/j.jacc.2011.11.001. PubMed PMID: 22152947.

309. Zhu Y, Matsumura Y, Wagner WR. Ventricular wall biomaterial injection therapy after myocardial infarction: Advances in material design, mechanistic insight and early clinical experiences. Biomaterials. 2017;129:37-53. doi: 10.1016/j.biomaterials.2017.02.032. PubMed PMID: 28324864.

310. McLaughlin S, McNeill B, Podrebarac J, Hosoyama K, Sedlakova V, Cron G, Smyth D, Seymour R, Goel K, Liang W, Rayner KJ, Ruel M, Suuronen EJ, Alarcon EI. Injectable human recombinant collagen matrices limit adverse remodeling and improve cardiac function after myocardial infarction. Nature Communications. 2019;10:4866.

311. Koide T. Triple Helical Collagen-Like Peptides: Engineering and Applications in Matrix Biology. Connective Tissue Research. 2005;46:131-41. doi: 10.1080/03008200591008518.

312. Tanrikulu IC, Forticaux A, Jin S, Raines RT. Peptide tessellation yields micrometre-scale collagen triple helices. Nature Chemistry. 2016;8:1008-14. doi: 10.1038/nchem.2556. PubMed PMID: 27768103.

313. Hosoyama K, Lazurko C, Muñoz M, McTiernan CD, Alarcon EI. Peptide-based functional biomaterials for soft-tissue repair. Frontiers in Bioengineering and Biotechnology. 2019;7:205. doi: 10.3389/fbioe.2019.00205.

314. Swartzlander MD, Blakney AK, Amer LD, Hankenson KD, Kyriakides TR, Bryant SJ. Immunomodulation by mesenchymal stem cells combats the foreign body response to cell-laden synthetic hydrogels. Biomaterials. 2015;41:79-88. doi: 10.1016/j.biomaterials.2014.11.020. PubMed PMID: 25522967.

315. Artzi N, Oliva N, Puron C, Shitreet S, Artzi S, Bon Ramos A, Groothuis A, Sahagian G, Edelman ER. In vivo and in vitro tracking of erosion in biodegradable materials using non-invasive fluorescence imaging. Nature Materials. 2011;10:704-9. doi: 10.1038/nmat3095. PubMed PMID: 21857678.

316. Mertens ME, Hermann A, Bühren A, Olde-Damink L, Möckel D, Gremse F, Ehling J, Kiessling F, Lammers T. Iron oxide-labeled collagen scaffolds for non-invasive MR imaging in tissue engineering. Advanced Functional Materials. 2014;24:754-62. doi: 10.1002/adfm.201301275.

317. Paine MRL, Kooijman PC, Fisher GL, Heeren RMA, Fernández FM, Ellis SR. Visualizing molecular distributions for biomaterials applications with mass spectrometry imaging: A review. Journal of Materials Chemistry B. 2017;5:7444-60. doi: 10.1039/c7tb01100h. PubMed PMID: 32264222.

318. Kokesch-Himmelreich J, Woltmann B, Torger B, Rohnke M, Arnhold S, Hempel U, Müller M, Janek J. Detection of organic nanoparticles in human bone marrow-derived stromal cells using ToF-SIMS and PCA. Analytical and Bioanalytical Chemistry. 2015;407:4555-65. doi: 10.1007/s00216-015-8647-9. PubMed PMID: 25869483.

319. Ulrich TA, Lee TG, Shon HK, Moon DW, Kumar S. Microscale mechanisms of agarose-induced disruption of collagen remodeling. Biomaterials. 2011;32:5633-42. doi: 10.1016/j.biomaterials.2011.04.045. PubMed PMID: 21575987.

320. Chen S, Xiong C, Liu H, Wan Q, Hou J, He Q, Badu-Tawiah A, Nie Z. Mass spectrometry imaging reveals the sub-organ distribution of carbon nanomaterials. Nature Nanotechnology. 2015;10:176-82. doi: 10.1038/nnano.2014.282. PubMed PMID: 25652170.

321. Klerk LA, Dankers PYW, Popa ER, Bosman AW, Sanders ME, Reedquist KA, Heeren RMA. TOF-secondary ion mass spectrometry imaging of polymeric scaffolds with surrounding tissue after in vivo implantation. Analytical Chemistry. 2010;82:4337-43. doi: 10.1021/ac100837n. PubMed PMID: 20462187.

322. Groseclose MR, Andersson M, Hardesty WM, Caprioli RM. Identification of proteins directly from tissue: in situ tryptic digestions coupled with imaging mass spectrometry. Journal of Mass Spectrometry. 2007;42:254-62. doi: 10.1002/JMS.1177.

323. Ahmadi A, McNeill B, Vulesevic B, Kordos M, Mesana L, Thorn S, Renaud JM, Manthorp E, Kuraitis D, Toeg H, Mesana TG, Davis DR, Beanlands RS, DaSilva JN, deKemp RA, Ruel M, Suuronen EJ. The role of integrin alpha2 in cell and matrix therapy that improves perfusion, viability and function of infarcted myocardium. Biomaterials. 2014;35(17):4749-58. Epub 2014/03/19. doi: 10.1016/j.biomaterials.2014.02.028. PubMed PMID: 24631247.

324. Blackburn NJ, Sofrenovic T, Kuraitis D, Ahmadi A, McNeill B, Deng C, Rayner KJ, Zhong Z, Ruel M, Suuronen EJ. Timing underpins the benefits associated with injectable collagen biomaterial therapy for the treatment of myocardial infarction. Biomaterials. 2015;39:182-92. Epub 2014/12/04. doi: 10.1016/j.biomaterials.2014.11.004. PubMed PMID: 25468370.

325. Powers TW, Neely BA, Shao Y, Tang H, Troyer DA, Mehta AS, Haab BB, Drake RR. MALDI imaging mass spectrometry profiling of N-glycans in formalin-fixed paraffin embedded clinical tissue blocks and tissue microarrays. PLoS ONE. 2014. doi: 10.1371/journal.pone.0106255.

326. Sugi Y. Periostin Expression is Altered in Aortic Valves in Smad6 Mutant Mice. Journal of Neonatal Biology. 2012;01. doi: 10.4172/2167-0897.1000101.

327. Saeed AI, Bhagabati NK, Braisted JC, Liang W, Sharov V, Howe EA, Li J, Thiagarajan M, White JA, Quackenbush J. TM4 Microarray Software Suite. Methods in Enzymology. 2006;411:134-93. doi: 10.1016/S0076-6879(06)11009-5. PubMed PMID: 16939790.

328. Calcific Aortic Valve Disease "Omics" Is Timely, But Are We Looking Too Late?, (2020).

329. Razek T, Olthoff K, Reilly PM. Issues in potential organ donor management. Surgical Clinics of North America. 2000;80:1021-32. doi: 10.1016/S0039-6109(05)70111-0.

330. Key factors in paediatric organ and tissue donation: An overview of literature in a chronological working model, (2012).

331. Deng XS, Meng X, Zeng Q, Fullerton D, Mitchell M, Jaggers J. Adult aortic valve interstitial cells have greater responses to toll-like receptor 4 stimulation. Annals of Thoracic Surgery. 2015;99:62-71. doi: 10.1016/j.athoracsur.2014.07.027. PubMed PMID: 25442996.

332. Duan B, Hockaday LA, Das S, Xu C, Butcher JT. Comparison of Mesenchymal Stem Cell Source Differentiation Toward Human Pediatric Aortic Valve Interstitial Cells within 3D Engineered Matrices. Tissue Engineering - Part C: Methods. 2015;21:795-807. doi: 10.1089/ten.tec.2014.0589. PubMed PMID: 25594437.

333. Antequera-González B, Martínez-Micaelo N, Alegret JM. Bicuspid Aortic Valve and Endothelial Dysfunction: Current Evidence and Potential Therapeutic Targets. Frontiers in Physiology. 2020;11:1015. doi: 10.3389/fphys.2020.01015.

334. The collagen family members as cell adhesion proteins, (2007).

335. Šteiner I, Stejskal V, Žáček P. Mast cells in calcific aortic stenosis2017. doi: 10.1016/j.prp.2017.07.016.

336. Ivo˘ivošteiner I, Krbal L, Rozkoš T, Harrer J, Laco J. Calcific aortic valve stenosis: Immunohistochemical analysis of inflammatory infiltrate. Pathology-Research and Practice. 2012;208:231-4. doi: 10.1016/j.prp.2012.02.009.

337. Babu AN, Meng X, Zou N, Yang X, Wang M, Song Y, Cleveland JC, Weyant M, Banerjee A, Fullerton DA. Lipopolysaccharide Stimulation of Human Aortic Valve Interstitial Cells Activates Inflammation and Osteogenesis2008. doi: 10.1016/j.athoracsur.2008.03.008.

338. Mohler ER, Gannon F, Reynolds C, Zimmerman R, Keane MG, Kaplan FS. Bone Formation and Inflammation in Cardiac Valves2001.

339. Hjortnaes J, Butcher J, Figueiredo J-L, Riccio M, Kohler RH, Kozloff KM, Weissleder R, Aikawa E. Valvular heart disease Arterial and aortic valve calcification inversely correlates with osteoporotic bone remodelling: a role for inflammation. doi: 10.1093/eurheartj/ehq237.

340. Gorres KL, Raines RT. Prolyl 4-hydroxylase. Critical Reviews in Biochemistry and Molecular Biology. 2010;45:106-24. doi: 10.3109/10409231003627991. PubMed PMID: 20199358.

341. Wu Y, Puperi DS, Grande-Allen KJ, West JL. Ascorbic acid promotes extracellular matrix deposition while preserving valve interstitial cell quiescence within 3D hydrogel scaffolds. Journal of Tissue Engineering and Regenerative Medicine. 2017;11:1963-73. doi: 10.1002/term.2093. PubMed PMID: 26631842.

342. Shen N, Lin H, Wu T, Wang D, Wang W, Xie H, Zhang J, Feng Z. Inhibition of TGF-β1-receptor posttranslational core fucosylation attenuates rat renal interstitial fibrosis. Kidney International. 2013;84:64-77. doi: 10.1038/KI.2013.82. PubMed PMID: 23486519.

343. Lin H, Wang D, Wu T, Dong C, Shen N, Sun Y, Sun Y, Xie H, Wang N, Shan L. Blocking core fucosylation of TGF-β1 receptors downregulates their functions and attenuates the epithelial-mesenchymal transition of renal tubular cells. https://doiorg/101152/ajprenal004262010. 2011;300:1017-25. doi: 10.1152/AJPRENAL.00426.2010.

344. Richardson WJ, Holmes JW. Emergence of Collagen Orientation Heterogeneity in Healing Infarcts and an Agent-Based Model. Biophysical Journal. 2016;110:2266-77. doi: 10.1016/j.bpj.2016.04.014. PubMed PMID: 27224491.

345. Rogers JD, Holmes JW, Saucerman JJ, Richardson WJ. Mechano-chemo signaling interactions modulate matrix production by cardiac fibroblasts. Matrix Biology Plus. 2021;10:100055. doi: 10.1016/J.MBPLUS.2020.100055.

346. Zhang F, Zhang Z, Lin X, Beenken A, Eliseenkova AV, Mohammadi M, Linhardt RJ. Compositional Analysis of Heparin/Heparan Sulfate Interacting with Fibroblast Growth Factor 3 Fibroblast Growth Factor Receptor Complexes †. doi: 10.1021/bi9006379.

347. Yan J, Stringer SE, Hamilton A, Charlton-Menys V, Götting C, Müller B, Aeschlimann D, Alexander MY. Decorin GAG synthesis and TGF-β signaling mediate Ox-LDL-induced mineralization of human vascular smooth muscle cells. Arteriosclerosis, Thrombosis, and Vascular Biology. 2011;31:608-15. doi: 10.1161/ATVBAHA.110.220749. PubMed PMID: 21205989.

348. Stephens EH, Kearney DL, Grande-Allen KJ. Insight into pathologic abnormalities in congenital semilunar valve disease based on advances in understanding normal valve microstructure and extracellular matrix. Cardiovascular Pathology. 2012;21:46-58. doi: 10.1016/j.carpath.2011.01.002. PubMed PMID: 21349746.

349. Cornett DS, Mobley JA, Dias EC, Andersson M, Arteaga CL, Sanders ME, Caprioli RM. A Novel Histology-directed Strategy for MALDI-MS Tissue Profiling That Improves Throughput and Cellular Specificity in Human Breast Cancer *. Molecular & Cellular Proteomics. 2006;5:1975-83. doi: 10.1074/MCP.M600119-MCP200.

350. Angel PM, Rujchanarong D, Pippin S, Spruill L, Drake R. Mass Spectrometry Imaging of Fibroblasts: Promise and Challenge. Expert Re. 2021. doi: 10.1080/14789450.2021.1941893.

351. Endothelial-to-Mesenchymal Transition, (2019).

352. Angel PM, Saunders J, Clift CL, White-Gilbertson S, Voelkel-Johnson C, Yeh E, Mehta A, Drake RR. A Rapid Array-Based Approach to N-Glycan Profiling of Cultured Cells. Journal of Proteome Research. 2019;18:3630-9. doi: 10.1021/acs.jproteome.9b00303.

353. Taylor MJ, Lukowski JK, Anderton CR. Spatially Resolved Mass Spectrometry at the Single Cell: Recent Innovations in Proteomics and Metabolomics. Journal of

the American Society for Mass Spectrometry. 2021;32:872-94. doi: 10.1021/JASMS.0C00439.

354. Flint LE, Hamm G, Ready JD, Ling S, Duckett CJ, Cross NA, Cole LM, Smith DP, Goodwin RJA, Clench MR. Characterization of an Aggregated Three-Dimensional Cell Culture Model by Multimodal Mass Spectrometry Imaging. Analytical Chemistry. 2020;92:12538. doi: 10.1021/ACS.ANALCHEM.0C02389. PubMed PMID: 32786495.

355. Neumann EK, Djambazova KV, Caprioli RM, Spraggins JM. Multimodal Imaging Mass Spectrometry: Next Generation Molecular Mapping in Biology and Medicine2020. doi: 10.1021/jasms.0c00232.

356. Cirka HA, Uribe J, Liang V, Schoen FJ, Billiar KL. Reproducible in vitro model for dystrophic calcification of cardiac valvular interstitial cells: insights into the mechanisms of calcific aortic valvular disease. Lab on a Chip. 2017;17:814-29. doi: 10.1039/c6lc01226d. PubMed PMID: 28128382.

357. Lim J, Ehsanipour A, Hsu JJ, Lu J, Pedego T, Wu A, Walthers CM, Demer LL, Seidlits SK, Tintut Y. Inflammation Drives Retraction, Stiffening, and Nodule Formation via Cytoskeletal Machinery in a Three-Dimensional Culture Model of Aortic Stenosis. The American Journal of Pathology. 2016;186:2378. doi: 10.1016/J.AJPATH.2016.05.003. PubMed PMID: 27392969.

358. Bowler MA, David Merryman W. In vitro models of aortic valve calcification: solidifying a system2014. doi: 10.1016/j.carpath.2014.08.003.

359. Weber A, Pfaff M, Schöttler F, Schmidt V, Lichtenberg A, Akhyari P. Reproducible In Vitro Tissue Culture Model to Study Basic Mechanisms of Calcific Aortic Valve Disease: Comparative Analysis to Valvular Interstitials Cells. Biomedicines. 2021;9. doi: 10.3390/BIOMEDICINES9050474. PubMed PMID: 33925890.

360. Hjortnaes J, Camci-Unal G, Hutcheson JD, Jung SM, Schoen FJ, Kluin J, Aikawa E, Khademhosseini A. Directing valvular interstitial cell myofibroblast-like differentiation in a hybrid hydrogel platform. Advanced Healthcare Materials. 2015;4:121-30. doi: 10.1002/adhm.201400029. PubMed PMID: 24958085.

361. van der Valk DC, van der Ven CFT, Blaser MC, Grolman JM, Wu PJ, Fenton OS, Lee LH, Tibbitt MW, Andresen JL, Wen JR, Ha AH, Buffolo F, Mil Av, Bouten CVC, Body SC, Mooney DJ, Sluijter JPG, Aikawa M, Hjortnaes J, Langer R, Aikawa E. Engineering a 3d-bioprinted model of human heart valve disease using nanoindentation-based biomechanics. Nanomaterials. 2018;8. doi: 10.3390/nano8050296.

362. Duan B, Hockaday LA, Das S, Xu C, Butcher JT. Comparison of Mesenchymal Stem Cell Source Differentiation Toward Human Pediatric Aortic Valve Interstitial Cells within 3D Engineered Matrices. Tissue Engineering Part C: Methods. 2015;21:795-807. doi: 10.1089/ten.tec.2014.0589. PubMed PMID: 25594437.

363. Gee TW, Richards JM, Mahmut A, Butcher JT. Valve Endothelial-Interstitial Interactions Drive Emergent Complex Calcific Lesion Formation in Vitro. Biomaterials. 2021:120669. doi: 10.1016/j.biomaterials.2021.120669.

364. Mongkoldhumrongkul N, Latif N, Yacoub MH, Chester AH. Effect of Side-Specific Valvular Shear Stress on the Content of Extracellular Matrix in Aortic Valves. Cardiovascular engineering and technology. 2018;9:151-7. doi: 10.1007/s13239-016-0280-z. PubMed PMID: 27709350.

365. Weinberg EJ, MacK PJ, Schoen FJ, García-Cardeña G, Kaazempur Mofrad MR. Hemodynamic Environments from Opposing Sides of Human Aortic Valve Leaflets

Evoke Distinct Endothelial Phenotypes in Vitro. Cardiovascular Engineering. 2010;10:5-11. doi: 10.1007/s10558-009-9089-9. PubMed PMID: 20107896.

366. Weston MW, Yoganathan AP. Biosynthetic activity in heart valve leaflets in response to in vitro flow environments. Annals of Biomedical Engineering. 2001. doi: 10.1114/1.1397794.

367. Wong AK, LLanos P, Boroda N, Rosenberg SR, Rabbany SY. A Parallel-Plate Flow Chamber for Mechanical Characterization of Endothelial Cells Exposed to Laminar Shear Stress. Cellular and molecular bioengineering. 2016;9:127-38. doi: 10.1007/s12195-015-0424-5. PubMed PMID: 28989541.

368. Yap CH, Saikrishnan N, Tamilselvan G, Yoganathan AP. Experimental Technique of Measuring Dynamic Fluid Shear Stress on the Aortic Surface of the Aortic Valve Leaflet. Journal of Biomechanical Engineering. 2011;133:061007. doi: 10.1115/1.4004232.

369. Duan B, Xu C, Das S, Chen JM, Butcher JT. Spatial Regulation of Valve Interstitial Cell Phenotypes within Three-Dimensional Micropatterned Hydrogels2019. doi: 10.1021/acsbiomaterials.8b01280.

370. Ford AJ, Rajagopalan P. Extracellular matrix remodeling in 3D: implications in tissue homeostasis and disease progression. Wiley Interdisciplinary Reviews: Nanomedicine and Nanobiotechnology. 2018. doi: 10.1002/wnan.1503.

371. Huebner P, Warren PB, Chester D, Spang JT, Brown AC, Fisher MB, Shirwaiker RA. Mechanical properties of tissue formed in vivo are affected by 3D-bioplotted scaffold microarchitecture and correlate with ECM collagen fiber alignment. Connective Tissue Research. 2020;61:190-204. doi: 10.1080/03008207.2019.1624733.

372. Blum KM, Drews JD, Breuer CK. Tissue-Engineered Heart Valves: A Call for Mechanistic Studies. doi: 10.1089/ten.teb.2017.0425.

373. Blum KM, Drews JD, Breuer CK. Tissue-Engineered Heart Valves: A Call for Mechanistic Studies. Tissue Engineering: Part B. 2018;24. doi: 10.1089/ten.teb.2017.0425.

374. A S Geha HL, H C Stansel Jr, J F Cornhill, J W Kilman, M J Buckley, W C Roberts. Late failure of porcine valve heterografts in children. J Thorac Cardiovasc Surg. 1979;78:351-64.

375. Ruzmetov M, Vijay P, Rodefeld MD, Turrentine MW, Brown JW. Evolution of aortic valve replacement in children: A single center experience B2006. doi: 10.1016/j.ijcard.2005.11.011.